JUSTUS-LIEBIG-
UNIVERSITÄT
GIESSEN

Functional Nanofibers Based on Transition Metal Dichalcogenides for Rigid and Flexible Energy Storage

Dissertation

Zur Erlangung des akademischen Doktorgrades

„Doctor rerum naturalium“

- Dr. rer. nat. -

Eingereicht am Fachbereich 08

Biologie und Chemie

der Justus-Liebig-Universität Gießen

von

Felix Boll

September 2024

Selbstständigkeitserklärung

Die vorliegende Arbeit und die zugrunde liegenden Experimente, sowie die daraus resultierenden Veröffentlichungen, wurden in der Zeit von Februar 2021 – Dezember 2024 am Physikalisch-Chemischen Institut der Justus-Liebig-Universität in den Arbeitsgruppen von Prof. Dr. Bernd Smarsly und Prof. Dr. Teresa Gatti angefertigt.

Ich erkläre:

Ich habe die vorgelegte Dissertation selbstständig und ohne unerlaubte fremde Hilfe und nur mit den Hilfen angefertigt, die ich in der Dissertation angegeben habe. Alle Textstellen, die wörtlich oder sinngemäß aus veröffentlichten Schriften entnommen sind, und alle Angaben, die auf mündlichen Auskünften beruhen, sind als solche kenntlich gemacht. Ich stimme einer evtl. Überprüfung meiner Dissertation durch eine Antiplagiat-Software zu. Bei den von mir durchgeführten und in der Dissertation erwähnten Untersuchungen habe ich die Grundsätze guter wissenschaftlicher Praxis, wie sie in der „Satzung der Justus-Liebig-Universität Gießen zur Sicherung guter wissenschaftlicher Praxis“ niedergelegt sind, eingehalten.

The present thesis and all practical work were prepared in the period of February 2021 – December 2024 at the Institute of Physical Chemistry of the Justus-Liebig-University Giessen in the working group of Prof. Dr. Bernd M. Smarlsy.

I declare

that I have completed this dissertation single-handedly without the unauthorized help of a second party and only with the assistance acknowledged therein. I have appropriately acknowledged and cited all text passages that are derived verbatim from or are based on the content of published work of others, and all information relating to verbal communications. I consent to the use of an anti-plagiarism software to check my thesis. I have abided by the principles of good scientific conduct laid down in the charter of the Justus Liebig University Giessen „Satzung der Justus-Liebig-Universität Gießen zur Sicherung guter wissenschaftlicher Praxis“ in carrying out the investigations described in the dissertation.

Datum	Unterschrift

Dekan:	Prof. Dr. Holger Zorn
Erstgutachter:	Prof. Dr. Bernd M. Smarsly
Zweitgutachterin:	Prof. Dr. Teresa Gatti
Diese Dissertation wurde eingereicht am:	25. September 2024
Termin der Disputation:	05. Dezember 2024

Danksagungen

Als erstes möchte ich Prof. Dr. Teresa Gatti für die Ermöglichung meines Doktors danken. Durch ihre tatkräftige Unterstützung, den wissenschaftlichen Austausch und die Ermöglichung von Forschungsreisen und interkulturellem Austausch, habe ich viele Erfahrungen sammeln können, die mir sonst verwehrt gewesen wären. Besonders möchte ich mich bei Prof. Dr. Bernd Smarsly bedanken, der mich seit dem Beginn meiner Bachelorarbeit vor über sechs Jahren betreut hat. Ohne diese Unterstützung hätte ich niemals Erlebnisse wie den Austausch nach Japan erleben können, der bis heute ein prägender Abschnitt meines Lebens ist und immer bleiben wird. Auch möchte ich Prof. Dr. Hiromitsu Kozuka und Dr. Pascal Cop danken, die mich auf dem Weg zum Wissenschaftler immer tatkräftig unterstützt haben und maßgeblich an meiner wunderbaren Zeit in Japan während des Studiums mitgewirkt haben. Ihr habt mir den Mut und das Wissen vermittelt mich auf den Pfad der Promotion zu begeben und ihr habt mir einen wunderbaren Teil von Wissenschaft, den Austausch, Respekt und Spaß vermittelt, den es bedeuten kann zu Forschen. Ich danke meinen Studenten Melissa Happel und Leonardo Merola, die viele Stunden im Labor verbrachten und mir tatkräftig für diese Arbeit zur Seite standen. Der wichtigste Unterstützer meines Studiums und der Promotion ist Luka Dornseifer, danke für deine tatkräftige Unterstützung und das gemeinsame Überwinden aller Hürden, die durch das und während des Studiums auf uns zu kamen. Und danke für die unvergessliche Zeit in Japan mit dir. <3

Die besten Freunde des Lebens sind für mich die größte Quelle und Stütze für Kraft und Motivation. Danke Marvin, Jonas, Julius, Luka, Mathis, Daniel, der kleine Marlon, Sophie, Laura, Mia, Svenja, Hanna und Leonie[2], die alle für mich die letzten zehn Jahre des Studiums, der Promotion und darüber hinaus zu dem gemacht haben, was sie waren. Danke an meine Familie, Mama, Papa, Laura und David, es ist schön so liebevolle, sich kümmernde Eltern und eine Schwester zuhaben, die immer ein offenes Ohr hat. Vielen Dank an euch für eine so tolle Familie. Ich danke auch meinen Freunden und Arbeitskollegen Raoul, Fabian, Talli, Paul, Christian, Lysander, Aline, Eric, Luca, Sara, Micaela, Matteo und Roberto, sowie Rafael und Sebastian. Ich bin sehr froh so viel Freude in diversen Mittagspausyeahn und Erlebnissen mit euch teilen zu können! Danke für den „Felix‘ supporting room“ und den ganzen Spaß!

Zuletzt gilt mein Dank Leonie, die mich seit über drei Jahren unterstützt, immer für mich da ist und mit mir auf unsere Zukunft hin fiebert. Danke. Ich liebe dich.

Zusammenfassung

Die Reduktion von CO_2 Emissionen ist eine unabdingbare Konsequenz für das Weiterbestehen des globalen Ökosystems. Zum Erreichen dieses Ziels muss die gesamte Weltwirtschaft den Übergang von einer rohölbasierten hin zu einer von erneuerbaren Energien angetriebenen Gesellschaft und Wirtschaft vollbringen. Energiespeicherung, ihre Nutzung und das Transportwesen sind die entscheidenden Sektoren für eine effiziente Energienutzung. Zentrale Bestandteile dieser Entwicklung sind neue Anwendungen und technische Lösungen für fortschrittliche Batterie- und Kondensatormaterialien. Nach der Entdeckung von Graphen vor 20 Jahren als das erste sogenannte „2D Material“, sind kohlenstoffbasierte Materialen aufgrund ihrer hohen spezifischen Oberfläche und der großen Leitfähigkeit zum Gegenstand und Mittelpunkt der Kondensatorforschung herangewachsen. Diese Eigenschaften sind ideal für die Entwicklung von Superkondensatoren, welche die Brücke bilden zwischen Batterien mit hoher Energiedichte und Kondensatoren mit hoher Leistungsdichte. Zusätzlich hat die Entdeckung von Graphen einen weiteren wissenschaftlichen Zweig eröffnet, die Forschung an zweidimensionalen Materialien. Hier sind besonders Übergangsmetalldichalkogenide hervorzuheben, die im Gegensatz zu Graphen eine Bandlücke aufweisen. Aufgrund ihrer Eigenschaften ist ein breites Forschungsspektrum für diese Materialien in den Bereichen von Energiespeicherung, Transistortechnik, Wasserstoffsynthese und Sensortechnik gewachsen. Die Kombination von Übergangsmetalldichalkogeniden mit Kohlenstoffmaterialien ist Gegenstand der Forschung für flexible und leichte Energiespeicherung, dessen Bedarf in der heutigen Welt stetig am Wachsen ist.

Diese Dissertation leistet in den Themen der Entwicklung und Optimierung von Energiespeichersystemen, mit besonderem Augenmerk auf Superkondensatoren und flexible Energiespeicher, ihren Beitrag. Auf der einen Seite liegt der Fokus auf fundamentaler Verbesserung im Herstellungsprozess und der Temperierung von Kohlenstoffnanofasern, zur Erhöhung der spezifischen Kapazität, welche eine wichtige Rolle als Trägermaterialien in Superkondensatoren einnehmen. Auf der anderen Seite untersucht diese Dissertation die Kombination von diversen Kohlenstoffmaterialien mit den oben genannten Übergangsmetalldichalkogeniden. Dafür wurde ein wasserbasierter Prozess zur Exfolierung von WS_2, MoS_2 und Bi_2S_3 Materialien verwendet, um flexible Kondensatoren und Dünnfilme herzustellen.

Besonderes Augenmerk wurde hierbei auf die Optimierung von Exfolierungsprozessen für das jeweilige Übergangsmetalldichalkogenid gelegt. Die jeweiligen Tenside und ihre idealen Konzentrationen für die Exfolierung wurden untersucht, um die Effizienz des Prozesses und die Konzentration der Suspensionen zu optimieren. Ziel ist die Verbesserung und Verwendung von wasserbasierten Verfahren als nachhaltigere Alternative für die Verwendung von N-Methyl-2-pyrrolidon, welches aufgrund seiner Eigenschaften häufig bevorzugt wird.

Das Wissen aus Exfolierung und der Herstellung von Nanofasern wurde genutzt, um flexible, symmetrische Kondensatoren basierend auf Polyethylennanofasern herzustellen. Hierfür wurde zweidimensionales WS_2 mit Kohlenstoffmaterialien wie Kohlenstoffnanoröhrchen und Ruß kombiniert. Durch diese Materialkombination konnten Kondensatoren hergestellt werden, die Synergieeffekte zwischen den aktiven Materialien aufzeigten. Diese Effekte ermöglichen verbesserte elektrochemische Eigenschaften wie zum Beispiel die Erhöhung der spezifischen Kapazität und leisten somit einen fundamentalen Beitrag zur Forschung an leichten und flexiblen Energiespeichersystemen.

Abstract

The urgent transition from a fossil fuel-based economy to one powered by renewable energy is critical for reducing CO_2 emissions and ensuring global ecosystem stability. Energy storage, energy consumption and transportation are the crucial sectors for efficient energy usage. Central to this effort are new approaches and technical solutions for advanced battery and capacitor materials. Carbon-based materials, particularly since the discovery of graphene as the first 2D material 20 years ago, have gained significant attention for their high surface area and conductivity. These properties are ideal for the development of supercapacitors, which are bridging the gap between high-power density materials like capacitors and high-energy density materials like batteries. After the discovery of graphene, transition metal dichalcogenides have emerged as interesting materials due to their intrinsic bandgap, which graphene lacks. Therefore, these materials are explored for various applications, including charge storage, transistors, hydrogen production and sensing. This dissertation contributes to the field by developing and optimizing charge storage devices, with particular emphasis on supercapacitors and flexible energy storage. On the one hand, it focuses on the fundamental improvement of carbon nanofibers, being a backbone and key material for supercapacitor applications. Here, the optimization of the temperature treatment was done to increase the specific capacitance and improve the performance of the supercapacitor. On the other hand, the dissertation explores the combination of carbon materials with transition metal dichalcogenides. Therefore, water-based exfoliation processes were used to obtain bidimensional WS_2, MoS_2 and Bi_2S_3 suspensions for applications as flexible capacitors or thin films. Emphasis was put on optimizing surfactant species and their concentrations for the individual transition metal dichalcogenides following the urge for greener methods in production using water-surfactant combinations instead of N-Methyl pyrrolidone. This knowledge gained from these studies was applied to combine carbon materials with bidimensional WS_2 to investigate the energy storage properties in flexible and symmetric capacitors produced from poly(ethylene oxide) fibers. Using the combination of carbon-based materials like carbon black and multi-walled carbon nanotubes with bidimensional WS_2 and polymer fibers as backbone material, we were able to demonstrate a flexible symmetric capacitor device.

Abbreviation List

Abbreviation	Description	Abbreviation	Description
2D	Bidimensional	NMP	N-Methyl pyrrolidone
AcAc	Acetyl acetate	OHP	Outer Helmholtz Plane
ALD	Atomic layer deposition	PANI	Polyaniline
BET	Brunauer-Emmet-Teller	P_d	Power density
CA	Cellulose acetate	PEDOT	Poly-3,4-ethylendioxythiophen
CB	Carbon black	PEO	Polyethylene oxide
CNFs	Carbon nanofibers	PI	Polyimide
CNTs	Carbon nanotubes	PLD	Pulse laser deposition
C_s	Specific capacitance	PMMA	Poly(methyl methacrylate)
CV	Cyclic voltammetry	PSS	Polystyrene sulfonate
CVD	Chemical vapor deposition	PVA	Polyvinyl alcohol
D	Directionality coefficient	PVP	Polyvinyl pyrrolidone
DFT	Density functional theory	rGO	Reduced graphene oxide
DLS	Dynamic light scattering	SA-LPE	Surfactant assisted liquid phase exfoliation
E_d	Energy density	SCs	Super capacitors
$E_{S,L}$	Surface energy liquid	SDBS	Sodium dodecylbenzene sulfonate
$E_{S,WS2}$	Surface energy WS_2	SDS	Sodium dodecyl sulfate
EDL	Electrical double layer	SEM	Scanning electron microscopy
EDLC	Electric double layer capacitor	SIBs	Sodium ion batteries
EDX	Energy dispersive X-ray spectroscopy	TEM	Transition electron microscopy
EtOH	Ethanol	TGA	Thermo gravimetric analysis
FWHM	Full Width at Half Maximum	TMDCs	Transition metal dichalcogenides
GO	Graphene oxide	UV-Vis	UV (ultra violet)-Vis (visible)
IHP	Inner Helmholtz Plane	v_0	Vibrational ground state
IPA	Isopropanol	v_1-v_6	Vibrational energy states 1 – 6
LIBs	Lithium Ion Batteries	VdW	Van-der-Waals
LPE	Liquid phase Exfoliation	XPS	X-ray photoelectron spectroscopy
MBE	Molecular beam epitaxy	XRD	X-ray diffraction
MWCNTs	Multi-walled carbon nanotubes	ZP	Zeta potential
NaCh	Sodium cholate		

Contents

1. Introduction

Climate crisis emphasizes the scientific community to focus on the development and improvement of key technologies for succeeding the transition from a fossil fuel-driven economy towards a less CO_2 emitting one. Energy production and its distribution is the largest CO_2-producing industry. With about 13 million barrels per day petrochemical industry is the second largest consumer of crude oil which is only 13.49 % of the daily production of 96.4 million barrels per day according to Statista.[1,2] Therefore, a majority of about 86 % of crude oil is used for energy production in the sectors of transportation, heating and electricity. Humanity's reliance on energy has intensified with advancements in technology and digitalization, leading to increased energy consumption. Additionally, the shift in the mobility sector from fossil fuel-driven engines to electric vehicles further amplifies energy demand. A majority of energy demand in the past was met by fossil fuels and as shown above, is mostly until today. However, in response to the climate crisis, the transition from fossil fuels to CO_2-neutral energy sources is becoming increasingly crucial. Addressing this need, primary energy production focuses on CO_2-neutral sources such as solar power, wind power, biomass, and hydroelectric power plants (see **Figure 1a**). From 2004 to 2022 the share of renewable energy production in Europe increased nearly 2.5-fold, rising from 15.9 % in 2004 up to 39.4 % in 2022.[3] As a result, renewable energy now constitutes the largest segment of primary energy production in Europe. However, the reliance on wind- and solar power introduces a challenge: These sources are characterized by an inconsistent power profile – if there is no wind and no sunlight, less or no power is generated. To address this issue, it is essential to store excess energy generated during periods of high production for use during low-power phases, such as at night. Consequently, a diversified energy storage system is crucial for balancing peak consumption and periods of low production, ensuring a stable and reliable electricity grid across Europe. Further, reliance on single elements and materials, such as lithium, poses risks to the European Union’s energy independence. Therefore, diversification is not only important for the energy grid but from the materials’ perspective as well. To mitigate these risks, a variety of energy storage solutions have been developed, including sodium-ion batteries (SIBs), Vanadium redox flow batteries, smart electricity grids including car batteries as a buffer, flywheels, hydroelectric storage, compressed air energy storage and many more types of batteries, capacitors and physical energy storage systems have that been developed to

diversify energy storage.[4] Among these, one promising example for energy storage devices are transition metal dichalcogenides (TMDCs). For instance, the substitution of graphite in lithium-ion batteries (LIBSs) with WS_2 for example was achieving 45 % higher capacitances referred to the theoretical limit of graphite.[5–7] The layered structure of TMDCs cannot only be used for LIBs but also for the intercalation of sodium for SIB applications.[8,9] Lastly, the large surface area that layered TMDCs provide addresses the major need for supercapacitor applications.[10,11] To fully leverage the advantageous properties of TMDCs, single layers have to be separated, as this transition from bulk material to monolayers results in a shift from an indirect to a direct band gap.[12] The interest towards 2D materials arose when Novoselov and Geim first excluded single layers of graphite into graphene in 2004.[13] As illustrated in **Figure 1b** between 2000 and 2005, exfoliation – the process of separating single layers of 2D materials – became prominent in the scientific community. With the rise of the liquid phase exfoliation (LPE), Coleman et al. in 2011 were exfoliating several different types of TMDCs enabling the effective application of TMDCs.[14] Especially for transistors, sensors and energy storage from 2013 many articles were published as depicted in **Figure 1c**. Since then, TMDCs have become integral to various scientific fields, going from solar cell applications and transistors to energy storage and flexible electronics. In recent years, aside from their applications in batteries, the research focus on TMDCs has increasingly shifted towards supercapacitors (SCs). This shift is driven by the large surface area of TMDCs, which is a critical factor for optimizing SC performance, as the surface area is key to maximize the charge storage. The potential of TMDCs in supercapacitors, demonstrating impressive energy density (E_d) and power density (P_d), represents a significant breakthrough. These properties not only promise advancements in large-scale energy storage but also hold considerable promise for flexible electronics. The high energy densities achievable with TMDC composites make them particularly attractive for applications in wearable devices, where flexibility and efficiency are crucial.[15,16] Low weight and flexibility are essential characteristics of electronic devices designed for everyday use. Given the synergistic effects observed between TMDCs and carbon composites in energy storage applications, I chose to investigate these material combinations in my dissertation.[7,9,14,17–19]

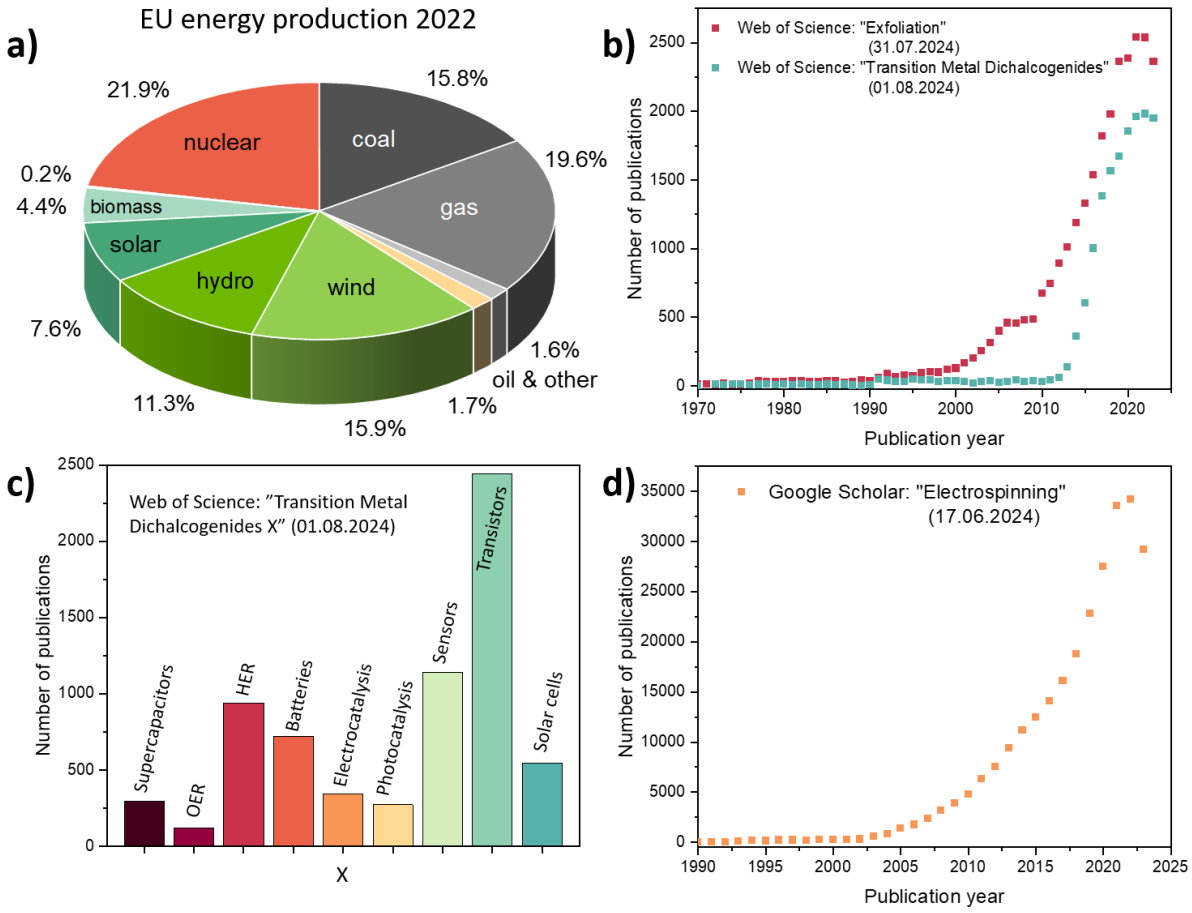

Figure 1: a) Energy production of the European Union in 2022, staggered by the producing source. **b)** The number of publications in the "Web of Science" using the keywords "Exfoliation" and "Transition Metal Dichalcogenides" plotted against the years going from 1970 until today. **c)** The number of publications in "Google Scholar" using the keyword "Electrospinning" plotted against the years from 1990 until today. **d)** The number of publications in the "Web of Science" using the keyword "Transition Metal Dichalcogenides X" plotted against X. X stands for the in the diagram described keywords.

By exploring the interplay between TMDCs and carbon materials, my research aims to leverage their combined properties to enhance the performance and practicality of energy storage solutions, particularly in flexible and wearable electronics. For clothing and flexible applications, fibers are an excellent choice as a backbone material due to their high surface area and inherent flexibility. Electrospinning allows the production of thin fibers ranging from several nm to µm, offering large surface-to-volume ratios and significant nano-porosity. These physical properties are beneficial, especially for SCs. With the rise of nanomaterials and their expanding range of applications, including TMDCs, electrospinning became a prominent field of research (see **Figure 1d**), enabling the implementation of nanomaterials into macroscopic tissues for devices, such as flexible electronics or membranes.[20,21]

During my dissertation, I focused on exploring nanomaterials for flexible energy storage devices, specifically addressing the exfoliation process and the preparation of fibrous materials using electrospinning. In **publication 1**, I concentrated on optimizing CNFs as backbone materials for SC applications. The samples were prepared by electrospinning polyacrylonitrile dissolved in dimethyl formamide, followed by various temperature treatments for carbonization. The stabilization temperature of the polymer fibers and their subsequent carbonization under a nitrogen atmosphere were found to significantly influence the final performance of the supercapacitors. Our work emphasized optimizing the charge storage capacity by controlling the surface area through precise heat treatments. Electrospinning also enabled the preparation of flexible substrates, which we further explored in **publication 2**. Here, we combined electrospinning with TMDC-exfoliation to investigate the synergetic effect of carbon-based materials, such as carbon nanotubes (CNTs) and carbon black (CB), with WS_2. The composites were dispersed into a polymer solution, enabling the electrospinning of suspensions to create flexible capacitors that leverage both their electrochemical properties and mechanical resilience. Our main focus was on optimizing the performance and spinnability by adjusting the ratios of active species. These flexible capacitors maintained their structure through several bending cycles and additionally demonstrated clear synergistic effects between the carbon materials and exfoliated WS_2 sheets. Given the promising results with 2D-WS_2 as a representative TMDC, the exfoliation process became a key area of focus in **Publications 3 and 4**. We investigated the exfoliation conditions for MoS_2, WS_2, and Bi_2S_3 to optimize their application in gels, fibers, and thin films. Various surfactants at different concentrations were tested to understand their impact on the stability, concentration, and degree of exfoliation in the resulting TMDC suspensions. Further analysis of the stable 2D-WS_2 suspensions was conducted in **Publication 5**, where these suspensions were applied to gel-like materials. My role involved characterizing and producing exfoliated WS_2 nanosheets, which Matteo Crisci then used to create WS_2-polyaniline (PANI) hybrid materials for flexible energy storage and pressure sensing applications. In summary, the exfoliation of various suspensions and electrospinning techniques were central to my work as a doctoral student, as I sought to combine nanoparticle production with manufacturing methods to develop devices suited for energy storage and flexible applications.

2. Theoretical Background

2.1. Production of Transition Metal Dichalcogenides

The topic of exfoliation arose in 2004 when Novoselov and Geim were the first being able to produce monolayers of graphite – graphene. Additionally, they were able to show excellent conductive properties of graphene for electric currents.[13,22,23] There was significant interest in this new material due to its unique properties, such as large in-plane conductivity and high mechanical strength. This interest extended to graphene-derived species like CNTs, nanoribbons, graphene oxides, and graphene-based composites.[24–28] With the successful delamination quickly other materials got into the focus of the scientific community having properties different to graphene. The zero bandgap of graphene is exceptional for electronic conductivity but excludes graphene in next-generation semiconductor applications.[29] Here, TMDCs jump in having tuneable band gap compositions with an indirect-direct bandgap transition in the bidimensional state.[30,31] Comparable to graphite the structure of TMDCs is characterized by in-plane covalent bonds between the chalcogenides and the metal atoms. Out-of-plane only weak Van-der-Waals (VdW) interactions are present facilitating the mechanical exfoliation of individual layers of the material.[12,14,30,32,33] During this separation quantum confinement occurs causing a change of the electronic structure affecting the band-gap.[31,34] For technical applications, the direct band gap of two-dimensional MoS_2, is particularly interesting because, unlike graphene, it does not require complex fabrication to achieve a tuneable bandgap. The first example of a transistor based on MoS_2 monolayers was given by Radisavljevic et al. in 2011.[35] The quantum confinement of the d-electrons in materials like MoS_2 leading to an indirect-direct band gap transition that was proven by Splendiani et al. in 2010 showing strong photoluminescence after exfoliation. This discovery highlighted the potential for precisely tuning the electronic structure on the nanoscale.[33]

2.1.1 Exfoliation

The production of bidimensional materials in general is able by following two approaches: Bottom-up and Top-down as shown in **Figure 2**. Bottom-up syntheses like chemical vapour deposition (CVD), atomic layer deposition (ALD), electrochemical deposition or wet-chemical approaches like sol-gel or hydrothermal syntheses use small building blocks, molecules or atoms for the preparation of larger structures, special shapes or thin layers of product.[37,38]

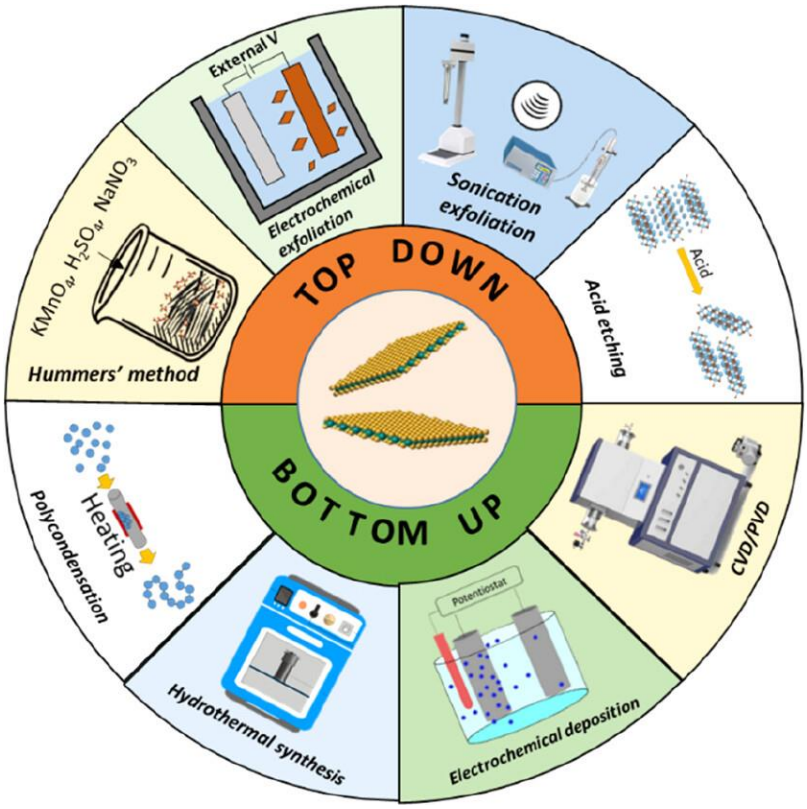

Figure 2: Differentiation between top-down and bottom-up approaches for the production of 2D materials. Reprinted with permission from Mengjiao Wang, Michal Langer, Roberto Altieri, Matteo Crisci, Silvio Osella, Teresa Gatti, ACS Nano 2024, 18, 13, 9245-84. Copyright 2024 American Chemical Society.[36]

As an example, we look at the WS_2 production. In CVD normally WS_2 is produced directly from the sulfurization of WO_3 using sulfur or H_2S as sulfur sources.[39–41] In the case of ALD normally quite expensive precursor materials are used like $W(CO)_6$ or bis(*tert*-butylimido)-bis(dimethylamido)-tungsten to produce monolayered materials of high quality.[42,43] In contrast, while other bottom-up approaches like hydrothermal synthesis allow for the growth of nanoparticles in various shapes, it does not offer precise control over their thickness or the number of layers.[44–48] On the other hand, methods like CVD and ALD can produce single layers of WS_2, but they come with significant drawbacks: the processes are long, expensive, and poorly scalable, yielding only small quantities of high-quality monolayered material.[49,50]

Starting from the other side, the top-down approaches show other difficulties. For example, in pulsed laser deposition (PLD) and molecular beam epitaxy (MBE) elemental W and S in a stochiometric ratio or WS_2 targets are typically used as precursors. These methods primarily yield polycrystalline and multi-layered systems.[51–53] Here, as for hydrothermal synthesis, controlling the number of layers is challenging since bulk material is randomly divided into smaller particles down to the nanoscale. The top-down approach of separating individual layers is feasible only for specific types of materials like graphite and TMDCs where distinct bonding interactions exist between layers.[32,33,54,55] This process, known as exfoliation, is unique because it requires applying enough force to overcome VdW forces between layers while keeping the atomic bonds within the material sheets intact.[14,56,57] Many approaches have been developed to successfully exfoliate 2D materials like graphite, following its initial exfoliation using scotch tape. Nowadays commonly used methods are electrochemical intercalation, ball milling, ultrasonication and shear mixing to name a few.[10,14,37,54,56–58] Ball milling is the simplest method but is less commonly used today due to issues with contamination and low scalability.[37] Ion intercalation, particularly with Li^+ ions, weakens VdW interactions by increasing the interlayer distance due to repulsive forces. However, this method also risks contamination. Additionally, electrochemical methods containing Lithium are expensive and energy-consuming.[10,59] Shear mixing and tip sonication will be discussed extensively, as we used these methods for exfoliation. They are commonly employed, easily scalable and cost-effective. Both techniques operate in liquid media, which is why they are collectively referred to as Liquid Phase Exfoliation (LPE).[60]

Here, the material is exfoliated using strong shock waves in the case of tip sonication or by large shear forces caused by a rotor-stator couple under high rotation speed.[37,54] For both methods a three-step process occurs during exfoliation: First, the VdW forces are overcome by energy input. The second step is the stabilization by penetration of solvent within the layers. In the final step, particles with varying average numbers of layers need to be separated. The exfoliated material is polydisperse which means that a spectrum of particle sizes and numbers of layers is obtained after exfoliation. This is shown from dried suspension Scanning electron microscopy (SEM) images and dynamic light scattering (DLS) data in **Figure 5b** & **c**. To separate well-exfoliated sheets from bulk-like particles, gravitational methods such as sedimentation or centrifugation are used to separate lighter from heavier particles.[60–62]

N-methyl pyrrolidone (NMP) has proven to be an ideal solvent for stabilizing exfoliated sheets of graphene, MoS_2 and WS_2 among other materials. However, its toxicity and the high cost disqualify it for large-scale applications. Surfactant-assisted liquid phase exfoliation (SA-LPE) offers a viable alternative to exfoliation in NMP. Surfactants effectively weaken VdW forces and prevent exfoliated particles from restacking by creating a physical barrier and increasing the distance between them. Commonly used surfactants include Sodium dodecyl sulfate (SDS), Sodium dodecylbenzene sulfonate (SDBS), Sodium Cholate (NaCh) and Polyvinyl pyrrolidone (PVP) in the process to substitute NMP with H_2O offering a more economical and environmentally friendly alternative.[10,32,60,61,63,64]

2.1.2. Shear Mixing

In shear mixing a combination of a rotor and a fixed stator is used to apply large shear forces into solutions and dispersions. The energy dissipation rate and the shear rate are directly correlated to the narrow gap between the rotor and stator which ranges from 100 – 3000 µm, and to the high rotor speeds of up to 50 m s^{-1} (as depicted in **Figure 3a**).[65] Shear rates can reach up to 10^5 s^{-1} resulting in significant energy dissipation rates into the solvent and contained particles of a suspension. Below shear rates of 10^4 s^{-1}, the delamination rate is low, and particle sheets are poorly exfoliated.[54,66] In the case of WS_2 even higher shear rates of $3.5 \cdot 10^4$ s^{-1} are needed for successful exfoliation in H_2O.[67] The highest shear forces, which are most effective for delamination, occur at the edges of the holes in the stator (**Figure 3a**). However, simulations and experimental studies by Utomo et al. have shown that only 7.6% of the energy is concentrated in these high-shear-force regions, with the remainder being dissipated through general volume agitation.[66] Two primary mechanisms drive the exfoliation process. First, there are pure shear forces (**Figure 3a**) and the interaction with the solvent layer (**Figure 3c**) to separate individual layers. Second, high velocities lead to jet cavitation, where microjets and shock waves deliver substantial energy to the material sheets (**Figure 4b**). Additionally, random collisions with other particles and the edges of the rotor and stator (**Figures 3b** and **3d**) further contribute to exfoliation. As a result, longer processing times and smaller volumes lead to higher concentrations of 2D materials, as increased collisions promote more effective exfoliation. However, due to polydispersity, monolayered material can be present even after short exfoliation times.[37,54,57,65,68] Nonetheless, a minimum shear rate must be reached to achieve effective exfoliation. The required shear rates for delamination are

highly dependent on the solvent, additives such as surfactants in SA-LPE, and the material being exfoliated, as determined by the following equation:

$$\dot{\gamma}_{min} = \frac{\left[\sqrt{E_{S,WS_2}} - \sqrt{E_{S,L}}\right]^2}{\eta L} \quad (1)$$

Where $\dot{\gamma}_{min}$ is the shear minimum, η the solvent viscosity, L is the minimal platelet length which can be exfoliated, E_{S,WS_2} and $E_{S,L}$ are the surface energies of WS_2 and the liquid.[67]

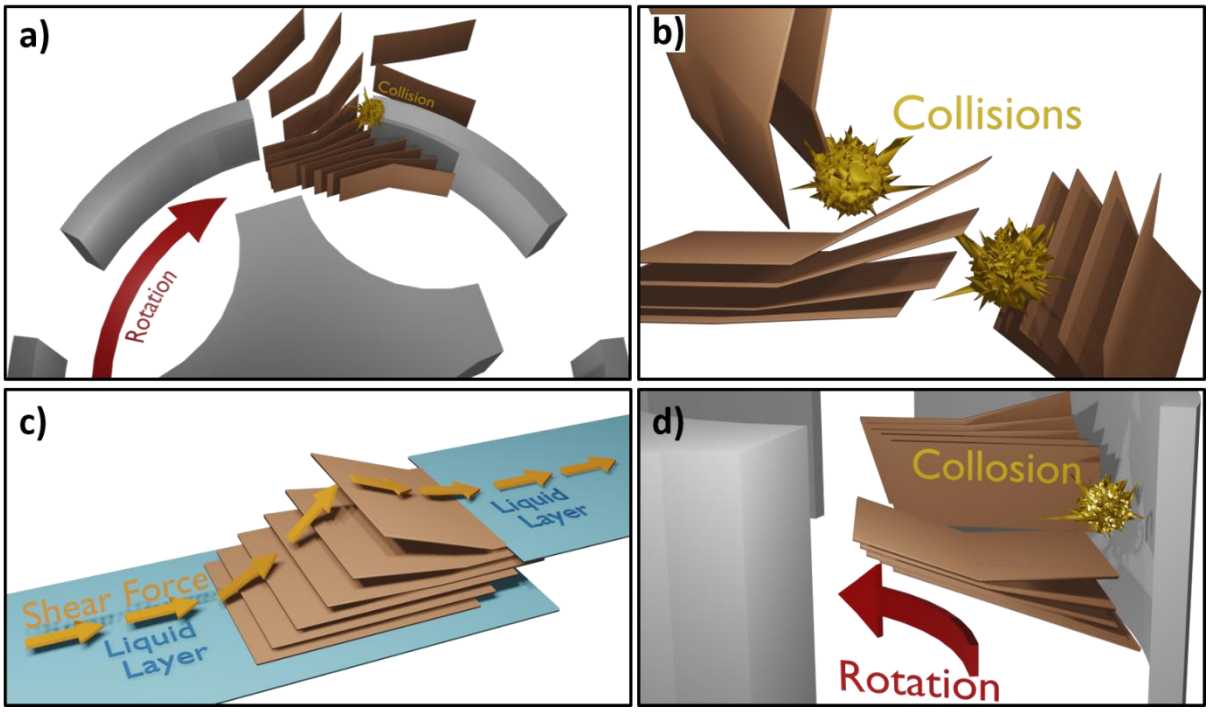

Figure 3: a) Stator-edge collision of a particle consisting of a bi-dimensionally stacked material in a shear mixer depicting the most effective exfoliation process in LPE using a Shear mixer. **b)** The particle-particle collision during LPE using a shear mixer causes exfoliation. **c)** Shear force and exfoliation of the wetting solvent layer on a bi-dimensionally stacked material in an LPE process using a shear mixer. **d)** Frontal particle-stator collision and exfoliation in a shear mixer Rotor-Stator setup during LPE.

2.1.3. Tip Sonication

The cavitation effect, previously mentioned as one of the primary mechanisms of exfoliation in shear mixers, is also the main driving force for exfoliation when using a tip sonicator (a metal probe inserted into a liquid medium). Cavitation bubbles induce chemical or physical changes in materials near the site of cavitation.[69] Ultrasonic waves propagate through the solvent, creating alternating high- and low-pressure regions that apply stress and strain to molecules and particles. Simultaneously, rarefaction causes microbubbles to form and grow with each high-frequent phase shift until a critical size is reached.[70] Upon reaching that size, the bubbles implode, generating extreme temperature changes and shockwaves with

cavitation temperatures reaching up to 5075 K, pressures up to 20 MPa and temperature gradients up to 10^9 K s^{-1}.[56,57,70,71] The collapse causes micro-jets directly applying a compressive stress wave into the particle. This wave is reflected at the borders of the particle and overlaps with other stress waves coming from the oscillating energy input delaminating individual layers by tensile stress (**Figure 4a**). A second process is also caused by the cavitation which is a direct shearing or "wedging" of individual sheets being ripped apart from each other (**Figure 4b**).[54,68] The efficiency of both processes is highly dependent on the volume, as energy transfer diminishes rapidly with increasing scale. Cavitation density decreases significantly with distance to the ultrasonic source, leading to greater polydispersity in larger batches, where material ranges from bulk particles to monolayers due to insufficient mixing.[72–75] The directionality coefficient (D) further illustrates the strong dependence of the energy transfer on the ultrasound propagation angle, as depicted in **Figure 4c,** ranging from – 60° to 60°:[76]

$$D = \left| \frac{\sin\left(\pi \frac{2a}{\lambda} \sin\theta\right)}{\pi \frac{2a}{\lambda} \sin(\theta)} \right| \qquad (2)$$

a is the diameter of the oscillator, λ the wavelength of ultrasound and θ the propagation angle. Directly beneath the ultrasonic source, exfoliation is effective; however, as batch size and diameter increase, the efficiency of the exfoliation process decreases if the ultrasonic source remains unchanged.[75,76]

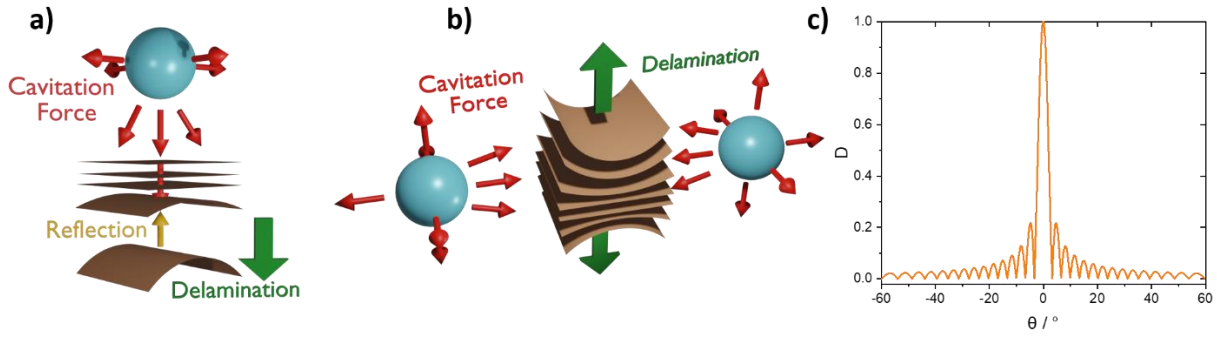

Figure 4: a) Delamination in a tip sonicator setup of single 2D layers of a bi-dimensionally stacked material caused by cavitation above the particle. Cavitation forces are reflected within the particle borders and separate single layers. **b)** Cavitation next to a bi-dimensionally stacked material particle. Cavitation forces shear apart individual sheets from a bi-dimensionally stacked material particle. **c)** Reproduction of the relationship between the acoustic directionality coefficient (D) and ultrasound propagation angle according to **Formula 2**. Going from -60 ° to 60 ° for θ, the assumptions were made using an ultrasonic wavelength λ = 7.5 mm and a diameter of the oscillator being 65 mm.[76]

2.2. Characterization Methods

Exfoliation is employed to separate bulk TMDCs into sheets, as explained in the previous chapter. The structural changes that accompany exfoliation are associated with alterations in the material's physical and optical properties that can be observed for example in Raman spectroscopy (see **Figure 5a**). The proof of these changes is given by several techniques that were used to analyse obtained suspensions after SA-LPE and subsequent centrifugation. Imaging techniques like Transmission Electron Microscopy (TEM) and SEM were used in all **publications 1** - **5** to obtain direct proof of the exfoliation of materials and the overall appearance of particles (see **Figure 5c**). However, this technique does not give further information about the physical properties. The surface area, e.g., an important parameter for SCs, was measured using physisorption measurements like in **publication 1**. Thermogravimetric analysis (TGA) was done to investigate the polymer decomposition of fibers to CNFs in **publication** 1. The thermal stability of WS_2 particles was investigated in **publication 2** using TGA. Besides thermal stability, mechanical stability was tested in Genova by Dr. Marta Fadda to investigate the stability towards stress and strain of the flexible energy storage material from **publication 2**. For structural analysis, X-ray diffractograms (XRD) were acquired to prove the phase stability and the crystallite size of WS_2 and carbon-based materials (**publications 1**, **2** and **5**). Additionally, in **publication 1**, the interlayer distance of the stacked carbon layers was determined from XRD data. For compositional analysis, Energy Dispersive X-ray spectroscopy (EDX) was used to do elemental analysis of fibrous materials, particles and powders in **publications 1** and **2**. Additionally, in **publication 1** x-ray photoelectron spectroscopy (XPS) analysis was done to obtain the ratio of differently bond nitrogen phases in the CNFs to understand chemical changes leading to differing specific capacitances (C_s). A significant portion of the characterization focuses on the suspension of TMDCs. To gain an initial understanding of these suspensions post-exfoliation, DLS was conducted, along with Zeta-Potential measurements (ZP). The exfoliation and separation through gravitational methods result in polydisperse suspensions, which are divided into 2D materials or few-layered materials and more bulk-like particles. DLS provides an initial indication by revealing the particle size distribution within the suspension (**Figure 5b**). ZP measurements are employed to assess the stability of particles in the solvent, as demonstrated in **publication 3** and **publication 4**. If stable suspensions with a small

polydispersity are produced, the properties of the suspensions differ from the bulk-like ones. UV-Vis-spectroscopy was done for suspensions to see an exciton formation at 550 nm and 650 nm as shown in **Figure 5d**, which is not visible for the bulk-like suspensions.[77] However, Raman spectroscopy is the most reasonable method to prove the presence of bidimensional materials.[12] Using this technique, the existence of bidimensional materials was verified not only in suspensions but also after redispersion, drying and integration into fibrous materials afterwards, as demonstrated in **publication 2** and shown in (**Figure 5a**).

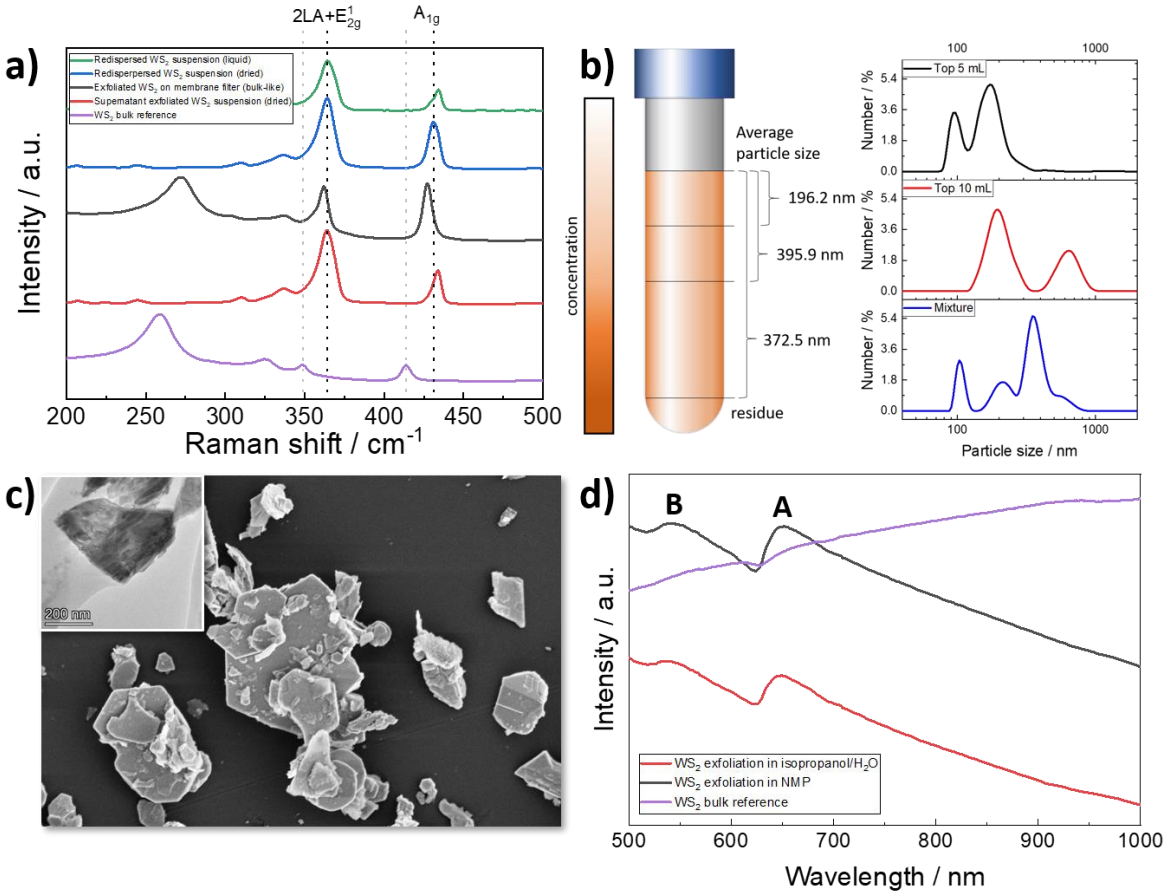

Figure 5: a) Raman spectra of bulk 2D-WS_2 (purple), dried supernatant suspension after exfoliation (red), filtered 2D-WS_2 suspension on a membrane filter (black), re-dispersed and dried 2D-WS_2 suspension after exfoliation and filtering (blue), liquid 2D-WS_2 suspension after exfoliation, filtering and redispersion (green). **b**) Average particle sizes of 2D-WS_2 suspensions after centrifugation including the particle size distribution from DLS experiments. **c)** TEM and SEM images of 2D-WS_2 particles showing the polydispersity of particles at a magnification of 50.000. **d)** UV-Vis spectra of bulk WS_2 suspensions (purple), exfoliated 2D-WS_2 in a mixture of isopropanol/H_2O (red) and exfoliated 2D-WS_2 in NMP (black) showing excitons A and B at 550 nm and 650 nm, respectively.[77]

2.2.1. Raman Spectroscopy of Tungsten Disulfide

In order to analyse exfoliated materials as described in the previous chapters, Raman spectroscopy is used. Initially, a typical spectrum is provided for a suspension containing exfoliated WS_2 particles, taken at different depths of a bottle that has been at rest for an extended period without agitation (**Figure 6**). If we compare the purple reference graph in **Figure 5a** with the exfoliated materials and the stable suspension from **Figure 6**. The transitions from bulk material to exfoliated and restacked particles (**Figure 5a**, black line), and then to the suspensions, are observable by comparing the intensities of the Raman bands at 360 cm^{-1} and 430 cm^{-1}. In addition to shifts in intensity, the position of the peaks also changes. Therefore, this method provides a "fingerprint" not only of the material itself but also of the specific chemical structure of the molecule stacks within the material.

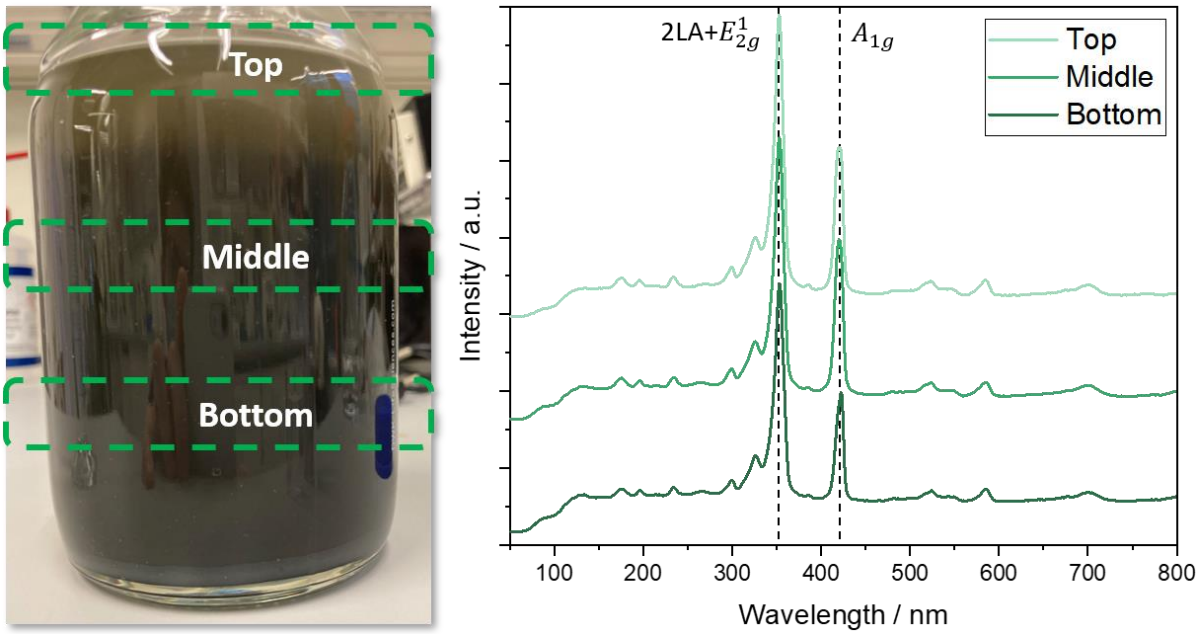

Figure 6: 2D-WS_2 suspension in an IPA/H_2O mixture of 7:3 after sedimentation for 40 days (left). From the suspension, the three depicted regions top, middle and bottom, carefully liquid was withdrawn and investigated using Raman spectroscopy (right) to prove the degree of exfoliation throughout the entire 500 mL bottle.

Raman spectroscopy peaks arise from the inelastic scattering of photons from a monochromatic light source, typically lasers, that are scattered by chemical bonds and molecules. Infrared absorption and thermal motion induce rotation or vibration of molecular bonds, increasing the probability of electrons being excited into specific vibrational energy states (v_1-v_6) as illustrated in **Figure 7**. The energy levels of these states are unique to each material and bond, depending on the energy present within the system. This uniqueness

allows the individual identification of materials using Raman spectroscopy.[78] The interaction of photons in this process is a high-energy event, exciting electrons to much higher virtual energy states compared to energy levels associated with vibrations, phonons and other excitations within the material system (v_1-v_6). The three existing processes of excitation and recombination are depicted in **Figure 7**. Rayleigh scattering is the most probable process. The energy of the initial photon enforces an electron excitation into a virtual energy state. From there, electrons recombine into the ground state (v_0) back again and emit another photon with the same frequency – an elastic collision. This process dominates in terms of intensity, overshadowing the other possible scattering processes and does not contribute towards electron excitation into vibrational modes or phonon formation within the system. The process of Stokes-Raman scattering occurs when an excited electron transitions from the ground state to the virtual state but does not recombine into the ground- but an excited vibrational energy state. Here, excitation of the system occurs into a vibrational energy mode v_1-v_6 after recombination. As a consequence, a photon with a reduced energy is emitted experiencing a redshift of the wavelength– this process is inelastic (red arrow). If the energy of the photon after recombination is larger than initially, this is called an Anti-Stokes-Raman process (purple arrow). The electron already has been in an excited state due to previous absorption (v_1-v_6) and recombines into the ground state v_0 after the scattering. During this process, energy is transferred to the photon, shifting its wavelength towards higher energies after recombination. Since this process depends on two absorption events, it is the least likely to occur.[78–80]

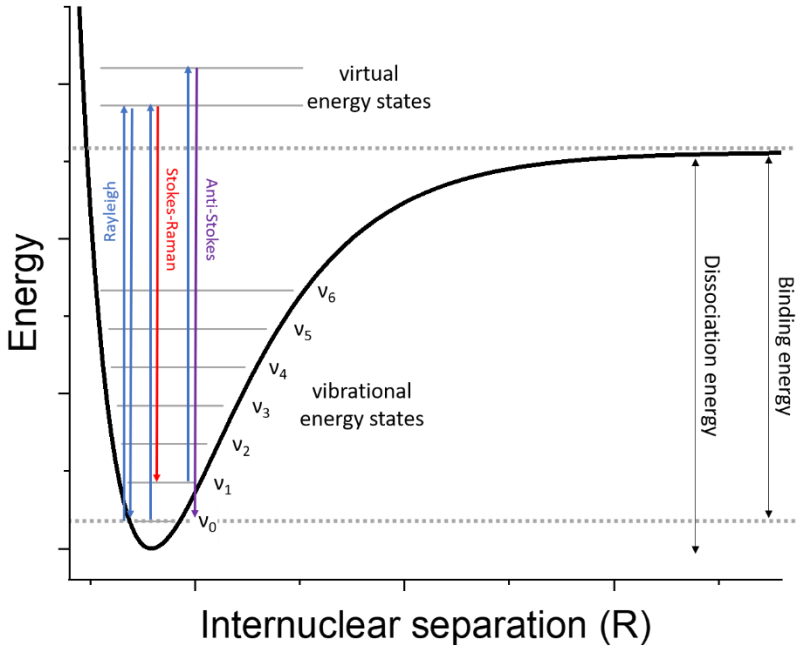

Figure 7: Depiction of the Morse potential according to the following equation: $F(R) = (1.6 \cdot \exp(-4.5 \cdot R))^2$. Shown are the dissociation energy and binding energy of electrons as well as the vibrational and virtual energy states after excitation with a laser. Depicted are all possible electron excitation mechanisms: Rayleigh scattering (blue), Stokes-Raman scattering (red), and Anti-Stokes scattering (violet).

The vibrational energy states are individual for each material. Consequently, the energy shift and wavelength of emitted photons are individual for each molecular bond. Based on shifts of the wavenumber and intensities of peaks, phase switching, physical changes and implemented defects can be quantified and qualitatively analysed as it is possible for example in WS_2 to distinguish bulk- from monolayered material. WS_2 as well as most TMDCs under ambient conditions are present in the trigonal prismatic phase, also known as hexagonal or 2H-phase which is shown in **Figure 8a**.

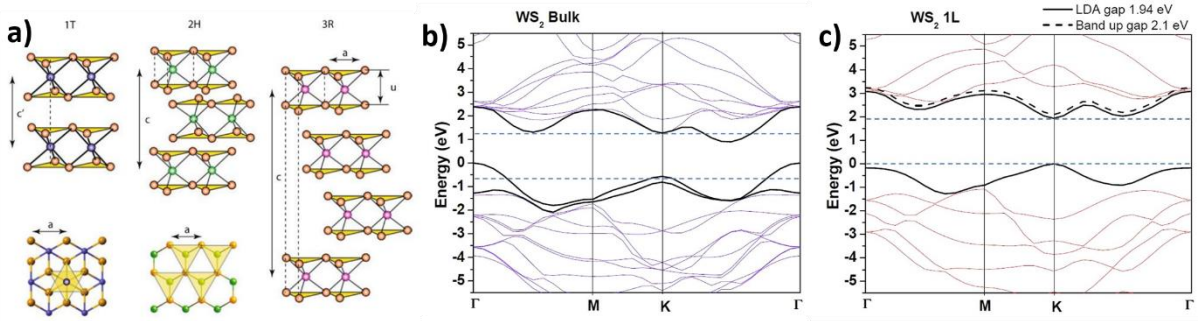

Figure 8: a) Metal coordination and stacking sequences of the trigonal prismatic (1T-phase), hexagonal (2H-phase) and rhombohedral (3R-phase) phases of TMDCs. Reprinted from Kolobov A, Tominaga J, Springer Series in Material Science, 2016, 29-77, 239 with permission from Springer Nature. Copyright 2016 Springer Nature.[81,82] **b)** Electronic band structure of WS_2 bulk and **c)** the monolayer of WS_2, both showing the direct band gap at the K point and the decrease of the band structure from Γ-K and Γ-M going from the bulk to the monolayer. Adapted with permission Berkdemir, A., Gutiérrez, H., Botello-Méndez, A. et al. Identification of individual and few layers of WS_2 using Raman Spectroscopy. Sci Rep **3**, 1755 (2013). https://doi.org/10.1038/srep01755. With permission from Springer Nature. Copyright 2013 Springer Nature.[12]

WS_2 and MoS_2 typically crystallize in the hexagonal phase under ambient conditions, while the metallic 1T-phase represents a metastable phase with an octahedral structure. These different phases can be distinguished by using Raman spectroscopy since the metallic phase reveals additional Raman modes.[5,83] In the metallic phase no bandgap occurs due to overlapping of the density of states which is different to the typically obtained 2H-phase.[19,84]

In the 2H phase, Berkdemir et al. showed that with a degree of exfoliation the band alignment changes and switches to a direct bandgap of 2.1 eV in the monolayer. Additionally, electron energy loss spectroscopy was used by Kumar and Ahluwalia to prove the changes in the electronic structure going from the bulk to a monolayer. [12,34] Experimentally, the direct band gap of WS_2 has been found to range from 1.54 eV to 1.79 eV and even 2.1 eV.[12,31,85] Berkdemir et al. show accurate calculations between experimental data and DFT calculations (see **Figure 8b** and **8c**). The identification of single-layer sheets up to several layers and the bulk material were identified by using Raman spectroscopy in combination with AFM measurements as discussed before. They were able to differentiate between single sheets, and two or three layers by conducting investigations by changing the laser frequency. Obtained from DFT analysis the longitudinal acoustic phonon around the M point of the Brillouin zone was experimentally found to be the Raman mode at 176 cm^{-1} with 514 nm irradiation wavelength. The exact double of this frequency at 352 cm^{-1} is considered to be the second-order mode of the LA(M) frequency. This 2LA(M) mode in WS_2 is special. At this specific laser wavelength, a change of intensity of the A_{1g} and ($2LA+E_{2g}$) bands is observed with layer thickness. While the A_{1g} band in the case of the bulk down to two layers is prominent over the ($2LA+E_{2g}$) band, a drastic change occurs in the monolayer state due to a double resonance process. The intensity and full width at half maximum (FWHM) completely changed towards the ($2LA+E_{2g}$) band when a monolayered WS_2 flake was investigated. For the wavelengths of 488 nm and 647 nm, this was not observed.[12,30,34,58,86] Additionally, UV-Vis spectroscopy is a suitable and non-invasive technique to identify exfoliated WS_2. Absorption increases with smaller particle sizes and a higher degree of exfoliation since the indirect-to-direct bandgap transition also facilitates direct absorption of light. Additionally, literature commonly reports a blueshift towards higher energies of all excitonic absorption peaks in exfoliated WS_2.[14,55,77,87] Using these two techniques it was possible to identify the degree of exfoliation of WS_2 in composite materials, blends, inks and finally fibers as it was done in **publications 2 – 5**.

Exfoliation techniques and subsequent analysis have confirmed the successful production of a class of 2D materials with remarkable potential for energy storage applications. These materials can feature exceptionally large surface areas and additionally show a high capacity for ion intercalation, including ions like Li^+, and BF_4^-, and molecules such as acetonitrile, attributed to their bidimensional layers stacking. These nanomaterials are of interest not only for electrochemical applications and energy storage but for flexible energy storage devices as well. For flexible energy storage, 2D nanomaterials can be implemented in all sorts of materials due to their small size, the probability of failure of an electrochemical cell is drastically reduced as long as conductivity is preserved.[88]

2.3. Flexible Energy Storage

Rising demand for smart devices and the growing integration of technology into daily life, the intersection between humans and electronics is expanding. Smart watches, glasses and phones are already in close proximity to the human body and the requirements towards lighter and better technology is further accelerating this trend. Flexible devices that can be worn directly on the skin or integrated into flexible materials like clothing are becoming increasingly important. Especially, sensing and data acquisition using bioelectrical sensors for health care have a need for long-term applications and the health systems of societies. Effective and long-lasting sensors are important for the optimization of patient treatment or purposes of disease prevention.[88] The primary challenge for the scientific community is lightweight energy storage. While sensors with low weight, compact size, and diverse data acquisition capabilities are feasible, powering these devices over extended periods remains difficult, especially for those implanted in the human body. From skin applications to biosensors attached to individual organs, these small devices have the potential to significantly impact human health. Low-power devices with long lifespans that can withstand mechanical strain and bending, typical of human tissue, are a key factor for the future of smart medicine. Furthermore, flexible screens, foldable smartphones or rollable solar cells are important for lightweight and space-efficient devices for daily-life applications regarding energy production as well as energy storage and space applications. In the transition from rigid to more strain-resistant electronics, several approaches are explored in the scientific community. Conductive polymers like Polyacrylonitrile (PANI) and Poly-3,4-ethylendioxythiophen (PEDOT) combine electronic conductivity with flexibility enabling flexible electronic devices. These polymers have been used to create thin films, membranes, fibers and nanoparticle-based composites for a wide range of applications including sensing, energy storage and more.[20,21] Besides using inherently flexible materials like the above-mentioned polymers, silica and carbon-based materials are also being implemented into flexible structures. The reduction of particle sizes to the nanoscale, including 0D, 1D and 2D nanomaterials, tremendously decreases rigidity. By reducing the size of active materials, the risk of mechanical failure is decreased since small particle sizes are less likely to break apart. Further, these materials exhibit a range of properties: nanoparticles often have large surface areas, 2D materials often show increased charge storage capacitance, 1D materials like CNTs

provide enhanced conductivity, and 0D quantum dots besides all other mentioned materials display strong quantum confinement effects.[88] Improving resilience towards deformation and strain is not just a challenge but an opportunity and might be accompanied by performance improvement for energy storage as well as sensing. To further advance flexible energy storage technologies, it is essential to develop materials that combine both mechanical flexibility and high electrochemical performance. This is where electrospinning comes into play as a versatile technique. By creating nanofibers with large surface areas and tuneable porosity, electrospinning offers a powerful tool for fabricating materials tailored for energy storage applications. Electrospun nanofibers have demonstrated significant potential by enhancing the flexibility and conductivity of supercapacitors and batteries, thereby advancing the field of flexible energy storage. This technique not only facilitates the development of adaptable energy devices but also paves the way for their integration into wearable technologies. To delve deeper into this promising method, the next chapter will explore the origins of electrospinning, detail the underlying techniques and methodologies, and provide a comprehensive overview of current research in the field.[89]

2.4. Electrospinning

Electrospinning is grounded in the physical principles first mathematically described by Rayleigh in 1882, where a high potential causes a spill of solutions by overcoming the surface tension of a liquid.[90] This concept was further developed by Morton in a 1902 patent, which describes the potential-driven dispersion of fluids.[91] This electro-spraying process was first adapted into electrospinning by A. Formhals adding cellulose acetate (CA) or mixed esters into solutions.[92] The large molecular weight solutions form continuous jets instead of small droplets leading to continuous fibrous materials after drying.[92–94] The most prominent person in the field of electrospinning is Geoffrey Taylor, who developed a mathematical model describing the shape a droplet disintegrates under the influence of a high electric potential – now known as the Taylor cone.[95,96] Apart from his fundamental work in the 1970s, the field of electrospinning did not garner widespread interest, as evidenced by the limited number of publications per year during that period, as shown in **Figure 1c**. Finally, electrospun fibers protruded due to comparably small diameters achieved for a multifaceted set of polymer materials down to 16 nm for polyethylene oxide (PEO) and polyvinyl alcohol (PVA) e.g.[97,98] Consequently, the emerging interest towards nanomaterials and nanotechnologies caused a growing interest into electrospun materials. Based on the work of Reneker et al.[99] in 1995 which explored the process and applications of electrospun fibers, there has been a significant, almost exponential rise in interest within the scientific community over the past 25 years. This surge in interest appears to be reaching a saturation point recently, as illustrated in **Figure 1c**. Mainly, the large surface area[100,101], large aspect ratios[102–105] and small dimensions were considered to be ideal for various applications as a backbone material, active material or membranes.[93,94,98,99,106,107] Reasonably this technique was used in **publication 1** and **publication 2** to prepare fibrous SCs exploiting all of the benefits going from flexibility towards large surface area carbon materials and composite materials.

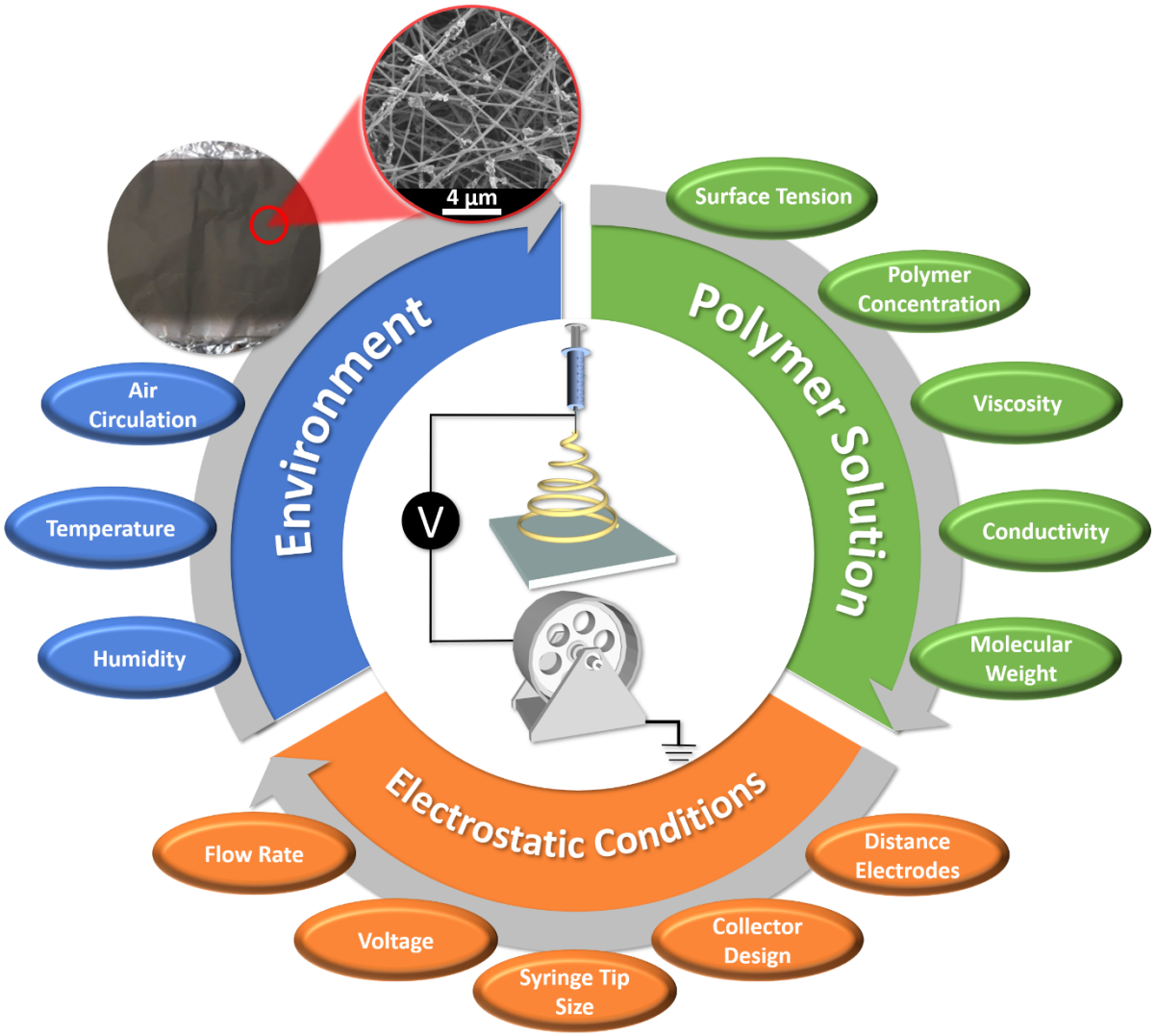

Figure 9: Depicted are the schematic image of the electrospinning process and the three different processing parameters. The polymer solution, the processing and the environment during the electrospinning are the crucial parameters to control to precisely adjust the electrospinning and the resulting fibers. As one example a clipping of a fiber mat and an SEM images of the PEO-WS_2-CB-MWCNT composite fibers from **publication 2** are shown.

2.4.1. Setup and Process

The process of electrospinning is straightforward: a charged polymer solution is steadily and slowly extruded through a needle tip using a syringe pump (typically at ~ 0.2 mL h^{-1}). A potential up to 40 kV is applied between the needle tip and a counter electrode generating low currents around 10^{-9}- 10^{-6} A, driven by charges on the polymer solutions surface. These charges as well as the surrounding electric field cause deformation of the surface of the polymer solution which is known as the above-described Taylor-Cone, depicted in **Figure 10a & b**.[95,99,108–110]At a certain threshold potential the surface tension of the polymer solution is overcome by the large electric force. As a consequence, the polymer solution accelerates and forms a so-called jet towards the contradictorily charged electrode.[111] In

electrospinning, long-chain polymers are employed to produce continuous fibers. The acceleration of the polymer solution during the process results in the formation of ultra-thin fibers, with diameters ranging from µm to several nm in thickness. However, to be able to prepare a versatile set of various fibrous materials this simple setup must be optimized and becomes more complex. The solvent, polymer concentration and polymer chain length are crucial factors for controlling the surface tension, conductivity and viscosity of the solution. These parameters are essential for enabling, adjusting and optimizing electrospinning processes. Electrospraying can occur as a result of low polymer concentrations or insufficient chain length, that adequate entanglement of the polymer chains cannot be ensured. Further, fragmentation of the polymers is possible since large electric forces combined with high surface tension can rip the polymer chains apart.[112] Besides the spinning solution there are several parameters that can be controlled using an electrospinning setup as they are collected in **Figure 9**: The electric field is primarily influenced by the applied potential of the two electrodes, their distance, and the shape of the collector. A higher potential and closer electrode placement increase the applied electric field, leading to greater acceleration of the polymer jet. This increased acceleration enhances the elongation of the spun fibers, affecting their thickness. Consequently, the thickness of the fibers is directly influenced by the magnitude of the electrical force applied during the process.[113–116] The fiber-collecting electrode can come in various shapes such as simple plates, rotating drums (shown in **Figure 9**), or sticks. The choice of electrode shape influences how the fibers are collected and assembled, tailoring the fiber arrangement to suit specific applications. The polymer solution flow is also influenced by the applied potential. Greater acceleration results in increased consumption of the polymer solution, which can lead to bead formation along the fiber if the supply is inconsistent.[117,118] Therefore, an equilibrium must be established between the flow rate, applied potential and electrode distance for each specific polymer solution. In addition to the factors mentioned, solvent evaporation during electrospinning is crucial for forming stable polymer fibers. The rate of evaporation is significantly influenced by the atmosphere and its flow dynamics. Therefore, temperature and humidity in the electrospinning setup must be carefully monitored and controlled to ensure reproducibility and maintain stable conditions.[110,119]

2.4.2. Jet Instabilities

Establishing an equilibrium for a stable electrospinning process is complex. However, the trajectory of the polymer jet can be affected by physical instabilities caused by various interactive forces, as illustrated in **Figure 10**. By adjusting the above-mentioned processing parameters – such as electrostatic conditions, the ambient environment, and the polymer solution properties – it is possible to transition between different instability modes. The three existing modes are Rayleigh, Axisymmetric and Whipping. Understanding these instability patterns can help to address and rectify stability issues in a non-stable electrospinning process.[120,121]

The Rayleigh instability (**Figure 10a**) is observed for all liquids and describes the segmentation of a liquid into smaller droplets. This occurs due to driving forces that decrease the surface area, thereby lowering the system's free energy by reducing surface tension.[120,121] Prevention is possible by imposing a sufficiently strong electric field that the viscoelastic force suppresses the break-up mechanism caused by surface tension.[120,122] However, by exceeding the electric field above a certain threshold, the jet diameter decreases until the so-called varicose jet break-up occurs and droplets form again.[120]

The Axisymmetrical instability (**Figure 10b**) is charge-driven and is caused by variations in surface charge density ($\sigma_0+\Delta$ and $\sigma_0-\Delta$). Statistical fluctuations in the jet's thickness lead to corresponding changes in surface charge distribution. These imbalances create tangential forces that further push the solution toward areas with a thicker radius. Consequently, this exacerbates thickness variations, resulting in bead-like structures along the fibers, with beads aligning along the thinner radius of the fibers.[119,123,124]

Whipping instability (**Figure 10c**) of the fiber is the final and most significant instability occurring during electrospinning. Here, instability is caused by perturbations of the surface charge density ($\sigma_0+\Delta$ and $\sigma_0-\Delta$) causing tangential stress imbalances on the surface and electric attractions that both cause fiber bending (indicated by the arrows). Whipping occurs when interacting external forces like viscous drag or high charge densities interact with the fiber.[120] As the electric field increases, this effect intensifies, causing the fibers to enter a rapid spiral motion with an increasing radius causing fiber stretching while tapering its diameter.[123] The physical instabilities can hinder the process and need to be precisely controlled, but in the first

place whipping is the reason to enable the formation of nanometer-thin fibers without decomposition. No other technique is capable of achieving stretching rates up to 10^5 s^{-1}, as well as large orientation and a high degree of polymer crystallization unlike electrospinning.[119]

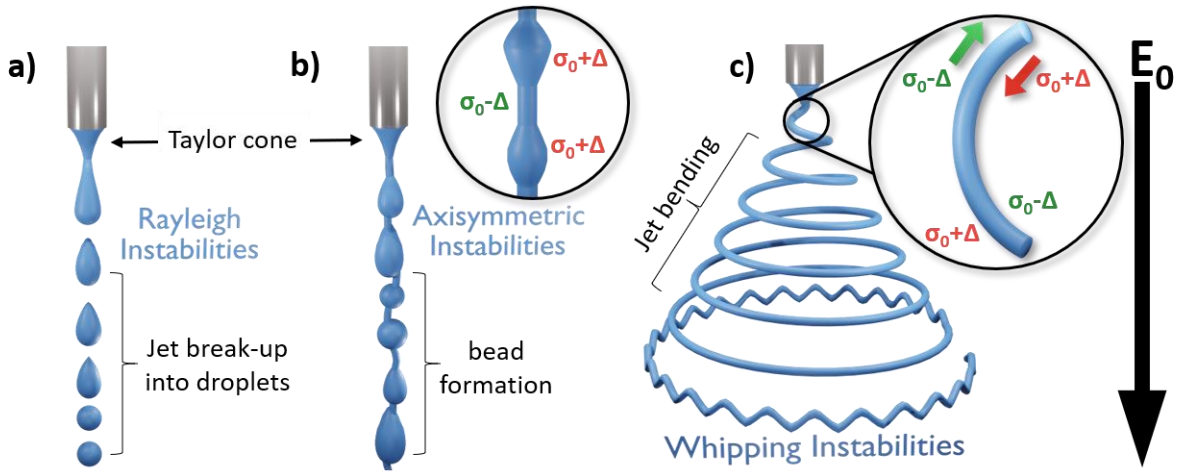

Figure 10: With E_0 being the external electric potential, different instabilities can occur that are depicted. **a)** Rayleigh Instabilities showing the jet-breakup and droplet formation. **b)** Axisymmetric Instabilities caused by perturbations of the surface charge in thinner and thicker regions of a fiber (inlet). **c)** Whipping instabilities caused by surface charge perturbations bending the fiber due to attractive forces.

2.4.3. Composites from Electrospinning

Besides single-phase polymers, there are methods to produce composite polymer fibers using electrospinning. Organic precursors, emulsions or particles can be used in the polymer solution to either produce oxide fibers, induce porosity, or distribute particles throughout the nanofibers. A wide range of fibers with different additives has been produced in the past, allowing for tailored properties and functionalities in the resulting composite fibers. Mainly PVP, PVA and PEO are used for their solubility in less toxic solvents like Acetyl acetone (AcAc), isopropanol (IPA), H_2O and ethanol (EtOH). However, these examples represent just a fraction of many successful electrospun material systems. The nanoscale nature of electrospun fibers, whether incorporating particles or bulk materials, has garnered significant interest from the scientific community. Numerous examples exist of active materials created from electrospun fibers, including: Al_2O_3-fibers for microelectronics and catalysis[125], CeO_2-fibers for pollutant removal[126], CuO- and CuS-fibers as H_2S detectors or semiconductors[127], fibrous Co_3O_4 for glucose detection[128], Fe_2O_3 as photoanodes[129], IrO_2/Pt as membranes for OER[130], $LiCoO_2$ for energy storage as electrode materials[131], MoS_2 for H_2 storage and catalysis[132], NiO as anode material[133], for large surface membranes of SiO_2 for catalysis[134], as gas sensors made from

SnO_2 or WO_3 and ZnO[135–137], TiO_2 as DSSCs and photocatalyst[138] and ZnO for health applications.[139]

However, there must be a distinction between precursor and sol-gel-based approaches for fiber preparation and the incorporation of nanoparticles into fibers. In certain cases, material properties can only be achieved by using pre-designed particles. For example, SiO_2 particles with tailored surface areas, multiwalled carbon nanotubes (MWCNTs) that must be produced in advance, or exfoliated MoS_2 or WS_2, where 2D sheets need to be prepared in solution before being incorporated into fibers, all require specialized preparation to obtain desired characteristics.[48,62,109,134,140] Producing WS_2 or MoS_2 from sol-gel or wet chemical methods typically results in bulk-like particles rather than monolayers, which affects material properties as discussed previously in **chapter 2.1.** Blair et al. found that the loading and size of particles (up to 10 µm) in dispersion do not significantly impact the fiber thickness, provided there is no clogging of the nozzle. The primary influence on fiber structures comes from changes in the viscosity and conductivity of the dispersion, which affect the process of electrospinning according to the above-mentioned physical instabilities.[141] From this perspective, the proceeding of dispersions, sol-gel-based mixtures, or pure polymer solutions is similar as long as the procedure parameters are within the above-discussed range of the solution parameters and the applied potential.

After knowing that active particles like exfoliated TMDCs can be easily incorporated into fibrous materials without disturbing the structural benefits of nanofibers, these materials can be exploited for the preparation of flexible charge storage materials. Exfoliated TMDCs like MoS_2 and WS_2 in combination with electrospun polymers or carbon precursors are capable of storing surface charges. Especially carbon-based materials are considered to show capacitive behaviour. They are called supercapacitors since large surface areas enable the storage of many charges at the surface. The definition of a capacitor, supercapacitor and pseudo capacitor is given in the following chapter to understand the effective exploitation of these composite materials as energy storage devices.

2.5. Supercapacitors and Electrochemistry

To understand the functionality of capacitors and supercapacitors, it is essential to consider several foundational models that describe the behaviour of ions in an electrolyte when a metal surface is introduced. These models, depicted in **Figure 11**, trace the evolution of capacitor theory, illustrating how our understanding of ion orientation and movement at the electrode-electrolyte interface has advanced over time. Each model represents a significant step in the development of capacitor theory, providing deeper insights into the mechanisms governing energy storage in these devices.

2.5.1. Helmholtz-Model

In 1879, H. Helmholtz introduced the concept of the electrical double layer (EDL), a fundamental idea in electrochemistry. At the interface of a solid electrode and an electrolyte, an EDL forms due to the concentration shift of ions in the electrolyte and the corresponding charge shift of electrons in the electrode.[142] This dynamic interaction is crucial because the ionic conductivity of the electrolyte and the electronic conductivity of the electrode significantly influence the behaviour and efficiency of these systems. The formation of the EDL plays a vital role in the performance of capacitors and other electrochemical devices, as it directly impacts how charge is stored and transferred at the interface. When a negatively charged electrode – common in carbon-based materials – is introduced, cations from the electrolyte coordinate around the electrode. These cations directly adsorb onto the electrode surface, forming a compact layer, while the electrode itself accumulates electrons at the electrode-electrolyte interface. This arrangement establishes the foundation of the electrical double layer, crucial for the functioning of capacitors and supercapacitors. However, in Helmholtz's theory, only metal electrodes have been described. Additionally, this rigid layer proposed by Helmholtz does not include diffusion of ions in the electrolyte. In fact, the model did not meet the experimental data observed.[143,144]

2.5.2. Gouy-Chapman-Model

In 1910 and 1913, Gouy and Chapman introduced the concept of a diffusive layer of ions, which expanded upon Helmholtz's earlier model of the EDL.[144] They proposed that, beyond the rigid Helmholtz layer, ions in the electrolyte experience thermal motion, leading to a diffusive layer where ions are not rigidly adsorbed but are instead in constant motion. This thermal diffusion causes a continuous exchange of charges at the boundary of the Helmholtz layer, resulting in a reduction of the space-charge region. The extent of this reduction depends on the ion concentration in the electrolyte, adding a dynamic aspect to the structure of the electrical double layer. The potential decreases as a function of the distance to the electrode surface and follows a Poisson-Boltzmann distribution leading to an exponential decrease of the potential with increasing distance to the electrode. In this model, rather than a single layer of ions being tightly coordinated at the electrode surface, a concentration gradient of charged ions extends from the metallic electrode across several molecular layers (see **Figure 11**). A layer of cations nearby, and coordinated around the electrode shield the negatively charged anode, this exerts attractive forces on nearby anions in the electrolyte that themselves attract further cations, respectively. This cascading effect converts into a concentration gradient of ions that forms around a charged electrode with decreasing concentrations of anions and cations with increasing distance to the electrode.[143,144]

2.5.3. Gouy-Chapman-Stern-Model

The Gouy-Chapman model, while innovative, faced limitations under conditions of high charge density. It struggled to accurately describe the behaviour of ions near the electrode surface when high charging states were reached. To address these shortcomings, in 1924 Stern combined the concepts of Helmholtz and Gouy-Chapman. A strongly adsorbed double layer is forming at the electrode surface following a linear decrease in the distance to the electrode similar to the Helmholtz model. The width of the linear region is defined by the diameter of solvated counterions in the nearest approach to the electrode's surface.[143,145] Beyond this rigid layer, the potential is described by the diffusive layer according to Gouy and Chapman. The potential follows a concentration gradient and therefore decreases with the distance according to Poisson-Boltzmann in an exponential decay with increasing distance (see **Figure 11**).[143]

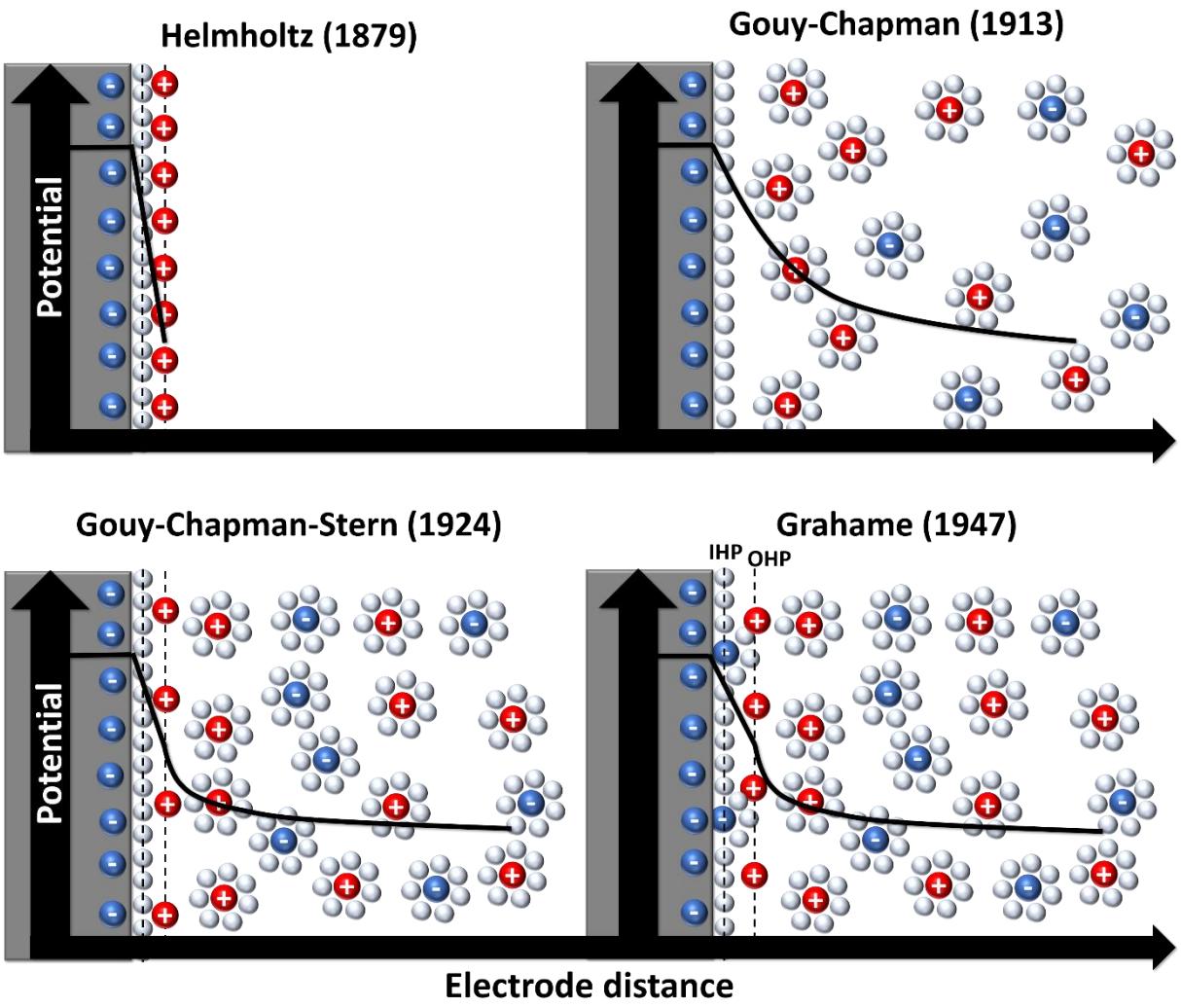

Figure 11: Depicted is the Helmholtz model from 1879 with the linear potential decrease of the fundamental electrochemical double layer. The Gouy-Chapman model from 1913, considers a diffusive layer due to thermal motion. The Gouy-Chapman-Stern model from 1924, combines the first two models especially for strong electric fields. Lastly, the Grahame model from 1947, including ion adsorption at the surface as an explanation for pseudocapacitive behaviour.

2.5.4. Grahame-Model

In 1947 Grahame further refined the Gouy-Chapman-Stern-Model and incorporated additional complexities into the descriptions of the EDL. The effect of the solvent, the dissolution of ions, as well as the specific and non-specific adsorption of ions at the electrode surface. The specifically adsorbed ions and solvent molecules closest to the electrode form the so-called Inner-Helmholtz-Plane (IHP). Specific adsorbed ions are in direct contact with the electrode, displacing solvent molecules, while non-specifically adsorbed ions remain surrounded by solvent molecules as they interact with the electrode.

The Outer-Helmholtz-Plane (OHP) refers to the ions that are coordinating around the IHP due to coulombic forces. These ions have an intact solvent shell. The two layers (IHP and OHP) are considered as a physical capacitor following the behaviour of **Formula 3**.[146]

$$C = \varepsilon_0 \, \varepsilon_r \, \frac{A}{d} \qquad (3)$$

Where C is the capacitance, ε_0 is the permittivity of vacuum, ε_r the the permittivity of the material in between the capacitor, A the area of the capacitor and d is the distance of the electrodes. In the above-described cases, the distance of the capacitor is in the range of molecular distances and physically described as the Debye length. It is defined as the distance at which the electrical potential of a local surplus charge decreases to $\frac{1}{e}$ (about 37 %) of its initial potential.[144] The non-ideal pseudocapacitive behaviour observed in real SCs was explained by Bockris et al. According to their explanation based on the Grahame model in **Figure 11**, specifically adsorbed ions in the electrolyte undergo redox processes by adopting the electrodes' polarity. Since this process is reversible ions can be re-dissolved and therefore contribute to a pseudo-capacitive behaviour through redox processes on the electrode's surface.[147]

2.5.5. Supercapacitors – Definition & Methods

Winter et al. define a supercapacitor using the Ragone plot (see **Figure 12**), positioning it within the energy and power density range between traditional capacitors and batteries.[146] Supercapacitors serve as energy storage systems that are thin, porous and use a separator for charge separation characterized by low intrinsic resistance.[144,146] The Ragone plot is a tool used to compare the power- and energy density of different materials, charge storage technologies and their applications – for a description of a supercapacitor these are the most important physical properties.[148–150] The power density (P_d) and energy density (E_d) are calculated by the following equations according to **publication 1**:

$$E_d = \frac{1}{2} C_s \Delta V^2 \frac{1}{3.6} = [Wh\ kg^{-1}] \qquad (4)$$

$$P_d = \frac{E_d}{\Delta t}\ 3600 = [W\ kg^{-1}] \qquad (5)$$

In these equations, Δ*V* represents the applied potential window, and Δ*t* is the discharge time. Besides the above-described pseudo-capacitive behaviour, a supercapacitor operates on the same charge storage mechanism as a capacitor where surface charging leads to the formation

of an EDL. The key difference is that supercapacitors use high-surface-area materials, such as porous carbon, in combination with aqueous electrolytes to enhance their performance.[146]

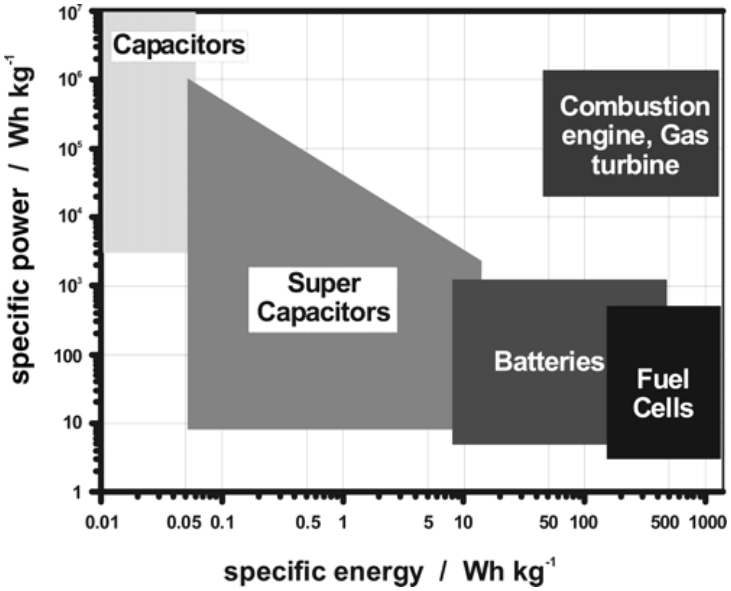

Figure 12: Simplified Ragone plot of the energy storage domains for the various electrochemical energy conversion systems compared to an internal combustion engine, turbines and conventional capacitors. Reprinted with permission from Martin Winter and Ralph J. Brodd., Chem. Rev. 2004, 104, 10, 4245–4270, https://doi.org/10.1021/cr020730k, Copyright 2004 American Chemical Society.

In order to calculate E_d electrochemical analysis must be conducted to determine the capacitance and C_s values as required for **Equation 4**. For the analysis of SCs, potentiostatic or galvanostatic methods, such as cyclic voltammetry (CV), are commonly used to measure capacitance. Cyclic voltammetry is a potentiostatic method where a defined potential sweep is applied to a system. It was used in **publication 1** and **publication 2** for the electrochemical characterization. The scan rate is defining how large the potential sweep will be as a response the resulting current is measured by a potentiostat. It is given by the following equations:[89]

$$C = \frac{1}{\mathrm{E}v}\int_{v_1}^{v_2} i\, dV \qquad (6)$$

E is the potential window, with v_1 and v_2 are the potential boundaries. v is the scan rate, i as the charge-discharge currents and dV is the potential change.

$$C_s = \frac{1}{\mathrm{mE}v}\int_{v_1}^{v_2} i\, dV \qquad (7)$$

To obtain C_s, the integral of the current over the potential range is divided by the potential window (E), the mass (m) and the scan rate (v). In **Equations 6** and **7** the area enclosed between the charge and discharge curves during cyclic voltammetry is directly related to the mass and the specifics of the measurement.

Consequently, C_s is a function of the scan rate. The potential window typically is chosen as large as possible to maximize the performance and capacity of the supercapacitor. However, it is crucial to avoid degradation processes, as excessive potential can trigger chemical reactions within the system. Such reactions can lead to irreversible changes, compromising the reproducibility and reliability of the results. Therefore, the potential window must be carefully selected to balance high performance with the stability and longevity of the material.

Besides the potential range, the velocity of the changing potential, the scan rate, is a crucial factor of a cyclic voltammetry measurement. With increasing scan rate the system cannot follow the potential change due to diffusion limitation. This is because the diffusion layer, which is the region within which the electroactive species diffuse to the electrode surface, becomes thinner. As a result, the current increases due to the reduced thickness of the diffusion layer, which intensifies the concentration gradients of the electroactive species near the electrode.[151] Generally, an increased scan rate reveals a more pronounced non-equilibrium state in the system. Diffusion is limited and charging and discharging become less effective due to ion diffusion through the electrolyte. As a consequence, a lower C_s is observed with increasing the scan rate even if the current increases. The ideal, rectangular shape of a SC becomes more and more “leaf”-like, as shown in **publications 1** and **2** in several examples.

Another way to measure C_s is to acquire galvanostatic-charge-discharge curves (GCD). A constant current which is defined by the active mass of the measured system is applied and the potential as a function of time is obtained. Galvanostatic measurements were conducted in **publication 1**, **publication 2** and **publication 5**. C_s is calculated by the integral in the following equation:

$$C_s = \frac{1}{V}\int_{t_1}^{t_2} I\, dt \qquad (8)$$

The capacitance is given by the quotient of the integral of the current over time and the potential. The current density is calculated based on the active mass of the system according to the following equation:

$$J = \frac{I}{m} = [A\ g^{-1}] \quad (9)$$

Common values of the current density range from 10 mA g^{-1} up to 5000 mA g^{-1}. It is recommended to use a range of current densities for the calculation of capacitance to obtain a comprehensive understanding of the material's performance under different conditions. Additionally, as it was done in **publications 1** and **2** this technique is used for long-term electrochemical stability tests. In real-life applications, energy storage devices undergo repeated charging and discharging over several hundreds and even thousands of cycles. This way the lifetime of energy storage devices is simulated to see changes in the charging and discharging behaviour over the years of usage. C_s depends on the current density since large currents always cause diffusion limitation and a decrease in the diffusion layer. Here, large potential changes over time are the consequence. Both galvanostatic charge-discharge and cyclic voltammetry methods can be used to determine C_s for capacitors and supercapacitor materials. However, these methods apply primarily to those, which are based on charge storage mechanisms such as electric double layer formation and pseudo capacitance since battery-like behaviour cannot be described by these equations due to electrochemical processes, such as more complex redox reactions.

2.5.6. Transition Metal Dichalcogenides as Energy Storage Materials

TMDCs such as MoS_2 and WS_2, are emerging as promising charge storage materials for several reasons. While graphite is widely used as an anode material in LIBs due to its ability to store Li^+-ions within its layers, its charge storage capacity of 372 mA h g^{-1} limits its application in high-energy contexts.[152] This has driven significant interest in alternative two-dimensional materials like TMDCs.[5,7,153,154] Here, TMDCs are of interest to the scientific community towards high-energy electrochemical applications, especially in three decisive fields of research.[7] First, there is the substitution of graphite in LIBs to increase charge storage capacity. It was found to achieve 674.8 mA h g^{-1} for WS_2 electrodes instead of graphite.[6] Furthermore, an additional stress-induced increase of the capacitance was observed when Li^+-ions intercalate into the WS_2 lattice.[155] Secondly, the intercalation of ions into layered materials enhances their charge storage properties, making TMDCs particularly promising for SIBs.[8,9] Wang et al. demonstrated

that a MoS_2-carbon composite material could achieve a capacity of 390 mA h g^{-1} when used as an electrode in SIBs, highlighting the potential of TMDCs for improved energy storage in these systems.[156] The third area where TMDCs are promising candidates is in supercapacitors. As explained in **Chapter 2.5.1.** – **2.5.5.**, supercapacitor charge storage involves the formation of an EDL as well as pseudo-capacitive effects resulting from chemical changes according to the model of Grahame.[157–159] The layered structure of TMDCs is advantageous for both mechanisms. The large surface area of 2D-layered structures is the first argument for their applicability getting close to graphene reaching up to 2630 m^2 g^{-1}.[10,11,160,161] For the electric double layer capacitor (EDLC) a large accessible surface area is crucial and mandatory for their effectiveness. The individual layers cause a large surface-volume ratio for these materials as long as no restacking of the sheets is ensured.[16,19,49,156,162] With increasing surface area and surface-volume ratio the number of active sites increases as well.[18,41,163] These active sites undergo partial surface restructuring and redox reactions giving a pseudocapacitive character to the charge storage behaviour of TMDCs.[19,45,64,164] The primary drawback of MoS_2 and WS_2 is their intrinsic low conductivity when they are in the stable and semiconducting 2H-phase, which prohibits extraordinary performances as SCs or batteries.[7,18,19,45,165] During the in-depth literature research conducted as a part of this thesis, the literature does not report SCs made from pure WS_2 or MoS_2 phases due to these conductivity limitations.

To address the limitation of low conductivity in MoS_2 and WS_2, composite materials are produced by incorporating conductive species or by preparing conductive backbone materials. For instance, conductive polymer scaffolds such as PANI or PEDOT:PSS are combined with TMDCs or a direct polymerization of EDOT on TMDC sheets is performed. Both polymers enhance the overall capacitance not only due to an increase in conductivity but by inducing a pseudo-capacitive species to the system. PEDOT and PANI undergo a redox reaction within charging and discharging.[21,64,166] Most TMDC-based supercapacitors are developed by coupling TMDCs with carbon-based materials such as CB, CNTs, CNFs, graphene oxide (GO), reduced graphene oxide (rGO), graphene, and graphite. This approach is prevalent in the scientific community due to the synergistic benefits it offers by enhancing the performance of supercapacitors.[7,9,14,18,62,161,167–175]

Summarizing: high-surface-area carbon materials have extraordinary capacitances due to the large surface areas that are achieved.[11] Additionally, they have high electric conductivity,

making them ideal complements to TMDCs. Besides adding conductive species, the trigonal prismatic structure can be transferred to the octahedral structure which causes a band transition from the semiconducting to the metallic phase which is the intrinsically more conductive phase of TMDCs.[5,83] Consequently, metallic phases of MoS_2 and WS_2 are frequently used for composites with mixtures of 2H- and 1T-phase or in other combinations with carbon materials e.g.[11,171,176,177] Hydrothermally produced MoS_2 for example always contains a mixture of the metallic and semiconducting phases as seen in the literature.[178] XPS data of my research underline these results by finding mixtures of both phases at the particle surface of hydrothermally produced MoS_2 in **Figure 13**. Interestingly, a similar transition from the semiconducting 2H-phase towards the metallic 1T-phase is observed for TMDC materials if combined with carbon materials. This transition occurs at the carbon-TMDC interface, providing an additional benefit of integrating these two material classes.[19] However, the same effect is observed when intercalation of Li^+ into MoS_2 layers is done. The increasing layer distance causes the same phase transition.[164,179,180]

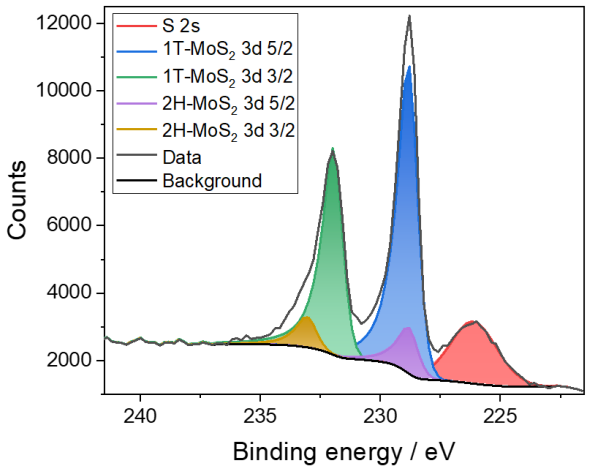

Figure 13: XPS spectra of hydrothermally produced MoS_2 after a reaction time of 18 hours in an autoclave, showing a high degree of 1T-phase production of about 87 %, but never full conversion.

Therefore, the synergistic effect of carbon materials combined with TMDCs is observed many times in the literature that also was observed for the carbon-WS_2 interfaces in **publication 2**, where a synergy of the combined materials was observed leading to larger C_s of the capacitors compared to the individual species. Convincingly, one can assume that the effect of the surface transition of the TMDCs paired with large porous systems of carbon-based materials will become important for future developments. In addition, with the tuneable direct band gap of the monolayered WS_2 and MoS_2, high-energy electronics, new-generation transistors and improved sodium storage, TMDCs are having manifold future applications.[8,35,49,180]

3. Publications

My publications as first author, a shared first authorship, and two publications as co-author are listed in the following. For each publication, a short introduction addresses the scientific context and current state of literature when it was published for reasons of justification. To differentiate my contribution from the co-authors' work each contribution of myself and the other authors is described for each publication:

Publication 1 is based on the master thesis of Leonardo Merola, my former student who was supervised by myself and Prof. Teresa Gatti. He achieved a major part of the experimental data reported in this publication during his thesis period. I performed additional physisorption measurements, SEM, TGA, electrochemical impedance spectroscopy (EIS) and CV measurements. Data interpretation was carried out by myself, Leonardo Merola, Francesco Lamberti (a collaborator of Prof. Gatti from the University of Padova, Italy) and Prof. Teresa Gatti. Matteo Crisci measured XPS spectra and also helped analyse them. I prepared all drafts of the manuscript, supporting information and figures with the supervision of Prof. Gatti, who gave fruitful suggestions for manuscript improvement. Dr. Lamberti also helped in the organization of the drafts.

Publication 2 is a result of experimental work and sample production done by Melissa Happel, a former master's student who was supervised by Prof. Gatti and myself. Melissa produced samples and conducted a major part of CV measurements in the *Swagelok* cells. I conducted other CVs, EIS, Raman, XRD, SEM, EDX, conductivity measurements, TGA, bending tests and electrochemical stability tests. Mechanical stress-strain tests were done by Marta Fadda, supervised by Dr. Giovanni Perotto, both members of the Smart Materials Group at the Italian Institute of Technology in Genova (Italy). Both also contributed to the analysis and interpretation of mechanical stress-strain curves. Interpretation of the datasets was done by me and discussed with Prof. Gatti. The figures, the manuscript text and the supporting information were drafted by me and discussed with all co-authors before submission.

Publication 3 is a shared first authorship between Matteo Crisci, Micaela Pozzati and myself. The experimental concept was mainly outlined by myself and Matteo Crisci. I produced a majority of samples and conducted Raman measurements. Additionally, I wrote the paragraph on Raman analysis in the manuscript and contributed to its overall finalization. Matteo Crisci did sample preparation and DLS measurements. Micaela Pozzati contributed to sample preparation and measured UV-Vis spectroscopy data and TEM, she also wrote major parts of the manuscript. Analysis and interpretation of data was done in a collaboration between all of us while being supervised by Dr. Mengjiao Wang and Prof. Teresa Gatti.

Publication 4 is another co-authorship where I contributed with my work on exfoliation. Similarly to publication 3, I conducted a major part of the sample preparation and Raman analysis. DLS measurements were carried out by Matteo Crisci. All other data were gathered by Micaela Pozzati, namely UV-Vis spectroscopy, TEM, SEM and thin film preparation. Interpretation of the Raman data and the elaboration into a paragraph were my contributions to the manuscript, which was then completed and assembled by Micaela Pozzati, supervised by Dr. Wang and Prof. Teresa Gatti.

Publication 5 is a work from Matteo Crisci. My contribution is based on the production of the bidimensional 2H-phase of WS_2 in suspension, which was used as electrochemically active material in composites with a conducting polymer (PANI). I provided UV-Vis spectroscopy and Raman spectroscopy data, including their interpretation, as characterization tools for the WS_2. My contribution is to the chapter “Liquid-phase exfoliation of WS_2”.

3.1. List of Publications

Publication 1:

"Assessing the Effect of Stabilization and Carbonization Temperatures on Electrochemical Performance of Electrospun Carbon Nanofibers from Polyacrylonitrile"

Advanced Energy & Sustainability Research 2023, 4, 2300121,
https://doi.org/10.1002/aesr.202300121

Publication 2:

"Multicomponent Synergistic Contribution in Nanoengineered Nanofibers for Flexible Energy Storage"

ACS Applied Energy Materials, 2024, *7*, 11, 4733 – 4744,
https://doi.org/10.1021/acsaem.4c00417

Publication 3:

"Systematic Investigation on the Surfactant-Assisted Liquid-Phase Exfoliation of MoS_2 and WS_2 in Water for Sustainable 2D Material Inks"

Physica Status Solidi Rapid Research Letters, 2024, 2400039, 1 – 9,
https://doi.org/10.1002/pssr.202400039

Publication 4:

"Water-Based Bi_2S_3 Nano-Inks Obtained with Surfactant-Assisted Liquid Phase Exfoliation and Their Direct Processing into Thin Films"

Colloids and Interfaces, 2024, *8*, 28, https://doi.org/10.3390/colloids8030028

Publication 5:

"Nanostructures 2D-WS_2@PANI nanohybrids for electrochemical energy storage"

Frontiers in Chemistry, 2022, *10*, 1 – 11, https://doi.org/10.3389/fchem.2022.1000910

3.2. Contributions to Conferences

EUROMAT 2021, 2021, Graz, Austria (online)

Preparation of Porous Thin Films from „Green“ 2D Material Inks of WS_2 from Liquid Phase Exfoliation in Low Toxicity Solvents

Felix Boll, Matteo Crisci, Lara M. Gronych, Teresa Gatti, Bernd M. Smarsly

Poster presentation

Graphene 2021, 2021, Grenoble, France

Preparation of Porous Thin Films from „Green“ 2D Material Inks of WS_2 from Liquid Phase Exfoliation in Low Toxicity Solvents

Felix Boll, Matteo Crisci, Lara M. Gronych, Teresa Gatti, Bernd M. Smarsly

Poster presentation – winner poster prize

Graphene 2022, 2022, Aachen, Germany

Nanocomposite Materials for Porous Electrodes Based on 2D Transition Metal Dichalcogenides

Felix Boll, Matteo Crisci, Melissa Happel, Leonardo Merola, Teresa Gatti, Bernd M. Smarsly

Poster presentation

E-MRS 2022 Fall Meeting, 2022, Warsaw, Poland

Nanocomposite Materials for Porous Electrodes Based on 2D Transition Metal Dichalcogenides

Felix Boll, Matteo Crisci, Melissa Happel, Leonardo Merola, Teresa Gatti, Bernd M. Smarsly

Poster presentation

POLYSTORAGE Winterschool, 2023, Sestriere, Italy

Nanofibrous Energy Storage Architectures from Ternary Blends of 2D-WS_2, Carbon nanotubes, Carbon Black and Polyethylene Oxide

Felix Boll, Martda Fadda, Matteo Crisci, Melissa Happel, Giovanni Perotto, Teresa Gatti, Bernd M. Smarsly

Poster presentation

3.3. Publication 1

Polyacrylonitrile (PAN) is considered one of the most commonly used precursor polymers for high conductivity and large capacitive CNFs.[181] According to the literature, countless examples of CNFs are produced from several imaginable precursor materials, from synthetic polymers to nature-based ones. PAN, PVP, CA which was electrospun first by A. Formhals[92], PVA, Polymethyl methacrylate (PMMA) and polyimide (PI) are only some of the most used precursors.[181,182] The literature consistently highlights the significant impact of temperature treatment on the properties of CNF. Ramos et al. as one example demonstrated the clear dependency of the (Brunauer-Emmet-Teller) BET surface area with increasing temperature, ranging from 500 °C to 3000 °C. Towards larger temperatures, graphitization and sintering of the carbon material occur leading to a decrease in surface area of the CNFs.[105,183] For capacitive applications especially the surface area is a substantial property of a material for its success. CNFs provide huge surface areas of up to 720 $m^2 g^{-1}$ or even 1230 $m^2 g^{-1}$, owing to their high meso- and nano-porosity.[184,185] For nearly all types of CNFs, regardless of precursor material or heating treatment, a range of structural analyses are typically conducted, including BET measurements, XRD, Raman, infrared spectroscopy (IR), SEM and TEM images.[105,183,186–191] These methods provide valuable insights into the structure, stacking, defect ratio and overall appearance of fibrous material can be observed quite well. The structure can be related to the surface area that is – as mentioned – strongly depending on the temperature treatment.

To gain insights into charge storage behaviour and internal resistance, it is essential to perform charge-discharge cycles, CV, EIS or volume resistance measurements.[185,187–189,191] These techniques are widely used in the field and provide crucial information on the performance and efficiency of supercapacitors, beyond what structural properties alone can reveal. In the aforementioned publications, no clear trend can be observed to understand the resulting C_s by only looking at the BET surface area. The capacitance cannot be directly related to only the surface area, moreover, the composition of the final product is of tremendous importance for the final performance.

Besides Carbon, additionally Nitrogen and Oxygen are incorporated into the fiber's structure, diffuse into the fiber and form active sites and defects, contributing to C_s.[192–195] The presence and distribution of these heteroatoms depend on the temperature treatment and the composition of the initial fibers. There are four different kinds of nitrogen atoms bonding into the carbon lattice, all contributing differently to the charge storage capacitance.[196] Additionally, not only one but two distinct temperature treatments with stabilization and carbonization are needed to produce cyclic structures in the carbon lattice to enable efficient graphitization. The complex stabilization where dehydrogenization, oxidation and cyclization occur, is drastically affecting the fibers' composition.[197–199] Therefore, stabilized PAN fibers exhibit skin-core structure due to diffusion effects during the stabilization process. Consequently, a different chemical environment is present at the surface of the CNFs compared to its core after the stabilization step, leading to variations in composition and properties across the fiber.[191–195]

This was the starting point for the following publication. Kim et al.[189] presented a versatile analysis focusing solely on the structural characteristics, C_s and the chemical composition but only for the final CNFs. However, our work extends beyond this, by providing an analysis of the structural and compositional changes of CNFs not only addressing the carbonization process, but also the crucial stabilization step. To achieve this, we supplemented traditional analysis methods such as Raman spectroscopy, XRD, SEM etc. with XPS data. XPS, being highly surface-sensitive, provided detailed information on the oxidation states of nitrogen and oxygen species present at the CNF surface. Further, we correlated the measured C_s of the symmetric supercapacitor device with the surface area and the surrounding elements differently bonded to the surface. In this manner, we optimized not only the CNF's performance in terms of C_s in their final state but also were able to show the effect of the stabilization treatment on the CNFs towards their C_s.

RESEARCH ARTICLE

ADVANCED ENERGY & SUSTAINABILITY RESEARCH Open Access

www.advenergysustres.com

Assessing the Effect of Stabilization and Carbonization Temperatures on Electrochemical Performance of Electrospun Carbon Nanofibers from Polyacrylonitrile

*Felix Boll, Matteo Crisci, Leonardo Merola, Francesco Lamberti, Bernd Smarsly, and Teresa Gatti**

Supercapacitors (SCs) are considered a promising alternative to batteries to power up portable and wearable devices. Among different categories of materials for SCs, carbon nanofibers (CNFs) are particularly appealing for their electrochemical, morphological, and mechanical properties, coupled with the ease of synthesis. Electrospinning is a simple and low-cost technique to prepare the polymer-based precursors for CNFs, allowing to obtain fibers with a tunable morphology and a diameter in the nanometer range. However, even if electrospun CNFs were intensely studied over the years, in the literature there is a lack of information regarding the optimization of the thermal treatment to prepare bare CNFs with high specific capacitance (C_s). Herein, a systematic study on the optimization of the stabilization and carbonization temperatures for electrospun CNFs prepared from polyacrylonirtile is reported, achieving a maximum C_s of 49 F g^{-1} at 0.5 A g^{-1} in a symmetrical SC device based on 1 M H_2SO_4 electrolyte. Aspects related to the specific surface area, nitrogen doping, and carbon microstructure are examined concerning the different thermal treatments, allowing to define structure–property–function relationships in these capacitive nanoarchitectures.

1. Introduction

Portable and wearable devices will increasingly play a crucial role in our everyday lives. Even if markets for portable and wearable technologies are set to grow tremendously, these devices require an efficient energy storage system (ESS) as a powering source.[1,2] There are different ESS types based on factors such as energy density (E_d), power density (P_d), and operation lifetime. ESSs can be divided into electromechanical, electromagnetic, electrochemical, chemical, and electrostatic.[2] Among all energy storage devices, rechargeable batteries and electrochemical capacitors, also known as supercapacitors (SCs), are the most suitable choices to store energy for portable and wearable devices. SCs are indeed considered valuable alternatives to batteries for these applications because they allow superior durability and an ultrafast charge–discharge time, enabling high P_d.

From a general point of view, electrodes for SCs should have high electrical conductivity, good chemical stability, high specific surface area (SSA) for contact with the electrolyte, resistance to corrosion, and thermal stability. Currently, several different categories of materials can be employed to fabricate an electrode for SCs, such as nanostructured carbon-based materials, conducting polymers, transition metal oxides, or other new emerging categories of materials like metal–organic frameworks (MOFs),[3,4] MXenes,[5] transition metal dichalcogenides, metal nitrides (MNs), and black phosphorus.[6]

Within this list, nanostructured carbon is one of the most studied and developed classes, with the longest history in research. Activated carbon,[7–10] graphene,[11,12] carbon nanotubes,[13–16] carbon aerogels,[17–19] carbon nanofibers (CNFs),[20] and laser-induced graphene[21,22] are some examples of the multitude of carbon-based materials used as scaffold electrodes for SC applications. Between all these different materials

F. Boll, M. Crisci, L. Merola, B. Smarsly
Institute of Physical Chemistry
Justus Liebig University
Heinrich-Buff-Ring 17, 35392 Giessen, Germany

The ORCID identification number(s) for the author(s) of this article can be found under https://doi.org/10.1002/aesr.202300121.

DOI: 10.1002/aesr.202300121

F. Boll, M. Crisci, B. Smarsly, T. Gatti
Center for Materials Research
Justus Liebig University
Heinrich-Buff-Ring 17, 35392 Giessen, Germany

L. Merola, F. Lamberti
Department of Chemical Sciences
University of Padova
via Marzolo 1, 35131 Padova, Italy

T. Gatti
Department of Applied Science and Technology
Politecnico di Torino
Corso Duca degli Abruzzi 24, 10129 Torino, Italy
E-mail: teresa.gatti@polito.it

ADVANCED SCIENCE NEWS
www.advancedsciencenews.com

ADVANCED ENERGY & SUSTAINABILITY RESEARCH
www.advenergysustres.com

CNFs have attracted the interest of the scientific community due to their relatively high surface area (400–600 $m^2 g^{-1}$), enabling efficient contact with the electrolyte, high electrical conductivity (1–10^2 S cm^{-1}), tuneable pore size distribution, lack of insulating binder to support the microstructure ease of synthesis process, and relatively low cost of fabrication.[23] CNFs can be easily prepared through electrospinning deposition of polymer-based precursor fibers, which, after a thermal treatment, are converted into CNFs. These polymer-based precursor fibers can be obtained from different polymers, among others, polyacrylonitrile (PAN), polyvinylpyrrolidone (PVP), cellulose acetate (CA), polyvinyl alcohol (PVA), polymethyl methacrylate (PMMA), polyimide (PI), and from different solvents like dimethylsulfoxide (DMSO), dimethylacetamid (DMAc), dimethyl sulfone, and tetramethyl sulfide.[23,24] PAN produces CNFs with the highest mechanical strength and carbon yield among all the other polymer precursors. Moreover, PAN has a higher electrospinning ability compared to the other polymers.[23] It is already well established that the preparation of CNFs from electrospun PAN nanofiber precursors involves two steps in different temperature ranges. The first one is the oxidative stabilization of PAN fibers in air between 200 and 350 °C. This step is essential to create a cyclic molecular structure through oxidation, dehydrogenization, and cyclization reactions. The second step is the carbonization of the stabilized PAN fibers between 600 and 1300 °C under N_2 or Ar flow, although the mostly employed temperature is 800 °C. During this last step, an aromatic honeycomb structure is formed due to the condensation of the stabilized PAN structure and the removal of nitrogen and oxygen atoms through formation of gaseous nitrogen oxides.[25,26] SCs devices based on CNFs are still characterized by relatively low values of C_s.[27–29] Indeed, there is a huge number of works discussing the possibility to tune the graphitization degree, to increase the surface area accompanied by controlled pore size distribution, and to increase the mechanical stability and we invite the interested reader to refer to ref. [23] to obtain a complete overview of the topic. However, the correlation between structure and physicochemical properties with capacitive behavior is only seldomly discussed and no systematic investigations have been carried out on understanding the effect of changing the thermal treatment parameters in order to tune C_s. In addition, the majority of the existing works is not examining in detail the electrochemical performance of pure CNFs, but always in combination with other active materials, in hybrid or composite structures, which does not allow to understand the actual role of the carbon species.[30–32] However, the optimization of PAN-based materials as CNFs templates for energy storage is extremely fruitful for the development of an emergent class of capacitors realized with block copolymers, in which the carbon matrix (such as PAN) is attached to a sacrificial block.[33,34] The research in this field is mainly focused on the stabilization of PAN at 300° and subsequent carbonization in nitrogen environment for forming the final porous carbon backbone,[35] thus maximizing the pseudocapacitive behavior by achieving the largest possible active area. It is thus important to better understand the potential of PAN-derived carbon nanomaterials in the field of energy storage, also given their versatility for combination with many other species, by fine-tuning the preparative process, in order to infer structure–property–function relationships.

With this work, we present an in-depth study on the optimization of CNFs production conditions from electrospun PAN and examine different stabilization (T_s) and carbonization (T_c) temperatures, in order to identify the best conditions for balancing N-doping, electrical conductivity, SSA, and pore size distribution, which are the main parameters influencing C_s in SC architectures.[36] We do this on the sole CNFs, and not on hybrid architectures with other active species, in order to understand their intrinsic electrochemical performance. This study is also motivated by the scarcity of investigations on this specific topic because the effect of the two thermal treatments on the indicated parameters is significant and these last ones are, in turn, determinant for driving capacitive behavior. The particular approach chosen here is to first compare different T_s while keeping fixed T_c, to characterize the influence of the former on the identified variables, and then to proceed with optimization of the latter. With this method, an ideal two-step temperature treatment to obtain the best capacitance from CNFs can be identified.

2. Results and Discussion

CNFs were prepared in three steps, by first electrospinning PAN to obtain polymeric nanofibers, followed by stabilization of the resulting fibrous scaffolds in air and by final carbonization under nitrogen. The stabilization and carbonization temperatures were varied within a range, in order to understand the effect of these thermal treatments on the physical and electrochemical properties of the resulting CNFs. **Figure 1** shows a schematic representation of the process, with details on operative conditions for each involved step.

A rational systematic variation of conditions was applied to prepare the different CNFs samples, by considering first the tuning of T_s while maintaining T_c at the classical 800 °C, which is the most common condition used in the literature for this second step. Then, within these samples, the T_s of the best performing one from the electrochemical point of view (vide infra) was kept fixed and a variation of ±100 °C was applied to the standard T_c, i.e., T_cs of 700, 800, 900 °C were investigated. This approach allows to understand in two separate steps the effect of stabilization and carbonization processes leading to optimized electrochemical performance of CNF-based electrode materials.

The electrochemical performances of symmetrical SC based on CNFs in 1 M of H_2SO_4 are reported in **Figure 2**. The GCD curves at 2 A g^{-1}, presented in Figure 2a, underline the linear relationship between the potential and the time which leads to a triangular charge/discharge curve which is characteristic of electric double-layer materials (experimental CV and GCD curves for all samples are shown in Figure S4 and S6, Supporting Information). In each GCD curve it is possible to identify the IR drop, which is associated with the internal resistance.[37] The CV curves at 50 mV s^{-1} (Figure S4, Supporting Information) show a characteristic rectangular shape of electric double-layer materials, in accordance with GCD measurements. However, although the CV curves have a symmetric and almost ideal rectangular shape, the presence of equivalent series resistance (ESR) and equivalent parallel resistance (EPR) lead to small deviations from the ideal shape.[38] In addition, a slightly asymmetric shape, most likely caused by the distribution of ions in the double layer

ADVANCED SCIENCE NEWS
www.advancedsciencenews.com

ADVANCED ENERGY & SUSTAINABILITY RESEARCH
www.advenergysustres.com

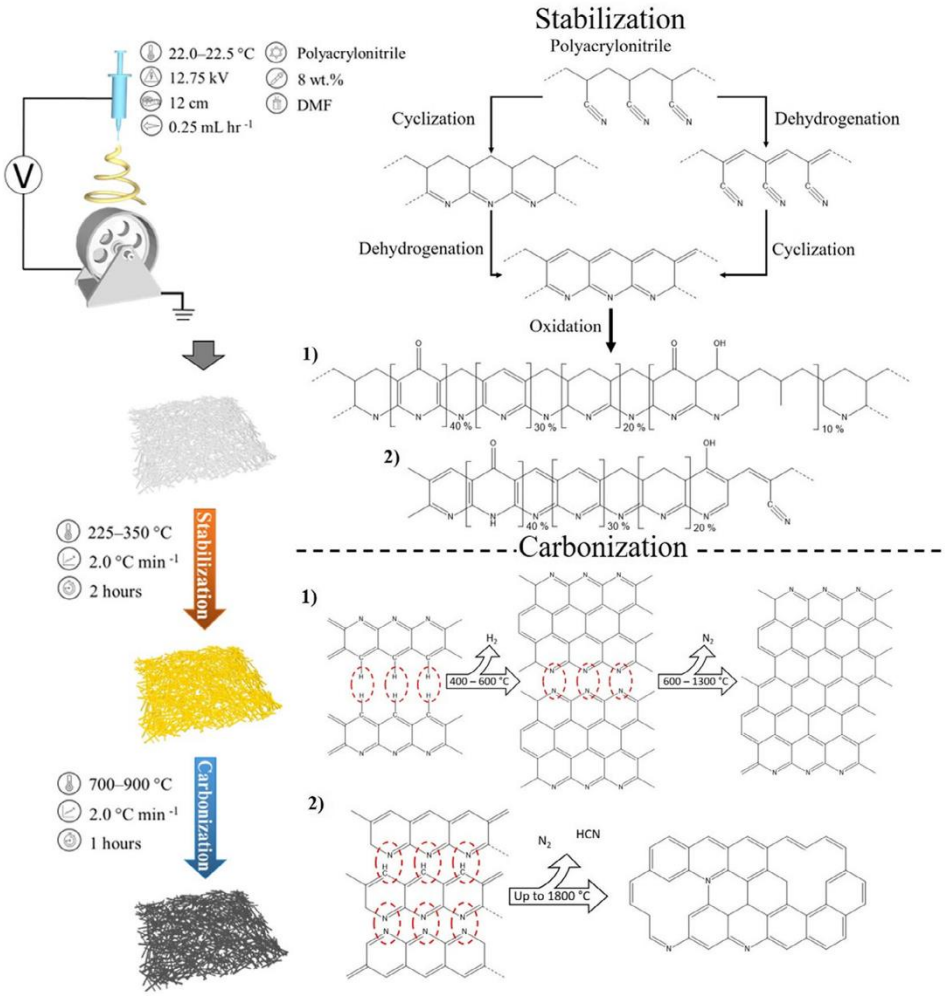

Figure 1. Schematic representation of the entire CNFs production process, including the electrospinning of PAN, stabilization, and carbonization steps parameters employed. The details on the chemical processes happening during the two steps are also shown for 1) defect-free[25] and 2) defect-rich phases.[82]

during the charge and discharge process, is observed. Especially at high scan rates, tail-like shapes are probably formed by redox processes (reactions) with the electrolyte or solvent. During the charging, fewer ions are in the proximity of the electrode surface, reducing the number of total charges detected by the external circuit. On the contrary, during the discharging, the electric double layer is larger due to the presence of more ions which increases the effective capacitance.[38] In the CVs, it is possible to identify some weak and broad peaks that can be associated with redox reactions due to the pseudocapacitance of nitrogen or impurities adsorbed on the surface.

A long discharge time in the GCD curves and a large area within the CV curves of the CNFs—325–800 sample implies a higher C_s than that of the all other samples examined. Indeed, as reported in Figure 2c,d, device based on CNFs—325–800 achieved the highest average value of C_s for all the current densities tested, except for 20 A g^{-1}. At 0.5 A g^{-1}, such sample shows an average C_S of 49 ± 3 F g^{-1}, which is reduced to 30 ± 3 F g^{-1} at 20.0 A g^{-1}. The same trend is seen in the Ragone plots presented in Figure 2e,f, where it achieves the highest average E_d of 4.4 ± 0.2 Wh kg^{-1} at a P_d of 200 W kg^{-1}. These values are further reported in **Table 1** and **2** for the sake of clarity. The promising electrochemical performance of CNFs—325–800 can be explained by a combination of different factors, as it will be clarified later in the text by analyzing XPS, physisorption, SEM, and EDX data.

EIS measurements were carried out to study the impedance behavior of the CNF-based devices and to confirm their capacitive properties. **Figure 3**a and S6, Supporting Information, represent the Nyquist plots of the SCs in the frequency range

ADVANCED SCIENCE NEWS
www.advancedsciencenews.com

ADVANCED ENERGY & SUSTAINABILITY RESEARCH
www.advenergysustres.com

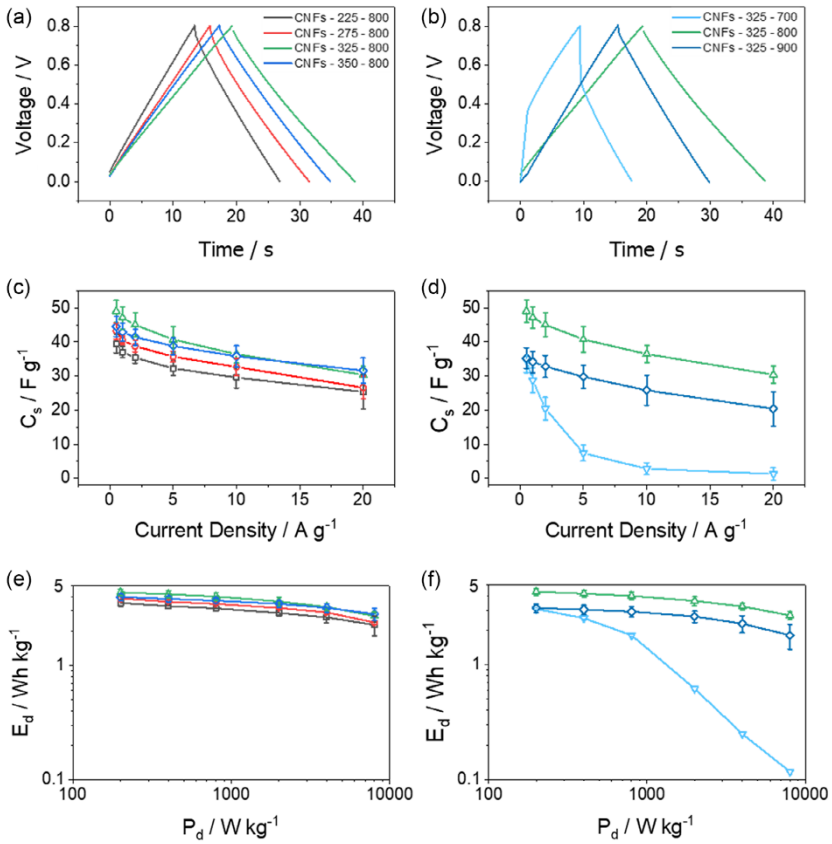

Figure 2. Comparison of the electrochemical performance of symmetric SCs based on the different CNFs used as electrode materials: a) GCD curves obtained at 2.0 A g^{-1} in the 0–0.8 V range in 1 M H_2SO_4 electrolyte at different T_s; b) GCD curves obtained at 2.0 A g^{-1} in the 0–0.8 V range in 1 M H_2SO_4 electrolyte at different T_c; c) trends in C_s as a function of current density for the different examined T_s; d) trends in C_s as a function of current density for different examined T_c; Ragone plots for e) different T_s and f) different T_c.

Table 1. Values obtained from the fittings of the EIS curves recorded for devices based on CNFs samples prepared at different T_s or T_c.

Device based on	R_s [Ω]	R_{ct} [Ω]	CPE_1 [10^{-5} S]	N_1	C_{dl} [μF]	CPE_2 [S]	N_2
CNFs—225–800	0.94	23.78	6.50	0.82	15.69	0.069	0.94
CNFs—275v800	0.85	14.60	5.20	0.83	17.78	0.084	0.96
CNFs—325–800	0.90	5.96	14.20	0.77	26.92	0.042	0.97
CNFs—350–800	1.00	14.50	15.10	0.77	21.83	0.052	0.93
CNFs—325–700	0.88	46.50	9.00	0.75	15.45	0.071	0.92
CNFs—325–900	0.90	1.70	13.00	0.81	18.04	0.062	0.92

between 200 kHz and 10 mHz. The Nyquist plot can be divided into three regions. In the first one, the high-frequency region, the intercept with the real axis (Z'_{Re}) is related to the internal resistance (R_s) induced by the resistance of the electrolyte. In the second one, the midfrequency, the semicircle is associated with surface properties, which are related to the charge-transfer resistance (R_{ct}) between the electrode and electrolyte or contact between the electrode and current collector. In the last one, the low-frequency region, the straight line is related to the electric double layer's impedance. However, for an ideal capacitor, this line is parallel to the imaginary axis ($-Z'_{Im}$). Instead, for a real capacitor, this line has a slope determined by the presence of resistances.[39,40] The experimental data were fitted with a modified Randles circuit to evaluate the values of R_s, R_{ct}, and double-layer capacitance (C_{dl}), as reported in the inset in Figure S6, Supporting Information and in Table 1.[41] Constant phase elements (CPEs) were chosen for modeling the Warburg element and C_{dl}. With CPEs, the nonideality of the device can be modeled with more accuracy and include the role of each element. CPE_1 is related to the C_{dl}, while CPE_2 is associated with the Warburg coefficient, determined by the semi-infinite diffusion of the ions in the electrolyte.[42,43] The C_{dl} was calculated using the equation reported by Bard and Faulkner.[44] From the fittings, all the samples exhibit slightly different values of R_s, within 10% error. Indeed, the impedance behavior of the devices is mainly determined by R_{ct}, which shows

ADVANCED SCIENCE NEWS
www.advancedsciencenews.com

ADVANCED ENERGY & SUSTAINABILITY RESEARCH
www.advenergysustres.com

Table 2. Comparison of electrochemical performances for the symmetric devices indicated in Figure 8. ΔV stands for the potential range used for the measurements. If it is indicated with a minus sign, it means that the devices were tested in a negative potential range.

Type of sample	P_d [W kg^{-1}]	E_d [Wh kg^{-1}]	Electrolyte	$\Delta V/V$	Ref.
Flexible porous CNFs	600	3.2	0.5 M H_2SO_4	1.2	[71]
Activated CNFs	900	5.0	1.0 M Na_2SO_4	1.8	[72]
AC	1500	4.2	1 M H_2SO_4	1.0	[74]
CNTs with N-doped carbon	200	1.0	1 M H_2SO_4 (Swagelok cell)	0.8	[73]
B, N co-doped CNs	600	4.2	1 M H_2SO_4	0.8	[75]
Oxigenated N-doped CN	1200	3.4	6 M KOH	-1.0	[76]
N, F co-doped CNFs	248	8.7	1 M H_2SO_4 (Gel electrolyte)	1.0	[77]
Porous AC/graphene	8000	4.4	6 M KOH (Coin cell)	0.8	[78]
CNFs—325–800	800	4.0 ± 0.3	1 M H_2SO_4 (Swagelok cell)	0.8	This work

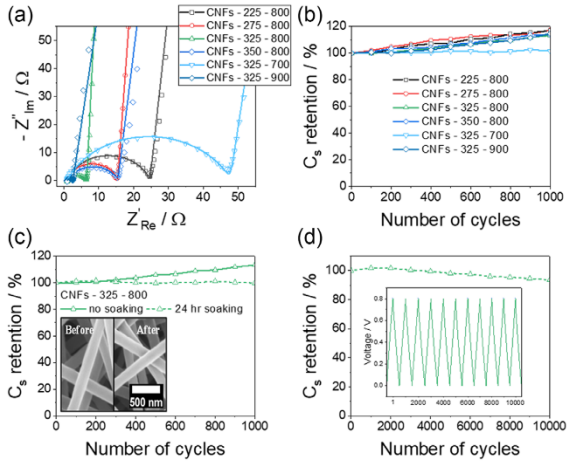

Figure 3. a,b) Nyquist plots obtained from EIS of CNFs samples prepared at different T_s or T_c. c) Capacitance retention of the devices based on CNFs—325–800 after 1000 cycles. The dashed blue line indicates the data associated to the device with the electrode materials soaked in the electrolyte solution for 24 h. The solid line refers instead to the data obtained when the electrode materials were not soaked before the preparation of the device. e) Capacitance retention of the devices based on CNFs—325–800 after 10 000 cycles. The electrode materials were previously soaked for 24 h in the electrolyte solution.

the most prominent difference between each sample. Indeed, an ideal double-layer capacitor does not exhibit a R_{ct} because there is no charge transfer but only electrostatic interactions between the electrodes and electrolyte. In addition, all the devices were closed by applying the same pressure. It is reasonable, therefore, that these values of R_{ct} are probably due to the presence of nitrogen, which introduces a pseudocapacitive behavior to the system. As it can be tracked from Table 1, the R_{ct} follows indeed the, later explained, same trend of nitrogen concentration in the samples (Table S2, Supporting Information). The straight line in the low-frequency region achieves the highest slope for the device based on CNFs—325–800, suggesting a better capacitive behavior. This is also confirmed by the calculation of the C_{dl}, which is the highest for CNFs—325–800. In conclusion, EIS results further confirm that CNFs—325–800 has the best electrochemical properties as a SC, compared to the other samples.

Regarding the stability of the best SC device (i.e., the one based on the CNFs—325–800 sample), Figure 3c shows the capacitance retention tested at a current density of 2.0 A g^{-1} for 1000 cycles. All the examined samples achieved comparable and stable cycle performances, with capacitance retention between 113% and 117%. The increase in capacitance retention has already been reported for other carbon-based materials and it can be associated to a self-activation process and/or to the pore size distribution.[45–47] The self-activation process induces changes in the surface morphology, especially because it may increase the SSA. Also cycling the sample may cause changes in the equilibrium states of the sample. These states might be induced by the repeating charging/discharging, modifying the morphology, and further exposing the electrochemically active sites to the electrolyte.[48,49] In the inset in Figure 3c, SEM images of CNFs—325–800 before and after the stability test are reported. As far as it can be observed, the surface morphology has not changed after 1000 cycles. Regarding the pore size distribution, as the CNFs are characterized by micropores, the electrolytes take time to fill all the pores. As a result, at the beginning of the measurements, not all the surface is in touch with the electrolyte and contributes to the capacitance. To verify this assumption, the stability test for CNFs—325–800 was repeated but the electrode materials were previously immersed in the electrolyte solution for 24 h (Figure 3c, dashed green line). As it can be seen, the capacitance retention after the 1000 cycle does not increase but remains stable, also indicating a good cycle performance, which is confirmed after 10 000 cycles (94% of capacitance retention), reported in Figure 3d. The excellent capacitance retention can be explained by the large SSA of up to 220 m^2 g^{-1} and the existence of short pore channels. The small capacitance decrease can be attributed to changes in the defects structure during cycling.[50]

Figure 4a,b and S7a–e, Supporting Information, present the SEM images of carbonized PAN fibers. For each sample, the diameter is distributed uniformly, and the fibers do not show any particular defect (such as bead defects), underlying that the electrospinning deposition process was optimized. T_c appears to be the key parameter defining the final CNF diameter,

ADVANCED SCIENCE NEWS
www.advancedsciencenews.com

ADVANCED ENERGY & SUSTAINABILITY RESEARCH
www.advenergysustres.com

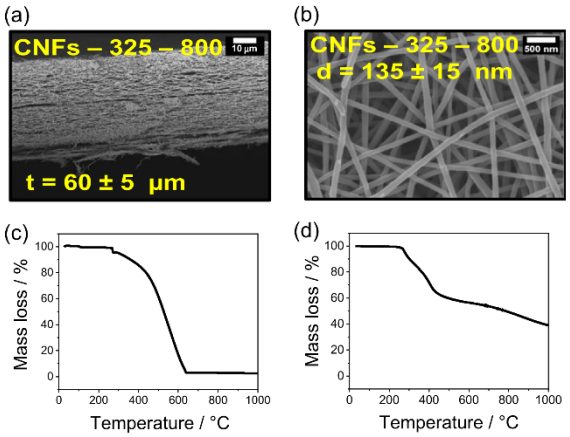

Figure 4. a) Cross-sectional SEM image of the CNF—325–800 sample. The thickness (t) is reported. b) Top-view SEM image of the same sample. c) TGA analysis of electrospun PAN fibers heated up to 1000 °C in synthetic air (stabilization conditions). d) TGA analysis of stabilized PAN fibers heated up to 1000 °C under nitrogen atmosphere (carbonization conditions).

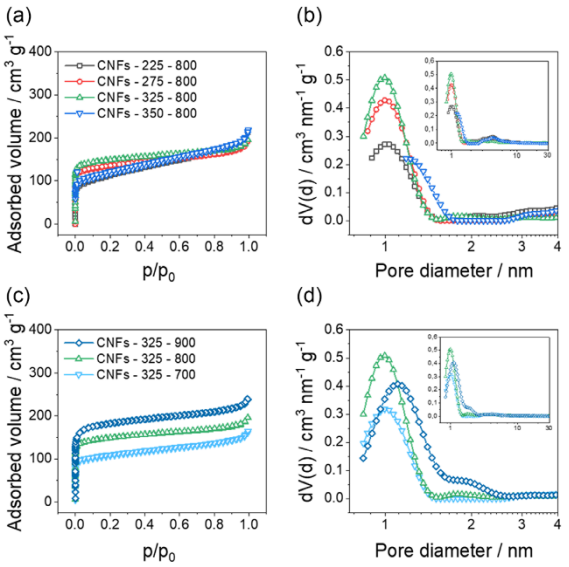

Figure 5. a–c) Nitrogen physisorption isotherms and b–d) relative pore size distribution curves for CNFs samples prepared at different T_s or T_c (the graph is a zoom at the lowest pore sizes of the inset, reporting the entire distribution up to 30 nm).

while T_s is not affecting the thickness. This can be explained by the mass loss during the stabilization and carbonization processes, which can be determined by TGA analysis, as reported in Figure 4c,d. During stabilization (225–350 °C, Figure 4c) the mass loss is around ≈6 wt%. On the other hand, during carbonization, (700–900 °C, Figure 4d) the mass loss is increasing up to ≈13 wt%. Indeed, the value slowly approaches a plateau (within the error bar) when the stabilization temperature is increased. When T_c is increased from 700 up to 900 °C instead, the diameter decreases significantly (Figure S7, Supporting Information). Finally, the thickness of the deposited fiber mats can be determined from cross-sectional SEM analysis to be in the 60 µm range for all samples. Figure 4a shows a prototypical image, referring to the sample treated at 325 and 800 °C for, respectively, T_s and T_c.

Nitrogen physisorption was performed to evaluate specific information regarding fibers' morphology, namely, SSA and pore size distribution. For the applications of CNFs as electrode material for SC devices, a large electrode–electrolyte interfacial contact is indeed essential to enhance the charge transfer and the charge adsorbed. However, a high SSA is useless if the pore size distribution is not optimized because this last one may limit the accessible surface to the electrolyte. In **Figure 5**a–d, the isotherms and pore size distributions are reported. As it can be deduced from the reported values in the graphs, SSAs vary mostly in relation to changes in T_c, with variations of 100–220 $m^2 g^{-1}$ when this temperature is raised by 100 °C (see Figure 5c). Pore sizes are also quite homogeneous in relation to different T_s and same T_c, while they tend to change slightly more when T_s is taken stable and T_c is varied. In general, their distribution is centered around 1 nm, with a population more shifted at higher values (up to 2 nm) for the sample treated at the highest T_c (900 °C).

XPS measurements were performed to understand how nitrogen heteroatoms, acting as N-dopants, are inserted into the main graphitic structure of the CNFs. This evaluation is extremely important to better understand the structural and electrochemical performance of CNFs. As displayed in **Figure 6**a, CNFs exhibit four main types of nitrogen bonding, namely pyridinic (N-6, at 398.1–398.3 eV), pyrrolic (N-5, 399.8–401.2 eV), graphitic (N-Q, 401.1–402.7 eV), and oxidized (N-O, 403–406 eV).[51,52] Therefore, the chosen energy range for XPS analysis was between 200 and 600 eV to detect the O 1s, N 1s, and C 1s signals (see the whole spectrum in Figure 6b for one prototypical case and all the others in Figure S8, Supporting Information). The signal of C 1s localized at 284.8 eV mainly shows the sp^2-hybridization (graphitic) of the carbon atoms in the CNFs, whereas the peak asymmetry toward higher binding energies can be ascribed to the presence of defects based on sp^3-hybridized carbon species like C–C (284.7 eV) or C–OH (285.4 eV) present within the CNF lattice.[53,54]

In the region of the N 1s peak between 394 and 408 eV, more detailed spectra were recorded, to precisely analyze the above-described multiple nitrogen species and to define their contribution to the nitrogen peak in each spectrum (see also Table S2, Supporting Information). In order to first understand the influence of different T_s in the range 225–350 °C (Figure 6c and S9, Supporting Information), XPS data as well as EDX atomic percentages (at%) were employed for the evaluation (Table S2, Supporting Information). A trend in progressive nitrogen removal from the fibrous structure is observed from 225 °C (with ≈7.2–7.3%) up to 325 °C (with 5.1–6.0%), while stabilization at 350 °C brings to an increase for both elemental analysis methods between 6.0% and 6.8%, which is, to the best of our

ADVANCED SCIENCE NEWS
www.advancedsciencenews.com

ADVANCED ENERGY & SUSTAINABILITY RESEARCH
www.advenergysustres.com

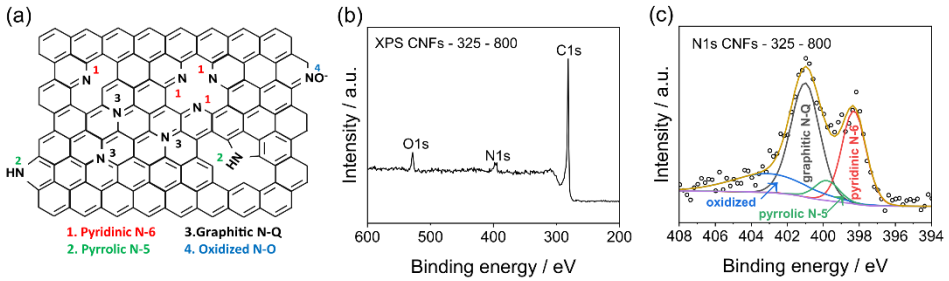

Figure 6. a) Schematic representation of different nitrogen species present in the CNF structure. b) Full XPS spectrum for CNFs—325–800 sample (the entire spectra for all other examined cases are reported in Figure S3, Supporting Information). c) Detail of the N 1s peak for the same sample, with fittings of the different nitrogen contributions.

knowledge, here reported for the first time. The two fundamentally different techniques here used also allow to assume a homogenous distribution of the doping along the whole CNF diameter. While XPS is surface sensitive and a local technique, the penetration depth of EDX (depending on the acceleration potential) can go up to several hundreds of nm, plus a broader investigated area. Therefore, depending on the stabilization temperature, a constant atomic ratio of nitrogen can be found throughout the CNFs as well as on their surface. Previously obtained data on nitrogen contents for CNFs stabilized at 225 °C and carbonized at 800 °C were fully reproducible in our work.[55] Increase in T_s leads to larger contributions of graphitic nitrogen, as can be guessed from XPS spectra, from 40% at 225 °C to 45% at 350 °C. On the contrary, the contribution of pyrrolic and pyridinic nitrogen atoms decreases from 10% to 6% for the former and from 35% to 28% for the latter. The oxidized species tend also to increase from 15% to 21%. This is reasonable given the more efficient oxidation (as well as partially graphitization) at higher temperatures during stabilization. In the case of the stabilized sample at 350 °C, another peak is further visible, attributed to NO_2/C–ONO and NO_2^- nitrogen species, which can be formed at higher temperatures in the presence of oxygen and nitrogen.[56–58]

T_c is drastically affecting the amount of graphitic carbon within the CNFs. From 700 to 900 °C at a constant T_s (325 °C), an increase from 24% at 700 °C to 53% at 900 °C was detected. As a consequence, the pyrrolic and pyridinic species contributions diminish from 22% down to 5% (N-5) and from 38% to 17% (N-6). These changes in composition are well described in literature, with the less stable pyrrolic nitrogen converting into graphitic nitrogen above 600 °C, while pyridinic nitrogen converting in the same species above 700 °C.[55,59,60] This is indeed confirmed by our experiments, where N-5 content decreases already drastically from 700 to 800 °C (22% to 7%), while N-6 content experiences a drop from 38% to 17% over the whole examined T_c range (700–900 °C).

Raman and XRD analyses were carried out to study changes in the graphitic microstructure of the CNFs and to determine the influence of nitrogen concentration and types of nitrogen. The Raman spectrum of the electrochemically best performing CNF sample is presented in **Figure 7**a, while the list of parameters calculated from Raman spectroscopy for all the samples is reported in Table S3, Supporting Information. For comparison, the other Raman spectra are shown in Figure S10, Supporting Information. Peaks deconvolution shows that all samples have four contributions. Peaks at ≈1590 and ≈1350 cm^{-1} are associated with the G and D bands, related to ordered and disordered graphitic structures, respectively.[61,62] The D″ band at ≈1500 cm^{-1} is related to the amorphous carbon and the I band at ≈1220 cm^{-1} is associated with the bond between sp^2 and sp^3 carbons.[63–65] One of the most important parameters for carbon materials is the I_D/I_G ratio. As G bands correspond to the E_{2g}

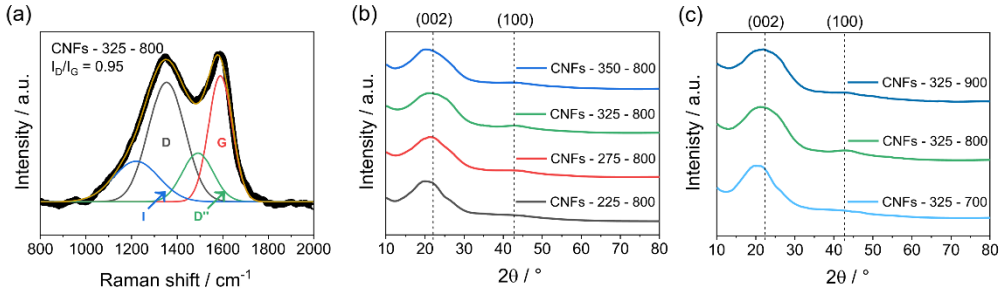

Figure 7. a) Raman spectrum of the CNF—325—800 sample. b) XRD patterns of CNFs samples prepared with varying T_s from 225 °C up to 350 °C and a constant T_c at 800 °C. c) XRD patterns of CNFs stabilized at 325 °C with varying T_c from 700 °C up to 900 °C. These structures correspond to JCPDS 00-056-0159.

ADVANCED SCIENCE NEWS
www.advancedsciencenews.com

ADVANCED ENERGY & SUSTAINABILITY RESEARCH
www.advenergysustres.com

phonon which is always present, the D band, on the contrary, is related to the breathing mode and therefore requires defects to be activated. Indeed, the more defects are present in the graphitic structure the higher the I_D/I_G ratio will be.[61,62] Defects are not only atomic vacancies or distortion of the structure but also defined by the presence of heteroatoms (see Figure 6a). As already reported, the amount of carbon defects in nitrogen-doped carbon materials is strongly depending on nitrogen amount and relative bonds involved.[66] From XPS and EDX measurements emerges how the overall nitrogen amount decreases with higher T_s and T_c and, at the same time, graphitic carbon content increases. This also affects the order of CNF microstructure. Indeed, I_D/I_G ratio (Table S3, Supporting Information) shows the same trend of graphitic nitrogen contribution (Table S2, Supporting Information): it generally decreases at larger T_s and T_c. The rising G band in comparison to the D band is indicating a more structured carbon lattice at higher temperatures.[61,62] From the collected dataset however, deriving a clear trend in either changes of amorphous carbon content (D″ band) or sp^2–sp^3 bonds (I band) is not possible in a reliable manner.

A further proof of the influence of nitrogen concentration on CNFs microstructure can be determined by XRD measurements. Figure 7b,c and Table S4, Supporting Information, show the XRD data and a list of parameters calculated from the diffractograms, respectively. Those diffractograms are characterized by a major Bragg peak at 21.0° and a weak reflex at 43.0°, which are related to crystal planes (002) and intralayer scattering (100) of graphite.[67,68] An important parameter for materials with a graphite-like structures is the interlayer distance along the (002) direction: $d_{(002)}$. This parameter is essential because the presence of nitrogen atoms, and consequently a more disordered graphitic structure, leads to higher values of $d_{(002)}$ compared to that of graphite 3.335 Å.[55,67–69] Indeed, the values of $d_{(002)}$ (Table S4, Supporting Information) are higher than 3.335 Å due to the presence of nitrogen atoms. Moreover, $d_{(002)}$ show the same trend of the nitrogen concentration reported in Table S2, Supporting Information: it decreases with the increasing of stabilization and carbonization temperatures.

Other important parameters that can be evaluated from Raman spectroscopy and XRD measurements are related to the crystallite size: in-plane crystallite size L_a along *a*-direction and average stacking height L_c along the *c*-direction. Through this analysis, preferential growth directions of the microstructure can be determined. Values of L_a, reported in Table S3, Supporting Information, can be easily determined from Raman spectra by using the Tuinstra–Koening equation, while values of L_c, presented in Table S4, Supporting Information, can be estimated from XRD diffractograms by applying the Scherrer equation. As reported, graphitic structure grows along L_a with the rising temperatures; on the contrary, L_c decreases. The decrease along *c*-direction can be explained by two possible phenomena: 1) changes in stacking and order for graphitic structure along due to the release of gases during the thermal treatments[55] and 2) curvature of the graphene sheets due to the presence of nitrogen doping heteroatoms.[70]

To summarize, the low concentration of nitrogen, especially with a high contribution of graphitic nitrogen, leads to a more ordered graphitic structure (low $d_{(002)}$ and I_D/I_G). Moreover, CNFs structure grows mainly along in-plane *a*-direction, as evidenced by the increase of L_a. On the other hand, the growth of graphite sheets along the *c*-direction is disturbed and reduced.

The results as a whole give a fully satisfactory picture of the CNFs functional behavior, allowing to provide a speculative, but pragmatic, correlation between electrochemical performance and morphological/structural properties. By examining the reported effects on stabilization derived from physisorption and XPS measurements, it is possible to understand electrochemical data more precisely. Indeed, the CNFs—325–800 sample, which is the most performing one, has also the highest SSA compared to other samples treated at different T_s. Regarding the effect of T_c, the electrochemical performances of CNFs—325–800 is a consequence of the balance between the SSA, total amount of nitrogen, and the contribution of each nitrogen bond-type. CNFs—325–700 has the highest amount of nitrogen, the lowest contribution of graphitic nitrogen, and lowest value of SSA, leading to a lower average value of C_s. On the contrary, even if CNFs—325–900 shows the highest SSA, it does not achieve the average value of C_s of CNFs—325–800, due to the lower nitrogen concentration, leading to a too low defect density. Indeed, this result is further corroborated by Raman analysis, in which the lattice defects density, in terms of graphitic nitrogen contribution, is diminished at higher T_s and T_c. In addition, the lattice parameters are also strongly influenced by the nitrogen doping as highlighted by the XRD outcomes: the best electrochemical samples are the ones in which the interlayer distance $d_{(002)}$ is among the smallest (4.1 Å), with an anisotropic growth on the in-plane *a*-direction.

In the literature, numerous works on the preparation and application of carbon-based materials in energy storage devices are reported. **Figure 8** compares the performance of the devices tested in this work with different similar symmetrical SCs. The best obtained values of E_d and P_d from the here studied CNFs are compared with that of other relevant cases of carbon-based materials, such as flexible porous CNFs (3.2 Wh kg^{-1} at a P_d of 600 W kg^{-1}),[71] activated CNFs (5.0 Wh kg^{-1} at a P_d of 900 W kg^{-1}),[72] CNTs with N-doped carbon (1.0 Wh kg^{-1} at a P_d of 200 W kg^{-1}),[73] AC (4.2 Wh kg^{-1} at a P_d of 1500 W kg^{-1}),[74] B, N co-doped CN (4.2 Wh kg^{-1} at a P_d of 600 W kg^{-1}),[75] and oxygenated N-doped CN (3.4 Wh kg^{-1} at a P_d of 1200 W kg^{-1}).[76] Obviously, there are examples of carbon-based materials with more promising performance.

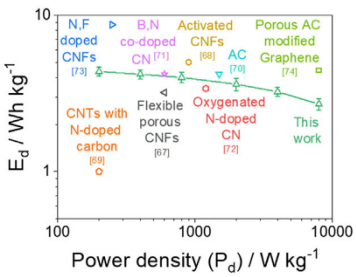

Figure 8. Ragone plot for the symmetrical device based on CNFs—325–800 compared with other symmetrical devices based on different carbon-based active electrode materials.

ADVANCED SCIENCE NEWS
www.advancedsciencenews.com

ADVANCED ENERGY & SUSTAINABILITY RESEARCH
www.advenergysustres.com

For example, Na et al. have successfully prepared highly porous N, F co-doped CNFs achieving an E_d of 8.7 Wh kg^{-1} at a P_d of 248 W kg^{-1}, but they used a vacuum plasma treatment with C_4F_8 after the carbonization step.[77] Chen et al. produced porous graphitic layers on both sides of graphene sheets through hydrothermal and activations steps, achieving an E_d of 4.4 Wh kg^{-1} at 8000 W kg^{-1}.[78] However, it is important to underline that CNFs produced in this work are made without any further processes such as activation or chemical etching and without any further additive. They indeed achieve these significant E_d value only by optimizing the heat treatment temperatures. In addition, as reported in Table 2, the devices tested in this work have been cycled in a potential range of 0.0–0.8 V ($\Delta V = 0.8$ V). As E_d is proportional to ΔV (Equation (6)), by increasing the latter E_d increases significantly. For a more complete comparison, Equation (S4), Supporting Informationm was used to estimate C_s of the single electrode. In Table S7, Supporting Information, the values of C_s for other CNFs are compared to the ones of the CNFs tested in this work. CNFs produced in this work are made without any specific processes of activation and chemical etching and without any further additives such as PVP or Co_3O_4. Indeed, as can be seen from Table S7, Supporting Information, the calculated C_s of CNFs prepared in this work is comparable with that one of other studies.

3. Conclusions

A systematic study to reveal the effect of different T_s and T_c on CNFs electrochemical performance was carried out in this work, by correlating their structural and compositional changes to C_s of symmetrical SC devices based on these pure materials as the only active electrode components. The different thermal treatments affect the SSA of the fibers, the amount of nitrogen atoms within their crystalline lattices, and the type of bonding that these heteroatomic dopants establish with carbon. The last two features also influence the microstructure of the CNFs and all together have a tremendous impact on the electrochemical behavior. As a rule of thumb, one can recognize that, with increasing temperatures, the SSA and the amount of graphitic (N–Q) nitrogen in the lattice increase, which lead to larger C_s and thus better energy storage performance.

A T_s of 325 °C for the produced PAN fibers was found to be ideal because the attainable SSA is the largest. Furthermore, these fibers contain the lowest nitrogen concentration, including the largest ratio of graphitic nitrogen compared to all the other samples produced at T_s of 225, 275, and 350 °C. Below the ideal temperature, the larger nitrogen content, as well as their bonding type (lowest ratio of graphitic nitrogen), leading to a more unorganized carbon structure, and the lower SSA give rise to poorer electrochemical performances. On the other hand, stabilization at 350 °C might cause pore blocking, that is negatively affecting the SSA and deteriorates electrochemical performance, due to a lower effective area and a less accessible surface.

The ideal T_c for the stabilized fibers was found to be 800 °C, once again because of optimal SSA, nitrogen concentration, and nitrogen bonding types. Higher temperatures are thus not necessary to improve electrochemical quality. Even if the high nitrogen concentration generates several defects for possible charge storage processes, the comparably lower SSA at 700 °C causes a less accessible surface for the electrolyte–CNFs interaction, which worsen the electrochemical performance. On the other hand, the sample carbonized at 900 °C has the largest SSA and, therefore, the largest accessible area for the electrode–electrolyte interaction, but nitrogen content is the lowest in all the examined samples. In conclusion, there is a net trade-off between a large pseudocapacitive contribution of pyrrolic and pyridinic nitrogen species in the CNFs and a low SSA or vice versa, to be taken into consideration to achieve optimized energy storage performance. This aspect will most likely have an impact also for the use of CNFs in other electrochemical devices, such as batteries or sensors, and therefore the optimization here described will have a broader impact for the electrochemical community.

One key factor for optimized electrode materials based on carbon is to find the ideal temperatures for stabilization and carbonization, to maximize the defects contributing to the pseudocapacitive behavior and to achieve the largest possible accessible area, which is one of the big advantages of using similar materials for electrochemical applications. Then, even without further doping, complex processing and treatments and coupling with other materials, it is possible to produce competitive carbon-based active electrodes for SCs by only tuning thermal treatments, thus improving the sustainability of the production process.

4. Experimental Section

All chemicals and solvents were purchased from Sigma–Aldrich and used as received, unless otherwise specified. Milli-Q water was used as solvent for the preparation of the electrolytes for the electrochemical measurements.

CNFs Production: For the preparation of CNFs, a solution of 8 wt% of PAN (>99.0%, M_w 150 000) in DMF was prepared by dissolving 1.131 × g of PAN in 15 mL of DMF. A home-made electrospinning setup was employed (Figure S1, Supporting Information), made of two high voltage power supplies (Scientific Instruments, TSI-HV), a syringe pump (HARVARD APPARATUS, PHD 2000 Infusion), a syringe, a needle (inner diameter 1.2 mm, 18 G), and an aluminum foil-covered rotating drum collector (radius of 5 cm). The deposition parameters were chosen by following the work of Einert et al.[55] The tip-to-collector distance was fixed at 12 cm and the rotation speed of the drum at 65 rpm. The flow rate was set to 0.25 mL h^{-1} and a voltage of 12.75 kV was applied between the tip and the collector (+10.75 kV at the needle and −2.00 kV at the collector). As the electrospinning setup is placed in a closed box, the relative humidity is controlled and was set between RH = 30% and 35% at a temperature of 21 °C. The precursor PAN fiber mats appeared as reported in Figure S1b,c, Supporting Information. After the electrospinning deposition, the fibers were stabilized at 225, 275, 325, or 350 °C for 2 h, with a heat rate of 2 °C min^{-1} in air in a Nabertherm N7/H-P320 oven. Afterward, the stabilized fibers were carbonized under nitrogen flow at 100 °C for 1 h followed by a temperature increase up to 700, 800, or 900 °C for 1 h using a tube furnace (Nabertherm R80/300/11-P300). The nitrogen flow was fixed at 100 mL min^{-1} (100 sccm) and the heating rate at 2 °C min^{-1}.

CNFs Electrochemical Characterization and SC Assembly: To classify the produced samples based on their electrochemical performances, all electrochemical measurements were carried out in a two electrode Swagelok cell setup, as sketched in Figure S2, Supporting Information. The electrolyte was a 1 M aqueous solution of H_2SO_4 (1 mL). A glass microfiber separator without binder purchased by ALBET LabScience (GF 50 150) was used between the two half cells to prevent short-circuiting.

ADVANCED SCIENCE NEWS
www.advancedsciencenews.com

ADVANCED ENERGY & SUSTAINABILITY RESEARCH
www.advenergysustres.com

The electrochemical analyses were performed using the potentiostat and galvanostat Autolab (Metrohm). The software used to collect the data was Nova 2.1 (Metrohm). Electrochemical impedance spectroscopy (EIS) measurements were carried out with a SP 200 potentiostat from BioLogic. The software used to collect EIS data was EC-lab. Cyclic voltammetry (CV) measurements were carried out to verify the electric double-layer behavior of CNFs. In particular, the measurements were performed between 0 and 0.8 V at different scan rates of 100, 50, 30, 20, and 10 mV s^{-1}. Moreover, each cycle was performed four times and only the last one was used for data analysis to ensure reproducible voltammograms in equilibrium. Galvanostatic charge–discharge (GCD) measurements were performed to determine the capacitance retention of the Swagelok cell setup as well as the power and energy densities of the SCs. First, devices were cycled ten times between 0 and 0.8 V at 1.0 A g^{-1}. Then, charge and discharge curves were measured between 0 and 0.8 V at different current densities of 0.5, 1.0, 2.0, 5.0, 10.0, and 20.0 A g^{-1}. The specific capacitance was calculated with the following equation

$$C_s = \frac{I\Delta t}{m\Delta V} = [\mathrm{F\,g^{-1}}] \quad (1)$$

where I is the charge–discharge current, Δt the discharge time, m the total mass of the electrodes (≈15.0 mg), and ΔV the potential range of the measurements (0.8 V). Each measurement, at the same current density, was performed three times and only the last one was used for data analysis. E_d and P_d can be calculated directly from the results obtained from the charge and discharge curves. E_d and P_d were calculated by the following equations

$$E_d = \frac{1}{2} C_s \Delta V^2 \frac{1}{3.6} = [\mathrm{Wh\,kg^{-1}}] \quad (2)$$

$$P_d = \frac{E_d}{\Delta t} 3600 = [\mathrm{W\,kg^{-1}}] \quad (3)$$

The values reported for C_s, E_d, and P_d are average values calculated by repeating the measurements with at least three different devices for each sample. To study the life cycle stability of the device, capacitance retention was calculated by cycling the device for 1000 and 10 000 cycles at a moderate current density of 2.0 A g^{-1}. EIS measurements were carried at a constant potential mode of 0 V. Frequency range was varied between 200 kHz and 10 mHz at an amplitude of 5 mV. Before each EIS measurement, five GCD curves were recorded at 1.0 A g^{-1} to stabilize the devices. The software to fit the obtained EIS data was RelaxIS3.

CNFs Physicochemical and Morphological Characterization: Raman spectroscopy measurements were performed on a Bruker Senterra Raman Microscope equipped with a 532 nm solid-state laser. As the fibers are free-standing, to obtain more detailed spectra, samples were attached to a silicon wafer (1 cm × 1 cm) with double tape. The in-plane crystallite dimension (L_a) can be calculated using the Tuinstra–Koening equation[79]

$$L_a = (2.4 \times 10^{-10}) \lambda^4 \left(\frac{I_D}{I_G}\right)^{-1} = [\mathrm{nm}] \quad (4)$$

where λ is the wavelength of the laser in nm, and I_D/I_G is the intensity ratio between the D and G bands.

X-Ray diffraction (XRD) measurements were carried out on a PANanalytical X'Pert PRO MRD (Cu Kα radiation, $\lambda = 1.5406$ Å) utilizing a grazing incident geometry (GIXRD). The diffractograms were recorded between $2\theta = 10°$ and 80° with an emission current of 40 mA and an acceleration voltage of 40 kV. The step size and the acquisition time were fixed at 0.03° and 2 s, respectively. The interlayer distance $d_{(hkl)}$ between the crystallographic plane (hkl) can be estimated by using the well know Bragg's law[80]

$$n\lambda = 2d_{(hkl)} \sin\theta \quad (5)$$

where n is the diffraction, λ is the wavelength of X-Ray in Å, and θ is the Bragg angle in radiant. If the diffraction order is 1, the Equation (2) can be written as follows

$$d_{(hkl)} = \frac{\lambda}{2\sin\theta} = [\mathrm{Å}] \quad (6)$$

The crystallite size (L_c) can be calculated using the Scherrer equation[81]

$$L_c = \frac{K\lambda}{\mathrm{FWHM}\cos\theta} = [\mathrm{Å}] \quad (7)$$

where K is a constant called shape factor (≈0.9 for spherical particles), λ is the wavelength of X-Ray in Å, FWHM is the full width at the half maximum of the reflection, and θ is the Bragg angle. FWHM and θ must be radiant.

Thermogravimetric analysis (TGA) was run on a Netzsch STA409PC instrument. ≈10 mg of vacuum-dried PAN fibers were heated between 30 and 1200 °C with a ramp of 2 °C min^{-1} in nitrogen and synthetic air atmosphere.

Nitrogen physisorption was carried out in an automated gas adsorption station at 77 K with a Quantachrome Corporation Autosorb iQ2. Before each measurement, the sample was degassed at 120 °C for 18 h. The instrument's software supports the calculation of SSA by applying the Brunauer–Emmett–Teller (BET) model and pore size distribution, cumulative surface area, and pore volume with the quenched solid density functional theory (QSDFT, "cylindric pores, QSDFT adsorption branch").

X-Ray photoelectron spectroscopy (XPS) measurements were conducted with a PHI 5000 VersaProbe II Scanning ESCA Microprobe (Physical Electronics) with a monochromatized Al Kα X-Ray source in high power mode (beam size 1300 µm × 100 µm, X-Ray power: 100 W). The sample surface was charge neutralized with slow electrons and argon ions, and the pressure was in the range of 10^{-7} to 10^{-6} Pa during the measurements. The electron energy analyzer was working at a constant pass energy of 187.85 and 23.50 eV for survey and detail spectra, respectively. Data analysis was performed using the CasaXPS software. The C 1*s* line at 284.8 eV was used as binding standard energy to correct the position of the spectra. The Shirley-type function was used for background subtraction. The N 1*s* peaks were fitted by a mixed Gaussian/Lorentzian function (GL30).

The morphology of CNFs was investigated by scanning electron microscopy (SEM) on *a* Zeiss Merlin with an emission current of 100 pA and an acceleration voltage of 3 kV. The PAN and PAN-stabilized fibers, which are insulating, were sputtered with platinum for 60 s prior to each SEM measurement, using an Edwards scancoat six. The atomic concentration of carbon, nitrogen, and oxygen was determined by energy-dispersive X-Ray (EDX) analysis using an Oxford Instrument Inca Energy System X-Max 50 Silicon Drift Detector with a 50 mm^2 active area, an emission current of 2000 pA and an acceleration voltage of 5 kV. To obtain a more precise atomic concentration, EDX measurements were performed six times for each sample to calculate an average value.

Supporting Information

Supporting Information is available from the Wiley Online Library or from the author.

Acknowledgements

F.B., M.C., B.S., and T.G. wish to thank the financial support of the European Commission through the H2020 FET-PROACTIVE-EIC-07-2020 project LIGHT-CAP (project number 101017821).

Conflict of Interest

The authors declare no conflict of interest.

Data Availability Statement

The data that support the findings of this study are available from the corresponding author upon reasonable request.

Keywords

carbon nanofibers, electrospinning, polyacrylonitrile, stabilization and carbonization temperature, supercapacitors

Received: June 28, 2023
Revised: August 3, 2023
Published online: August 22, 2023

[1] A. Ometov, V. Shubina, L. Klus, J. Skibińska, S. Saafi, P. Pascacio, L. Flueratoru, D. Q. Gaibor, N. Chukhno, O. Chukhno, A. Ali, A. Channa, E. Svertoka, W. Bin Qaim, R. Casanova-Marqués, S. Holcer, J. Torres-Sospedra, S. Casteleyn, G. Ruggeri, G. Araniti, R. Burget, J. Hosek, E. S. Lohan, *Comput. Networks* **2021**, *193*, 108074.
[2] R. T. Yadlapalli, R. Alla, R. Kandipati, A. Kotapati, *J. Energy Storage* **2022**, *49*, 104194.
[3] S. Cao, Y. Li, Y. Tang, Y. Sun, W. Li, X. Guo, F. Yang, G. Zhang, H. Zhou, Z. Liu, Q. Li, M. Shakouri, H. Pang, *Adv. Mater.* **2023**, *35*, https://doi.org/10.1002/adma.202301011.
[4] S. Zheng, Q. Li, H. Xue, H. Pang, Q. Xu, *Natl. Sci. Rev.* **2020**, *7*, 305.
[5] Y. Bai, C. Liu, T. Chen, W. Li, S. Zheng, Y. Pi, Y. Luo, H. Pang, *Angew. Chemie* **2021**, *133*, 25522.
[6] Poonam, K. Sharma, A. Arora, S. K. Tripathi, *J. Energy Storage* **2019**, *21*, 801.
[7] O. Barbieri, M. Hahn, A. Herzog, R. Kötz, *Carbon* **2005**, *43*, 1303.
[8] J. Gamby, P. L. Taberna, P. Simon, J. F. Fauvarque, M. Chesneau, *J. Power Sources* **2001**, *101*, 109.
[9] X. Li, C. Han, X. Chen, C. Shi, *Microporous Mesoporous Mater.* **2010**, *131*, 303.
[10] L. Z. Fan, Y. S. Hu, J. Maier, P. Adelhelm, B. Smarsly, M. Antonietti, *Adv. Funct. Mater.* **2007**, *17*, 3083.
[11] Y. Wang, Z. Shi, Y. Huang, Y. Ma, C. Wang, M. Chen, Y. Chen, *J. Phys. Chem. C* **2009**, *113*, 13103.
[12] X. Cao, Y. Shi, W. Shi, G. Lu, X. Huang, Q. Yan, Q. Zhang, H. Zhang, *Small* **2011**, *7*, 3163.
[13] H. Pan, J. Li, Y. P. Feng, *Nanoscale Res. Lett.* **2010**, *5*, 654.
[14] P. L. Taberna, G. Chevallier, P. Simon, D. Plée, T. Aubert, *Mater. Res. Bull.* **2006**, *41*, 478.
[15] C. Emmenegger, P. Mauron, P. Sudan, P. Wenger, V. Hermann, R. Gallay, A. Züttel, *J. Power Sources* **2003**, *124*, 321.
[16] C. Niu, E. K. Sichel, R. Hoch, D. Moy, H. Tennent, *Appl. Phys. Lett.* **1997**, *70*, 1480.
[17] R. Saliger, U. Fischer, C. Herta, J. Fricke, *J. Non. Cryst. Solids* **1998**, *225*, 81.
[18] P. Hao, Z. Zhao, J. Tian, H. Li, Y. Sang, G. Yu, H. Cai, H. Liu, C. P. Wong, A. Umar, *Nanoscale* **2014**, *6*, 12120.
[19] J. Li, X. Wang, Q. Huang, S. Gamboa, P. J. Sebastian, *J. Power Sources* **2006**, *158*, 784.
[20] C. Merino, P. Soto, E. Vilaplana-Ortego, J. M. De Gomez Salazar, F. Pico, J. M. Rojo, *Carbon* **2005**, *43*, 551.
[21] Z. Peng, J. Lin, R. Ye, E. L. G. Samuel, J. M. Tour, *ACS Appl. Mater. Interfaces* **2015**, *7*, 3414.
[22] A. Lamberti, F. Perrucci, M. Caprioli, M. Serrapede, M. Fontana, S. Bianco, S. Ferrero, E. Tresso, *Nanotechnology* **2017**, *28*, 174002.
[23] G. Nie, X. Zhao, Y. Luan, J. Jiang, Z. Kou, J. Wang, *Nanoscale* **2020**, *12*, 13225.
[24] S. K. Nataraj, K. S. Yang, T. M. Aminabhavi, *Prog. Polym. Sci.* **2012**, *37*, 487.
[25] M. S. A. Rahaman, A. F. Ismail, A. Mustafa, *Polym. Degrad. Stab.* **2007**, *92*, 1421.
[26] M. L. Minus, S. Kumar, *Jom* **2005**, *57*, 52.
[27] A. Moyseowicz, A. Śliwak, G. Gryglewicz, *J. Mater. Sci.* **2016**, *51*, 3431.
[28] D. Hulicova-Jurcakova, X. Li, Z. Zhu, R. de Marco, G. Q. Lu, *Energy and Fuels* **2008**, *22*, 4139.
[29] J. R. McDonough, J. W. Choi, Y. Yang, F. La Mantia, Y. Zhang, Y. Cui, *Appl. Phys. Lett.* **2009**, *95*, https://doi.org/10.1063/1.3273864.
[30] M. H. Al-Saleh, U. Sundararaj, *Carbon* **2009**, *47*, 2.
[31] W. Lu, M. Zu, J.-H. Byun, B.-S. Kim, T.-W. Chou, *Adv. Mater.* **2012**, *24*, 1805.
[32] A. S. Wu, T.-W. Chou, *Mater. Today* **2012**, *15*, 302.
[33] J. P. McGann, M. Zhong, E. K. Kim, S. Natesakhawat, M. Jaroniec, J. F. Whitacre, K. Matyjaszewski, T. Kowalewski, *Macromol. Chem. Phys.* **2012**, *213*, 1078.
[34] T. Liu, G. Liu, *J. Mater. Chem. A* **2019**, *7*, 23476.
[35] A. Álvarez-Gómez, J. Yuan, J. P. Fernández-Blázquez, V. San-Miguel, M. B. Serrano, *Polymers* **2022**, *14*, 5109.
[36] Y. Tan, D. Lin, C. Liu, W. Wang, L. Kang, F. Ran, *J. Mater. Res.* **2018**, *33*, 1120.
[37] R. D. Oliveira, C. S. Santos, J. R. Garcia, M. Vidotti, L. F. Marchesi, C. A. Pessoa, *J. Electroanal. Chem.* **2020**, *878*, 114662.
[38] D. Boonpakdee, C. F. Guajardo Yévenes, W. Surareungchai, C. La-O-Vorakiat, *J. Mater. Chem. A* **2018**, *6*, 7162.
[39] V. Vivier, M. E. Orazem, *Chem. Rev.* **2022**, *122*, 11131.
[40] H. D. Yoo, J. H. Jang, J. H. Ryu, Y. Park, S. M. Oh, *J. Power Sources* **2014**, *267*, 411.
[41] T. Q. Nguyen, C. Breitkopf, *J. Electrochem. Soc.* **2018**, *165*, E826.
[42] F. Lamberti, D. Ferraro, M. Giomo, N. Elvassore, *Electrochim. Acta* **2013**, *97*, 304.
[43] M. Crisci, F. Boll, L. Merola, J. J. Pflug, Z. Liu, J. Gallego, F. Lamberti, T. Gatti, *Front. Chem.* **2022**, *10*, 1.
[44] A. J. Bard, L. R. Faulkner, H. S. White, *Electrochemical Methods: Fundamentals and Applications*, Wiley-VCH Verlag, Hoboken, NJ **2000**.
[45] Q. Wu, T. He, Y. Zhang, J. Zhang, Z. Wang, Y. Liu, L. Zhao, Y. Wu, F. Ran, *J. Mater. Chem. A* **2021**, *9*, 24094.
[46] C. Hsiao, C. Lee, N. Tai, *J. Energy Storage* **2022**, *46*, 103805.
[47] L. Zhang, Y. Jiang, L. Wang, C. Zhang, S. Liu, *Electrochim. Acta* **2016**, *196*, 189.
[48] M. Shao, F. Ning, Y. Zhao, J. Zhao, M. Wei, D. G. Evans, X. Duan, *Chem. Mater.* **2012**, *24*, 1192.
[49] Z. Gao, J. Wang, Z. Li, W. Yang, B. Wang, M. Hou, Y. He, Q. Liu, T. Mann, P. Yang, M. Zhang, L. Liu, *Chem. Mater.* **2011**, *23*, 3509.
[50] Y. Zhai, Y. Dou, D. Zhao, P. F. Fulvio, R. T. Mayes, S. Dai, *Adv. Mater.* **2011**, *23*, 4828.
[51] H. Zhou, H. Chen, S. Luo, G. Lu, W. Wei, Y. Kuang, *J. Solid State Electrochem.* **2005**, *9*, 574.
[52] O. Norouzi, F. Di Maria, A. Dutta, *J. Energy Storage* **2020**, *29*, 101291.
[53] Q. Xu, H. Jiu, L. Zhang, W. Song, T. Gao, H. Wei, C. Wang, Y. Zhang, X. Li, *Ionics* **2022**, *28*, 1657.
[54] C. L. Chiang, J. M. Yang, *Flame Retardance and Thermal Stability of Polymer/Graphene Nanosheet Oxide Composites*, Elsevier Ltd, Amsterdam **2015**.
[55] M. Einert, C. Wessel, F. Badaczewski, T. Leichtweiß, C. Eufinger, J. Janek, J. Yuan, M. Antonietti, B. M. Smarsly, *Macromol. Chem. Phys.* **2015**, *216*, 1930.
[56] J. L. Hueso, J. P. Espinós, A. Caballero, J. Cotrino, A. R. González-Elipe, *Carbon* **2007**, *45*, 89.
[57] E. A. Arkhipova, A. S. Ivanov, N. E. Strokova, K. I. Maslakov, S. A. Chernyak, S. V. Savilov, *J. Therm. Anal. Calorim.* **2022**, *147*, 1081.

[58] B. Pollack, S. Holmberg, D. George, I. Tran, M. Madou, M. Ghazinejad, *Sensors* **2017**, *17*, 1.
[59] J. R. Pels, F. Kapteijn, J. A. Moulijn, Q. Zhu, K. M. Thomas, *Carbon* **1995**, *33*, 1641.
[60] L. Sun, C. Tian, Y. Fu, Y. Yang, J. Yin, L. Wang, H. Fu, *Chem. - A Eur. J.* **2014**, *20*, 564.
[61] A. C. Ferrari, *Solid State Commun.* **2007**, *143*, 47.
[62] C. Casiraghi, S. Pisana, K. S. Novoselov, A. K. Geim, A. C. Ferrari, *Appl. Phys. Lett.* **2007**, *91*, 1.
[63] A. Sadezky, H. Muckenhuber, H. Grothe, R. Niessner, U. Pöschl, *Carbon* **2005**, *43*, 1731.
[64] T. Jawhari, A. Roid, J. Casado, *Carbon* **1995**, *33*, 1561.
[65] X. Tian, X. Li, T. Yang, K. Wang, H. Wang, Y. Song, Z. Liu, Q. Guo, C. Chen, *Electrochim. Acta* **2017**, *247*, 1060.
[66] O. L. Li, S. Chiba, Y. Wada, G. Panomsuwan, T. Ishizaki, *J. Mater. Chem. A* **2017**, *5*, 2073.
[67] N. M. Keppetipola, M. Dissanayake, P. Dissanayake, B. Karunarathne, M. A. Dourges, D. Talaga, L. Servant, C. Olivier, T. Toupance, S. Uchida, K. Tennakone, G. R. A. Kumara, L. Cojocaru, *RSC Adv.* **2021**, *11*, 2854.
[68] X. B. Xie, D. Wu, H. Wu, C. Hou, X. Sun, Y. Zhang, R. Yu, S. Zhang, B. Wang, W. Du, *J. Mater. Sci. Mater. Electron.* **2020**, *31*, 18077.
[69] F. M. Hassan, V. Chabot, J. Li, B. K. Kim, L. Ricardez-Sandoval, A. Yu, *J. Mater. Chem. A* **2013**, *1*, 2904.
[70] A. C. M. Carvalho, M. C. Dos Santos, *J. Appl. Phys.* **2006**, *100*, https://doi.org/10.1063/1.2357646.
[71] Y. Liu, J. Zhou, L. Chen, P. Zhang, W. Fu, H. Zhao, Y. Ma, X. Pan, Z. Zhang, W. Han, E. Xie, *ACS Appl. Mater. Interfaces* **2015**, *7*, 23515.
[72] Z. Fan, J. Yan, T. Wei, L. Zhi, G. Ning, T. Li, F. Wei, *Adv. Funct. Mater.* **2011**, *21*, 2366.
[73] M. Sevilla, W. Sangchoom, N. Balahmar, A. B. Fuertes, R. Mokaya, *ACS Sustain. Chem. Eng.* **2016**, *4*, 4710.
[74] Q. P. Luo, L. Huang, X. Gao, Y. Cheng, B. Yao, Z. Hu, J. Wan, X. Xiao, J. Zhou, *Nanotechnology* **2015**, *26*, 304004.
[75] Z. Ling, Z. Wang, M. Zhang, C. Yu, G. Wang, Y. Dong, S. Liu, Y. Wang, J. Qiu, *Adv. Funct. Mater.* **2016**, *26*, 111.
[76] C. Chen, G. Xu, X. Wei, L. Yang, *J. Mater. Chem. A* **2016**, *4*, 9900.
[77] W. Na, J. Jun, J. W. Park, G. Lee, J. Jang, *J. Mater. Chem. A* **2017**, *5*, 17379.
[78] Z. Chen, K. Liu, S. Liu, L. Xia, J. Fu, X. Zhang, C. Zhang, B. Gao, *Electrochim. Acta* **2017**, *237*, 102.
[79] L. G. Cançado, K. Takai, T. Enoki, M. Endo, Y. A. Kim, H. Mizusaki, A. Jorio, L. N. Coelho, R. Magalhães-Paniago, M. A. Pimenta, *Appl. Phys. Lett.* **2006**, *88*, 1.
[80] H. G. J. Moseley, *Proc. R. Soc. A* **1913**, *88*, 471.
[81] J. I. Langford, A. J. C. Wilson, *J. Appl. Cryst.* **1977**, *11*, 102.
[82] E. Frank, F. Hermanutz, M. R. Buchmeiser, *Macromol. Mater. Eng.* **2012**, *297*, 493.

3.3.1. Supporting Information – Publication 1

Supporting information for:

Assessing the effect of stabilization and carbonization temperatures on electrochemical performance of electrospun carbon nanofibers from polyacrylonitrile

Felix Boll,[1,2] Matteo Crisci,[1,2] Leonardo Merola,[1,3] Francesco Lamberti,[3] Bernd Smarsly,[1,2] Teresa Gatti[2,4*]

[1] Institute of Physical Chemistry, Justus Liebig University, Heinrich-Buff-Ring 17, 35392 Giessen, Germany

[2] Center for Materials Research, Justus Liebig University, Heinrich-Buff-Ring 17, 35392 Giessen, Germany

[3] Department of Chemical Sciences, University of Padova, via Marzolo 1, 35131 Padova, Italy

[4] Department of Applied Science and Technology, Politecnico di Torino, Corso Duca degli Abruzzi 24, 10129, Torino, Italy

Table of Contents

- Summary of XPS and SEM-EDX data for CNFs prepared at different T_S and T_C (Table S2)
- Summary of Raman data for the different CNF samples (Table S3)
- Summary of XRD data for the different CNF samples (Table S4)
- Average values of C_s with related errors for each type CNF sample (Table S5)
- Average values of E_d with errors for each type of CNF sample (Table S6)
- Comparison of the electrochemical performance of CNFs as single electro-active materials for SC applications (Table S7) and method used for carrying out such comparison

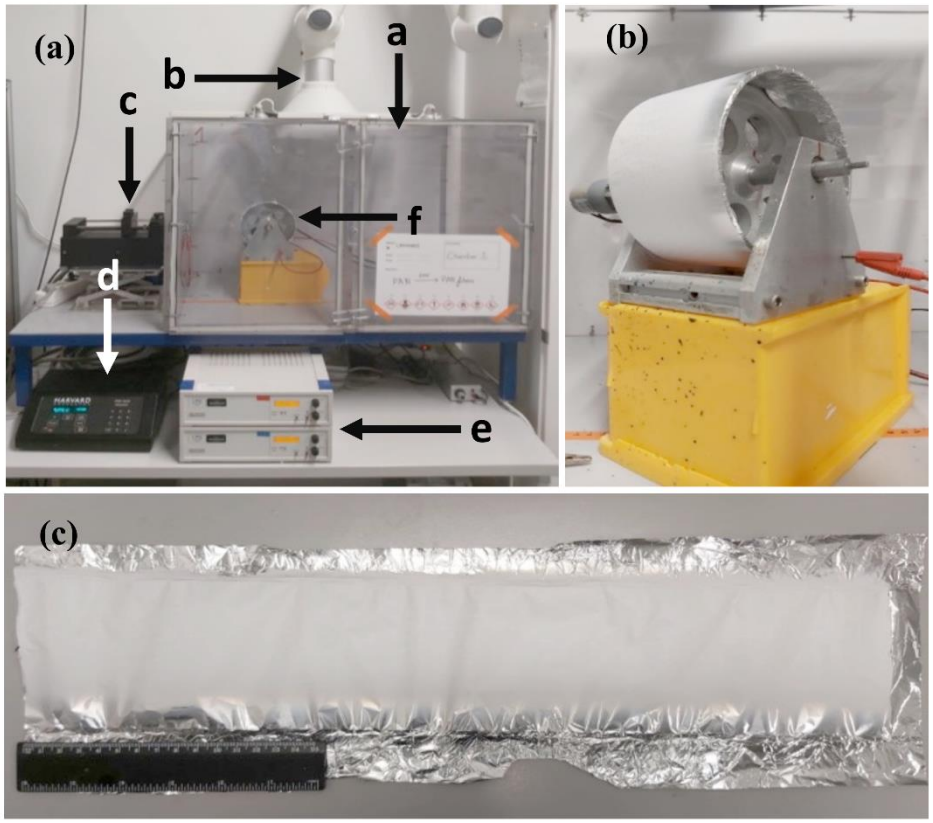

Figure S1. a) Electrospinning setup. All different components are indicated in the images: a. electrospinning chamber, b. fumehood, c. syringe pump, d. syringe pump controller, e. power supplies and f. aluminum-covered rotating drum. b) Aluminum-covered rotating drum with PAN fibers mat (white part) upon it. c) PAN fibers mat on aluminum foil removed from the rotating drum.

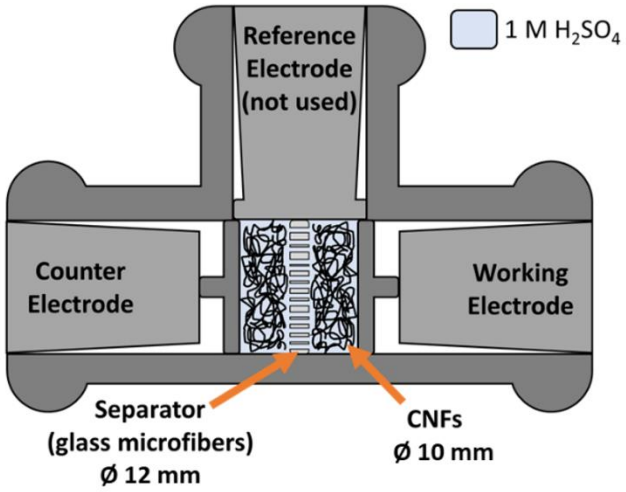

Figure S2. Schematic illustration of the symmetrical SC based on CNFs inside the Swagelok cell.

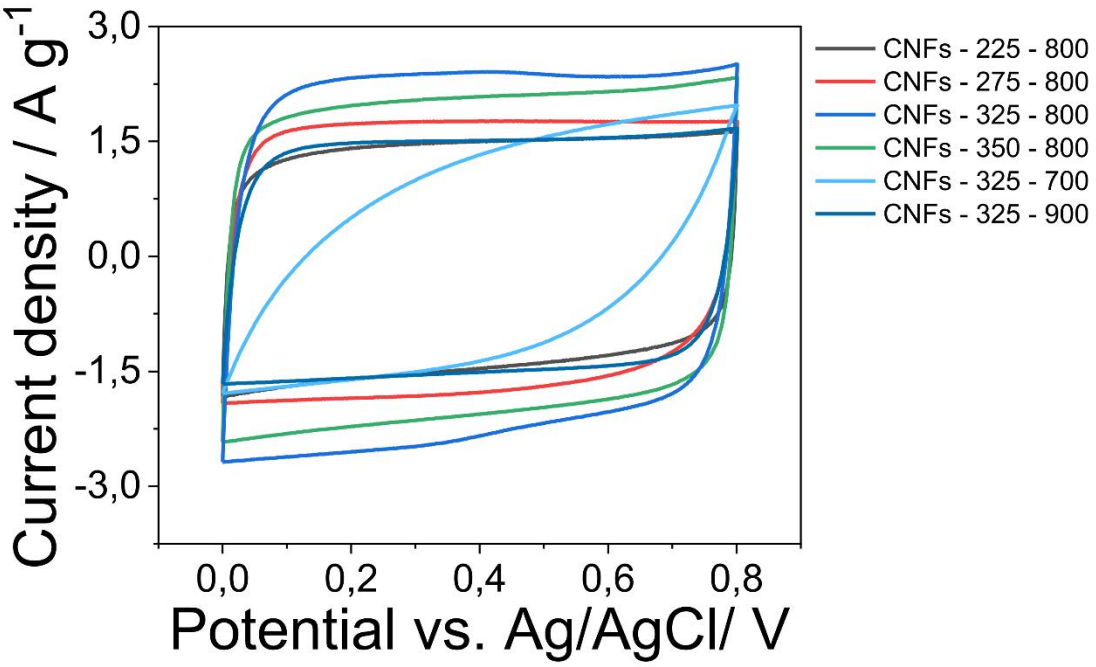

Figure S3. CV curves obtained at 50 mV s^{-1} scan rate vs. Ag/AgCl reference electrode for the different CNF-based SCs.

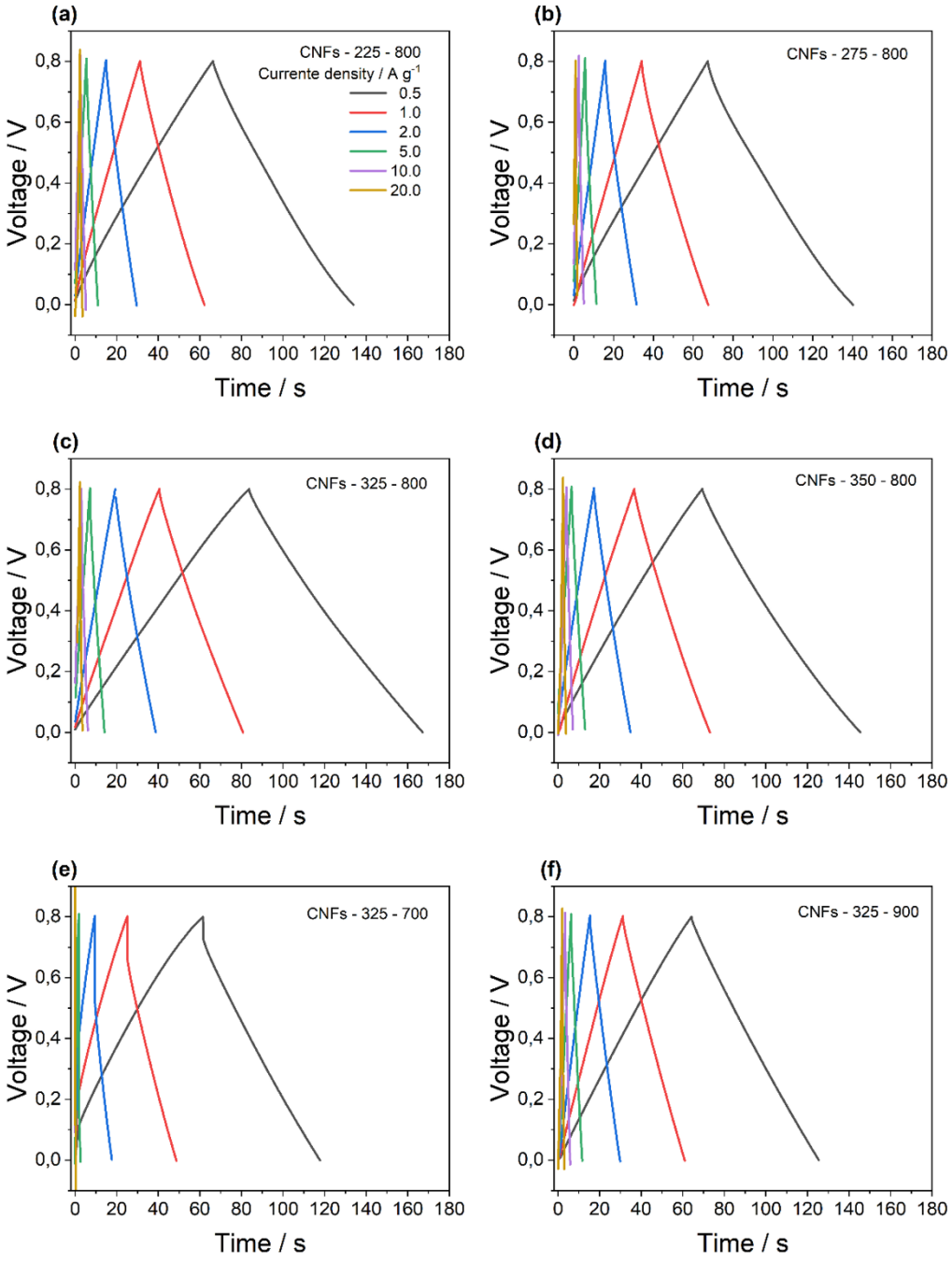

Figure S4. a-f) GCD curves at a different scan rate from symmetrical SCs based on the different CNF samples studied in this work as active energy storage materials.

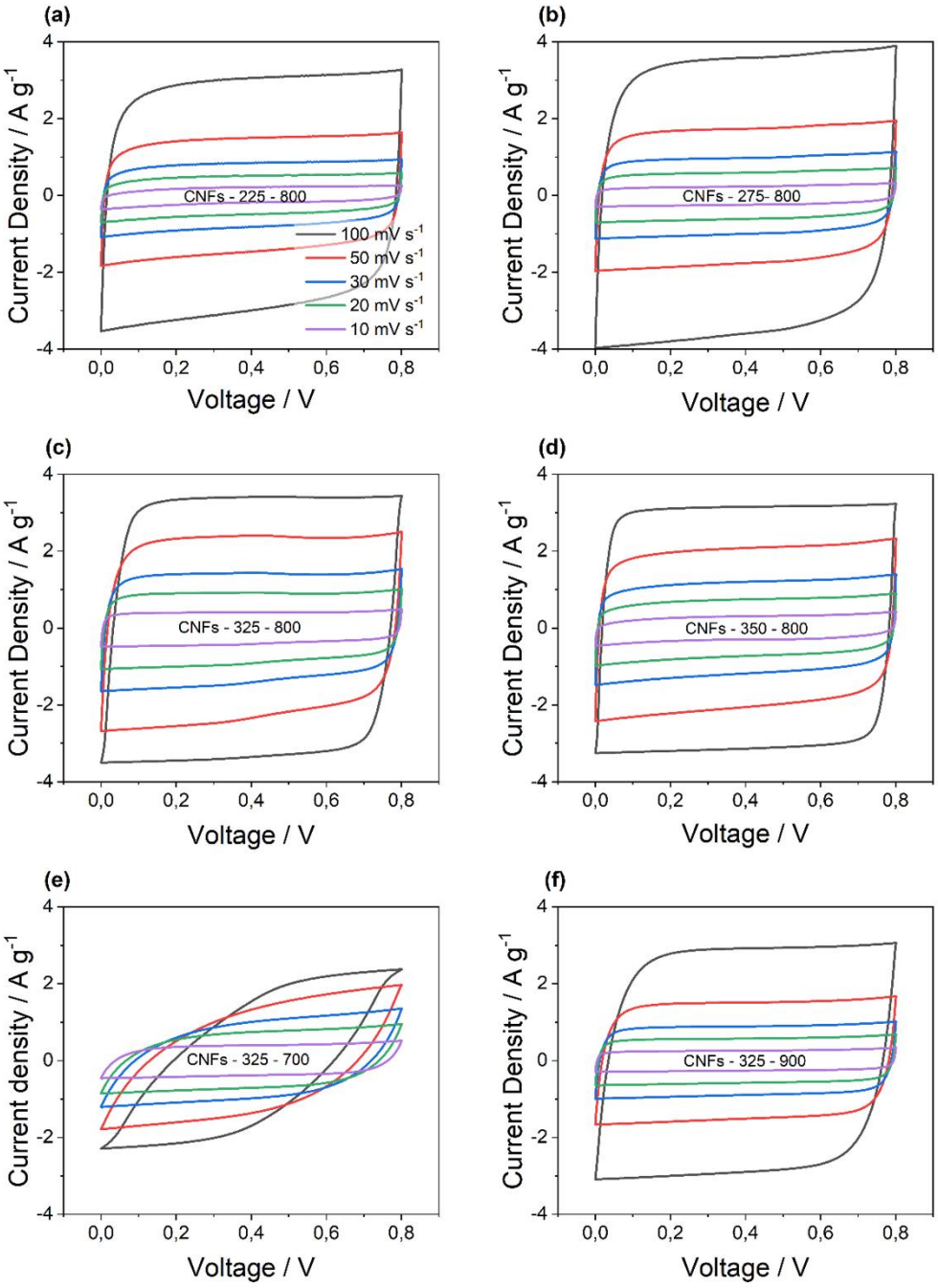

Figure S5. a-f) CV curves at different scan rate from symmetrical SCs based on the different CNF samples studied in this work as active energy storage materials.

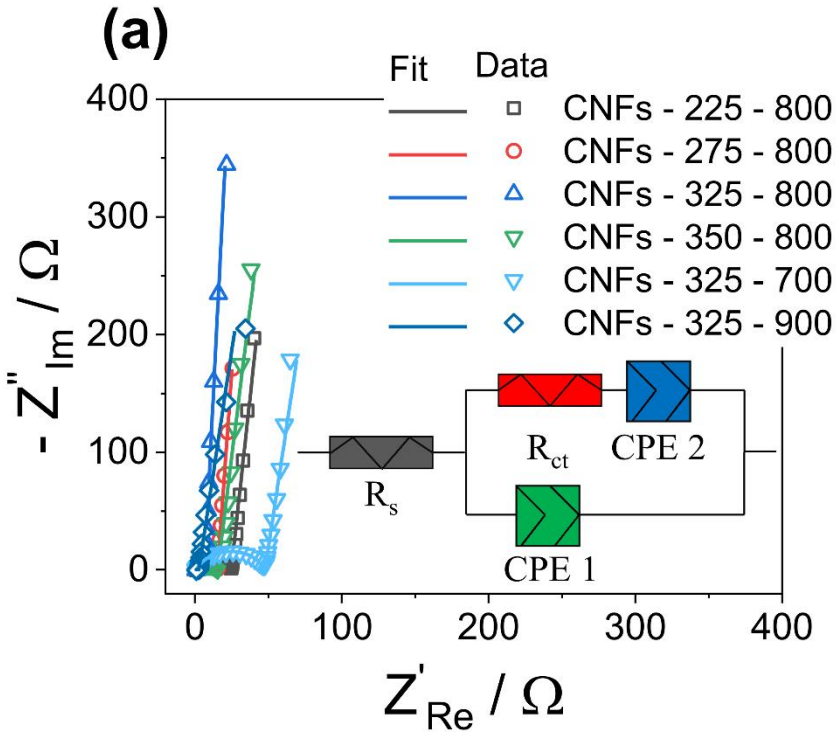

Figure S6. Nyquist plots obtained from EIS analysis with the assumed and simulated circuit diagram for the different CNF-based SCs.

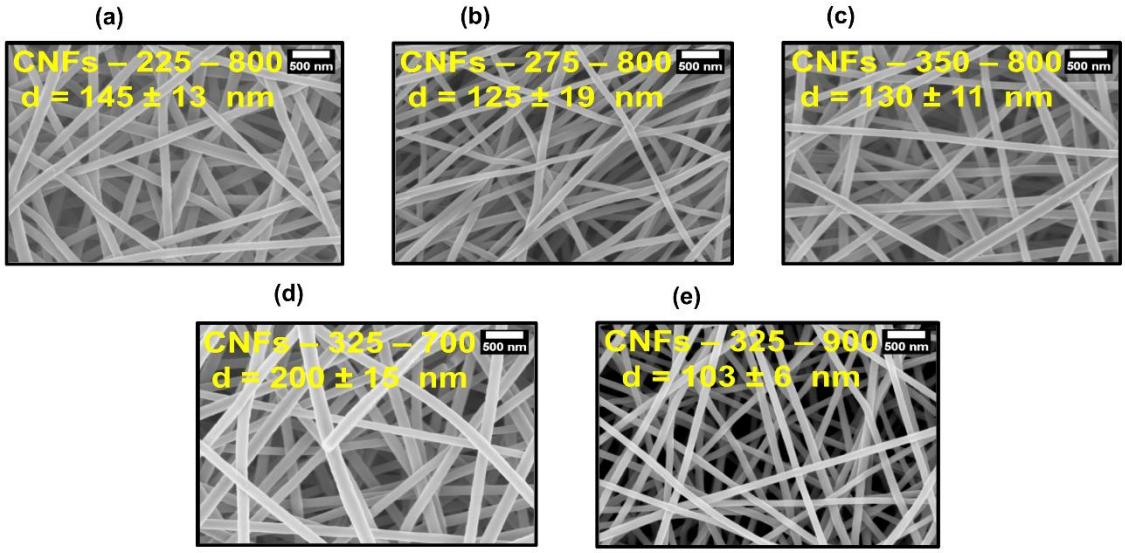

Figure S7. SEM images of CNFs samples prepared at different T_s or T_c. The average diameter (d) is reported for each sample based on 50 measurements using the graphic tool *ImageJ*.

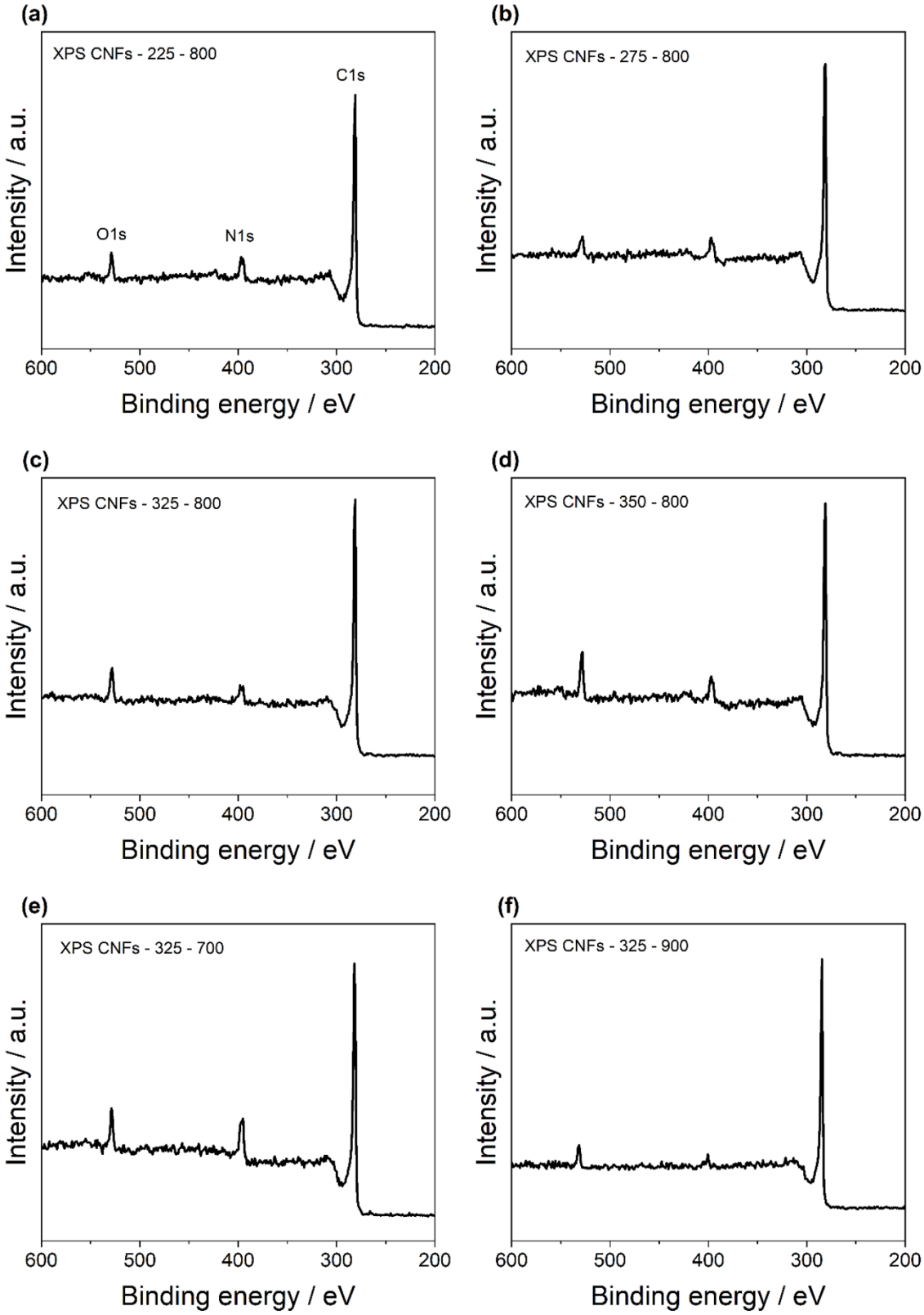

Figure S8. XPS spectra of CNFs treated at different T_S and T_C.

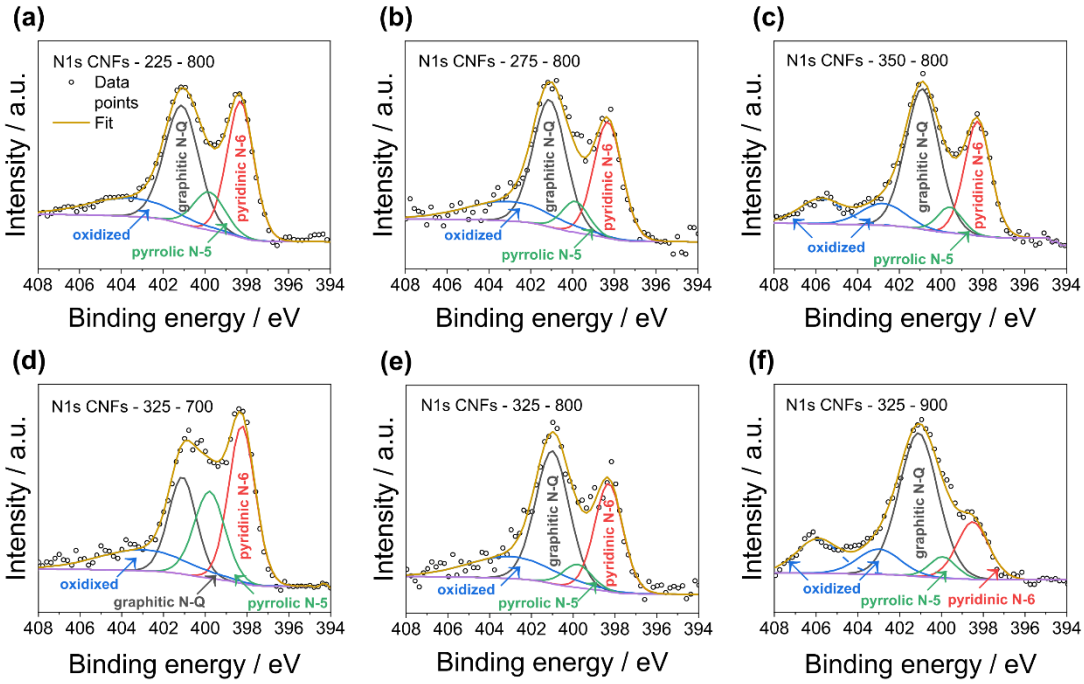

Figure S9. Deconvolutions of the N1s peak of CNFs prepared at different T_s or T_c.

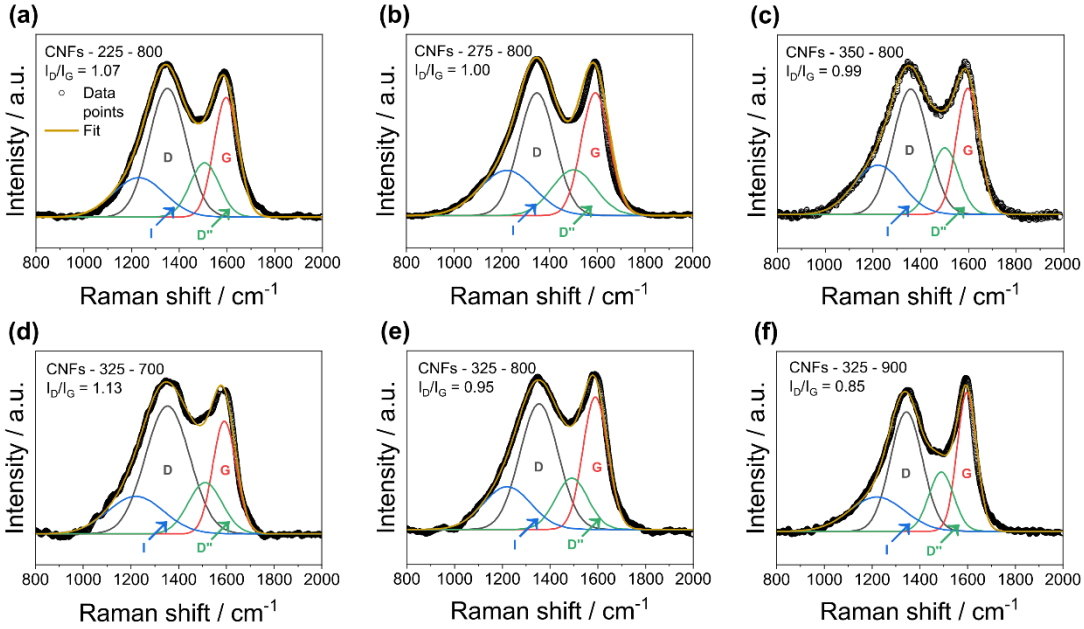

Figure S10. Deconvolutions of Raman D and G peaks for CNFs samples prepared at different T_s and T_c.

Table S1. Summary of physisorption data obtained for the different CNF samples examined in this work.

Sample name CNFs-(T_s)-(T_c)	Specific surface area / $m^2\ g^{-1}$	Total pore volume / $cm^3\ g^{-1}$	Average pore diameter / nm
CNFs-225-800	491	0.348	1.20
CNFs-275-800	538	0.285	1.00
CNFs-325-800	577	0.260	1.00
CNFs-350-800	543	0.037	1.79
CNFs-325-700	401	0.222	1.00
CNFs-325-900	700	0.330	1.10

Table S2. Summary of elemental analysis data obtained for the different CNF samples examined in this work through XPS and SEM-EDX methods. From XPS, also the content of the various type of nitrogen species was calculated.

Sample name CNFs-(T_s)-(T_c)	Total N conc. At.%		N-Q / %	N-6 / %	N-5 / %	N-O / %
	XPS	EDX				
CNFs-225-800	7.2	7.3	40	35	10	15
CNFs-275-800	6.4	5.8	42	33	8	17
CNFs-325-800	6.0	5.1	44	30	7	19
CNFs-350-800	6.8	6.0	45	28	6	21
CNFs-325-700	11.6	12.2	24	38	22	16
CNFs-325-900	2.6	1.0	53	17	5	25

Table S3. Summary of Raman data for the different CNF samples examined in this work.

Sample name CNFs-(T_s)-(T_c)	**D-Band / cm^{-1}**	**G-Band / cm^{-1}**	**I_D/I_G**	**L_a / nm**
CNFs-225-800	1350	1595	1.07	18.0
CNFs-275-800	1347	1592	1.00	19.0
CNFs-325-800	1353	1590	0.95	20.2
CNFs-350-800	1355	1597	0.99	19.5
CNFs-325-700	1352	1592	1.13	17.0
CNFs-325-900	1344	1597	0.85	22.6

Table S4. Summary of XRD data for the different CNF samples examined in this work.

Sample name CNFs-(T_s)-(T_c)	**2 ϑ**	**$d_{(002)}$ / Å**	**FWHM / rad**	**L_c / Å**
CNFs-225-800	20.2	4.4	0.15	9.3
CNFs-275-800	21.2	4.2	0.16	8.6
CNFs-325-800	21.3	4.1	0.18	8.0
CNFs-350-800	20	4.4	0.18	8.0
CNFs-325-700	19.5	4.6	0.15	9.6
CNFs-325-900	22.5	3.9	0.19	7.5

Table S5. Average values of C_s with related errors for each type of CNF sample.

Current density / A g^{-1}	C_s / F g^{-1}					
	CNFs-225-800	CNFs-275-800	CNFs-325-800	CNFs-350-800	CNFs-325-700	CNFs-325-900
0.5	40 ± 3	43 ± 2	49 ± 3	45 ± 3	34.6 ± 0.6	35 ± 3
1.0	37 ± 2	40.5 ± 1.3	47 ± 3	43 ± 3	28.7 ± 0.8	34 ± 3
2.0	35 ± 2	38.8 ± 0.8	45 ± 3	41 ± 2	20.4 ± 0.4	33 ± 3
5.0	32 ± 2	35.7 ± 0.6	41 ± 3	39 ± 3	6.9 ± 0.3	30 ± 4
10.0	30 ± 3	32.7 ± 0.5	36 ± 3	36 ± 3	2.8 ± 0.7	26 ± 4
20.0	25 ± 5	26.6 ± 1.3	30 ± 3	32 ± 4	1.3 ± 0.8	20 ± 3

Table S6. Average values of E_d with errors for each type of CNF sample.

P_d / W kg^{-1}	E_d / Wh kg^{-1}					
	CNFs-225-800	CNFs-275-800	CNFs-325-800	CNFs-350-800	CNFs-325-700	CNFs-325-900
200	3.5 ± 0.2	3.8 ± 0.2	4.4 ± 0.3	3.9 ± 0.3	3.08 ± 0.05	3.1 ± 0.2
400	3.3 ± 0.2	3.60 ± 0.11	4.2 ± 0.3	3.8 ± 0.2	2.55 ± 0.07	3.0 ± 0.3
800	3.2 ± 0.2	3.45 ± 0.06	4.0 ± 0.3	3.7 ± 0.2	1.81 ± 0.03	2.9 ± 0.3
2000	2.9 ± 0.2	3.17 ± 0.05	3.6 ± 0.3	3.5 ± 0.2	0.62 ± 0.03	2.6 ± 0.3
4000	2.6 ± 0.3	2.91 ± 0.12	3.2 ± 0.2	3.2 ± 0.3	0.251 ± 0.011	2.3 ± 0.4
8000	2.3 ± 0.4	2.36 ± 0.11	2.7 ± 0.2	2.8 ± 0.3	0.117 ± 0.005	1.8 ± 0.5

Comparisons with literature: single electrodes

From the C_s of the devices ($C_{s,\,device}$) is possible to estimate the C_s of the single electrode ($C_{s,\,elect.}$). The definition of the C_s of the electrode is:

$$C_{s,elect} = \frac{C_{elect}}{m_{elect}} \quad \text{(E1)}$$

Where C_{elect} is the capacitance of the single electrode and m_{elect} is its mass. However, the device is built with two electrodes which are connected in series. Indeed, the capacitance of the device is:

$$C_{elect} = 2\, C_{device} \quad \text{(E2)}$$

Moreover, it can be assumed, as an approximation, that the relationship between the mass of the single electrode and the mass of the electrodes in the device (m_{device}) is:

$$m_{elect} = \frac{m_{device}}{2} \quad \text{(E3)}$$

Combing the equations, it is possible to obtain the specific capacitance of single electrode:

$$C_{s,elect} = \frac{4\, C_{device}}{m_{device}} = 4\, C_{s,device} \quad \text{(E4)}$$

The $C_{s,device}$ coincides with that calculated experimentally from Eq. E1.

To compare CNFs prepared in this work with other similar materials as single electrodes Eq. E4 was used.

Table S7. Comparison of the electrochemical performance of CNFs as single electro-active materials for SC applications. A summary of precursors and processes for the preparation of the electrode materials is also reported. The letter I stand for current density.

Types of samples	Precursor and Process	C_s (F g^{-1}) / I (A g^{-1}) / Electrolyte	Ref.
N-doped CNFs	Hydrothermal synthesized Te@C nano cable. Etching for 12 hr. Carbonized at 900 (N_2) for 2 hr.	202 / 1.0 / 6 M KOH	[153]
P-doped CNFs	Carbonization at 800 °C (N_2) for 2 hr and activation at 650 °C (N_2) for 30 min of PANI nanofibers network	280 / 1.0 / 6 M KOH	[154]
CNFs	Electrospinning of PAN/DMF. Stabilization at 280 °C for 3 h. Carbonization at 800 °C (N_2) for 1 h. Activation at 800 °C for 30 min in a steam atmosphere.	153 / 1.0 / 6 M KOH	[155]

	Same process but without the activation step.	82.3 / 1.0 / 6 M KOH	
CNFs	Electrospinning of PAN/DMF. Activation with KOH for 12 hr. Stabilization at 280 °C for 3 hrs. carbonization at 800 °C (N_2) for 1 hr.	186.8 / 1.0 / 6 M KOH	156
Porous-CNFs	Electrospinning of PAN-$Co(NO_3)_2$-PVP/DMF. Stabilization at 220 °C for 4hr. Pre-carbonization at 350 °C (Ar) for 4hr. Carbonization at 800 °C (Ar) for 2 hr. Acid corrosion with 10M HCl for 48 hr.	104 / 0.5 / 0.5 M H_2SO_4	145
Porous-CNFs	Electrospinning of PAN/Nafion. Stabilization at 280 °C. Carbonization 700 °C (Ar) for 1 hrs. Post-carbonization 800 °C (Ar) for 1 h.	210 / 1.0 / 1 M H_2SO_4	157
P-doped CNFs/PEG	Electrospinning of PAN-PEG/DMF with polyphosphoric acid. Stabilization at 250 °C for 1 hr. Carbonization at 800 °C for 1 hr.	228.7 / 0.5 / 1 M H_2SO_4	158
	Same procedure but without the polyphosphoric acid	120.4 / 0.5 / 1 M H_2SO_4	
N-doped porous CNFs	Electrospinning of PAN-PVP-SiO_2 nanosphere/DMF. Stabilization at 250 °C 1hr. Carbonization at 800 °C (N_2) for 2 hr. Etching with 1 M NaOH for 1 hr.	242 / 0.2 / 1 M H_2SO_4	159
	Same procedure but without SiO_2 nanosphere	120.4 / 0.2 / 1 M H_2SO_4	
N, F-codoped CNFs	Electrospinning PAN-PVP/DMF. Hydrothermal methods with an autoclave at 160 °C for 12hr. Stabilization at 270 °C. Carbonization at 800 °C. Vacuum plasma treatment with C_4F_8.	252.6 / 0.5 / 1 M H_2SO_4	151
Co_3O_4-CNFs	Electrospinning of Strach-PVA/DI. Stabilization at 250 °C	137 / 1.0 / 1 M H_2SO_4	160

	for 1 hr. Carbonization in vacuum at 1500 °C. Activation at 800 °C (CO_2) for 30 min. Functionalization at 250 °C (air) for 1 hr. Dip coating of the CNFs in 0.2 M $Co(C_2H_4O_2)$ solution. Calcination at 450°C for 2 hr		
	Same procedure but without the dip coating step	35 / 1.0 / 1 M H_2SO_4	
CNFs-325-800	Electrospinning of PAN/DMF. Stabilization at 325 °C for 2 hr. Carbonization at 800 °C (N_2) for 1 hr.	196 / 0.5 / 1 M H_2SO_4 188.6 / 1.0 / 1 M H_2SO_4	This work

3.4. Publication 2

In the context of electrospinning for SCs, carbon is widely utilized due to its large surface area, especially CNFs as shown in the previous publication are considered state-of-the-art. However, pure carbon-based materials contain one large drawback – their inherent brittleness.[192] Despite offering excellent conductivity and a large surface area, which contribute to their ideal charge storage capabilities as previously dicussed.[105,182] The problem with carbon-based networks and matrices lies in their unsuitability for flexible charge-storage devices. In brittle materials, bending, tilting or any form of rumpling can lead to breakage and contact loss, creating an insurmountable hurdle for maintaining device integrity. In order to overcome this issue, plenty of approaches to prepare flexible charge-storage devices have been done going from foils, over membranes, towards flexible and conductive polymers, printed inks on flexible substrates, skeleton-structured hybrid films, hydrogels and most likely even more.[10,20,64,107,200–207] Another factor that comes into play is the sustainable approach that is a crucial demand for future devices in an industrial context. Recycling is especially crucial for Europe, where resource availability is limited, as highlighted by the "European Critical Raw Materials Act", published annually.[208] The act underscores the importance of recycling solid waste, particularly waste generated by batteries due to their lithium content. Ensuring effective recycling processes is essential to conserve these critical resources. Rare elements need to be recycled to ensure an intact supply chain but also for more abundant materials like graphite, with a far-reaching view, recycling is considered to be important.[208–214]

From this starting point we were inspired to work on flexible nanofibrous materials for energy storage using simple, abundant resources and sustainable and non-toxic preparation methods. The primary demand for such charge-storage solutions arises from wearable and portable devices designed for close proximity to the human body which further pushes research towards non-hazardous chemicals in this field of research.[88,205,215] From the literature 2D-material based composites made from any sort of conductive carbon species and bidimensional materials like MoS_2 and WS_2 are frequently used for supercapacitor applications obtaining large C_s as it was discussed previously.[170,177,207,216–220] As **publications 2 – 5** indicate, over the years I was able to collect an expertise in the field of top-down exfoliation methods like shear mixing, tip sonication, intercalation methods and

electrochemical exfoliation. It was used to prepare mono- and few-layered WS_2 for charge storage. Here, Raman spectroscopy is a valid choice of analysis method to prove the two-dimensionality since the intensity and position of the ($2LA+E_{2g}$) and A_{1g} bands change with decreasing number of layers.[12,29,31,221] For wet chemical top-down approaches mainly NMP is used as solvent in the literature since the highest yields of exfoliated material were achieved. The drawback is its toxicity and the high price which brought me to the choice of a water-isopropanol mixture to reduce cost and facilitate recyclability.[14,67,222–224] As backbone materials I also decided to follow the philosophy of simplicity. PEO is the most prominent polymer for electrospinning due to its easy handling, low price and the possibility of using H_2O as a solvent.[102,109,225–227] To overcome the issue of low conductivity of PEO, I used a nanoparticle-based approach adding MWCNTs and CB conductive species besides 2D-WS_2 to combine the properties of all these materials. Indeed, using a versatile set of data analysis including imaging methods like SEM, and compositional methods like XRD, Raman and EDX we were able to prove the presence of all species in the produced fibers. Subsequently bending tests and stability tests were conducted to prove the fibers' flexibility. Electrochemical analysis revealed a synergistic effect contributing to higher C_s compared to each individual species. This effect is related to the overall enlargement of conductivity but also an intimate contact between carbon materials and 2D-WS_2 as TEM, SEM, EDX and TGA obtain. The nanoengineering of functional materials in different compositions led to a flexible device using sustainable working processes being potentially embedded into low-power and lightweight electronics.

ACS APPLIED ENERGY MATERIALS

www.acsaem.org Article

Multicomponent Synergistic Contribution in Nanoengineered Nanofibers for Flexible Energy Storage

Felix Boll, Marta Fadda, Melissa Happel, Matteo Crisci, Athanassia Athanassiou, Bernd Smarsly, Federico Bella, Francesco Lamberti, Giovanni Perotto, and Teresa Gatti*

Cite This: https://doi.org/10.1021/acsaem.4c00417 Read Online

ACCESS | Metrics & More | Article Recommendations | Supporting Information

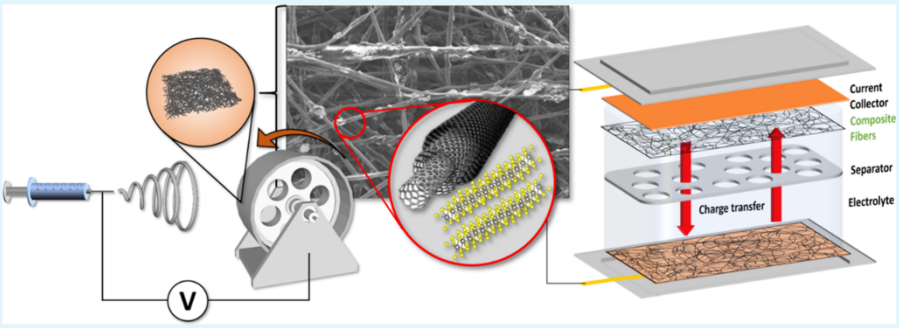

ABSTRACT: Lightweight and flexible energy storage devices are gaining interest due to their potential integration into wearable electronics. They might work for the long-term powering of sensors, for example, but they need to be operative after the application of different types of mechanical stress. Conductive and semiconducting nanomaterials have been largely investigated as active components for this type of application but need to be coupled to an elastic matrix, such as a polymeric one, in order to be functional in flexible technologies. In this work, we investigate the production of electrospun nanofibers based on a ternary blend of 2D layered WS_2, multiwalled carbon nanotubes, and carbon black in poly(ethylene oxide) and characterize their electrochemical behavior in symmetric supercapacitor architectures within bendable pouch cells, in conjunction with a robust analysis of the active materials' mechanical properties. We find optimized specific capacitance values of up to 9 F g^{-1} after mechanical adjustment of the device and excellent capacitance retention after multiple bending cycles, revealing the potential of similar scaffolds for use in wearable energy storage devices to activate low-power electronics.

KEYWORDS: *polymer nanofibers, nanocomposite, electrospinning, energy storage, flexible device*

1. INTRODUCTION

With the emergence of a continuously increasing request of smart electronic devices in portable and wearable shapes, also the demand for flexible power sources is outpacing, to prevent any limitation in terms of functionality and design.[1] Especially for sensors and applications in the health sector, biocompatible, lightweight, and nonhazardous power sources are of interest to ensure safety.[2,3] However, for running stretchable sensors and devices, the storage of electrical energy is considered to be the current bottleneck to allow the effective commercialization of these technologies. Since many sensors are already well functioning and largely available, their powering over long term is considered a major issue.[4,5] In this context, several eco-friendly and flexible supercapacitors and triboelectric generators have been reported in the last years as successful examples of energy devices with potential for future application as power units for wearable and lightweight electronics.[6−8]

Mainly carbon-based materials are used for the fabrication of electrochemical double-layer capacitors (EDLCs). Long-term cycle stability and fast charge/discharge behavior are exceptional arguments in favor of the usage of these devices. Also, differing shapes for the active layer can be adopted, from fibers to membranes, depending on the specific need.[9−11] Carbon-based species, especially carbon nanotubes and graphene-based materials, are interesting for this scope due to the excellent electrical conductivity and good mechanical resistance, with, for instance, Young's moduli of up to 950 GPa for multiwalled carbon nanotubes (MWCNTs).[12] Unfortunately, stacking,

Received: February 19, 2024
Revised: May 7, 2024
Accepted: May 13, 2024

aggregation, and entanglement in these nanomaterials can drastically decrease their theoretical capacitive performance.[13] To further push the specific capacitance (C_s) of nanocarbons, their combination with transition metal dichalcogenides (TMDs) could be a valuable strategy to pursue. Especially, WS_2 emerges for its performance, with a large C_s of about 1439.5 F g^{-1} reported in a three-electrode setup at 5 mA cm^{-2} in a 3 M KOH electrolyte medium.[14] In general, many works on TMD-based materials in their layered (2D) form, as well as in both their semiconducting and metallic phases, can be found in the literature in which they are often combined with carbon-based backbones like carbon cloth, carbon nanofibers (CNFs), and other carbon materials.[15−20]

However, CNFs, for instance, are mainly produced from polyacrylonitrile or polyvinylpyrrolidone, where toxic solvents like *N*,*N*-dimethylformamide and tetrahydrofuran have to be used for preparation. Furthermore, large temperatures up to 900 °C under a reducing atmosphere are commonly used to produce them.[21,22] Also for exfoliation of TMDs, toxic solvents are generally used, being *N*-methylpyrrolidone the most prominent example.[23−25] However, also nontoxic solvents can be employed for both fiber production and for the exfoliation of TMDs. To adhere as much as possible to green methods, ethanol, isopropanol (IPA), and water are good choices of liquid media for processing.[26]

Polyethylene oxide (PEO) is the most common polymer source for producing nanofibers with the above-described solvents.[27,28] Since PEO is a highly insulating polymer, conductive carbon sources like MWCNTs and carbon black (CB) produced from recycled tires were used in this study to significantly increase the electrical conductivity in polymeric nanofibers obtained by electrospinning.[29] For PEO films mixed with MWCNTs, the conductivity was reported to increase by 7 orders of magnitude.[30] A similar strong increase (almost 12 orders of magnitude) was obtained for PEO-MWCNTs electrospun fibers, at 1 wt % of MWCNTs.[31] The percolation threshold is greatly dependent on the aspect ratio of the MWCNTs and therefore mainly influenced by the degree of dissolution in the solvent preventing aggregation.[31−33] Inks of 2D-WS_2 can be sustainably produced through a top-down approach using surfactant-assisted liquid phase exfoliation (SA-LPE), in a mixture of IPA and water.[34] By using SA-LPE with nontoxic solvents, expensive and toxic precursor materials can be avoided, while no large and expensive equipment has to be used, as it is the case for bottom-up methods like chemical vapor deposition and atomic layer deposition.[35]

In this work, we report on composite nanofibers based on PEO filled with 2D-WS_2, MWCNTs, and CB, where mass ratios were tuned to enable good electrical conductivity and capability of storing charges, through a synergistic contribution of all the three involved components, which does not take place in simpler mixtures like the monofiller or binary ones.[36,37] By resorting to the use of low-cost methods and green solvents like IPA and water as well as abundant and recycled materials, we propose a novel platform for capacitive energy storage, with the added value of featuring good flexibility for incorporation into wearable technologies. These nanoengineered items show a notable resilience against mechanical stress, and we demonstrate this by investigating the influence of repetitive bending on the charge-storage ability in symmetric capacitor architectures. All of these characteristics are important for enabling the development of flexible EDLCs for smart and wearable devices.

2. EXPERIMENTAL SECTION

2.1. Materials and Methods. All solvents and chemicals were purchased from Sigma-Aldrich and used directly without further purification unless otherwise specified. Two-dimensional WS_2 particles were produced following an already established protocol elaborated and described in a former publication by some of us, based on the SA-LPE method.[34] The supernatant obtained from this method is filtered using a poly(tetrafluoroethylene) (PTFE) filter with a pore size of 200 μm utilizing a filter setup, as shown in the Supporting Information. The 2D-WS_2 particles are then redispersed in a mixture of IPA and water in a 7:3 (70%v/v IPA, 30%v/v H_2O) ratio using an ultrasonic bath (USB) for 10 min at a frequency of 37 kHz. The concentrated suspension is placed into a drying furnace at 120 °C for 12 h to evaporate both solvents. The residual powder is scratched out of the vessel and can be used after redissolution in aqueous solutions with a precise weight ratio. As shown in the Supporting Information, it can be proved by Raman measurements that the mono- and few-layered composition of the exfoliated sample is retained even after the filtration and redispersion procedures. The suspension of MWCNTs was produced by dissolving PEO with an average molecular weight of 1.000.000 g mol^{-1} at a concentration of 0.5 mg mL^{-1} into a mixture of IPA and H_2O in a 7:3 ratio. Carboxylic acid-functionalized MWCNTs were added into the solution, at a concentration of 0.5 mg mL^{-1}. For producing a homogeneous suspension of functionalized MWCNTs, a tip sonicator Sonoplus HD 2200 from Bandelin Electronic was utilized, as shown in the Supporting Information.

Scanning electron microscopy (SEM) images were collected on a Gemini SEM 560 instrument from Zeiss with an acceleration voltage of 3 kV and an aperture size of 20.0 μm. The images were collected with a secondary electron detector. Energy-dispersive X-ray spectroscopy (EDS) measurements were performed by using an Ultimax detector from Oxford Instruments with an acceleration voltage of 5 kV and an aperture size of 75.0 μm. Samples were observed also through scanning transmission electron microscopy (STEM) with a nonaberration-corrected microscope (Talos F200X, ThermoScientific) operated at 200 kV. Images were recorded on a 16Mpxls CMOS camera with a 1 s exposure time. STEM images and EDS maps were acquired with the same microscope operated in STEM mode with a probe current of 750 pA. EDS spectra were acquired with an in-column 4-quadrant detector. Elemental maps were elaborated from machine acquisition software (Velox, V. 3.6.0). Raman spectra were recorded with a Senterra infinity 1 from Bruker in a range from 200−1700 cm^{-1}, with an optical microscope for adjusting and a magnification factor of 50. The excitation laser was operating at a wavelength of 532 nm. X-ray diffraction (XRD) data were obtained with an X'Pert Pro MRD from Malvern Panalytical. A Cu Kα source (λ = 0.154178 nm) was used at a voltage of 40 kV and a current of 40 mA. The incident beam angle was set to 0.5°, with a 2 mm mask and a cover slit of 1/16°. Samples were measured in the 2θ range of 10−80°. Thermogravimetric analysis (TGA) coupled with mass spectrometry was carried out in synthetic air (79 vol % N_2 and 21 vol % O_2) using a STA40PC thermoscale provided by Netzsch within a temperature ranging from 30 until 700 °C with a heating ramp of 2 K min^{-1}.

The mechanical properties of nanofibrous composites were evaluated by uniaxial tension tests using a dual-column universal testing machine, Instron 3365 (Instron, Norwood, MA, USA). Since fiber mats are very fragile and thin, they could not be cut in the typical dog bone shape. To perform the measurement, first, fiber mats were cut in specimens with a width of 4 mm and length of 25 mm and then placed in a paper frame as a support. At least 10 samples for each type were tested in order to improve the reliability of the results. Before the test, all of the samples were conditioned at 24 °C and 50% relative humidity in an Espec SH-262 Environmental Chamber (ESPEC, Hudsonville, MI, USA). Displacement was applied at a rate of 10 mm min^{-1}. The Young's modulus (YM), ultimate tensile strength (UTS), and elongation at break (EB) were reported. Electrochemical characterization was performed with the Autolab PGSTAT302 from

https://doi.org/10.1021/acsaem.4c00417
ACS Appl. Energy Mater. XXXX, XXX, XXX−XXX

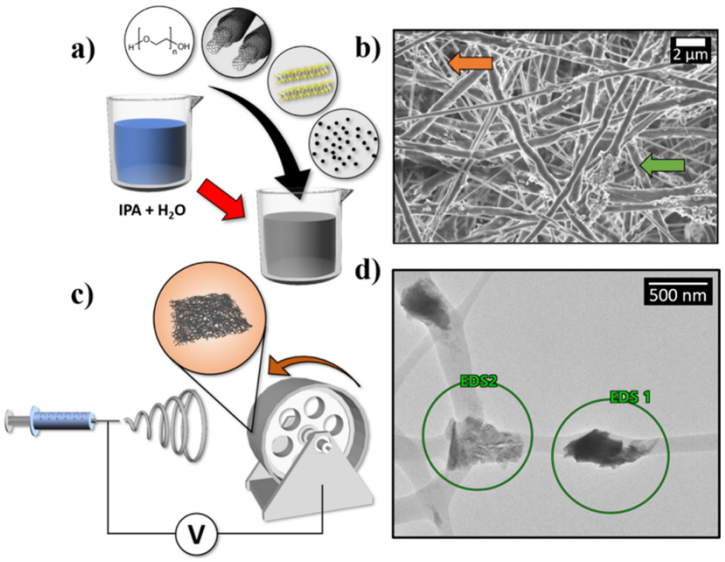

Figure 1. (a) Schematics of blend composition, based on PEO (M_w = 1.000.000), functionalized MWCNTs, 2D-WS_2, and CB particles dissolved in an IPA/water mixture. (b) Typical SEM image of the produced ternary blend-based fibers, with thicker fibers indicated by the green arrow and thinner fibers indicated by the orange arrow. (c) Schematics of the electrospinning process using a standard syringe and gathering the produced fibers on a drum roll current collector, by applying a potential between the syringe and the collector. (d) STEM image of a single fiber deposited on a TEM grid, where EDS1 can be correlated to a carbon-based particle, while EDS2 is ascribed to an agglomerate of 2D-WS_2 sheets (see Figure S4 for EDS spectra).

Metrohm and Nova Software (version 2.1). Cyclic voltammograms were recorded in the range from −0.25 to 0.6 V with scan steps of 2.44 mV at different scan rates of 10, 20, 50, 100, 150, 200, 250, and 500 mV s^{-1}. The cycling was done six times to ensure the equilibrium state of samples, and only the polygon area of the last cycle was used for calculating the specific capacitance using the polygon area function of OriginPro (2021). The measurements were the same for all types of cells (Swagelok and pouch cells). Potentiostatic electrochemical impedance spectroscopy (PEIS) measurements were done using the galvanostatic potentiostat BioLogic from the frequency range of 0.1 Hz up to 100.000 Hz in combination with a Swagelok electrochemical cell.

2.2. Blend Preparation and Electrospinning. The as-prepared precursor materials were employed for the preparation of blends for the electrospinning process. As liquid basis, the 0.5 mg mL^{-1} concentrated MWCNT suspension was mixed with a CB produced from recycled tires, the synthesis of which was already reported by some of us,[29] with a mass ratio of 0.1 wt %, namely, a concentration of 1 mg mL^{-1}. The mixture was homogenized using an USB at a frequency of 37 kHz for 30 min to ensure the proper mixing of the CB (see the Supporting Information). Subsequently, exfoliated 2D-WS_2 was added under stirring for 30 min, with a mass ratio of 1.25 wt %. The USB was again used for homogenization at 37 kHz and 30 min. The fourth and last additive, PEO (M_w = 1.000.000 g mol^{-1}), was added to the suspension with a mass ratio of 2.5 wt %. The mixture containing MWCNTs, CB, 2D-WS_2, and PEO was stirred and mixed for another 2 h to ensure the complete dissolution of PEO. Afterward, the suspension was added to a planetary ball mill at a rotation speed of 250 rpm for 3 h to further homogenize and finally produce the blends, by decreasing the size of all dissolved or suspended species (depicted in the Supporting Information). The particle size is essential for the electrospinning process since the tip of the syringe easily gets clogged using nonideal, heterogeneous suspensions. Furthermore, a continuous flow of the blend must be ensured, since the production of fibers necessarily demands a stable Taylor cone to get reproducible appearances and diameters and to avoid electrospraying. After another 12 h of stirring, the blend was ready to be spun in the electrospinning setup. A potential of −2 kV was applied to a rotating drum roll as a fiber collector, which was covered with aluminum foil (for easy and clean removal), where the rotation enables a more homogeneous production of fibers compared to a static current collector. A syringe tip was used as a counter electrode at a distance of 25 cm apart from the drum roll and an applied potential of 14 kV was used while electrospinning. For the processing, the blend was put into a syringe with the before mentioned syringe tip, having a diameter of 0.5 mm. Finally, a constant flow rate of 0.3 mL h^{-1} was set, and the drum collector rotated at 60 rpm.

2.3. Fabrication of Pouch Cells. For the preparation of pouch cells, a flexible CB-PTFE current collector (CB-PTFE CC) was produced using a commercially available CB (Beyond Battery, Singapore) and PTFE. An aqueous PTFE dispersion (60 wt %) containing traces of polyethylene glycol trimethyl nonyl ether was mixed with 2 mL of ethanol and with the CB. The ratio between CB and PTFE was set to 95:5 wt %. The suspension was stirred to successively evaporate the ethanol. Once a rubbery consistency was achieved, ethanol was added dropwise to the mixture and kneaded into the clump using a spatula. After 10−15 min during which the mixture was homogenized, a glass plate and glass rod were used to roll a sheet with a thickness in the range 70−100 μm. The as-prepared sheets were dried overnight at 80 °C. The current collector was placed while electrospinning, fibrous materials can be directly deposited onto the CB-PTFE CC (see in the Supporting Information). After preparation of the current collector-fiber composites, the stacked material was punched into coin-shaped pieces with diameters of 12 and 14 mm to produce flexible pouch cell devices. The different diameters ensure total area overlapping so that direct charge transfer is guaranteed. A round SiO_2 nanofiber piece with a diameter of 17 mm was used as a separator. The pouch cells were assembled using 140 μL of 1 M tetra ethylammonium tetrafluoroborate ($TEABF_4$) in propylene carbonate (PC) as an electrolyte. Nickel tabs were used as contacts for both sides of the pouch cell, since a symmetric device was produced. Finally, the cells were closed under vacuum using pouch cell bags and a sealing device (Sealervac) from Sealershop, with an evacuation time of 60 s and a sealing time of 5 s.

2.4. Electrochemical Testing. Two different cell types were used for electrochemical characterization. First, a symmetric supercapacitor

https://doi.org/10.1021/acsaem.4c00417
ACS Appl. Energy Mater. XXXX, XXX, XXX−XXX

device was built in a typical Swagelok cell type, as shown in the Supporting Information. Two pieces of composite fibers of 12 mm diameter were separated by a Whatman SiO_2 nanofiber sheet (14 mm). All components, different from the pouch cells, were contacted with 120 μL of electrolyte, that is, a 0.5 M $TEABF_4$ solution in PC. Finally, the Swagelok cell was pressurized by springs, closed, and contacted for measuring. The second cell type was the as-prepared pouch cells, and the fabrication of which is described above. The cells were directly connected to a potentiostat using crocodile clamps. Mainly, we used electrochemical cyclic voltammetry data (CV) to elaborate the C_s of the produced ternary nanofibers (see the Supporting Information). The measurements were done at a constant temperature of about 23 °C. The potential window has been set between −0.25 and 0.6 V, which is the maximum range of the non-Faradaic region. For referencing CV data, a 0.5 M $TEABF_4$ solution in PC was mixed with ferrocene to enable comparability with other electrochemical systems. In the ascribed region, no redox processes are responsible for charge accumulation but surface charging.[38−40] Different scan rates were used from 10 to 500 mV s^{-1} (see above).

3. RESULTS AND DISCUSSION

The different steps for the blend preparation described under sections 2.1 and 2.2 are summarized in Figure S1. From these blends, nanofibers are produced by using electrospinning, as sketched in Figure 1. Pictures of the drum-roll collector used to prepare the nanofibers are shown in Figure S2. Figures 1b and S3 show typical SEM images of the thus produced ternary blend-based fibers. As indicated by the orange and green arrows in Figure 1b, different thicknesses of the fibers can be observed. Two classes of thinner and thicker fibers are visible. From this image, 50 different diameters at the thicker fibers and 50 different diameters at thinner fibers were averaged by using the ImageJ software to obtain individually the average fiber thickness of both classes. The average thickness of the thinner fibers (orange arrow) was calculated to be 159 nm, while the thicker fibers have an average diameter of 845 nm. These two trends in the distribution indicate that in some fibers, the pure PEO component is prevailing, while in some of the others, the presence of the three types of fillers is more concentrated and contributes to an expansion of the diameter. From the images, no preferential direction or, in other words, no directional order of the fibers created by the rotating motion of the drum-roll collector is visible. Therefore, we assume that the velocity of the accelerated fibers is greater than the rotating motion of the collector.

The produced fibers show a homogeneous distribution in the micrometer scale of the layered WS_2 particles in the fibers, as proven by EDS analysis. In Figure S3, sulfur (light blue) and tungsten (pink) EDS signals are present throughout the entire image. TEM micrograph of the fibers (Figure 1d) shows two different spots where two different particle agglomerates are clearly visible in the fibrous material (the spectra for EDS1 and EDS2 are shown in Figure S4). The first spot (EDS1) can be ascribed to a carbon-based material, which can be either MWCNTs or CB added into the blends, since the carbon contribution is larger compared to the tungsten and sulfur contribution. The EDS2 measurement shows an agglomerate of several mono- or few-layer WS_2 sheets within the PEO matrix, with an increased contribution attributed to tungsten and sulfur. From the insights of SEM and STEM images and their elemental analysis, it can be proven that layered WS_2 is present in the composite fibers.

Raman analysis was used to further characterize the presence of layered WS_2 in the produced fibers. Coleman et al. described the method for the LPE of 2D materials like TMDs.[24] The changes in band structure from indirect-to-direct bandgap were calculated and proven when going from the bulk to the mono- and few-layered WS_2 and MoS_2.[41,42] Raman spectroscopy can be used to differentiate between bulk and low-dimensional form, as it was described by Berkdemir et al.[43] Raman spectra of various WS_2 samples are shown in Figure S5. For the bulk material, the $(2LA + E_{2g})/A_{1g}$ ratio was observed to be 0.55 and 0.47 at an excitation wavelength of 514 and 514.5 nm, respectively.[43,44] Since the measurements were carried out at 532 nm excitation wavelength and the sensitivity for the number of layers and the effect on the spectra depend on the excitation wavelength, bulk WS_2 was used as a reference to compare the degree of exfoliation to the literature.[43,45]Figure S5 confirms that the literature-reported values are in agreement with the experimentally obtained ratio $(2LA + E_{2g})/A_{1g}$ = 0.499 from the reference bulk WS_2 powder. Therefore, the $(2LA + E_{2g})/A_{1g}$ ratio at 532 nm remains a suitable proof of the exfoliation degree. The single sheets always possess $(2LA + E_{2g})/A_{1g}$ ratios above 2, while double layers achieve ratios around 1.[43,46] As Figure S6 shows, all measured spectra that contain WS_2 feature ratios far above 1, with 1.34 for the binary fibers containing functionalized MWCNTs and WS_2, 1.74 for the fibers containing only WS_2, which means that in these fibers, mainly double- and monolayers of the TMD are present. For the ternary fibers, a ratio of 2.08 results from Raman peaks analysis, indicating that the WS_2 particles predominantly exist as monolayers in this sample[18] In the range between 1250 and 1700 cm^{-1}, the detection of MWCNTs was also possible. As also indicated in Figure S6, D- and E_{2g} bands of carbon are found at Raman shifts of 1352 and 1585 cm^{-1}, respectively. The D-band position (1352 cm^{-1}) strongly depends on the utilized excitation wavelength and shifts toward larger wavenumbers with increasing excitation energy: this can be attributed to electronic states emerging in disordered graphitic materials that couple resonantly with the excitation laser, causing the observed wavelength-depending shifts.[47,48] However, it is clear that MWCNTs are present in all samples by looking at E_{2g} and D-bands, except for the PEO-2D-WS_2 sample, which does not contain them. The low intensity, large defect concentration, and poor ratio between the two bands I_{E2g}/I_D result from different causes. The first effect is caused by the overall concentration of the MWCNTs in the prepared suspension, being low compared to the other components (around 1.28 wt %), which is why WS_2 signals simply dominate the spectra. The comparably large defect band is caused by the utilized MWCNTs. For better dissolution in the water/IPA mixture, functionalized MWCNTs with carboxylic acid were used. As a consequence, more defects are present on the nanotube surface disturbing the graphitic order, which is the main reason for the low-intensity E_{2g}-band contribution resulting in the poor, above-described, ratio.[47,49]

Figure S7 displays the XRD patterns of all different PEO-based nanofibers that were produced from the prepared blends. PEO fibers naturally show a certain crystallinity after the electrospinning process, which is seen throughout all different samples.[50,51] In 2001, Deitzel et al. ascribed the reflexes (indicated as the red dots) directly to the crystalline phase of PEO.[27] Besides the comparably small reflexes of PEO, larger relative intensities can be ascribed to WS_2 reflexes, and there is no doubt that crystalline WS_2 is present in the fibers originated from the 2D-WS_2-containing blends (indicated by the blue rectangles in Figure S7). The (002) reflex at 14.3° (d_{002} = 1.01053 Å) from the reference is the most prominent reflex for

https://doi.org/10.1021/acsaem.4c00417
ACS Appl. Energy Mater. XXXX, XXX, XXX−XXX

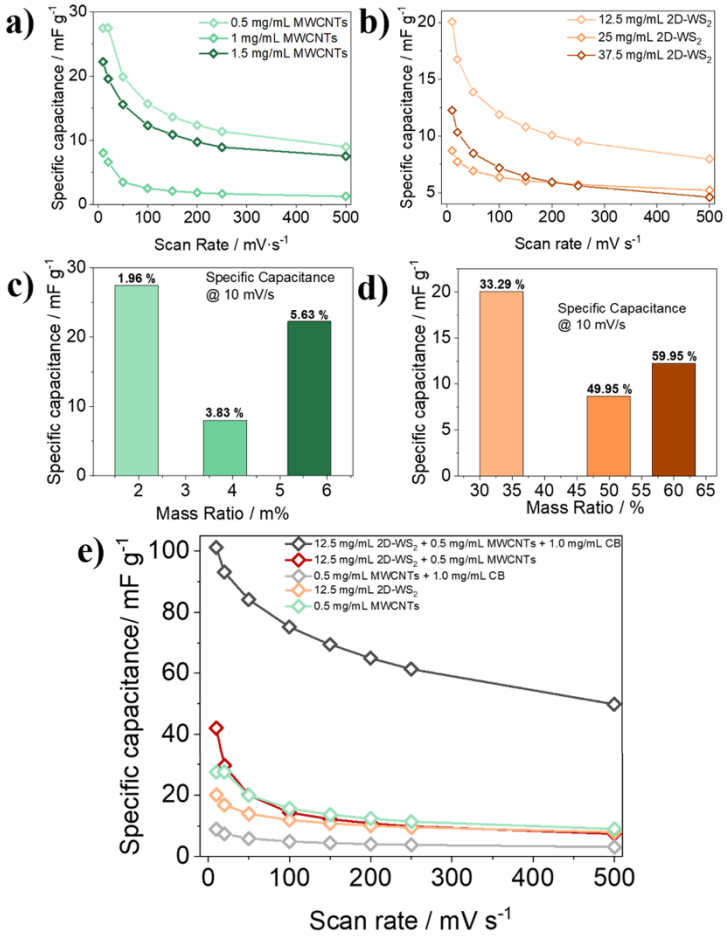

Figure 2. C_s for differing concentrations of (a) PEO-MWCNTs fibers from 0.5 to 1.5 mg mL^{-1} and (b) 2D-WS_2 from 12.5 to 37.5 mg mL^{-1}. (c, d) The C_s vs mass ratio in % at a scan rate of 10 mV s^{-1} for 2D-WS_2-PEO fibers and MWCNT fibers. (e) Data for the best performing samples from panels (a) and (b), that is, for fibers containing MWCNTs-CB at a concentration of 0.5 mg mL^{-1} for MWCNTs and 1 mg mL^{-1} for CB, the mixture of 2D-WS_2 and MWCNTs with optimized concentrations (dark red), and the mixture of both additives at optimized concentrations, including the addition of CB at a concentration of 1 mg mL^{-1}. The measurements were done in a Swagelok electrochemical cell using $TEABF_4$ at a concentration of 0.5 M dissolved in PC as an electrolyte. The measurements were done at 10, 20, 50, 100, 150, 200, 250, and 500 mV s^{-1} in a range between −0.25 and 0.6 V (non-Faradaic region).

the 2H phase of the TMD. No side phases, such as WO_3 or 1T-WS_2, were produced during exfoliation and fiber spinning. In the case of WS_2, the exfoliation might affect the reflex position and, further, the *d*-spacing of the layers. The deviation of the reflex positions for all samples corresponds, compared to the reference, to *d*-spacing differences from 0.0051 to 0.8447%. The exfoliation of bulk WS_2, dissolved in suspensions and finally electrospun, therefore, did not affect the distance of the d_{002} plane of the 2H WS_2 phase, and no phase transitions were observed.

The electrochemical characterization of the composite fibers, aimed at determining the most performing composition in terms of fillers type and quantity, was carried out through CV in a Swagelok cell-type device (see Figure S8) by using a nonaqueous electrolyte. Due to the polar nature of PEO, which is soluble in most typical solvents used for electrolytes, PC, a high boiling, nonpolar solvent was used for dissolving $TEABF_4$, which acts as the charge transferring species (electrolyte) within the electrochemical cell. Different blends with increasing concentrations of MWCNTs and 2D-WS_2 as shown in Figure 2a,b were produced and analyzed. From the CV traces (Figure S9), the specific capacitance was calculated by using the following equation:[52,53]

$$C_s = \frac{A}{\Delta V \cdot \nu \cdot m}$$

where C_s is the specific capacitance, m is the sample mass in grams, ΔV is the potential window, ν is the scan rate in mV s^{-1}, and A is the area of the voltammograms in Figure S9. The potential window was chosen between −0.25 and 0.6 V, which was found to be the non-Faradaic region for the composite fibers. Since referring this material system to a reference electrode is difficult due to the high solubility of PEO in aqueous solvents, a pseudo reference (ferrocene) was used to be able to contextualize the applied potential window. Figure S10 shows the anodic and cathodic peaks of the ferrocene couple (Fc/Fc^+) in the used electrolyte system of $TEABF_4$ and PC at a 0.5 M concentration. The offset potential can be

https://doi.org/10.1021/acsaem.4c00417
ACS Appl. Energy Mater. XXXX, XXX, XXX−XXX

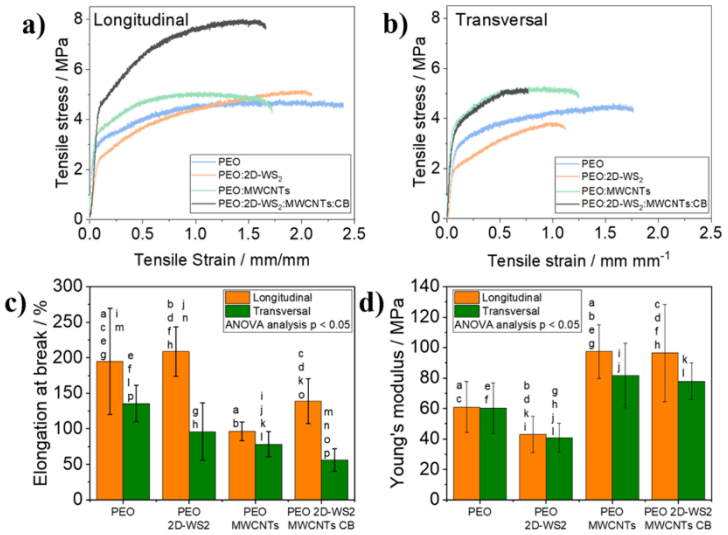

Figure 3. Representative stress−strain curves of pure PEO (light blue), PEO-WS_2 (light orange), PEO-MWCNTs (dark red), and PEO-WS_2-MWCNTs-CB (black) in the (a) longitudinal direction and (b) transversal direction. (c) The average values of the EB and the error bars for all samples with the added letters for the statistical analysis from ANOVA with a p-value of 0.05. If the p-value is above 0.05, then, there is a significant difference in the two compared data sets. This difference is indicated with a letter in the diagrams showing that the two data sets are significantly different. (d) The average values of the YM and the error bars for all samples with the added letters for the statistical analysis from ANOVA with a p-value of 0.05. The explicit values for panels (c) and (d) can be found in Table 1.

derived from the middle of the two peak potentials. The offset of 0.74 V, which is obtained from these curves, is then subtracted from the applied potential and corresponds to the potential range −0.99 to −0.14 V vs Fc/Fc^+ shown in Figure S9. Inside this region, no redox reactions are occurring, and measured currents are a consequence of surface charging instead of electrochemical reactions, which enables the determination of C_s. By adding more charge-conductive species, namely, MWCNTs and 2D-WS_2, intuitively the capacitance of the fabricated fibers should increase. A larger concentration should enable a larger C_s, since more active material is present for charge storage. However, there is no such trend visible in the obtained data summarized in Table S1. With increasing scan rates, the size of the diffusion layer decreases, due to the electrolyte diffusion toward the electrode, which explains the overall larger currents shown in Figure S9.[54] For all samples, but especially for the PEO-WS_2 and PEO-WS_2-MWCNTs-CB composites, a rectangular shape is measured, proving the capacitive behavior. The overall shrinking of C_s, with raising the scan rate, has its origin in the diffusion limitation of charges into the material and is commonly seen for CV-type measurements.[38] Therefore, the obtained values discussed from now on are those measured at a scan rate of 10 mV s^{-1} (Figure S9). Again, for optimization of concentrations of 2D-WS_2 and MWCNTs in the fibers, 2D-WS_2-PEO and MWCNTs-PEO were measured in the Swagelok cells in Figure 2a,b. It was determined that by doubling the concentrations to 25 mg mL^{-1} for WS_2 and 1 mg mL^{-1} for MWCNTs, a rapid drop of the specific capacitance from 20.06 to 8.69 mF g^{-1} in the case of 2D-WS_2 and from 27.47 to 8.03 mF g^{-1} for the MWCNTs containing fibers was obtained, as visualized in Figure 2c,d. Afterward, at a concentration of 37.5 mg mL^{-1} for 2D-WS_2 and at 1.5 mg mL^{-1} for MWCNTs, the specific capacitance increases again to 12.24 mF g^{-1} for 2D-WS_2 and up to 22.22 mF g^{-1} in the case of MWCNTs fibers. Due to the insolubility issues, there is a limit to the amount of material that can be added to the suspensions for each species, which was reached or exceeded at these concentrations of 1.5 mg mL^{-1} for MWCNTs and 37.5 mg mL^{-1} for WS_2. The particles of 2D-WS_2 and carbon species, which are present in the blends shown in Figure 1b,d, have lateral sizes around 500 nm up to a few μm. By addition of more of these large particles into the blends, homogeneity cannot be longer ensured. We observed that high concentrations lead to poor dispersion and agglomeration and that the overall distribution of 2D-WS_2 and MWCNTs in the fibers becomes worse compared to blends with lower concentrations.

In Figure 2e, the mixture of the best-performing concentrations from Figure 2a,b is reported, together with the binary composites of 2D-WS_2-MWCNTs, as well as the composite of MWCNTs-CB. It is important to underline that fibrous samples with binary composition 2D-WS_2 + CB do not appear among the ones tested in Figure 2e. The CB-based fibers not containing all the three additives together provided too inhomogeneous mats, which were not possible to remove from the aluminum foil after the electrospinning deposition process, making their electrochemical characterization not feasible. In contrast, the ternary mixture is clearly outpacing all the investigated binary and monofiller compositions, with a remarkable value of C_s reaching almost 100 mF g^{-1} at the slowest utilized scan rate and decreasing to 50% of this value at the fastest one. Electrical conductivity measurements prove that the addition of CB contributes mainly to a decrease in resistance, as can be seen in Figure S11. Due to a lack of mechanical stability, also fibers produced from a simple PEO-CB blend were not studied electrochemically, due to inability of detaching them from the collector foil in the electrospinning setup. The composite fibers based on the binary 2D-WS_2-MWCNTs mixture in PEO show an increase of the electrochemical performance up to 42.05 mF g^{-1} compared

https://doi.org/10.1021/acsaem.4c00417
ACS Appl. Energy Mater. XXXX, XXX, XXX−XXX

Table 1. YM (MPa), EAB (%), and UTS (MPa) of PEO, PEO WS_2, PEO MWCNTs, and PEO- WS_2- MWCNTs-CB[a]

parameter	PEO	PEO:2D-WS_2	PEO:MWCNTs	PEO:2D-WS_2:MWCNTs:CB
YM − long. (MPa)	61.00 ± 16.71	42.99 ± 11.92	97.40 ± 17.69	96.47 ± 31.90
YM − trans. (MPa)	60.33 ± 16.50	40.87 ± 9.40	81.63 ± 21.13	77.87 ± 12.17
EB − long. (%)	195.07 ± 74.64	208.69 ± 34.95	95.57 ± 13.21	139.04 ± 31.68
EB − trans. (%)	136.60 ± 25.56	96.00 ± 40.43	78.18 ± 17.63	56.03 ± 15.79
UTS − long. (MPa)	4.78 ± 0.81	5.33 ± 0.97	4.90 ± 0.31	7.11 ± 1.17
UTS − trans. (MPa)	4.54 ± 0.39	3.68 ± 0.95	5.12 ± 0.26	2.75 ± 0.22

[a]All of the data are reported as average ± standard deviation. ANOVA test ($p < 0.05$).

to the reference fibers with only one of the two fillers, demonstrating a beneficial cooperative effect between the two nanomaterials. Notably, a binary blend of MWCNTs and CB in PEO, at the same concentration kept in the ternary one, shows poor electrochemical performance, other that being a very brittle and electrostatic sample, with incompatible mechanical properties for use in flexible device architectures. These fibers appear inhomogeneous, which is most likely caused by agglomeration of the carbon fillers. Therefore, clogging of the syringe tip while electrospinning is expected, resulting in low fiber stability and inhomogeneous distribution of active species. Consequently, a reduced number of conductive paths through the fibrous matrix is formed, triggering low-capacitive performance. In the ternary composite instead, where CB was added to improve the electrical conductivity, the strong enhancement in C_s suggests a beneficial interaction between 2D-WS_2 and the carbon species, which are consequently better distributed in the fibrous polymer matrix, as long as 2D-WS_2 is present.

We investigated the mechanical properties of the prepared nanocomposite fibers to prove their suitability for use in flexible devices. Mechanically, the fibrous mats show different properties, depending on the specific filler they contain. Therefore, their UTS, YM, and EB were measured to test their resilience against mechanical stress. Especially, the values of YM and EB play a crucial role in their use in flexible electronics and supercapacitors: the active material should not break and remain in its former shape when it is slightly bent. Since the fibers are spun on a rotating drum roll collector, the influence of the spinning process itself was investigated by measuring at least 10 samples along the spinning direction (longitudinal) and perpendicular to the spinning direction (transversal). As shown in Figure S12, it was noticed how the position on the mats, where the samples were gathered, influenced their mechanical behavior: the closer to the edges they were, the lower their maximum tensile stress was. Indeed, while electrospinning, the needle tip is positioned in the center of the drum collector, and therefore, fibers mats are centrally loaded and their thickness decreases as far away from the center. For this reason, samples were cut from the middle of the fiber mats to perform longitudinal measurements. Even if an orientation of fibers on the rotating collector was expected at first, the SEM images reported in Figures 1b and S3 did not show a preferential direction, which was explained by the low rotation speed. Since distances of 25 cm were used for producing the fibers and large acceleration voltages were present, the fibers reached the collector quickly. Within that time, the collector itself did not rotate a large distance since it was rotating at 60 rpm. This result is in agreement with a previous work by Kumar and Vasita,[55] where, to obtain aligned fibrous material, up to 2500 rpm was needed, while 300 rpm resulted in nonaligned fibers. Representative stress−strain curves of longitudinal and transverse samples for each filler mixture are shown in Figure 3a,b, respectively. One exception is the PEO-CB sample. As mentioned before, the CB-based fibers without all three fillers featured poor homogeneity and, thus, no delamination from the aluminum foil was possible without damaging the mats. As a consequence, their characterization could not be conducted. As can be noticed, from the comparison of the longitudinal samples (Figure 3a), an effective increase of the maximum tensile stress was observed in the presence of carbon-based fillers, whereas all the other fillers did not bring any improvement.

On the other hand, transversal samples (Figure 3b) did not show any difference in maximum tensile stress depending on the filler involved in the formulation. Therefore, only PEO-WS_2-MWCNTs-CB composite showed a significant difference in maximum tensile stress: a 40% reduction was observed from longitudinal to transversal samples. Mechanical properties of the composites were investigated in terms of YM, EB, and UTS, and results are reported in Table 1.

As can be noticed, both the YM (Figure 3d) and the EB (Figure 3c) of samples containing MWCNTs significantly differed from samples without MWCNTs, regardless of the longitudinal or transversal direction. Indeed, the YM of pure PEO increased from (61.00 ± 16.71) MPa up to (97.40 ± 17.69) MPa for PEO-MWCNTs. The addition of WS_2 and CB to PEO-MWCNTs did not show a change in YM (96.47 ± 31.90) MPa. Therefore, it could be stated that the improvement of the YM of the pure PEO was only due to the MWCNTs. Indeed, MWCNTs are significantly more rigid than PEO, with a YM in the range of 270−950 GPa, as measured by Yu et al.[12] Furthermore, the UTS data (Table 1) did not show significant changes in pure PEO after the addition of all of the fillers. The maximum value in the longitudinal direction was obtained by the ternary blend-based fibers with (7.11 ± 1.17) MPa, while the transversal direction was lacking in strength with just (2.75 ± 0.22) MPa performing worse compared to all other samples. The values for MWCNT-filled fibers differ from samples without MWCNTs. On the other hand, as expected, since the fibers are mechanically strengthened due to the nanotube addition, a decrease in the EB was observed;[31] conversely, pure PEO and PEO-WS_2 fibers showed EB 195 and 209% in the longitudinal direction and ∼96−137% in the transversal direction. The EB of PEO-MWCNT and PEO-WS_2-MWCNTs-CB composites showed a significant decrease with 96 and 139%, respectively, in the longitudinal direction, and 78% and 56% in the transversal direction (Figure 3c).

Theoretically, an MWCNT length of 1.5 μm is in a range where the tubes align along the produced PEO fibers (100−900 nm) and effectively contribute to the strength of the fibers.[31] Adding fillers, except for the MWCNTs with a comparably high tensile strength, the fibrous materials are

https://doi.org/10.1021/acsaem.4c00417
ACS Appl. Energy Mater. XXXX, XXX, XXX−XXX

weakened, most likely due to a limited dispersity of CB and 2D-WS_2. The EB suffered less from CB and 2D-WS_2 fillers. In contradiction to what was initially expected, throughout the whole set of samples, an anisotropic behavior was observed because the transversal direction significantly differs from the longitudinal direction with a lower elongation and with withstanding higher loads before breaking. Most likely, this can be ascribed to the deposition along the rotation axis of the current collector used in the electrospinning process: even if initially thought that the low rotation speed of the drum roll collector has no influence, it can be assumed that fibers are slightly aligned, unnoticeably by only watching at SEM images. The weakness of the transversal direction cannot be explained by the observed gradient of thickness; even if the sample position could not be adjusted like in the case of the longitudinal direction (see Figure S12), the total width of the drum roll was 10 cm, while the length of the cut samples was 2.5 cm and taken from the middle of the mats.

To characterize thermal stability, TGA was carried out on the composite fibrous materials, and the thermograms are shown in Figure S13. For any filler added, an increase in the degradation temperature of PEO was observed. Bare PEO fibers started rapidly decomposing at a temperature of 141 °C. By adding 0.5 wt % of MWCNTs, the decomposition temperature was raised up to 171 °C. Surprisingly, the PEO-WS_2 composite fibers obtained the overall largest burning temperature with 264 °C. The mixture of PEO-WS_2-MWCNTs was decomposed at 185 °C, while the ternary blend-based fibers were decomposed at 256 °C. At first, it is important to mention that the influence of WS_2 is the largest for all samples. This is simply because of the chosen mass ratios of the mixtures (PEO:WS_2:MWCNTs:CB = 50:25:1:2); therefore, WS_2 should naturally show a stronger effect. This can be seen at the remaining mass at 700 °C, which is mainly ascribed to the WO_3 mass, since all samples that do not contain WS_2 have significantly lower masses. This means that the lower the relative ratio of PEO, the higher the burning temperature. The only exception is the PEO-WS_2 sample. One possible explanation could be the agglomeration of the filler species inside the fibers. As shown in Figure 1d, most likely agglomerates of WS_2 and CB or MWCNTs appear in the produced blends and prevent more homogeneous mixing. Then, a lower amount of PEO is interacting with the WS_2 surface, because the carbon species block access to the latter. Since WS_2 can trap positive charges, numerous partial negative charges along the PEO chain interact with the WS_2 surface.[37] This weak interaction of PEO chains might cause larger temperatures for decomposing PEO close to the WS_2 particles. This could be highlighted by looking at the position of the ending of the mass drop in TGA data. The ternary blend-based mixture and the binary PEO-WS_2-MWCNTs composite show a rapid drop until 305−315 °C, while this state is reached around 360 °C for the PEO-WS_2 fibers. For decomposing residual PEO, close to the WS_2 particles, larger temperatures are necessary due to the PEO-WS_2 interactions. However, previously, it was found that metal oxide-WS_2 composites were able to effectively act as flame retardant for polyethylene implemented in a PE matrix: we also observed a comparable trend the produced WS_2-based composite fibers from PEO.[56]

After optimizing the concentration for each additive in the composite fibers, a flexible current collector was used as a substrate for direct fiber spinning in order to prepare the two main parts of a flexible symmetric supercapacitor. CB and PTFE were used to produce the current collector (CB-PTFE CC) used as a substrate (Figure S2), as described in the Experimental Section. PEIS was employed to characterize the electrical performance of the CB-PTFE CC. From these flexible substrates and the on-top deposited fibrous mats, pouch cell devices were fabricated as explained in the Experimental Section and shown in Figure 4a. As can be

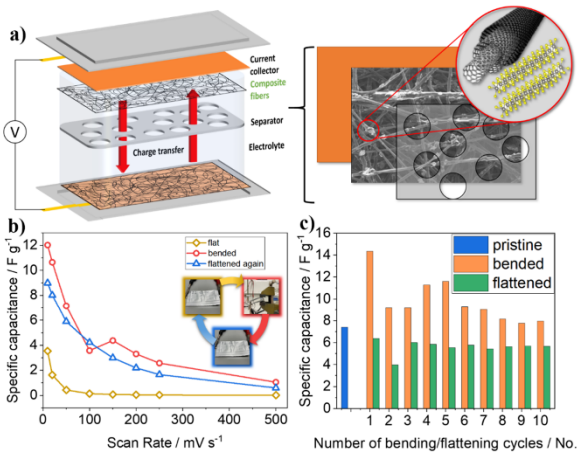

Figure 4. (a) Schematic of pouch cell architecture for the symmetric supercapacitor devices used for electrochemical analysis. The pouch cells are built using nickel tabs as current conductors, CB-PTFE coated with the ternary blend-based fibers, and a SiO_2 fibrous membrane (Whatman) as a separator. 1 M $TEABF_4$ (120 μL) dissolved in PC was used as electrolyte. The measurements were done at 10, 20, 50, 100, 150, 200, 250, and 500 mV s^{-1} in a range from −0.25 to 0.6 V. Panel (b) shows the specific capacitance depending on the scan rate before bending (yellow), during the first bending (red), and after the first bending (blue). The inlet visualizes the bending process. (c) Another symmetric cell (different sample from the one used in b) was bent 10 times, and the specific capacitance was measured in the bent as well as in the flat state at a scan rate of 10 mV s^{-1}.

deduced from Figure S14 and Table S2, PEIS measurements on CB-PTFE CC provide a resistance of 172 Ω with a double-layer capacitance of 2.6 nF, using a fitting model based on a Randles' circuit, which is an acceptable value for a flexible CC featuring electrical conductivity and some capacitive behavior as well.[57] Table S1 summarizes the values obtained from the experiments in Figure S15 of the assembled pouch cells, as well as from the data shown in Figure 4b. From Figure S15, it can be seen that the pure CB-PTFE CC shows a specific capacitance of 0.49 F g^{-1}, which is a factor of 4.65 larger than the ternary fibers measured in the Swagelok cell. The composite being produced from the CB-PTFE CC and the ternary fibers in Figure 4b (yellow graph) already shows a large increase of the specific capacitance up to 3.54 F g^{-1}. This drastic enlargement can be explained for several reasons. At first, as the reference in Figure S15 shows, there is a contribution of the CB-based current collector. It is well-known in the literature, especially for Li-ion and Na-ion batteries, that CB acts as a capacitive species.[58,59] Additionally, the CB affects the conductivity of the composite material. CB as a conductive material enables charge transport to the electrodes, as the diagram in Figure S11 indicates, while Figure S2 shows the ability of the substrate to conduct current and

https://doi.org/10.1021/acsaem.4c00417
ACS Appl. Energy Mater. XXXX, XXX, XXX−XXX

sustain a commercial LED. The aforementioned direct spinning process onto the CB-PTFE CC likely leads to good contact between the fibers and the conductive current collector. The decreased distance that charges have to overcome during the charge−discharge process in the PEO-based matrix is more probable when more contact points to the electrode material are present. Furthermore, the vacuum treatment used to produce pouch cells compresses the fibers as well as the separator, with overall densification of the cell structure. Being the distance between two electrodes in the capacitor reduced, C_s becomes logically higher, given the inverse proportionality.

The device with the best performance was used to conduct cyclability tests using capacitance retention measurements. Galvanostatic charge−discharge measurements were performed for 3000 cycles at a current density of 50 mA g^{-1} (Figure S16). C_s retention was found to be very effective, and the C_s was maintained constant over 3000 cycles, reaching up to 102.3% of the initial value. Coulombic efficiency also remained constant for 2000 cycles and then slightly shifted upward to a maximum value of 107.1%. This upward trend is known especially for carbon-based materials, where self-activation takes place by changes in the surface morphology concomitant with an increase in the specific surface area during successive electrolyte permeation cycles. Additionally, during cycling, some electrochemically active sites become better exposed to the electrolyte.[60,61] Overall, the constant performance for 3000 cycles shows that under cycling conditions, no degradation or parasitic chemical reactions in the system occur and that excellent stability of the composite-electrolyte system in the device is ensured.

Figure 4b discloses another beneficial effect on the specific capacitance: for flexible materials, the bending tests are highly relevant. To test the stability of a flexible supercapacitor, the active species within it must withstand several cycles of bending (at least 10). After the first bending cycle, C_s of the cell is even raised up to 12.019 F g^{-1}. While the bending pressure is applied to the cell, the internal components are compressed, which is beneficial for improving the contact among the different species. This effect also explains the differences observed when employing the same active materials (the fibrous mats) in different cell geometries, namely, Swagelok and pouch cells. By vacuum sealing, a pouch cell is most likely more compressed compared to a Swagelok cell.

Consequently, in the latter, stored charges are hindered to flow from the PEO fiber-based matrix into the current collector since less contact with the current collector exists in this architecture. This effect was also observed for lithium-ion pouch cells by Zhou et al., where, with increasing pressure, a decreasing internal resistance was observed, while the capacity was increasing.[62] Additionally, they also observed an irreversible increase of the capacitance even after removing pressurization, which is also seen in our samples after flattening in Figure 4b (blue curve). A decrease compared to the bent (pressurized) state of the C_s is observed (8.992 F g^{-1}), but nonetheless, it still remains larger compared to the initially prepared cell. The downward trend in C_s at 100 mV s^{-1} seen after the first bending cycle (red curve), followed by an increase at 150 mV s^{-1}, becomes understandable by looking at Figure 4c. In the bent configuration, fluctuations of C_s are always present, mainly caused by the change in pressure in the cell (not controlled here but done manually), which affects the distance of the two electrodes from each other and the electrolyte penetration. In the flat state, almost no fluctuations in C_s can be noticed. The stability tests in Figure 4c conducted on another device show the same upward trend on the first bending cycles. Depending on the cycle, C_s varies from a maximum of 14.35 F g^{-1} to a minimum of 7.77 F g^{-1} in the bent configuration. This is explained by the bending process itself. By hand, the pressure applied to the cell will always differ from one bending cycle to another. However, after three cycles of bending, a plateau of around 5.70 F g^{-1} can be observed. This means that pressurization reaches an equilibrium state where the capacitance remains more or less constant independent from the previous bent state.

We have compared our results with those of similar devices reported in the literature, mostly flexible supercapacitors based on carbon materials, polymers and TMD-based composites. Lamberti et al. produced laser-induced, flexible graphene sheets, which in device provided 0.2 mF cm^{-2} at a scan rate of 10 mV s^{-1}.[63] Also, Peng et al. also obtained 9.11 mF cm^{-2} at a current density of 0.5 mA cm^{-2} with a similar laser-induced flexible graphene material. In comparison, the areal capacitance of the composite fibers reported in this work achieves values of 107.7 mF cm^{-2} at a scan rate of 10 mV s^{-1}, which is comparable to or even better than the two cited cases. Zhou et al. prepared graphite papers using the exfoliation technique and obtained 101.5 mF cm^{-2} at a current density of 0.5 mA cm^{-2}, a value close to the one here presented.[8] More comparable with our architecture, a polymeric flexible system made of polypyrrole-stabilized polypeptides achieved 42 mF cm^{-2} (4 F g^{-1}) at a current density of 0.2 mA cm^{-2}, with our material featuring 5.70 F g^{-1} after 10 bending cycles at 10 mV s^{-1}.[7] Sun et al. presented a hybrid TMDC-carbon-based fiber material from MoS_2, reduced graphene oxide, and MWCNTs and obtained 4.8 F cm^{-3} at a current density of 0.5 A cm^{-3}. Roughly assuming a thickness of 0.02 cm for our composite electrode, we obtain a volumetric capacitance of 5.39 F cm^{-3} at the scan rate of 10 mV s^{-1}.[64] Here, our material performs better than or comparably to several published examples. From carbon-based materials, there are also works, especially in the field of CNFs, reporting larger C_s: in our previous work on CNFs, we reached 49 F g^{-1} at 0.5 A g^{-1}, while in other examples activated CNFs provided 83.3 F g^{-1} at a current density of 100 mA g^{-1} or 95 F g^{-1} at a scan rate of 10 mV s^{-1}.[10,21,36] However, it is worth noting that most CNF-based electrodes have limited flexibility, which makes them unsuitable for application in flexible energy storage devices.

4. CONCLUSIONS

In this work, we studied the effect on the electrochemical and mechanical performances of nanoengineering electrospun PEO nanofibers with layered WS_2, MWCNTs, and CB. The described achievements suggest that a capacitive behavior is clearly present in the composite material, with C_s values up to 0.1 F g^{-1} at 10 mV s^{-1} scan rate. It is important to note that this quantity does not derive from the simple sum of each individual component contribution but comes from a synergistic effect of the three different nanostructures, assembled in an optimized way within the fibrous scaffold. In fact, the structural characterizations performed (XRD, SEM, and TEM), coupled to thermogravimetric analysis, show an intimate contact between the nanomaterials, which justifies the establishment of cooperative effects in the transport and storage of electrical charges. The mechanical properties are also influenced by the presence of the nanofillers, with

https://doi.org/10.1021/acsaem.4c00417
ACS Appl. Energy Mater. XXXX, XXX, XXX−XXX

improved figures of merit and, notably, an increased UTS when CB is present and a 60% boosted YM when MWCNTs are used, whereas the EB is substantially reduced.

As proof of concept to demonstrate the potential for integration into flexible energy storage devices, we show the fabrication of a flexible symmetric capacitor and test its ability to maintain a good capacitance after multiple cycles of bending and reflattening, with only about 25% loss of the initial C_s after 10 cycles, that suggest how the plastic behavior of the device is supported by the effective mutual cooperation of its nanocomponents.

These findings reveal the impact of nanoengineering polymeric matrices with electrically active fillers to pave the way to new functional materials, which will promote a step-forward in the ideation of versatile energy storage units for low-power electronics embedded within portable and lightweight technologies.

■ ASSOCIATED CONTENT

Supporting Information

The Supporting Information is available free of charge at https://pubs.acs.org/doi/10.1021/acsaem.4c00417.

Schematic description of the production of 2D WS_2 powder, MWCNTs suspension, and steps for the preparation of the ternary blend (Figure S1); conductivity and flexibility tests on CB-PTFE mats and electrospinning process of polymer fibers onto the CB-PTFE mats (Figure S2); SEM and EDS images of fibers produced from the ternary blends (Figure S3); EDS spectra of two particles found in the ternary fibers (Figure S4); Raman spectra of the WS_2 bulk reference, produced 2D WS_2 powder, and redispersed 2D WS_2 (Figure S5); Raman analysis and spectra of various fibrous materials containing different mixtures of additives, including an inset magnifying the region of Raman shifts in the region of MWCNTs (Figure S6); diffractograms of various fibrous materials containing different mixtures of additives with the given reflexes for WS_2 and PEO (Figure S7); schematic of the Swagelok cell used for electrochemical characterization in a symmetrical supercapacitor configuration (Figure S8); CV scans on fibrous materials at the optimized additive concentrations at different scan rates (Figure S9); ferrocene redox reaction in 0.5 M $TEABF_4$/PC electrolyte (Figure S10); values of all calculated C_s from the CV curves at different scan rates shown in Figures 2, 4b, and S15 (Table S1); conductivity measurements done on pellets of fibrous mats (Figure S11); dependency of stress−strain curves from the position on the fiber mat shown for fibrous mats of the PEO-WS_2 composite material (Figure S12); thermogravimetric analysis of all produced fiber samples (Figure S13); schematic of the Swagelok-cell PEIS measurements on CB-PTFE mats with the corresponding Randles' circuit (Figure S14); values, error values, and error in percentage for the serial resistance, charge transfer resistance, and double layer capacitance calculated from the PEIS measurements of the DB-PTFE mats (Table S2); C_s from CV curves using pouch cells of CB-PTFE current collector and the composite with ternary fibers in a symmetrical supercapacitor configuration (Figure S15); C_s retention tests carried out using galvanostatic charge−discharge cycles on a pouch cell at 50 mA g^{-1} for 3000 cycles (Figure S16) (PDF)

■ AUTHOR INFORMATION

Corresponding Author

Teresa Gatti − *Institute of Physical Chemistry and Center for Materials Research, Justus Liebig University, Giessen 35392, Germany; Department of Applied Science and Technology, Politecnico di Torino, Corso Duca degli Abruzzi, Turin 10129, Italy;* orcid.org/0000-0001-5343-8055; Email: teresa.gatti@polito.it

Authors

Felix Boll − *Institute of Physical Chemistry and Center for Materials Research, Justus Liebig University, Giessen 35392, Germany*

Marta Fadda − *Smart Materials, Istituto Italiano di Tecnologia, Genoa 16163, Italy;* Present Address: Quantum Metrology and Nano Technologies Division, Istituto Nazionale di Ricerca Metrologica (INRiM), Strada delle Cacce 91, 10135, Torino, Italy

Melissa Happel − *Institute of Physical Chemistry and Center for Materials Research, Justus Liebig University, Giessen 35392, Germany*

Matteo Crisci − *Institute of Physical Chemistry and Center for Materials Research, Justus Liebig University, Giessen 35392, Germany*

Athanassia Athanassiou − *Smart Materials, Istituto Italiano di Tecnologia, Genoa 16163, Italy;* orcid.org/0000-0002-6533-3231

Bernd Smarsly − *Institute of Physical Chemistry and Center for Materials Research, Justus Liebig University, Giessen 35392, Germany;* orcid.org/0000-0001-8452-2663

Federico Bella − *Department of Applied Science and Technology, Politecnico di Torino, Corso Duca degli Abruzzi, Turin 10129, Italy;* orcid.org/0000-0002-2282-9667

Francesco Lamberti − *Department of Chemical Sciences, University of Padova, Padova 35131, Italy;* orcid.org/0000-0003-1720-8038

Giovanni Perotto − *Smart Materials, Istituto Italiano di Tecnologia, Genoa 16163, Italy;* orcid.org/0000-0001-8467-8748

Complete contact information is available at: https://pubs.acs.org/10.1021/acsaem.4c00417

Notes

The authors declare no competing financial interest.

■ ACKNOWLEDGMENTS

F.B., M.C., B.S., and T.G. wish to thank the financial support of the European Commission through the H2020 FET-PROACTIVE-EIC-07-2020 project LIGHT-CAP (project number 101017821). T.G. also acknowledge the support of the European Research Council through the project JANUS BI (project number 101041229) and of Fondazione Compagnia di San Paolo through the program "Attrazione e retention di docenti di qualità". The authors confirm that all figures in the manuscript, the supporting information, as well as the TOC graphic, were taken and created solely by Felix Boll and have never been published previously in any journal or report.

https://doi.org/10.1021/acsaem.4c00417
ACS Appl. Energy Mater. XXXX, XXX, XXX−XXX

REFERENCES

(1) Ding, Y.; Xu, W.; Wang, W.; Fong, H.; Zhu, Z. Scalable and Facile Preparation of Highly Stretchable Electrospun PEDOT:PSS@PU Fibrous Nonwovens toward Wearable Conductive Textile Applications. *ACS Appl. Mater. Interfaces* **2017**, *9* (35), 30014−30023.

(2) Jin, L.; Wang, T.; Feng, Z. Q.; Leach, M. K.; Wu, J.; Mo, S.; Jiang, Q. A Facile Approach for the Fabrication of Core-Shell PEDOT Nanofiber Mats with Superior Mechanical Properties and Biocompatibility. *J. Mater. Chem. B* **2013**, *1* (13), 1818−1825.

(3) Choi, J.; Lee, J.; Choi, J.; Jung, D.; Shim, S. E. Electrospun PEDOT:PSS/PVP Nanofibers as the Chemiresistor in Chemical Vapour Sensing. *Synth. Met.* **2010**, *160* (13−14), 1415−1421.

(4) Choi, S.; Lee, H.; Ghaffari, R.; Hyeon, T.; Kim, D. H. Recent Advances in Flexible and Stretchable Bio-Electronic Devices Integrated with Nanomaterials. *Adv. Mater.* **2016**, *28* (22), 4203−4218.

(5) Zhang, P.; Wang, F.; Yu, M.; Zhuang, X.; Feng, X. Two-Dimensional Materials for Miniaturized Energy Storage Devices: From Individual Devices to Smart Integrated Systems. *Chem. Soc. Rev.* **2018**, *47* (19), 7426−7451.

(6) Chen, H.; Xu, Y.; Zhang, J.; Wu, W.; Song, G. Enhanced Stretchable Graphene-Based Triboelectric Nanogenerator via Control of Surface Nanostructure. *Nano Energy* **2019**, *58*, 304−311.

(7) Li, Z.; Hu, K.; Li, Z.; Li, C.; Deng, Y. Polypyrrole-Stabilized Polypeptide for Eco-Friendly Supercapacitors. *Int. J. Mol. Sci.* **2023**, *24* (3), 2497.

(8) Zhou, H.; Liu, Y.; Ren, M.; Zhai, H. J. Mechanically Exfoliated Graphite Paper with Layered Microstructures for Enhancing Flexible Electrochemical Energy Storage. *Inorg. Chem. Front.* **2022**, *9* (9), 1920−1930.

(9) Liang, A.; Li, D.; Zhou, W.; Wu, Y.; Ye, G.; Wu, J.; Chang, Y.; Wang, R.; Xu, J.; Nie, G.; Hou, J.; Du, Y. Robust Flexible WS2/PEDOT:PSS Film for Use in High-Performance Miniature Supercapacitors. *J. Electroanal. Chem.* **2018**, *824*, 136−146.

(10) Tian, X.; Li, X.; Yang, T.; Wang, K.; Wang, H.; Song, Y.; Liu, Z.; Guo, Q.; Chen, C. Flexible Carbon Nanofiber Mats with Improved Graphitic Structure as Scaffolds for Efficient All-Solid-State Supercapacitor. *Electrochim. Acta* **2017**, *247*, 1060−1071.

(11) Na, W.; Jun, J.; Park, J. W.; Lee, G.; Jang, J. Highly Porous Carbon Nanofibers Co-Doped with Fluorine and Nitrogen for Outstanding Supercapacitor Performance. *J. Mater. Chem. A* **2017**, *5* (33), 17379−17387.

(12) Yu, M. F.; Lourie, O.; Dyer, M. J.; Moloni, K.; Kelly, T. F.; Ruoff, R. S. Strength and Breaking Mechanism of Multiwalled Carbon Nanotubes under Tensile Load. *Science (80-.).* **2000**, *287* (5453), 637−640.

(13) Iakunkov, A.; Skrypnychuk, V.; Nordenström, A.; Shilayeva, E. A.; Korobov, M.; Prodana, M.; Enachescu, M.; Larsson, S. H.; V.Talyzin, A. Activated Graphene as a Material for Supercapacitor Electrodes: Effects of Surface Area, Pore Size Distribution and Hydrophilicity. *Phys. Chem. Chem. Phys.* **2019**, *21* (32), 17901−17912.

(14) Sun, C.-B.; Zhong, Y.-W.; Fu, W.-J.; Zhao, Z.-Q.; Liu, J.; Ding, J.; Han, X.-P.; Deng, Y.-D.; Hu, W.-B.; Zhong, C. Tungsten Disulfide-Based Nanomaterials for Energy Conversion and Storage. *Tungsten* **2020**, *2* (2), 109−133.

(15) Liu, S.; Zeng, Y.; Zhang, M.; Xie, S.; Tong, Y.; Cheng, F.; Lu, X. Binder-Free WS2 Nanosheets with Enhanced Crystallinity as a Stable Negative Electrode for Flexible Asymmetric Supercapacitors. *J. Mater. Chem. A* **2017**, *5* (40), 21460−21466.

(16) Lyu, L.; Hooch Antink, W.; Kim, Y. S.; Kim, C. W.; Hyeon, T.; Piao, Y. Recent Development of Flexible and Stretchable Supercapacitors Using Transition Metal Compounds as Electrode Materials. *Small* **2021**, *17* (36), 1−41.

(17) Yun, Q.; Lu, Q.; Zhang, X.; Tan, C.; Zhang, H. Three-Dimensional Architectures Constructed from Transition-Metal Dichalcogenide Nanomaterials for Electrochemical Energy Storage and Conversion. *Angew. Chemie - Int. Ed.* **2018**, *57* (3), 626−646.

(18) Zeng, H.; Liu, G.-B.; Dai, J.; Yan, Y.; Zhu, B.; He, R.; Xie, L.; Xu, S.; Chen, X.; Yao, W.; Cui, X. Optical Signature of Symmetry Variations and Spin-Valley Coupling in Atomically Thin Tungsten Dichalcogenides. *Sci. Rep.* **2013**, *3*, 1608.

(19) Yang, X.; Li, J.; Hou, C.; Zhang, Q.; Li, Y.; Wang, H. Skeleton-Structure WS2@CNT Thin-Film Hybrid Electrodes for High-Performance Quasi-Solid-State Flexible Supercapacitors. *Front. Chem.* **2020**, *8* (June), 1−10.

(20) Zhang, D.; Wang, H.; Cheng, J.; Han, C.; Yang, X.; Xu, J.; Shan, G.; Zheng, G.; Cao, M. Conductive WS2-NS/CNTs Hybrids Based 3D Ultra-Thin Mesh Electromagnetic Wave Absorbers with Excellent Absorption Performance. *Appl. Surf. Sci.* **2020**, *528*, No. 147052.

(21) Boll, F.; Crisci, M.; Merola, L.; Lamberti, F.; Smarsly, B.; Gatti, T. Assessing the Effect of Stabilization and Carbonization Temperatures on Electrochemical Performance of Electrospun Carbon Nanofibers from Polyacrylonitrile. *Adv. Energy Sustain. Res.* **2023**, *4* (11), 2300121.

(22) Tan, Y.; Lin, D.; Liu, C.; Wang, W.; Kang, L.; Ran, F. Carbon Nanofibers Prepared by Electrospinning Accompanied with Phase-Separation Method for Supercapacitors: Effect of Thermal Treatment Temperature. *J. Mater. Res.* **2018**, *33* (9), 1120−1130.

(23) Biccai, S.; Barwich, S.; Boland, D.; Harvey, A.; Hanlon, D.; McEvoy, N.; Coleman, J. N. Exfoliation of 2D Materials by High Shear Mixing. *2D Mater.* **2019**, *6* (1), No. 015008.

(24) Coleman, J. N.; Lotya, M.; O'Neill, A.; Bergin, S. D.; King, P. J.; Khan, U.; Young, K.; Gaucher, A.; De, S.; Smith, R. J.; Shvets, I. V.; Arora, S. K.; Stanton, G.; Kim, H. Y.; Lee, K.; Kim, G. T.; Duesberg, G. S.; Hallam, T.; Boland, J. J.; Wang, J. J.; Donegan, J. F.; Grunlan, J. C.; Moriarty, G.; Shmeliov, A.; Nicholls, R. J.; Perkins, J. M.; Grieveson, E. M.; Theuwissen, K.; McComb, D. W.; Nellist, P. D.; Nicolosi, V. Two-Dimensional Nanosheets Produced by Liquid Exfoliation of Layered Materials. *Science* **2011**, *331* (6017), 568−571.

(25) Backes, C.; Campi, D.; Szydlowska, B. M.; Synnatschke, K.; Ojala, E.; Rashvand, F.; Harvey, A.; Griffin, A.; Sofer, Z.; Marzari, N.; Coleman, J. N.; O'Regan, D. D. Equipartition of Energy Defines the Size-Thickness Relationship in Liquid-Exfoliated Nanosheets. *ACS Nano* **2019**, *13*, 7050−7061.

(26) Griffin, A.; Nisi, K.; Pepper, J.; Harvey, A.; Szydłowska, B. M.; Coleman, J. N.; Backes, C. Effect of Surfactant Choice and Concentration on the Dimensions and Yield of Liquid-Phase-Exfoliated Nanosheets. *Chem. Mater.* **2020**, *32* (7), 2852−2862.

(27) Deitzel, J. M.; Kleinmeyer, J. D.; Hirvonen, J. K.; Beck Tan, N. C. Controlled Deposition of Electrospun Poly(Ethylene Oxide) Fibers. *Polymer (Guildf).* **2001**, *42* (19), 8163−8170.

(28) Cárdenas-Martínez, J.; España-Sánchez, B. L.; Esparza, R.; Ávila-Niño, J. A. Flexibleand Transparent Supercapacitors Using Electrospun PEDOT:PSS Electrodes. *Synth. Met.* **2020**, *267* (March), No. 116436.

(29) Schmitz, F.; Lago, N.; Fagiolari, L.; Burkhart, J.; Cester, A.; Polo, A.; Prato, M.; Meneghesso, G.; Gross, S.; Bella, F.; Lamberti, F.; Gatti, T. High Open-Circuit Voltage Cs2AgBiBr6 Carbon-Based Perovskite Solar Cells via Green Processing of Ultrasonic Spray-Coated Carbon Electrodes from Waste Tire Sources. *ChemSusChem* **2022**, *15* (22), No. e202201590.

(30) O'Connor, I.; De, S.; Coleman, J. N.; Gun'ko, Y. K. Development of Transparent, Conducting Composites by Surface Infiltration of Nanotubes into Commercial Polymer Films. *Carbon N. Y.* **2009**, *47* (8), 1983−1988.

(31) McCullen, S. D.; Stevens, D. R.; Roberts, W. A.; Ojha, S. S.; Clarke, L. I.; Gorga, R. E. Morphological, Electrical, and Mechanical Characterization of Electrospun Nanofiber Mats Containing Multiwalled Carbon Nanotubes. *Macromolecules* **2007**, *40* (4), 997−1003.

(32) Bauhofer, W.; Kovacs, J. Z. A Review and Analysis of Electrical Percolation in Carbon Nanotube Polymer Composites. *Compos. Sci. Technol.* **2009**, *69* (10), 1486−1498.

(33) Rashid, T. U.; Gorga, R. E.; Krause, W. E. Mechanical Properties of Electrospun Fibers—A Critical Review. *Adv. Eng. Mater.* **2021**, *23* (9), 1−26.

https://doi.org/10.1021/acsaem.4c00417
ACS Appl. Energy Mater. XXXX, XXX, XXX−XXX

(34) Crisci, M.; Boll, F.; Merola, L.; Pflug, J. J.; Liu, Z.; Gallego, J.; Lamberti, F.; Gatti, T. Nanostructured 2D WS2@PANI Nanohybrids for Electrochemical Energy Storage. *Front. Chem.* **2022**, *10*, 1000910.
(35) Delabie, A.; Caymax, M.; Groven, B.; Heyne, M.; Haesevoets, K.; Meersschaut, J.; Nuytten, T.; Bender, H.; Conard, T.; Verdonck, P.; Van Elshocht, S.; De Gendt, S.; Heyns, M.; Barla, K.; Radu, I.; Thean, A. Low Temperature Deposition of 2D WS2 Layers from WF6 and H2S Precursors: Impact of Reducing Agents. *Chem. Commun.* **2015**, *51* (86), 15692−15695.
(36) Sun, G.; Zhou, J.; Yu, F.; Zhang, Y.; Pang, J. H. L.; Zheng, L. Electrochemical Capacitive Properties of CNT Fibers Spun from Vertically Aligned CNT Arrays. *J. Solid State Electrochem.* **2012**, *16* (5), 1775−1780.
(37) Kriegel, I.; Ghini, M.; Bellani, S.; Zhang, K.; Jansons, A. W.; Crockett, B. M.; Koskela, K. M.; Barnard, E. S.; Penzo, E.; Hutchison, J. E.; Robinson, J. A.; Manna, L.; Borys, N. J.; Schuck, P. J. Light-Driven Permanent Charge Separation across a Hybrid Zero-Dimensional/Two-Dimensional Interface. *J. Phys. Chem. C* **2020**, *124* (14), 8000−8007.
(38) Torad, N. L.; Salunkhe, R. R.; Li, Y.; Hamoudi, H.; Imura, M.; Sakka, Y.; Hu, C. C.; Yamauchi, Y. Electric Double-Layer Capacitors Based on Highly Graphitized Nanoporous Carbons Derived from ZIF-67. *Chem. - A Eur. J.* **2014**, *20* (26), 7895−7900.
(39) Gogotsi, Y.; Penner, R. M. Energy Storage in Nanomaterials - Capacitive, Pseudocapacitive, or Battery-Like? *ACS Nano* **2018**, *12* (3), 2081−2083.
(40) Lukatskaya, M. R.; Dunn, B.; Gogotsi, Y. Multidimensional Materials and Device Architectures for Future Hybrid Energy Storage. *Nat. Commun.* **2016**, *7*, 12647.
(41) Kuc, A.; Zibouche, N.; Heine, T. Influence of Quantum Confinement on the Electronic Structure of the Transition Metal Sulfide TS2. *Phys. Rev. B - Condens. Matter Mater. Phys.* **2011**, *83* (24), 1−4.
(42) Splendiani, A.; Sun, L.; Zhang, Y.; Li, T.; Kim, J.; Chim, C. Y.; Galli, G.; Wang, F. Emerging Photoluminescence in Monolayer MoS2. *Nano Lett.* **2010**, *10* (4), 1271−1275.
(43) Berkdemir, A.; Gutiérrez, H. R.; Botello-Méndez, A. R.; Perea-López, N.; Elías, A. L.; Chia, C. I.; Wang, B.; Crespi, V. H.; López-Urías, F.; Charlier, J. C.; Terrones, H.; Terrones, M. Identification of Individual and Few Layers of WS2 Using Raman Spectroscopy. *Sci. Rep.* **2013**, *3*, 1−8.
(44) Abdelkader, A. M.; Kinloch, I. A. Mechanochemical Exfoliation of 2D Crystals in Deep Eutectic Solvents. *ACS Sustain. Chem. Eng.* **2016**, *4* (8), 4465−4472.
(45) Sourisseau, C.; Cruege, F.; Fouassier, M.; Alba, M. Second-Order Raman Effects, Inelastic Neutron Scattering and Lattice Dynamics in 2H-WS2. *Chem. Phys.* **1991**, *150* (2), 281−293.
(46) Gutiérrez, H. R.; Perea-López, N.; Elías, A. L.; Berkdemir, A.; Wang, B.; Lv, R.; López-Urías, F.; Crespi, V. H.; Terrones, H.; Terrones, M. Extraordinary Room-Temperature Photoluminescence in Triangular WS 2 Monolayers. *Nano Lett.* **2013**, *13* (8), 3447−3454.
(47) Zhang, H.-B.; Lin, G.-D.; Zhou, Z.-H.; Dong, X.; Chen, T. Raman Spectra of MWCNTs and MWCNT-Based H2-Adsorbing System. *Carbon* **2002**, *40* (13), 2429−2436.
(48) Eklund, P. C.; Holden, J. M.; Jishi, R. A. Vibrational Modes of Carbon Nanotubes; Spectroscopy and Theory. *Carbon N. Y.* **1995**, *33* (7), 959−972.
(49) Dresselhaus, M. S.; Dresselhaus, G.; Saito, R.; Jorio, A. Raman Spectroscopy of Carbon Nanotubes. *Phys. Rep.* **2005**, *409* (2), 47−99.
(50) Langford, J. I.; Wilson, A. J. C. Scherrer after Sixty Years: A Survey and Some New Results in the Determination of Crystallite Size. *J. Appl. Cryst.* **1977**, *11*, 102−113.
(51) Monshi, A.; Foroughi, M. R.; Monshi, M. R. Modified Scherrer Equation to Estimate More Accurately Nano-Crystallite Size Using XRD. *World J. Nano Sci. Eng.* **2012**, *02* (03), 154−160.
(52) Gharbi, O.; Tran, M. T. T.; Tribollet, B.; Turmine, M.; Vivier, V. Revisiting Cyclic Voltammetry and Electrochemical Impedance Spectroscopy Analysis for Capacitance Measurements. *Electrochim. Acta* **2020**, *343*, No. 136109.
(53) Simotwo, S. K.; Delre, C.; Kalra, V. Supercapacitor Electrodes Based on High-Purity Electrospun Polyaniline and Polyaniline-Carbon Nanotube Nanofibers. *ACS Appl. Mater. Interfaces* **2016**, *8* (33), 21261−21269.
(54) Rountree, K. J.; Mccarthy, B. D.; Rountree, E. S.; Eisenhart, T. T.; Dempsey, J. L. A Practical Beginner ' s Guide to Cyclic Voltammetry. *J. Chem. Educ.* **2017**, *95*, 197.
(55) Kumar, P.; Vasita, R. Understanding the Relation between Structural and Mechanical Properties of Electrospun Fiber Mesh through Uniaxial Tensile Testing. *J. Appl. Polym. Sci.* **2017**, *134* (26), 45012.
(56) Wenelska, K.; Maślana, K.; Mijowska, E. Study on the Flammability, Thermal Stability and Diffusivity of Polyethylene Nanocomposites Containing Few Layered Tungsten Disulfide (WS2) Functionalized with Metal Oxides. *RSC Adv.* **2018**, *8* (23), 12999−13007.
(57) Portet, C.; Yushin, G.; Gogotsi, Y. Electrochemical Performance of Carbon Onions, Nanodiamonds, Carbon Black and Multiwalled Nanotubes in Electrical Double Layer Capacitors. *Carbon N. Y.* **2007**, *45* (13), 2511−2518.
(58) Alcántara, R.; Jiménez-Mateos, J. M.; Lavela, P.; Tirado, J. L. Carbon Black: A Promising Electrode Material for Sodium-Ion Batteries. *Electrochem. commun.* **2001**, *3* (11), 639−642.
(59) Fransson, L.; Eriksson, T.; Edström, K.; Gustafsson, T.; Thomas, J. O. Influence of Carbon Black and Binder on Li-Ion Batteries. *J. Power Sources* **2001**, *101* (1), 1−9.
(60) Shao, M.; Ning, F.; Zhao, Y.; Zhao, J.; Wei, M.; Evans, D. G.; Duan, X. Core-Shell Layered Double Hydroxide Microspheres with Tunable Interior Architecture for Supercapacitors. *Chem. Mater.* **2012**, *24* (6), 1192−1197.
(61) Gao, Z.; Wang, J.; Li, Z.; Yang, W.; Wang, B.; Hou, M.; He, Y.; Liu, Q.; Mann, T.; Yang, P.; Zhang, M.; Liu, L. Graphene Nanosheet/Ni2+/Al3+ Layered Double-Hydroxide Composite as a Novel Electrode for a Supercapacitor. *Chem. Mater.* **2011**, *23* (15), 3509−3516.
(62) Zhou, L.; Xing, L.; Zheng, Y.; Lai, X.; Su, J.; Deng, C.; Sun, T. A Study of External Surface Pressure Effects on the Properties for Lithium-Ion Pouch Cells. *Int. J. Energy Res.* **2020**, *44* (8), 6778−6791.
(63) Lamberti, A.; Perrucci, F.; Caprioli, M.; Serrapede, M.; Fontana, M.; Bianco, S.; Ferrero, S.; Tresso, E. New Insights on Laser-Induced Graphene Electrodes for Flexible Supercapacitors: Tunable Morphology and Physical Properties. *Nanotechnology* **2017**, *28* (17), 174002.
(64) Sun, G.; Zhang, X.; Lin, R.; Yang, J.; Zhang, H.; Chen, P. Hybrid Fibers Made of Molybdenum Disulfide, Reduced Graphene Oxide, and Multi-Walled Carbon Nanotubes for Solid-State, Flexible, Asymmetric Supercapacitors. *Angew. Chemie - Int. Ed.* **2015**, *54* (15), 4651−4656.

https://doi.org/10.1021/acsaem.4c00417
ACS Appl. Energy Mater. XXXX, XXX, XXX−XXX

3.4.1. Supporting Information – Publication 2

Supporting Information for:

Multicomponent synergistic contribution in nano-engineered nano-fibers for flexible energy storage

Felix Boll,[1,2] Marta Fadda,[3] Melissa Happel,[1,2] Matteo Crisci,[1,2] Athanassia Athanassiou,[3] Bernd Smarsly,[1,2] Federico Bella,[4] Francesco Lamberti,[5] Giovanni Perotto,[3] Teresa Gatti[1,2,4*]

[1] Institute of Physical Chemistry, Justus Liebig University, Heinrich-Buff-Ring 17, 35392 Giessen, Germany

[2] Center for Materials Research, Justus Liebig University, Heinrich-Buff-Ring 17, 35392 Giessen, Germany

[3] Smart Materials, Istituto Italiano di Tecnologia, via Morego 30, 16163 Genoa, Italy

[4] Department of Applied Science and Technology, Politecnico di Torino, Corso Duca degli Abruzzi, 10129 Turin, Italy

[5] Department of Chemical Sciences, University of Padova, via Marzolo 1, 35131 Padova, Italy

* E-mail: teresa.gatti@polito.it

Table of Contents

- CV scans on fibrous materials at the optimized additive concentrations at different scan rates (**Figure S9**)
- Ferrocene redox reaction in 0.5 M $TEABF_4$/PC electrolyte (**Figure S10**)
- Values of all calculated C_s from the CV curves at different scan rates shown in **Figures 2**, **4b** and **S15** (**Table S1**)
- Conductivity measurements done on pellets of fibrous mats (**Figure S11**)
- Dependency of stress-strain curves from the position on the fiber mat shown for fibrous mats of the PEO-WS_2 composite material (**Figure S12**)
- Thermogravimetric analysis of all produced fiber samples (**Figure S13**)
- Schematic of the Swagelok-cell PEIS measurements on CB-PTFE mats with the corresponding Randles' circuit. (**Figure S14**)
- Values, error-values, and error in percentage for the serial resistance, charge transfer resistance, and double layer capacitance calculated from the PEIS measurements of the DB-PTFE mats (**Table S2**)
- C_s from CV curves using pouch cells of CB-PTFE current collector and the composite with ternary fibers in a symmetrical supercapacitor configuration (**Figure S15**)
- C_s retention tests carried out using galvanostatic charge-discharge cycles on a pouch cell at 50 mA g^{-1} for 3000 cycles. (**Figure S16**)

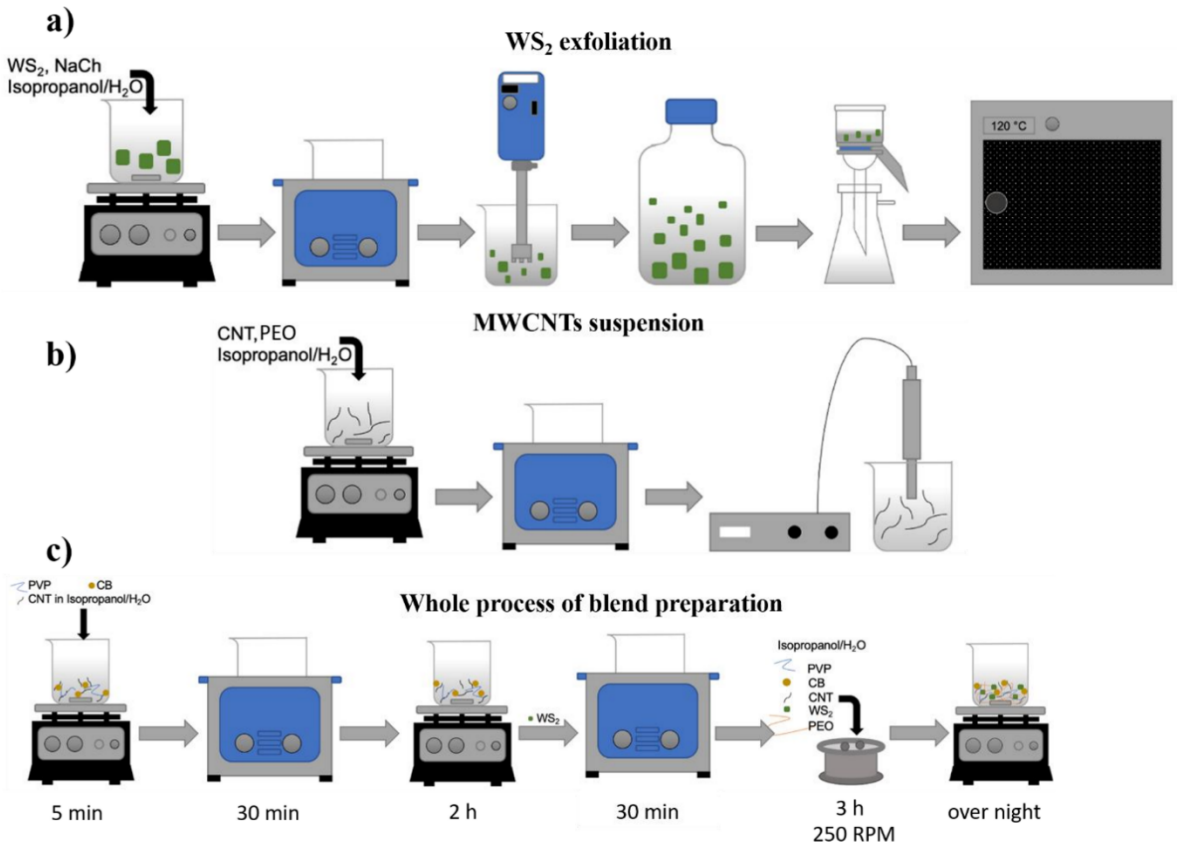

Figure S1. a) Schematic description of the WS_2 exfoliation process. **b)** Schematic description of the MWCNTs suspension preparation. **c)** Schematic of ternary blend production. See methods section for details.

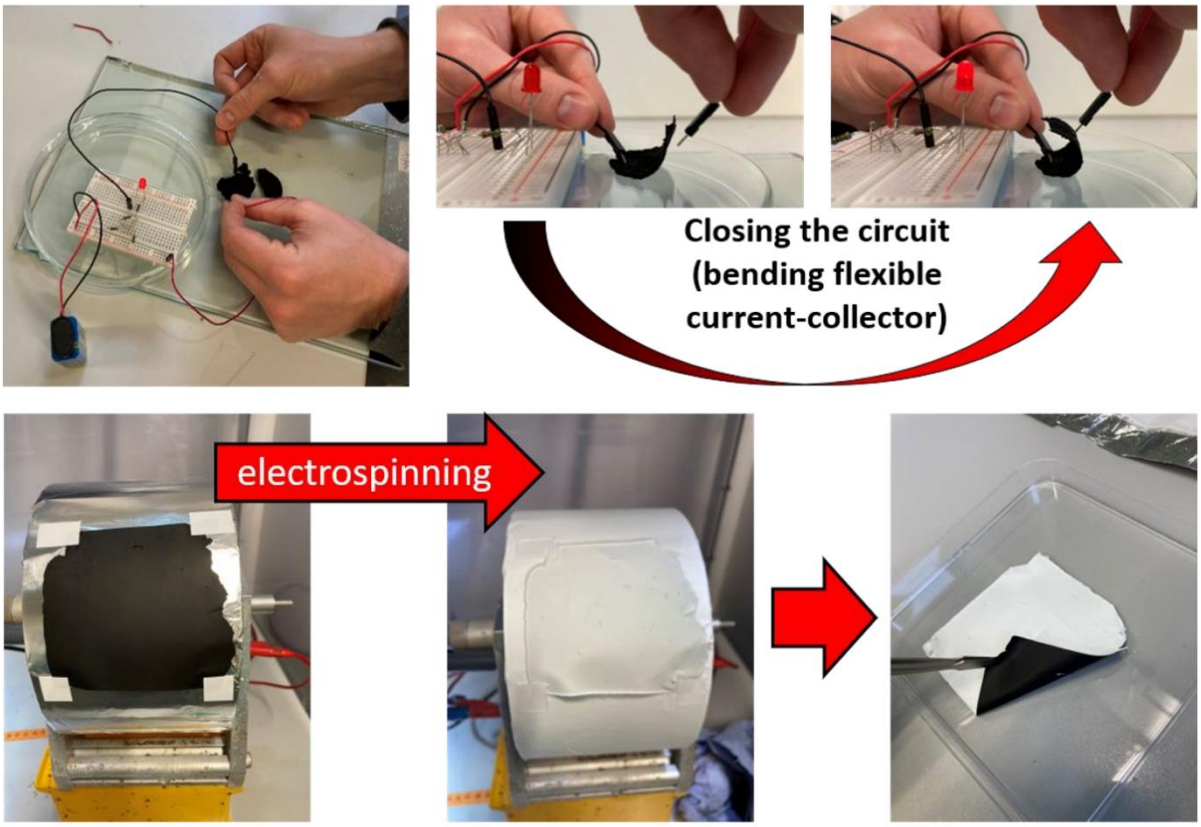

Figure S2. Current collector sheets made from CB and PTFE. Conductivity was proven by building a circuit to run an LED where the CB current collector was connected in series. These mats are directly electrospun, as it can be seen in the bottom images, without losing the flexible character (bottom right). For reasons of visibility (since fibers and current collector material both have a greyish/black appearance), pure PEO fibers with a white appearance were used to show the adhesion between fibers and current collector.

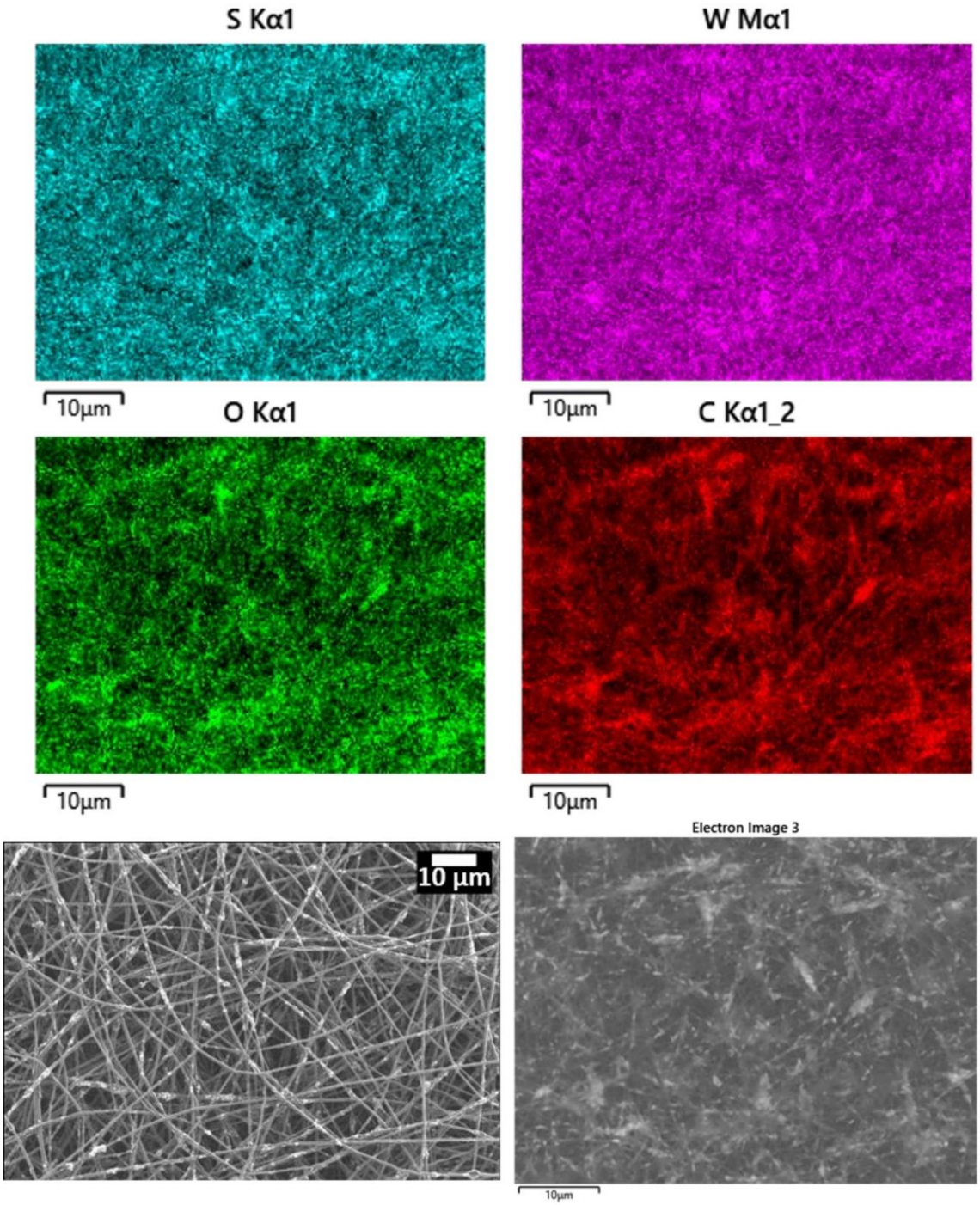

Figure S3. EDS images of S, W, O, and C distributions on the ternary blend-based fibers proving the well-distributed 2D WS_2 particles within the fibrous network, the SEM micrographs of which are also shown.

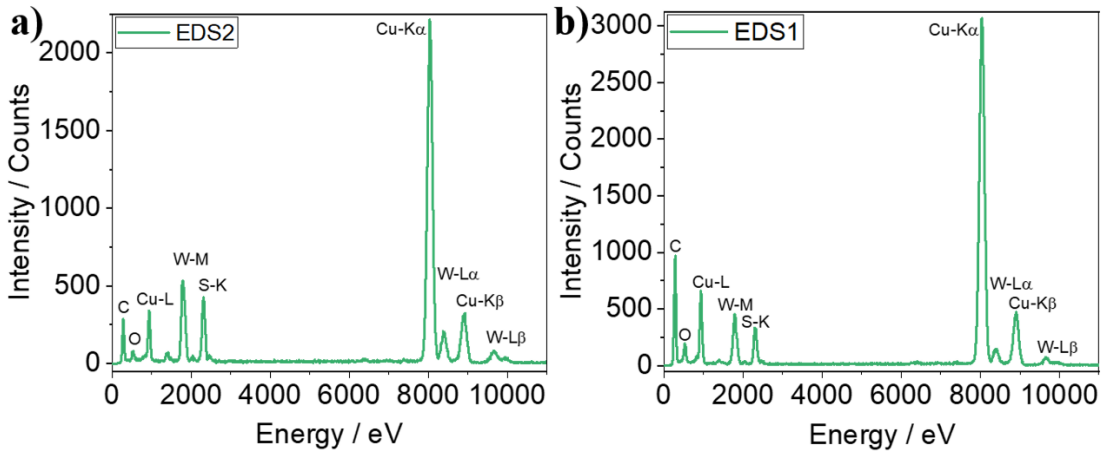

Figure S4. EDS measurements from STEM image for the two different particles shown in **Figure 1d** in the range from 0–11000 eV. EDS1 (b) is a carbon-based particle, while EDS2 (a) is ascribed to an agglomerate of WS_2 single sheets.

Raman analysis of the composite nanofibers

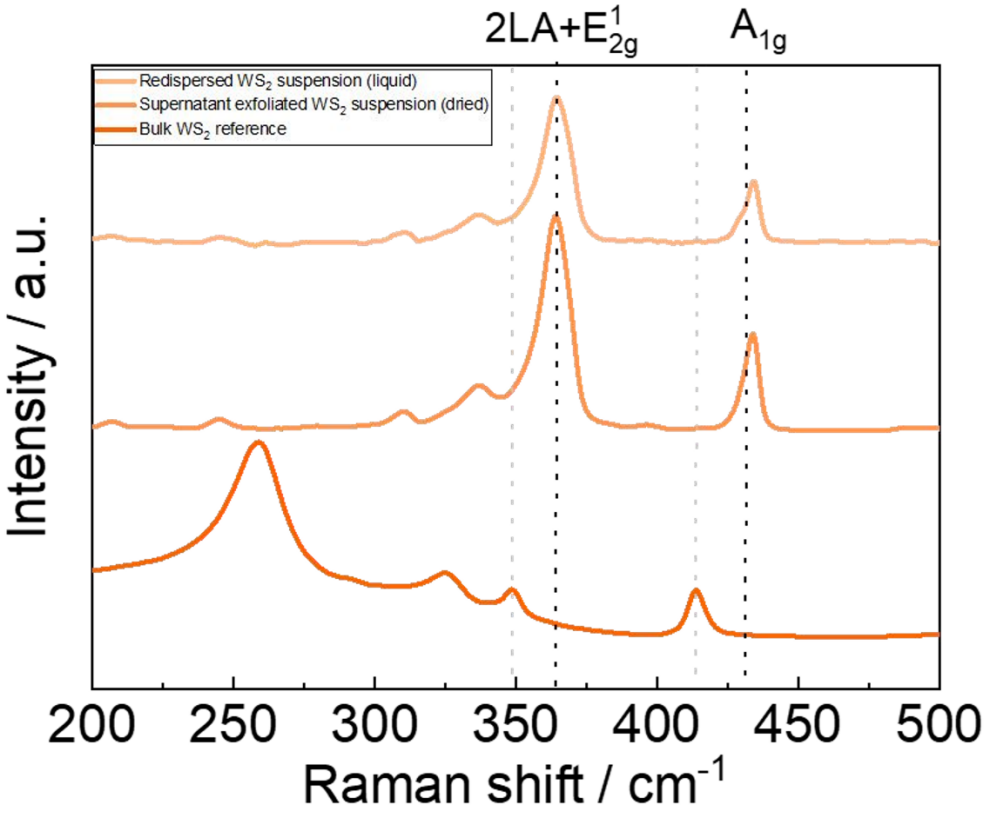

Figure S5. Raman spectra of the bulk WS_2 reference, the LPE dried powder, and the re-dispersed powder with focus on the 2LA+E^1_{2g} and A_{1g} peaks.

At 514.5 nm Raman peaks of second order increase in their intensity by lowering the number of layers in the bidimensional materials. From group theory, derived attributions for vibrational modes of $2LA(M)$ (second order), ${E_2}^1{}_g$ (first order), and A_{1g} (first order) describe the first order modes of A_{1g} and ${E_2}^1{}_g$. They represent the vibrational modes out of the plane of tungsten and sulfur, as well as within the W-S plane.[1,2] The longitudinal acoustic mode $2LA(M)$ was identified as a zone-edge mode, activated due to disorder in the system and propagating as a collective movement of the atoms along the in-plane direction.[3–5] This means that second-order Raman peaks, especially the $2LA(M)$, increase their intensity compared to the bulk when the number of layers is lowered, reaching a maximum for monolayers. Additional Raman modes are ascribed to the following wavenumbers: 235.7 cm^{-1} ($A_{1g} - LA$), 299.5 cm^{-1} ($2LA - 2{E_2}^2{}_g$), 327.2 cm^{1} ($2LA - {E_2}^2{}_g$), 524.3 cm^{-1} (${E_2}^1{}_g + LA$), 585.3 cm^{-1} ($A_{1g} + LA$).[1,3] However, second-order Raman modes, and especially the longitudinal phonons, experience a drastic increase in intensity when WS_2 is exfoliated as it is in the presented fibers. For this reason and because the ${E_2}^2{}_g$ and E_{1g} modes are energetically inhibited by following the forbidden selection rule in the

back-scattering geometry, characterization is done only by considering the below-described ratio in **Figure S6**.

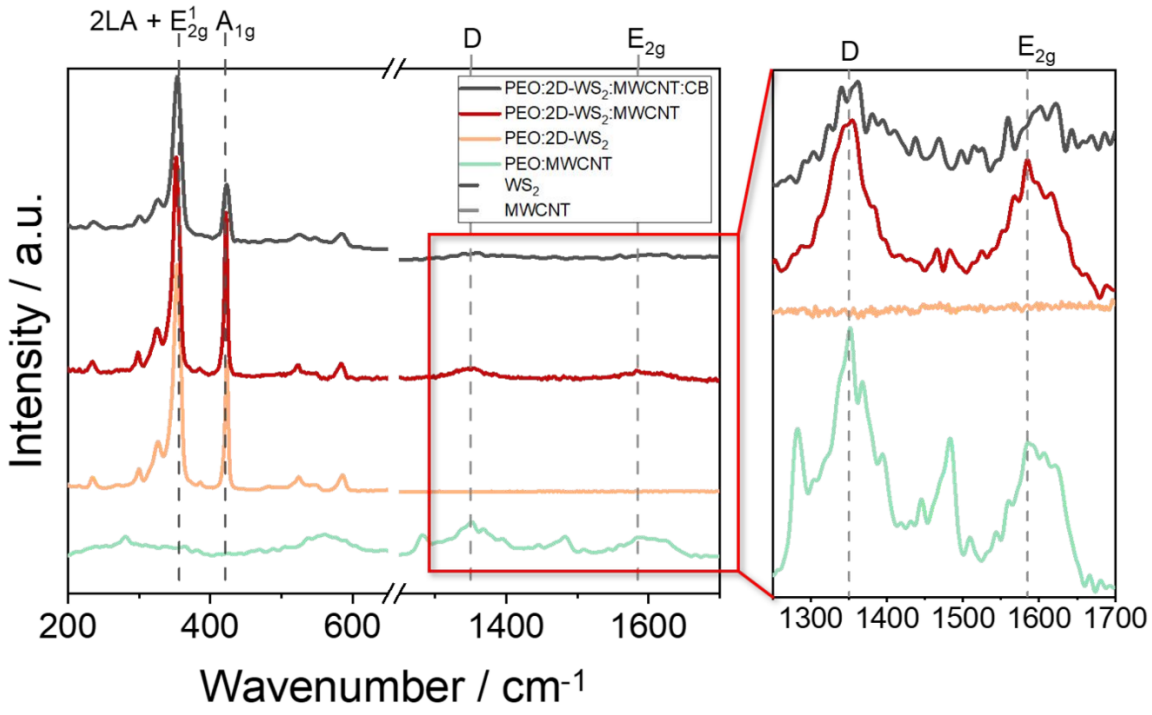

Figure S6. Raman spectra of various fibrous materials, starting from PEO-MWCNTs (light green), PEO-2D-WS_2 (light orange), PEO-2D-WS_2-MWCNTs (dark red) and PEO-2D-WS_2-MWCNTs-CB (black). The spectra focus on the range 200 – 600 cm^{-1}, to probe the presence of WS_2, as well as on the range 1250 – 1700 cm^{-1}, to detect MWCNTs and CB. The black dashed lines indicate the positions of the $2LA + E_2{}^1{}_g$ and the A_{1g} bands for identifying the quality of incorporated 2D-WS_2. The grey dashed lines show the positions of the D band (1352 cm^{-1}) and the E_{2g}-band (1585 cm^{-1}), caused by the graphitic structure, magnified in the inset on the right side.

XRD analysis

Figure S7 displays the XRD patterns of all different PEO-based nanofibers that were produced from the prepared blends. PEO fibers naturally show a certain crystallinity after the electrospinning process, which is seen throughout all different samples. By using the Scherrer equation with a K factor of 0.9 (ascribed to the assumption of spherical crystallites) and the reflex position at 19.15°, the crystallite size was calculated to be 0.259 nm for PEO with a maximum deviation of 0.058 nm, which corresponds to 22%.[6,7] In 2001, Deitzel et al. ascribed the reflexes (indicated as the red dots) directly to the crystalline phase of PEO Since no heat

treatment is applied to the fibers due to the low melting point of PEO, it is understandable that no large crystallites are produced during the electro-spinning process. However, neither ball milling nor the addition of differing kinds of particles into blends affects the crystallization and crystallite sizes of the PEO electrospun fibers.

Comparing the larger relative intensities of WS_2 to the PEO reflexes, there is no doubt that crystalline WS_2 is present in the fibers based on the 2D-WS_2-containing blends (indicated by the blue rectangles in **Figure S7**). The (002) reflex at 14.3° (d_{002} = 1.01053 Å) from the reference is the most prominent reflex for the 2H-phase of the TMD. No side phases, such as WO_3 or 1T-WS_2, were produced during exfoliation and fiber-spinning. In the case of WS_2, the exfoliation might affect the reflex position and, further, the d-spacing of layers. The deviation of the reflex positions for all samples corresponds, compared to the reference, to d-spacing differences from 0.0051% to 0.8447%. The exfoliation of bulk WS_2, dissolved in suspensions and finally electrospun, therefore, did not affect the distance of the d_{002} plane of the 2H-WS_2 phase and no phase transitions were observed.

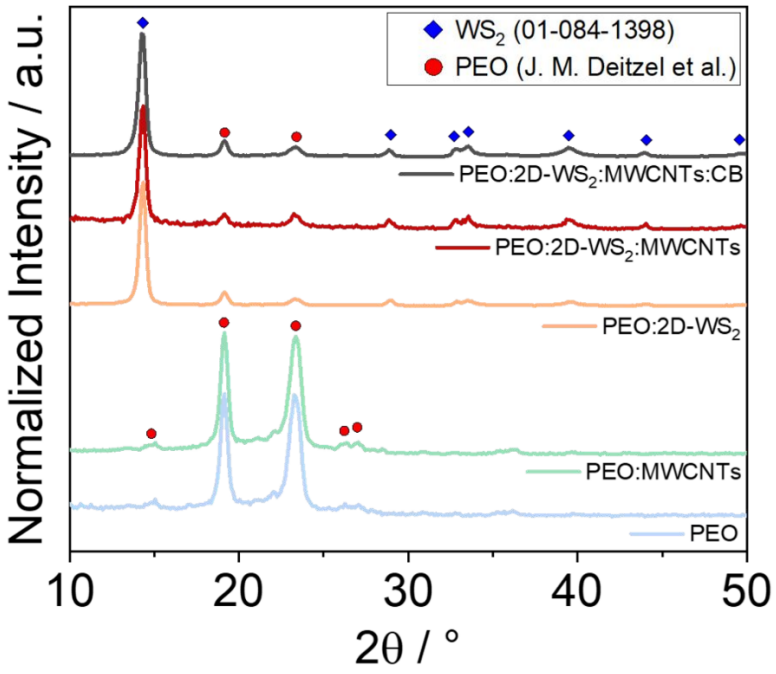

Figure S7. Normalized X-ray diffraction patterns of all produced fibrous samples: PEO (light blue), PEO-MWCNTs (light green), PEO-2D-WS_2 (light orange), PEO-2D-WS_2-MWCNTs (dark red), and PEO-2D-WS_2-MWCNTs-CB (black). The reflexes can be ascribed to PEO (red dots), as it was observed by Deitzel et al.[8], and WS_2 (blue rectangles).

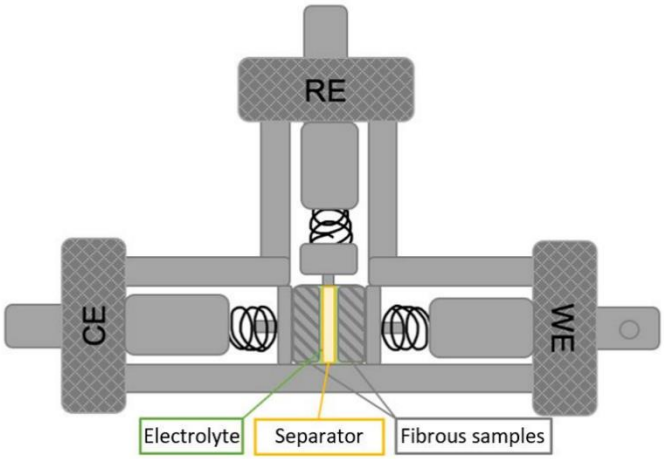

Figure S8. Schematic of the Swagelok-type cell used for characterizing the layers of fibrous materials in symmetric configuration separated by a Whatman SiO_2-fiber membrane using a PC solution with 0.5 M $TEABF_4$ as electrolyte.

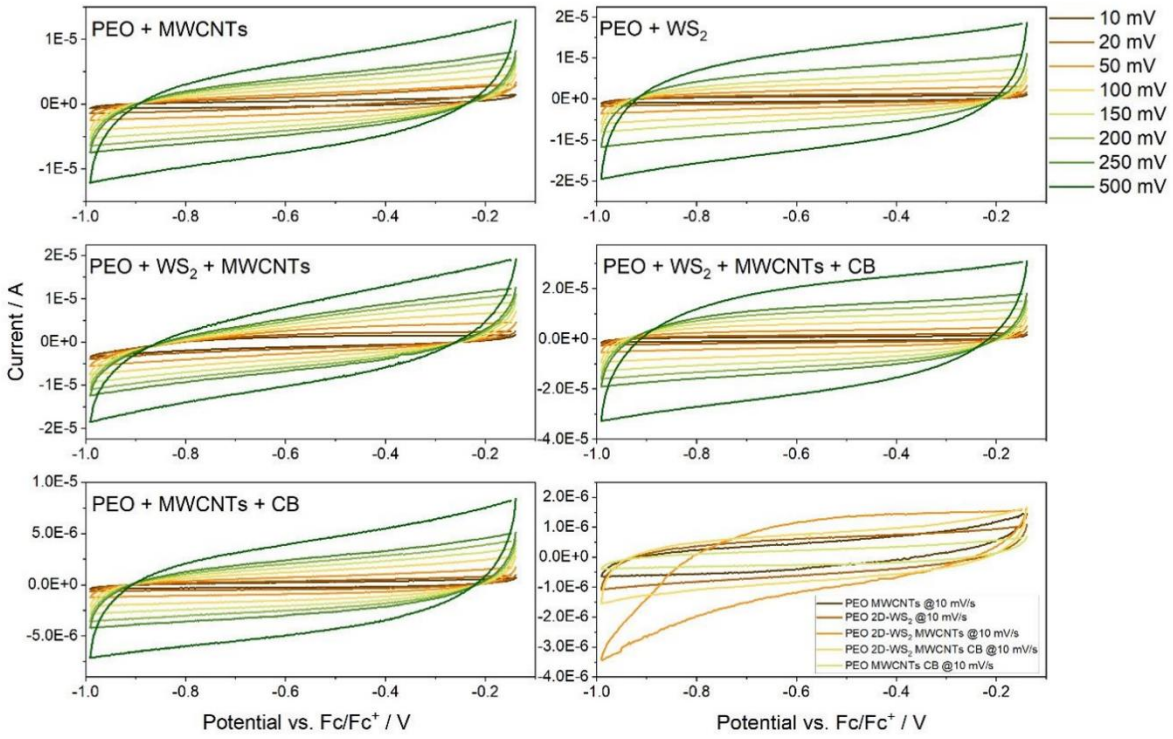

Figure S9. CV curves of the optimized additive concentrations and their mixtures used for calculating the C_s values shown in **Figure 2(a-e)**. The potential vs the Fc/Fc^+ couple (0.74 V) can be deduced from **Figure S10**. The masses for calculations of the specific capacitance were as following: m(PEO + MWCNTs) = 2.65 mg, m(PEO + WS_2) = 5.28 mg, m(PEO + WS_2 +

MWCNTs) = 4.3 mg, m(PEO + MWCNTs + CB) = 4.98 mg, m(PEO + WS_2 + MWCNTs + CB) = 1.44 mg.

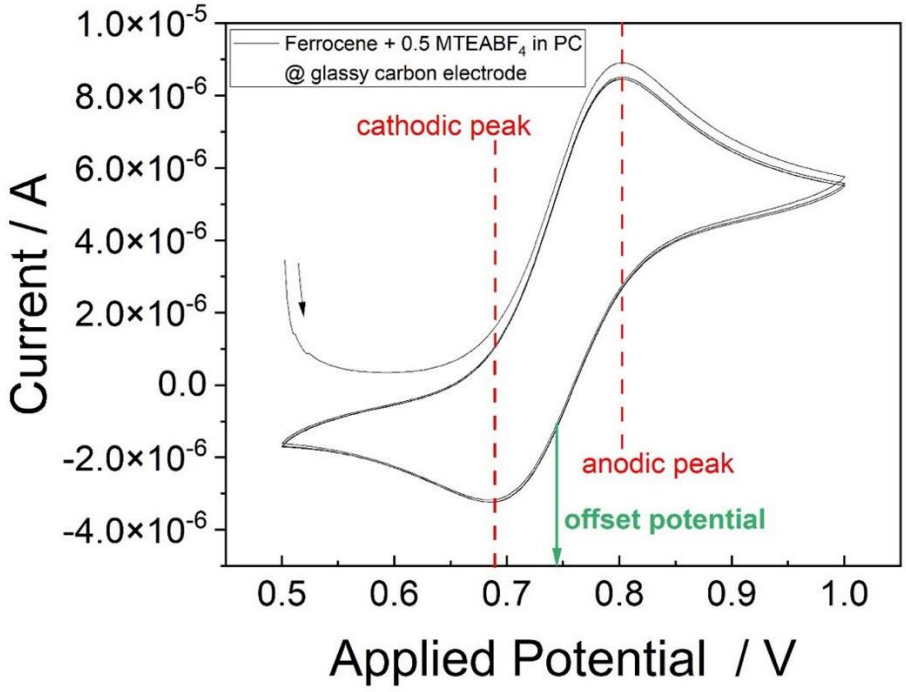

Figure S10. Ferrocene redox reaction for the used electrolyte.

Table S1. Values of all calculated C_s from the CV curves at different scan rates shown in **Figures 2**, **4**, and **S15**.

Sample	C_s @ 10 mV/s / F/g	C_s @ 20 mV/s / F/g	C_s @ 50 mV/s / F/g	C_s @ 100 mV/s / F/g	C_s @ 150 mV/s / F/g	C_s @ 200 mV/s / F/g	C_s @ 250 mV/s / F/g	C_s @ 500 mV/s / F/g
CB-PTFE Current Collector	0.49	0.243	0.090	0.032	0.015	0.009	0.006	0.003
CB-PTFE CC & ternary fibers	3.535	1.628	0.426	0.137	0.069	0.042	0.029	0.014
bended	12.019	10.646	7.150	3.572	4.374	3.302	2.568	1.049
Flattened	8.992	8.012	5.892	4.216	2.995	2.191	1.653	0.594
again								

	C_s @ 10 mV/s / mF/g	C_s @ 20 mV/s / mF/g	C_s @ 50 mV/s / mF/g	C_s @ 100 mV/s / mF/g	C_s @ 150 mV/s / mF/g	C_s @ 200 mV/s / mF/g	C_s @ 250 mV/s / mF/g	C_s @ 500 mV/s / mF/g

PEO-WS_2-MWCNTs-CB fibers	101.15	93.12	84.15	75.21	69.41	64.89	61.30	49.84
PEO-WS_2-MWCNTs-fibers	42.05	29.57	19.96	14.28	12.17	10.78	9.79	7.39
PEO–WS_2 12.5 mg/mL	20.06	16.76	13.88	11.88	10.80	10.05	9.50	7.96
PEO–WS_2 25.0 mg/mL	8.69	7.75	6.92	6.36	6.07	5.88	5.72	5.22
PEO–WS_2 37.5 mg/mL	12.24	10.32	8.47	7.19	6.41	5.96	5.61	4.61
PEO–MWCNTs 0.5 mg/mL	67.00	62.25	54.40	48.30	44.45	41.74	39.23	32.01
PEO–MWCNTs 1.0 mg/mL	8.03	6.61	3,50	2.51	2.11	1.85	1.68	1.27
PEO–MWCNTs 1.5 mg/mL	22.22	19.60	15.56	12.27	10.86	9.72	8.91	7.53

Cycle / No. @ 10 mV s^{-1}	Pristine	1	2	3	4	5	6	7	8	9	10
Pristine/ F g^{-1}	7.41										
Bent/ F g^{-1}		14.35	9.17	9.18	11.27	11.62	9.27	9.05	8.16	7.77	7.96
Flat/ F g^{-1}		6.38	3.98	6.01	5.86	5.54	5.76	5.43	5.64	5.69	5.66

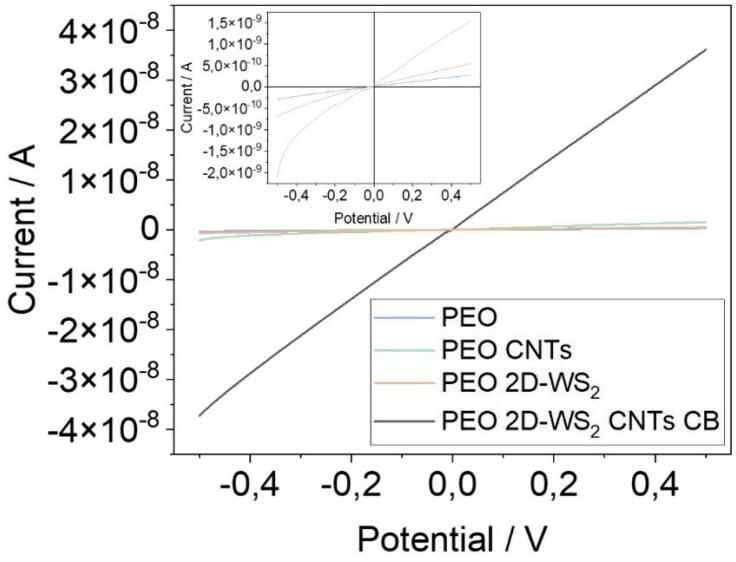

S12

Figure S2. Conductivity measurements done on pellets which were pressed out of large fiber mats. For contacting, a mask was used to place two silver-paste contacts in an equidistant position for all samples to ensure comparability.

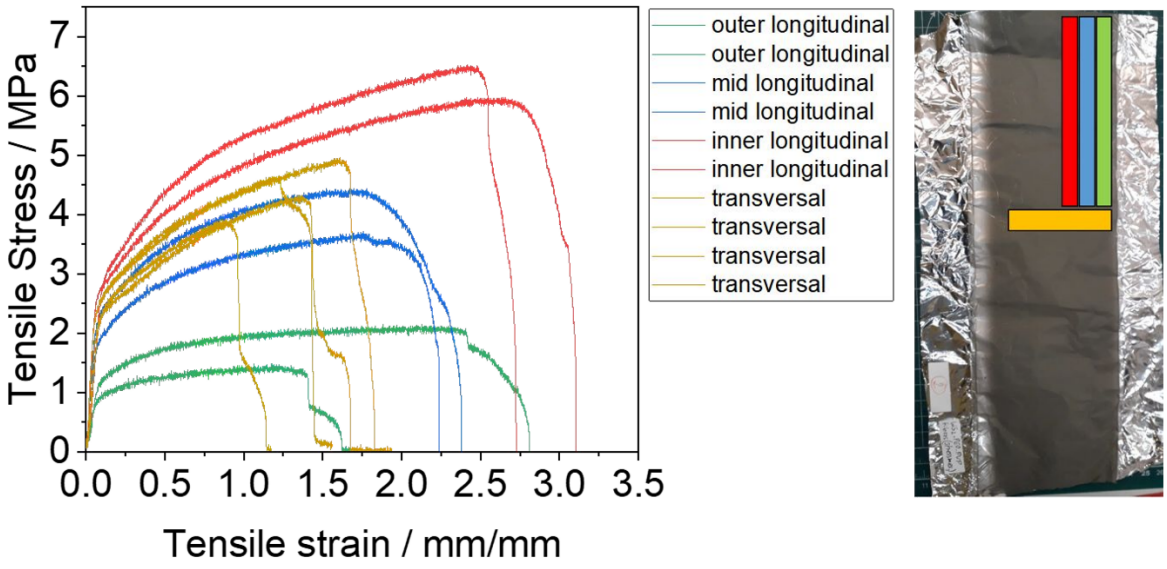

Figure S3. Dependency of stress-strain curves on position on the fibrous mat for the PEO-WS_2 composite material. The colors depict the positions on the right side where single samples for the stress-strain measurement were taken. Green curves (outer longitudinal) were obtained from fibers at the edge of the mat. The blue curves (mid longitudinal) were taken closer to the edge and the red curves (inner longitudinal) were directly taken from the center of the mat. The yellow curves (transversal) show observed values for samples taken transversal to the motion of rotation of the drum roll collector.

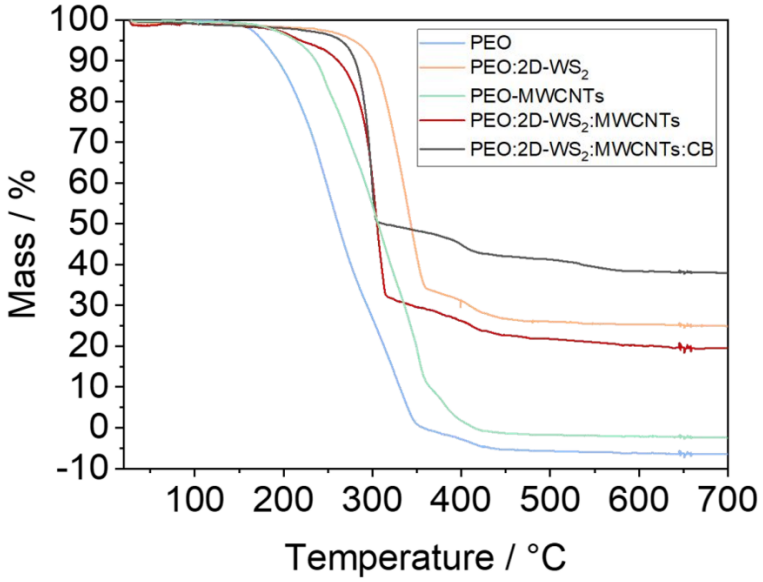

Figure S4. TGA of all produced fiber samples from room temperature up to 700 °C with a heating rate of 2 K min^{-1}.

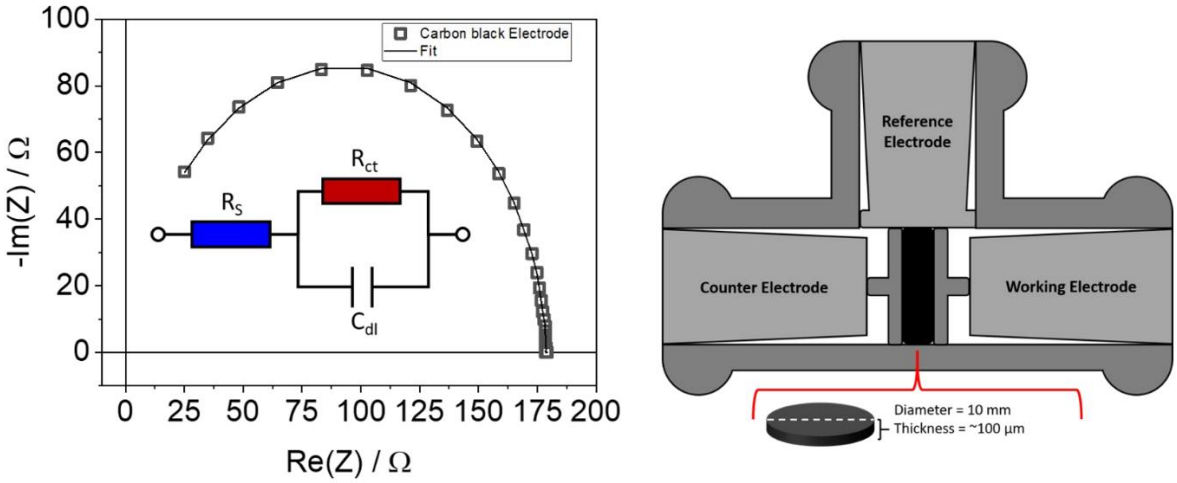

Figure S5. PEIS measurement carried out in a Swagelok cell for a single current collector (CB + PTFE) sheet and relative fitting using the Randles circuit shown in the diagram. On the right side, the schematic of the cell is shown.

Table S2. Values, error-values and error in percentage for the series resistance (R_s), the charge transfer resistance (R_{ct}), and the double layer capacitance (C_{dl}) from the fitted Randles' circuit (see **Figure S14**) for two different samples.

Sample	R_s / Ω	R_{ct} / Ω	C_{dl} / nF
PEIS2	6.94 ± 0.18 (2.57%)	171.67 ± 0.18 (0.10%)	2.6154 ± 0.0064 (0.25%)
PEIS3	6.06 ± 0.20 (3.32%)	172.43 ± 0.21 (0.12%)	2.5981 ± 0.0079 (0.30%)

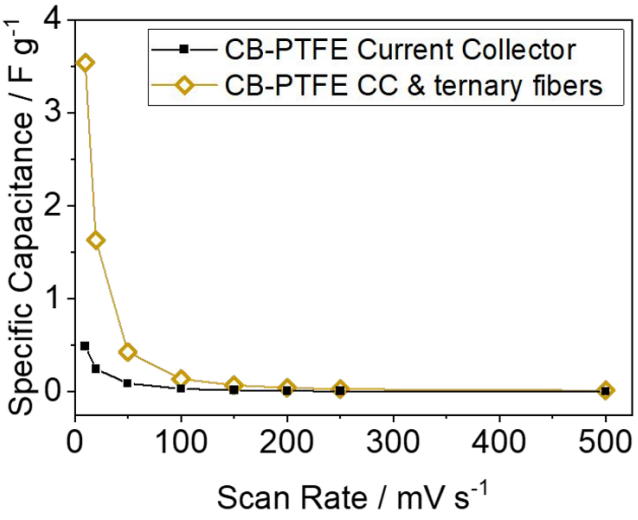

Figure S6. C_s from CV curves using pouch cells at different scan rates from 10 mV/s up to 500 mV/s in the range from -0.25 V to 0.6 V. The plain current collector (black) and the current collector with the on-top electrospun ternary blend-based fiber composite (yellow) are both displayed. 120 µL of electrolyte were used for the pouch cell preparation and the cells were closed using a vacuum sealer. (see methods section and **Figure 4a** for details).

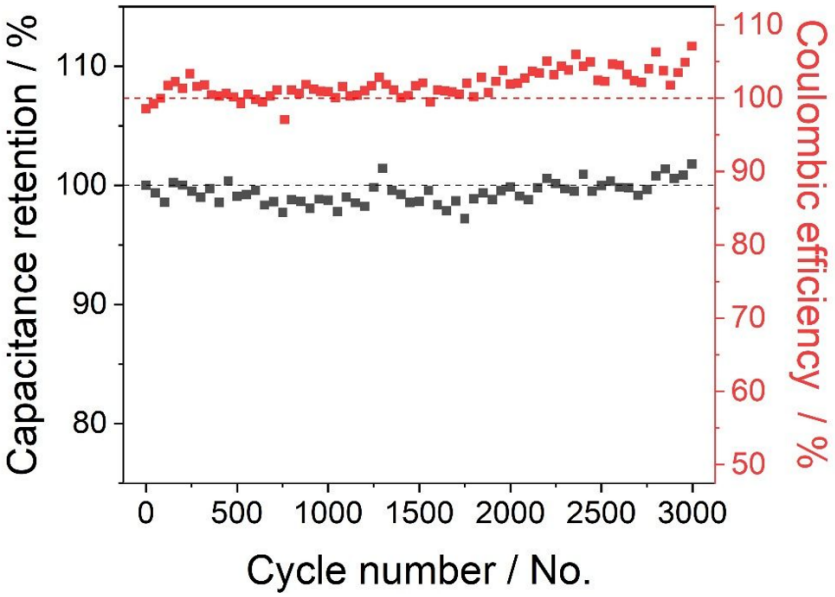

Figure S26. Galvanostatic charge-discharge cycles performed on a pouch cell at 50 mA g^{-1} for 3000 cycles. From the cycling test, the C_s retention (black-axis) and the coulombic efficiency (red-axis) were calculated. The dotted lines show the position of 100 % retention and efficiency.

References

(1) Zhang, X.; Qiao, X. F.; Shi, W.; Wu, J. Bin; Jiang, D. S.; Tan, P. H. Phonon and Raman Scattering of Two-Dimensional Transition Metal Dichalcogenides from Monolayer, Multilayer to Bulk Material. *Chem. Soc. Rev.* **2015**, *44* (9), 2757–2785. https://doi.org/10.1039/c4cs00282b.

(2) Zhao, W.; Ghorannevis, Z.; Amara, K. K.; Pang, J. R.; Toh, M.; Zhang, X.; Kloc, C.; Tan, P. H.; Eda, G. Lattice Dynamics in Mono- and Few-Layer Sheets of WS2 and WSe2. *Nanoscale* **2013**, *5* (20), 9677–9683. https://doi.org/10.1039/c3nr03052k.

(3) Sourisseau, C.; Cruege, F.; Fouassier, M.; Alba, M. Second-Order Raman Effects, Inelastic Neutron Scattering and Lattice Dynamics in 2H-WS2. *Chem. Phys.* **1991**, *150* (2), 281–293. https://doi.org/10.1016/0301-0104(91)80136-6.

(4) Stacy, A. M.; Hodul, D. T. Raman Spectra of IVB and VIB Transition Metal Disulfides Using Laser Energies near the Absorption Edges. *J. Phys. Chem. Solids* **1985**, *46* (4), 405–409. https://doi.org/10.1016/0022-3697(85)90103-9.

(5) Frey, G. L.; Tenne, R. Optical Properties of MS2 (M 5 Mo, W) Inorganic Fullerene- like and Nanotube Material Optical Absorption and Resonance Raman Measurements. *J. Mater. Res.* **1998**, *13* (9), 2412–2417.

(6) Langford, J. I.; Wilson, A. J. . C. Scherrer after Sixty Years: A Survey and Some New Results in the Determination of Crystallite Size. *J. Appl. Cryst. (1978).* **1977**, *11*, 102–113.

(7) Monshi, A.; Foroughi, M. R.; Monshi, M. R. Modified Scherrer Equation to Estimate More Accurately Nano-Crystallite Size Using XRD. *World J. Nano Sci. Eng.* **2012**, *02* (03), 154–160. https://doi.org/10.4236/wjnse.2012.23020.

(8) Deitzel, J. M.; Kleinmeyer, J. D.; Hirvonen, J. K.; Beck Tan, N. C. Controlled Deposition of Electrospun Poly(Ethylene Oxide) Fibers. *Polymer* **2001**, *42* (19), 8163–8170. https://doi.org/10.1016/S0032-3861(01)00336-6.

3.5. Publication 3

This publication is related to the top-down approach of producing monolayered and few-layered transition metal dichalcogenides and joins the ranks with the following publications (**publication 4** and **publication 5**). As a recap, it is essential to recognize the potential impact that TMDCs could have on the future of nanoscale electronics. The significance of these materials became evident in 2004 when Novoselov and Geim successfully produced monolayers of graphite, known as graphene, and demonstrated its exceptional conductive properties for electric currents.[13,22,23] From there on the scientific community quickly went on to the idea of single-layered semiconductors for transistor applications.[35,49] TMDCs were considered to be sufficient choices for monolayered materials based on the chemical structure having weak VdW-interactions between stacked layers instead of chemical bonds.[12,14,30,33] To obtain the monolayered material both top-down and bottom-up approaches can be employed. Bottom-up approaches like CVD typically yield higher quality, producing perfect triangular monolayers of MoS_2 or WS_2.[228,229] However, the top-down approach is more cost-effective, sustainable and scalable. Here, shear forces are used to exfoliate monolayers from the bulk material.[14,67,230] Normally, NMP is used as a solvent but in order to follow a sustainable approach we chose water-based LPE methods instead.[14,223] To increase the yield and concentration of 2D material the exfoliation process is supported by adding surfactants into TMDC-H_2O suspensions.[12,14,55,67,87,222,223,231] While most publications argue that there is a dependence between the surfactant concentration, the yield and the quality of exfoliation, some argue that the influence of concentration is negligible.[232,233] To understand a possible correlation between concentration and exfoliation yield we performed a series of experiments. The concentration of initially three different surfactants was varied from the CMC and stepwise below. SDS, SDBS and SHS were chosen as surfactants, having different molecular masses which gives tendencies if larger surfactant chains are beneficial for the exfoliation process. The quality of exfoliation was exploited using UV-Vis spectroscopy, Raman spectroscopy and the specific Zeta potentials for all suspensions. This approach allowed for the evaluation of various surfactants based on their effectiveness in stabilizing exfoliated MoS_2 and WS_2 suspensions. Key factors such as quality, exfoliation efficiency, band gap, suspension stability, and concentration were used to compare and classify each surfactant's performance. We observed that different surfactants and their concentrations yielded varying results for

WS_2 and MoS_2. For MoS_2, SHS at a concentration of 8.2 mM provided the best suspension stability, while SDBS at 1.0 mM was most effective in terms of yield. For WS_2, an intermediate concentration of 4.1 mM SHS achieved the best balance between suspension stability and exfoliation quality. It is important to learn two things from the conducted experiments. First of all, the most effective concentrations of SDBS and SHS were above the CMC for each surfactant resulting in the best performing suspensions. However, no single surfactant emerged as the definitive choice. The exfoliation process must be tailored for each material and its intended application, balancing suspension stability and exfoliation quality. This balance often involves compromises, as increasing the concentration of TMDCs or surfactants tends to negatively impact stability.

RESEARCH ARTICLE

physica status solidi pss rrl
www.pss-rapid.com

Systematic Investigation on the Surfactant-Assisted Liquid-Phase Exfoliation of MoS_2 and WS_2 in Water for Sustainable 2D Material Inks

Micaela Pozzati, Felix Boll, Matteo Crisci, Sara Domenici, Bernd Smarsly, Teresa Gatti, and Mengjiao Wang**

MoS_2 and WS_2 have gathered significant attention due to their tunable properties and wide range of applications. Liquid-phase exfoliation (LPE) is a facile method to prepare 2D MoS_2 and WS_2. Currently, the principally employed solvents for LPE of MoS_2 and WS_2 are expensive and toxic, and have high boiling points. These drawbacks encourage to find more sustainable alternatives to the liquid medium used for the preparation of 2D material inks. Water is the best option, but surfactants are necessary for LPE in water, since MoS_2 and WS_2 are hydrophobic. Organic molecules with amphoteric character such as sodium dodecyl sulfate, sodium dodecylbenzene sulfonate, and sodium hexadecyl sulfonate (SHS) are selected as suitable candidates for the role. However, the study of these surfactants used in LPE is barely systematically reported. In this work, a detailed investigation is presented on their impact on the LPE of MoS_2 and WS_2, which are representatives of transition-metal dichalcogenides. By characterizing and qualifying the products from average number of layers, it is found that all the surfactants work efficiently to exfoliate MoS_2 and WS_2 into few layers, and SHS stabilizes the 2D layers better than the other two. However, in terms of yield and relative surfactant concentration, a real trade-off is not identified between maximized quantity of exfoliated materials and minimized surfactant concentration, which prompts to select the colloidal ink based on the specific further needs for processing.

1. Introduction

Transition-metal dichalcogenides (TMDs) have gathered significant attention in a wide range of applications, such as energy storage, sensing, and optoelectronics.[1–3] In this broad family of materials, MoS_2 and WS_2 play important roles due to the possibility of preparing the 2D layered counterparts, which possess specific electronic and optical properties.[4–7] As shown in **Figure 1**, MoS_2 and WS_2 contain a layer of metal atoms sandwiched between two sulfur layers, and these sandwiched layers are linked to each other by van der Waals (vdW) forces in the bulk.[8–12] Due to the unique layered structure, it is possible to use top-down methodologies which are more scalable, versatile, and cost-effective compared to the bottom-up methods.[9] Therein, liquid-phase exfoliation (LPE) is commonly used to produce 2D layered materials. This procedure consists in delaminating the layers of the material dispersed in a solvent by mechanical forces such as ultrasonication and high shear mixing.[13] For instance, in the sonication-assisted LPE, the sonication generates the growth and collapse of microbubbles of the solvents, thus resulting in shock waves. These waves can produce shear forces on the bulk materials, break the vdW interactions between the layers of the 2D structures, and form layered materials eventually.[14,15] The type of solvent plays an important role on the yield and quality of the 2D materials. Typically, organic solvents such as N-methyl-2-pyrrolidone, dimethyl sulfoxide, and *N,N*-dimethyl formamide are the most commonly used in exfoliating MoS_2 and WS_2. However, they are expensive and toxic, and have high boiling point.[16–18] To avoid these disadvantages, water is applied as an alternative. Since most of the TMDs are hydrophobic, surfactants are needed to stabilize the 2D nanocrystals in water.

In LPE, ionic surfactants are applied for stabilizing the samples and thus increase the production yield in 2D layered colloids in water.[19,20] Thanks to the electrostatic forces, the ionic surfactants can compensate the vdW attraction between the layers of the material, thus preventing the restacking.[21,22] There are different kinds of surfactants that can be used in this process and the most reported one for MoS_2 and WS_2 is an anionic surfactant, namely sodium dodecyl sulfate (SDS), whose chemical structure is shown in Figure 1b.[23] It is characterized by a C_{12} alkyl chain that tends to aggregate on the nanosheets surface, avoiding the restacking.[20,24] Surfactants with a similar structure as SDS have

M. Pozzati, S. Domenici, T. Gatti, M. Wang
Dipartimento Scienza Applicata e Tecnologia (DISAT)
Politecnico di Torino
Corso Duca degli Abruzzi 24, 10129 Torino, Italy
E-mail: teresa.gatti@polito.it; mengjiao.wang@polito.it

F. Boll, M. Crisci, B. Smarsly, T. Gatti
Center for Materials Research (LaMa)
Justus Liebig University
Heinrich-Buff-Ring 17, 35392 Giessen, Germany

The ORCID identification number(s) for the author(s) of this article can be found under https://doi.org/10.1002/pssr.202400039.

DOI: 10.1002/pssr.202400039

ADVANCED SCIENCE NEWS
www.advancedsciencenews.com

physica status solidi pss rrl
www.pss-rapid.com

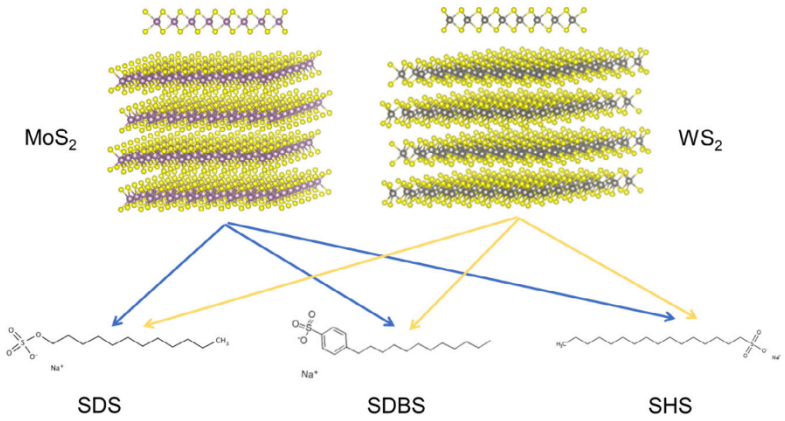

Figure 1. Structures of the two-layered TMDs considered in this study (MoS_2 and WS_2) in their semiconducting H-phase and modular structures of surfactants SDS, SDBS, and SHS.

been applied in LPE as well. Sodium dodecylbenzene sulfonate (SDBS) is also used as stabilizing agent. It is reported that the nonpolar benzene rings in SDBS combine with the 2D layers with a strong bind energy, thus improving at the same time the colloidal stability and yield in 2D MoS_2 in an aqueous solution.[25,26] Additionally, since it is reported that the length of the alkyl chain can have an impact on the stability of the dispersion, we have identified sodium hexadecyl sulfonate (SHS) as a new potential surfactant for stabilizing 2D nano-inks, considering its long C_{16} alkyl chain.[27] Plenty of previous studies suggest that the concentration of the surfactant has a great impact on the dispersion quality and final concentration.[20] Therefore, to tune, the concentration of the surfactants will be important for optimizing the LPE of MoS_2 and WS_2.

In this work, we perform a systematic investigation about the influence of the surfactant type and concentration on the quality of exfoliated MoS_2 and WS_2. As shown in Figure 1, three different surfactants, SDS, SDBS, and SHS have been selected for this study. These organic surfactants have a critical micellar concentration (CMC), and it was reported that surfactants can play a more efficient role in LPE when their concentration is less than the CMC.[28] However, some other reports have shown that the surfactant concentration has negligible influence on the yield and quality of exfoliated samples.[23] This confliction encourages us to systematically investigate the relationship between surfactant concentration and the exfoliated samples by LPE. Considering the CMC of SDS, SDBS, and SHS are respectively 8.2, 2.7, and 0.55 mM,[29–32] we chose the CMC of SDS as the highest surfactant concentration and set the concentrations to 8.2, 4.1, 2.0, 1.0, and 0.5 mM for comparison. By testing the UV–vis absorption, Raman spectra, zeta potential (ZP), we were able to compare the quality of the exfoliated MoS_2 and WS_2 in the aspect of layer thickness and stability. Eventually, the production yield is calculated for all the exfoliated samples. It is found that the thickness of the layers is not tightly related to the surfactant type and concentration, as almost all the samples are few layered for MoS_2 and mostly monolayered for WS_2. Meanwhile, SHS performs better than the other two surfactants in stabilizing the nanosheets, since LPE MoS_2 and WS_2 colloids have long-term stability with SHS.

2. Results and Discussion

The suspensions of MoS_2 and WS_2 were obtained with the surfactant-assisted LPE method described in Experimental Section, and the MoS_2 or WS_2 samples were labeled by the surfactant type and concentration. Transmission electron microscope (TEM) measurements were performed on selected MoS_2 and WS_2 suspensions to characterize the morphology of the exfoliated samples in detail. In **Figure 2**a, it is evident that the exfoliated MoS_2 are thin nanosheets with a lateral size of more than 500 nm. In Figure 2b, the TEM image with higher magnification displays a thin side view of less than 10 nm of the nanosheets. Since the interlayer spacing of MoS_2 is 0.615 nm, we expect that the exfoliated samples have less than 16 layers.[33] Figure 2c shows a TEM image of the exfoliated WS_2 nanosheets of more than 500 nm lateral size. In Figure 2d, it is easy to find the thickness of the WS_2 nanosheets of around 5 nm from the wrinkled part, which implies that the obtained WS_2 nanosheets have less than 8 layers.[34]

The effect of the surfactant on the optical properties of exfoliated MoS_2 was studied by UV–vis absorption spectroscopy. **Figure 3** shows the UV–vis normalized absorption spectra of LPE MoS_2 with SDS, SDBS, and SHS at different concentrations. All the spectra have shown the four characteristic excitons of MoS_2 at around 670 nm for the A exciton, 610 nm for the B exciton, 450 nm for the C exciton, and 395 nm for the D exciton, confirming the existence of the 2D layered material. Spectral changes are observed while varying the concentration of the surfactant. Therein, *A* and *B* excitons stands for direct excitonic transitions occurring at the *K* points in the first Brillouin zone, due to the spin–orbit splitting of the top of the valence band. *C* and *D* excitons are related to the optical transitions from the deep valence band to the conduction band.[35] In Figure 3a, the slope in the region between the *B* exciton and the *C* exciton becomes sharper while increasing the surfactant concentration, indicating

ADVANCED SCIENCE NEWS
www.advancedsciencenews.com

physica status solidi rrl
www.pss-rapid.com

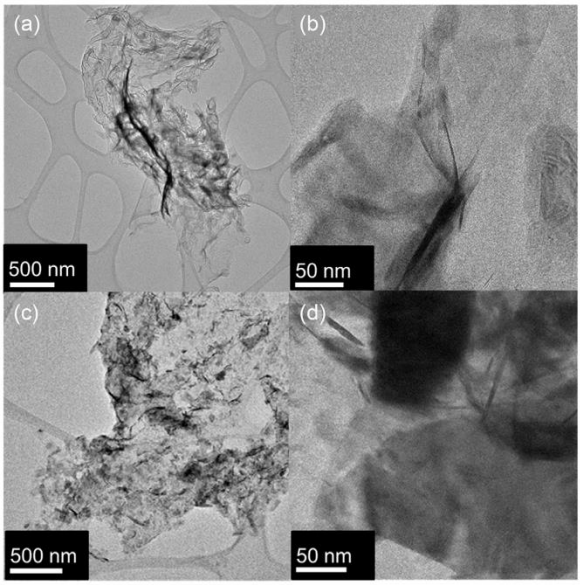

Figure 2. TEM images of a,b) MoS_2 SDBS 1.0 mM and c,d) WS_2 SDS 0.5 mM.

smaller and thinner nanosheets. In addition, the value of *A* exciton is closely related to the size of the product. As listed in **Table 1**, the position of the *A* exciton tends to shift to shorter wavelength while increasing the concentration, revealing smaller and thinner nanosheets as well.[20,36–38] It has to be mentioned that there is no linear relationship between ligand concentration and absorption intensity, since the linear increase of surfactant concentration does not result in the linear increase of sample concentration, which have direct influence on the absorbance intensity. While the relationship between product yield and concentration of the surfactant will be discussed in the following content.

In addition, the bandgap of the nano-colloids was calculated with the Tauc plot equation (Equation (1)):

$$(\alpha h\nu)^{1/n} = A(h\nu - E_g) \tag{1}$$

where α is the absorption coefficient, h is the Plank constant, ν is the frequency, E_g is the bandgap energy, and n is 2 for the indirect bandgap materials such as few-layered MoS_2 and WS_2.[39] The values obtained are listed in Table 1. It is obvious that all the exfoliated MoS_2 have a larger bandgap range of 1.38–1.65 eV compared to the bulk MoS_2 (1.2 eV).[40] When comparing values between different surfactants, SHS in general results in higher bandgap compared to other surfactants, which means MoS_2 can be exfoliated into thinner layers when SHS is applied. While comparing the values between different concentration of the same surfactant, higher concentration of surfactant tends to produce the samples with higher bandgap, which means thinner nanosheets.[41] At last, the MoS_2 SHS 8.2 mM sample features the broadest bandgap of 1.65 eV, which means it likely contains nanosheets with the smallest average number of layers among all the LPE MoS_2 samples.

The UV–vis spectra of WS_2 are shown in **Figure 4**a–c. We can observe the presence of the four characteristic excitons of WS_2 (*A*: ≈630 nm; *B*: ≈522 nm; *C*: ≈460 nm; and *D*: ≈430 nm) in all the spectra while varying the surfactant type and concentration, revealing the success of exfoliation in all the

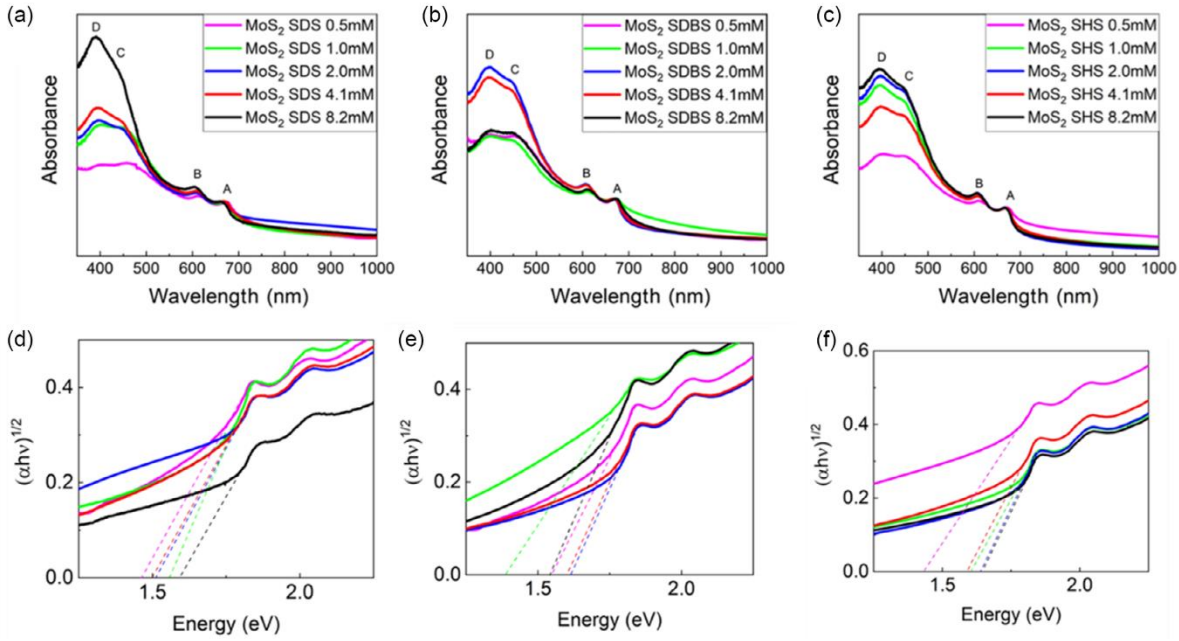

Figure 3. UV–Vis absorption spectra and corresponding Tauc plots of exfoliated MoS_2 with a,d) SDS, b,e) SDBS, and c,f) SHS.

ADVANCED SCIENCE NEWS
www.advancedsciencenews.com

physica status solidi pss rrl
www.pss-rapid.com

Table 1. Positions of A exciton and bandgap values for LPE MoS_2 samples with the three different surfactants.

Surfactant	Surfactant concentration [mM]	A exciton [nm]	Bandgap [eV]
	8.2	664.6	1.59
	4.1	671.1	1.50
SDS	2.0	668.9	1.51
	1.0	671.1	1.56
	0.5	673.4	1.46
	8.2	672.1	1.54
	4.1	670.1	1.60
SDBS	2.0	667.8	1.62
	1.0	672.1	1.38
	0.5	672.2	1.55
	8.2	667.8	1.65
	4.1	668.9	1.58
SHS	2.0	668.9	1.64
	1.0	669.3	1.61
	0.5	672.2	1.43

experiments.[38] Specifically, in Figure 4d, it is shown that the bandgap of exfoliated WS_2 increases from 1.42 to 1.74 eV with the increasing concentration of SDS from 0.5 to 8.2 mM. Therefore, higher concentration of SDS results in the exfoliated WS_2 with broad bandgap and thinner layers of the samples on average. In contrast, for SDBS and SHS, difference in concentration has negligible influence on the bandgap of the samples, as shown in Figure 4e,f, and the bandgap of the samples by SDBS and SHS is around 1.74 eV. However, there is an exception of WS_2 SHS 8.2 mM, which shows a bandgap of 1.43 eV. This might be because 8 mM is much more than the suitable concentration of SHS to exfoliate WS_2 and results in thicker layers than other concentrations. Although the concentrations from 0.5 to 4.1 mM are all more than the CMC of SHS (0.5 mM), we still obtained WS_2 thin layers. It means that for the exfoliation of WS_2 with SHS, the concentration of SHS is not limited to the CMC. This result is different from the exfoliation of MoS_2 with SHS, which all results in thick MoS_2 layers, as shown in Table 1. This might be because the different hydrophobicity of WS_2 and MoS_2 results in different interaction intensity between the TMDs and SHS.[42] All the A-exciton positions and bandgap values are listed in **Table 2**, for the sake of comparison.

Exfoliation from the bulk to a 2D layered material results in a change of chemical structure and electronic properties on the surface of the samples. Therefore, Raman spectroscopy is used as an effective technique for identifying the change in surface chemical bonding and characterizing these exfoliated MoS_2 and WS_2. As shown in **Figure 5**a–c, all the exfoliated MoS_2 samples display two characteristic peaks: the peak at around 383 cm^{-1} is assigned to the E_{2g} mode, while the peak at around 408 cm^{-1} is assigned to the A_{1g} mode.[43,44] E_{2g} and A_{1g} are related to the in-plane and out-of-plane vibrations within the stacked layers. The shift between the two peak positions at ≈383 and ≈408 cm^{-1} can be used to identify the number of layers in that exfoliated MoS_2 particles, since the thickness of the materials is correlated with the frequency.[43–46] For monolayered MoS_2, at an excitation wavelength of 532 nm, a difference between the A_{1g} and the E_{2g} peak at 18 cm^{-1} is expected. Few layered materials have shifts from 18 to 25 cm^{-1}. Above

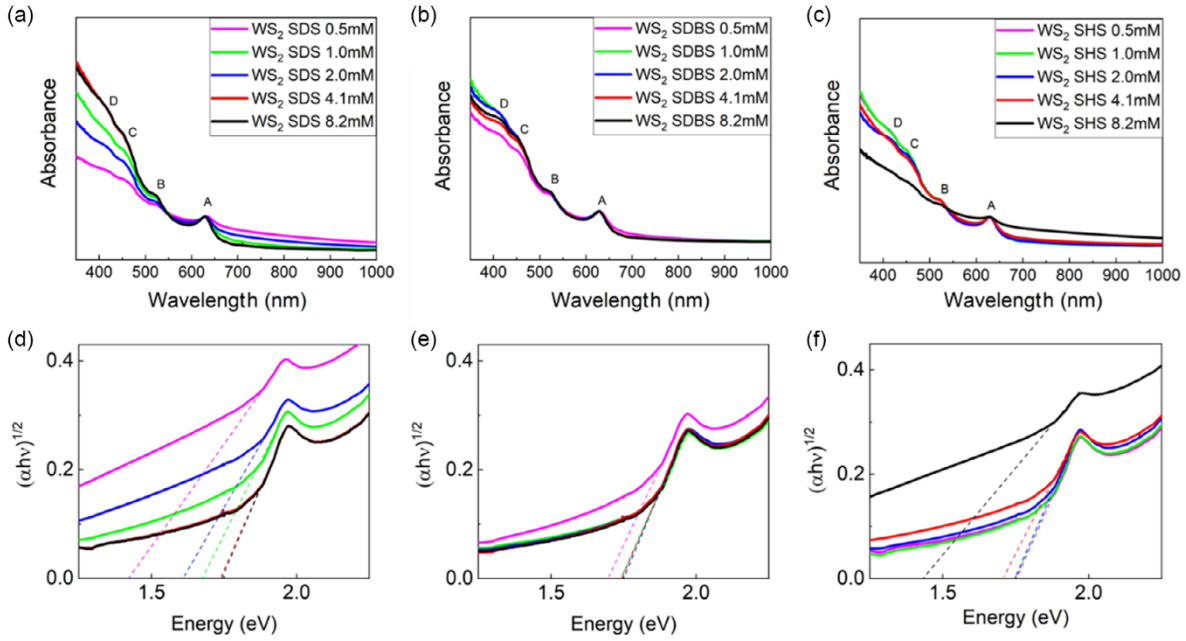

Figure 4. UV–Vis absorption spectra and corresponding Tauc plots of exfoliated WS_2 with a,d) SDS, b,e) SDBS, and c,f) SHS.

ADVANCED SCIENCE NEWS
www.advancedsciencenews.com

physica status solidi pss rrl
www.pss-rapid.com

Table 2. Positions of A exciton and bandgap values for LPE WS_2 samples with the three different surfactants.

Surfactant	Surfactant concentration [mM]	A-exciton position [nm]	Bandgap [eV]
	8.2	629.3	1.74
	4.1	629.3	1.74
SDS	2.0	630.3	1.61
	1.0	630.9	1.67
	0.5	632.1	1.42
	8.2	629.3	1.74
	4.1	629.3	1.74
SDBS	2.0	628.2	1.75
	1.0	628.2	1.74
	0.5	630.3	1.70
	8.2	628.2	1.43
	4.1	630.3	1.70
SHS	2.0	629.3	1.75
	1.0	629.3	1.75
	0.5	629.3	1.75

Table 3. Distance between E_{2g} and A_{1g} Raman peaks in LPE MoS_2 samples.

Surfactant	Surfactant concentration [mM]	$\Delta\nu$ [cm^{-1}]
	8.2	24.4
	4.1	25.1
SDS	2.0	24.6
	1.0	25.7
	0.5	25
	8.2	25
	4.1	24.9
SDBS	2.0	25.1
	1.0	25.0
	0.5	25.4
	8.2	25
	4.1	25
SHS	2.0	25
	1.0	25
	0.5	25.5

25 cm^{-1} samples are expected to be multilayered/bulk-like material. In **Table 3**, the distance of the two Raman peaks is shown for all samples with the three different surfactants and from 0.5 up to 8.2 mM. Apart from SDS 8.2 mM, SDS 2.0 mM, and SDBS 4.1 mM, all other samples show a shift of 25 cm^{-1} or bigger, which is a characteristic of a multilayered material. However, it is important to consider that a certain degree of restacking of the layers is expected during sample preparation, since for the Raman analysis the suspensions are evaporated and the residual dried particles are measured.[47]

Figure 5d–f summarizes the Raman spectra of all the exfoliated WS_2 samples. For all the samples, the peaks relative to $2LA + E_{2g}$ and A_{1g} vibrational modes can be observed, at around

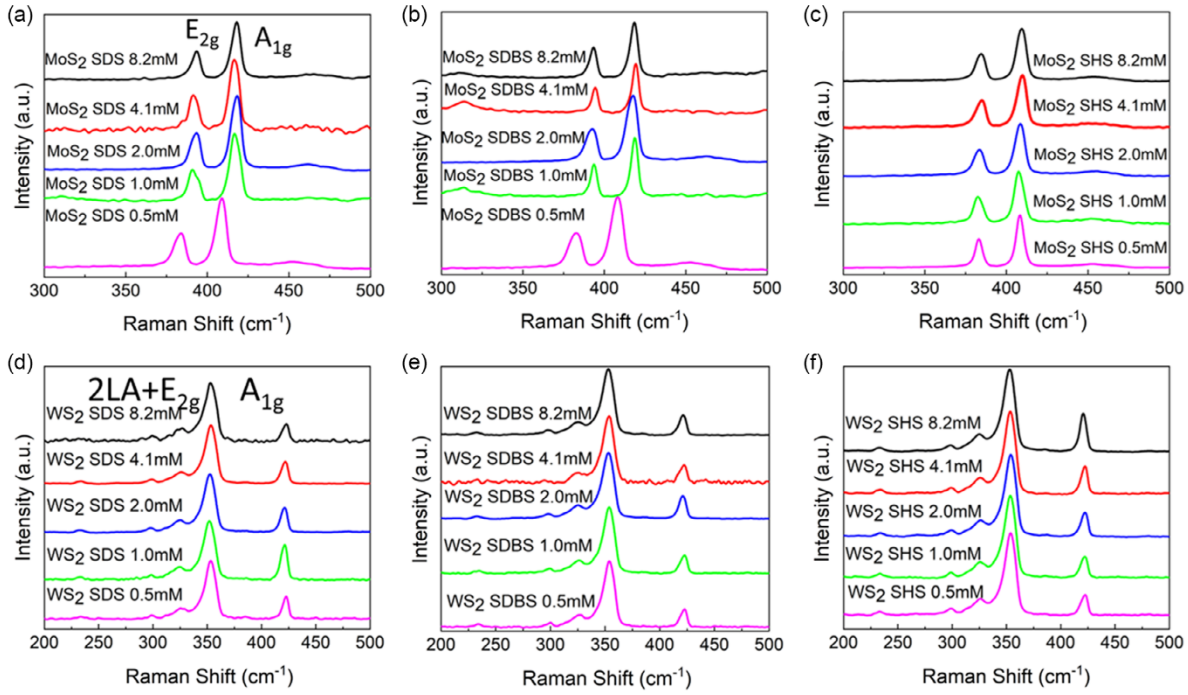

Figure 5. Raman spectra of LPE a–c) MoS_2 and d–f) WS_2.

ADVANCED SCIENCE NEWS
www.advancedsciencenews.com

physica status solidi pss rrl
www.pss-rapid.com

Table 4. $(2LA + E_{2g})/A_{1g}$ ratios in LPE WS_2 samples.

Surfactant	Surfactant concentration [mM]	$(2LA + E_{2g})/A_{1g}$ ratio
	8.2	3.38
	4.1	2.66
SDS	2.0	2.35
	1.0	1.69
	0.5	2.58
	8.2	3.67
	4.1	3.67
SDBS	2.0	2.90
	1.0	3.81
	0.5	3.34
	8.2	2.17
	4.1	3.00
SHS	2.0	3.40
	1.0	3.90
	0.5	4.05

355 and 417 cm^{-1}, respectively.[48,49] As reported by other works present in the literature, the increasing ratio of $(2LA + E_{2g})/A_{1g}$ is due to the decreasing the atomic layers of WS_2 nanosheets.[50] For bulk WS_2, the $(2LA + E_{2g})/A_{1g}$ ratio is around 0.5, while the ratio of monolayered WS_2 reaches above 2. When the ratio value is between 1 and 2, WS_2 nanosheets are present as few-layer-stacked particle layers.[51] As shown in Figure 5d–f and **Table 4**, independent from the type and concentration of the surfactant, all the exfoliated WS_2 samples are adequate for producing monolayer WS_2, except the case of SDS at a concentration of 1.0 mM where a few-layered system was obtained. This might be due to the restacking of the exfoliated samples during the preparation and Raman spectroscopy measurement. In general, for WS_2, we were able to show that all surfactants can produce water-based WS_2 suspension containing highly exfoliated nanosheets and the effect of restacking of the nanosheets is not apparent at the solid state.

ZP measurements were performed to characterize the stability of the obtained colloidal suspensions after LPE. As shown in **Figure 6**, all the samples of MoS_2 and WS_2 provide a ZP value lower than −20 mV, indicating that all the suspensions are colloidally stable and the suspended nanosheets negatively charged. However, when the ZP values are between −20 and −30 mV, the samples show a short-term stability, and a gradual sedimentation of materials was observed after several days. While samples with −30 mV ZP values show a long-term stability up to several months.[52] Specifically, for MoS_2, the application of SDS and SDBS mostly results in a short-term stability, independently from the surfactant concentration, since the ZP values are in the range of −20 and −30 mV, while SHS can increase the stability of the suspension dramatically, with the ZP values of SHS as −30 mV. In contrast, WS_2 suspensions show long-term stability with most of the investigated surfactants and concentrations, except with 1.0 mM SDS. Interestingly, the blue lines in Figure 6 clearly show that with SHS, the suspensions of both MoS_2 and WS_2 gain better stability than that of SDS and SDBS. When studying the impact of surfactant nature on the colloidal stability of the suspensions, no strict rule can be concluded by comparing the variable parameters. However, there is still a

Table 5. Product concentration and yield for LPE MoS_2 calculated from Lambert–Beer law and from weighted freeze-dried samples.

Surfactant	Surfactant concentration [mM]	Product concentration by UV–vis absorption [mg mL^{-1}]	Product concentration by freeze-drying [mg mL^{-1}]	Yield [%]
	8.2	0.028		0.28
	4.1	0.051		0.51
SDS	2.0	0.077		0.77
	1.0	0.021		0.21
	0.5	0.027		0.27
	8.2	0.085		0.85
	4.1	0.08		0.8
SDBS	2.0	0.093		0.93
	1.0	0.11		1.1
	0.5	0.043		0.43
	8.2	0.032	0.36	0.32
	4.1	0.042		0.42
SHS	2.0	0.027	1.35	0.27
	1.0	0.021		0.21
	0.5	0.061		0.61

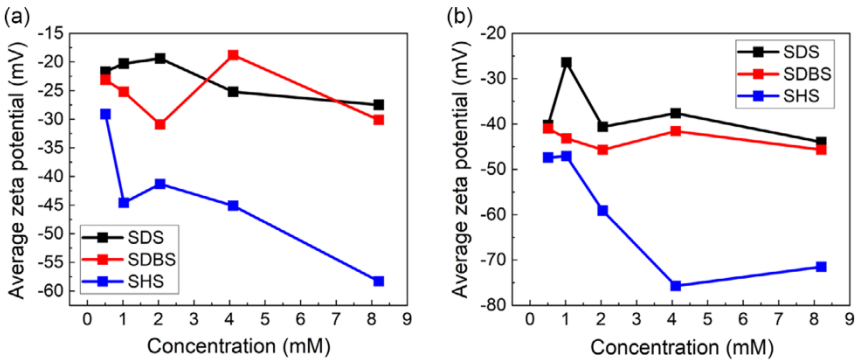

Figure 6. ZP trends for a) MoS_2 and b) WS_2 samples with different type and concentration of surfactants.

ADVANCED SCIENCE NEWS
www.advancedsciencenews.com

physica status solidi pss rrl
www.pss-rapid.com

Table 6. Product concentration and yield for LPE WS_2 calculated from Lambert–Beer law and from weighted freeze-dried samples.

Surfactant	Surfactant concentration [mM]	Product concentration by UV–vis absorption [mg mL^{-1}]	Product concentration by freeze-drying [mg mL^{-1}]	Yield [%]
	8.2	0.068		0.68
	4.1	0.097		0.97
SDS	2.0	0.13	0.23	1.3
	1.0	0.11		1.1
	0.5	0.23		2.3
	8.2	0.12	1.25	0.85
	4.1	0.12		0.8
SDBS	2.0	0.14		0.93
	1.0	0.11		1.1
	0.5	0.12		1.2
	8.2	0.33	0.56	3.3
	4.1	0.11		1.1
SHS	2.0	0.12		1.2
	1.0	0.10		1.0
	0.5	0.098		0.98

rough trend showing that, with all the surfactants used for MoS_2 and WS_2 exfoliation, higher concentrations increase the colloidal stability of the samples.

The yield in the exfoliated material is another important standard to evaluate the effect of the surfactants and the corresponding experimental parameters used. As described in Section "Calculation Methods of the Sample Concentration," UV–vis spectra are used to quantify the yield and final concentration of each suspension. The product concentration and the corresponding yield of MoS_2 and WS_2 are calculated and listed in **Table 5** and **6**, respectively. The product concentration values changed with surfactant type and concentration, as shown from the trends reported in **Figure 7**. For MoS_2 inks, SDBS results in a better product concentration, compared to the other two surfactants. With a surfactant concentration of 1.0 mM, it was possible to obtain an optimized MoS_2 concentration of 0.11 mg mL^{-1} and the highest yield of 1.1%. In contrast, for WS_2 inks there is no clear evidence showing that the type or the concentration of the surfactants has a relationship with the product concentration and yield. However, we are still able to find the best parameter with SHS 8.2 mM, which can result in an outstanding product concentration of 0.33 mg mL^{-1} and yield of 3.3% compared to other surfactant parameters. These results are comparable to the published works.[53,54] Meanwhile, for some selected samples with relatively high concentration, we were able to obtain the actual concentration from freeze-drying the suspensions. Interestingly, the concentration calculated from freeze-drying method is higher than the concentration obtained from UV–vis spectra. This might be due to the presence of residual surfactants left on the samples after prolonged dialysis, which indicates that the surfactant is tightly anchored on the nanosheet surfaces. These surfactants are necessary to hinder the aggregation of the exfoliated layers when the samples are extracted from inks, though they might influence the future application of the exfoliated products.[55]

3. Conclusion

In conclusion, a systematic study was conducted on the surfactant-assisted LPE of MoS_2 and WS_2 in water. With the aid of three different ionic surfactants (SDS, SDBS, and SHS), exfoliations were carried out in water to produce sustainable colloidal suspensions. By charactering the samples with different techniques, we were able to compare the quality of the exfoliated 2D MoS_2 and WS_2 nanosheets contained in the inks in terms of layer thickness, colloidal stability, and product yield.

For MoS_2, since most experimental parameters result in multilayer samples, the best parameters can be chosen considering the sample stability and product yield. Specifically, 8.2 mM SHS results in the best stability for LPE MoS_2 suspensions, while 1.0 mM SDBS can result in the highest yield of the product. Depending on the target application for the produced ink, one can thus decide whether to proceed with a colloid containing surfactant amount, which is relevant for certain purposes such as use in electronic or energy-related applications.

As for what concerns LPE WS_2, almost all the parameter combinations result in monolayered product, except 8.2 mM SHS, which anyway provides the highest yield in suspended WS_2. And, 4.1 mM SHS is likely the preferred choice to provide the most stable suspension of layered WS_2 in water. Considering that

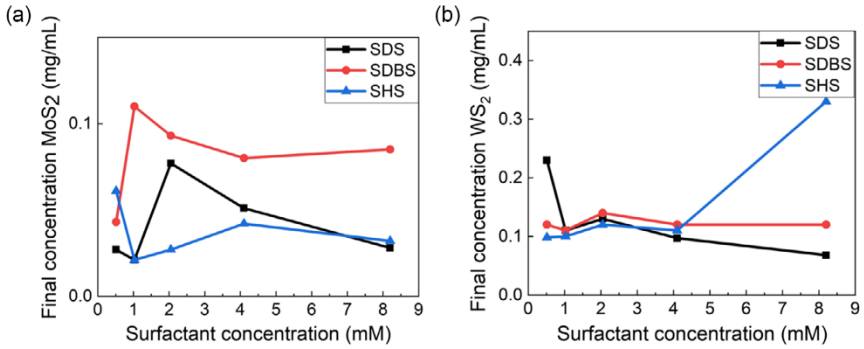

Figure 7. Product concentration trends for a) LPE MoS_2 and b) LPE WS_2 samples.

ADVANCED SCIENCE NEWS
www.advancedsciencenews.com

physica status solidi pss rrl
www.pss-rapid.com

the CMC of SHS is only 0.55 mM, our results surprisingly indicate that the best concentration of SHS in the LPE of MoS_2 and WS_2 is indeed highly above the CMC. As to the product yield, the all the experiments reported in this work obtain a yield of less than 3.3%, which is comparable but does not outperform other published works. Therefore, modifications such as new surfactants with different length of carbon chains and functional groups, or longer exfoliation time, are necessary to increase the product yield. With the detailed provision of a wide scenario of experimental conditions from which to select one's needs for a specific application, such as processing of thin films, nanochemistry, or even biomedicine, this study will constitute a useful tool for further research in the field of sustainable production of 2D material inks.

4. Experimental Section

Materials and LPE Process: MoS_2 (99%), WS_2 (99%), SDS, and SDBS were purchased from Sigma Aldrich and used without further purification. SHS was purchased from TCI Chemicals and used without further purification. All the exfoliations were performed using a tip sonicator and the samples were cooled down to 0 °C with an ice bath during the process. LPE was carried out on a Bandelin Sonopuls tip sonicator, operating with 80% power using pulses of 1 s on/1 s off for 4 h. In all the experiments, the suspension volume was kept fixed at 150 mL with a concentration of the bulk materials of 10 mg mL^{-1}. The concentration of all the surfactants was 8.2, 4.1, 2.0, 1.0, and 0.5 mM. After the sonication step, liquid cascade centrifugation was applied at two different rates. The suspensions obtained after the sonication were centrifuged for 30 min at 1500 rpm and, after keeping the supernatants, those were further centrifuged for 30 min at 3000 rpm with a Universal 320 Hettich centrifuge. Ultrapure water was obtained with the Milli-Q Direct Water Purification System. The detailed parameters of all the experiments performed in this work are listed in Table S1, Supporting Information.

Characterization: UV–visible (UV–vis) absorption spectra of the colloidal inks were recorded on a Goebel Uvikon spectrometer using a quartz cuvette of 1 cm optical length from 350 to 1000 nm with a scan interval of 0.25 nm. Raman spectra were recorded on a Bruker Senterra instrument using a 532 nm laser excitation source with a 2 mW of power, 6 s of integration, and 60 co-additions. The samples were prepared by drop-casting the suspensions over a silicon slide and then analyzed. ZP was measured on a Malvern Zetasizer Nano-ZS device three times and the results were averaged to obtain the final results. The samples were measured in Rotilabo precision glass cuvettes with a light path of 10 mm and a volume of 3.5 mL. TEM images were recorded using a non-aberration-corrected TALOS F200X (ThermoScientific, Eindhoven, Netherland) operated at 200 kV. Images were recorded on a 16Mpxls CMOS camera with a 1 s exposure time.

Calculation Methods of the Sample Concentration: UV analysis was employed to calculate the final concentration of the 2D materials. A calibration line was obtained using a set of dilutions from a suspension with a known concentration, obtained after filtration. The slope of the calibration line corresponded to the extinction coefficient of the dispersed material. The final concentrations of the MoS_2 and WS_2 were obtained with the Lambert–Beer law (Equation (2))

$$A = \varepsilon bc \tag{2}$$

where A stands for absorbance of the material, ε is the extinction coefficient of the dispersed nanosheets, and c is the concentration of the suspension. In this work, we used the absorption value of the A exciton as A. ε was obtained from the calibration lines from several standard MoS_2 and WS_2 suspensions with known concentrations. For MoS_2, the calculated ε was 7.85 mg mL^{-1} cm, while for WS_2 the ε was 3.91 mg mL^{-1} cm.

The other method used to obtain the final concentration was freeze-drying. Before freeze-drying, dialysis was performed using cellulose dialysis bag (Carl Roth) 14 kDa, filling each bag with 20–25 mL of the desired suspension and closing both sides with a plastic pin once filled. The bag was then left in a suitable Becker with Milli-Q water for 3 days, changing 3 times per day the water. Freeze-drying was performed at −10 °C for 16 h and a pressure of 1 mPa.

Supporting Information

Supporting Information is available from the Wiley Online Library or from the author.

Acknowledgements

M.P., F.B., and M.C. contributed equally to this work. This research was funded by the ERC StG project JANUS BI (grant agreement no. 101041229). M.W. and T.G. also thank Fondazione Compagnia di San Paolo for financial support through the "Bando TRAPEZIO - Paving the way to research excellence and talent attraction". T.G. further acknowledges Fondazione Compagnia di San Paolo for the support through the Starting Grant ERC program. M.C., F. B., and T.G. also acknowledge the support of the European Commission through the H2020 FET-PROACTIVE-EIC-07-2020 project LIGHT-CAP (grant no. 101017821). The authors declare no conflict of interest.

Conflict of Interest

The authors declare no conflict of interest.

Data Availability Statement

The data that support the findings of this study are available from the corresponding author upon reasonable request.

Keywords

2D materials, colloidal inks, green chemistry, surfactant-assisted liquid-phase exfoliations, sustainabilities, transition-metal dichalcogenides

Received: January 31, 2024
Revised: February 20, 2024
Published online:

[1] S. Ott, N. Wolff, F. Rashvand, V. J. Rao, J. Zaumseil, C. Backes, *Chem. Mater.* **2019**, *31*, 8424.
[2] X. Geng, J. Yi, *Nano-Sized Multifunctional Materials: Synthesis, Properties and Applications*, Elsevier, Amsterdam **2019**, pp. 117–144.
[3] Y. Guan, H. Yao, H. Zhan, H. Wang, Y. Zhou, J. Kang, *RSC Adv.* **2021**, *11*, 14085.
[4] C. Nie, J. Wang, B. Cai, B. Lai, S. Wang, Z. Ao, *Appl. Catal., B* **2024**, *340*, 123173.
[5] Z. Liang, R. Shen, Y. H. Ng, P. Zhang, Q. Xiang, X. Li, *J. Mater. Sci. Technol.* **2020**, *56*, 89.
[6] A. Sebastian, R. Pendurthi, T. H. Choudhury, J. M. Redwing, S. Das, *Nat. Commun.* **2021**, *12*, 693.
[7] C. Lan, C. Li, J. C. Ho, Y. Liu, *2D WS2: From Vapor Phase Synthesis to Device Applications*, Vol. *7*, Blackwell Publishing Ltd., Hoboken **2021**.

ADVANCED SCIENCE NEWS
www.advancedsciencenews.com

physica status solidi pss rrl
www.pss-rapid.com

[8] M. H. Kang, D. Lee, J. Sung, J. Kim, B. H. Kim, J. Park, *Comprehensive Nanoscience and Nanotechnology*, Elsevier, Amsterdam **2019**, pp. 55–90.
[9] S. Pinilla, J. Coelho, K. Li, J. Liu, V. Nicolosi, *Two-Dimensional Material Inks*, Vol. *7*, Nature Research, London **2022**, pp. 717–735.
[10] J. N. Coleman, M. Lotya, A. O'neill, S. D. Bergin, P. J. King, U. Khan, K. Young, A. Gaucher, S. De, R. J. Smith, I. V. Shvets, S. K. Arora, G. Stanton, H.-Y. Kim, K. Lee, G. T. Kim, G. S. Duesberg, T. Hallam, J. J. Boland, J. J. Wang, J. F. Donegan, J. C. Grunlan, G. Moriarty, A. Shmeliov, R. J. Nicholls, J. M. Perkins, E. M. Grieveson, K. Theuwissen, D. W. Mccomb, P. D. Nellist, et al., *Science* **2011**, *331*, 568.
[11] R. J. Smith, P. J. King, M. Lotya, C. Wirtz, U. Khan, S. De, A. O'Neill, G. S. Duesberg, J. C. Grunlan, G. Moriarty, J. Chen, J. Wang, A. I. Minett, V. Nicolosi, J. N. Coleman, *Adv. Mater.* **2011**, *23*, 3944.
[12] M. Chhowalla, H. S. Shin, G. Eda, L. J. Li, K. P. Loh, H. Zhang, *Nat. Chem.*, **2013**, *5*, 263.
[13] C. Backes, T. M. Higgins, A. Kelly, C. Boland, A. Harvey, D. Hanlon, J. N. Coleman, *Guidelines for Exfoliation, Characterization and Processing of Layered Materials Produced by Liquid Exfoliation*, Vol. *29*, American Chemical Society, Washington **2017**, pp. 243–255.
[14] Y. Xu, H. Cao, Y. Xue, B. Li, W. Cai, *Liquid-Phase Exfoliation of Graphene: An Overview on Exfoliation Media, Techniques, and Challenges*, Vol. *8*, MDPI AG, Basel **2018**.
[15] Z. Li, R. J. Young, C. Backes, W. Zhao, X. Zhang, A. A. Zhukov, E. Tillotson, A. P. Conlan, F. Ding, S. J. Haigh, K. S. Novoselov, J. N. Coleman, *ACS Nano* **2020**, *14*, 10976.
[16] A. Jawaid, D. Nepal, K. Park, M. Jespersen, A. Qualley, P. Mirau, L. F. Drummy, R. A. Vaia, *Chem. Mater.* **2016**, *28*, 337.
[17] C. X. Hu, Y. Shin, O. Read, C. Casiraghi, *Dispersant-Assisted Liquid-Phase Exfoliation of 2D Materials Beyond Graphene*, Vol. *13*, Royal Society of Chemistry, London **2021**, pp. 460–484.
[18] H. Tao, Y. Zhang, Y. Gao, Z. Sun, C. Yan, J. Texter, *Scalable Exfoliation and Dispersion of Two-Dimensional Materials-An Update*, Vol. *19*, Royal Society of Chemistry, London **2017**, pp. 921–960.
[19] T. Ivanković, J. Hrenović, *Arch. Ind. Hyg. Toxicol.* **2010**, *61*, 95.
[20] A. Griffin, K. Nisi, J. Pepper, A. Harvey, B. M. Szydłowska, J. N. Coleman, C. Backes, *Chem. Mater.* **2020**, *32*, 2852.
[21] Y. J. Lee, L. Huang, H. Wang, M. L. Sushko, B. Schwenzer, I. A. Aksay, J. Liu, *Colloids Interface Sci. Commun.* **2015**, *8*, 1.
[22] S. De, S. Malik, A. Ghosh, R. Saha, B. Saha, *RSC Adv.* **2015**, *5*, 65757.
[23] A. Gupta, V. Arunachalam, S. Vasudevan, *J. Phys. Chem. Lett.* **2015**, *6*, 739.
[24] H. Domínguez, *J. Phys. Chem. B* **2007**, *111*, 4054.
[25] Z. Guan, C. Wang, W. Li, S. Luo, Y. Yao, S. Yu, R. Sun, C. P. Wong, *Nanotechnology* **2018**, *29*, 425702.
[26] A. Roy, P. Kalita, B. Mondal, *J. Mater. Sci.: Mater. Electron.* **2023**, *34*.
[27] B. Zhang, M. Wang, M. Ghini, A. E. M. Melcherts, J. Zito, L. Goldoni, I. Infante, M. Guizzardi, F. Scotognella, I. Kriegel, L. De Trizio, L. Manna, *ACS Mater. Lett.* **2020**, *2*, 1442.
[28] B. Abreu, B. Almeida, P. Ferreira, R. M. F. Fernandes, D. M. Fernandes, E. F. Marques, *J. Colloid Interface Sci.* **2022**, *626*, 167.
[29] S. A. Markarian, L. R. Harutyunyan, R. S. Harutyunyan, *J. Solution Chem.* **2005**, *34*, 361.
[30] Y. Moroi, K. Motomura, R. Matuura, *The Critical Micelle Concentration of Sodium Dodecyl Sulfate-Bivalent Metal Dodecyi Sulfate Mixtures in Aqueous Solutions*.
[31] K. Yang, L. Zhu, B. Xing, *Environ. Sci. Technol.* **2006**, *40*, 4274.
[32] N. Baccile, A. Poirier, *Microbial Biobased Amphiphiles (Biosurfactants): General Aspects on CMC, Surface Tension and Phase Behaviour*, Vol. *1*, Elsevier, Amsterdam **2022**, pp. 1–38.
[33] G. Solomon, R. Mazzaro, V. Morandi, I. Concina, A. Vomiero, *Crystals* **2020**, *10*, 1.
[34] H. C. Kim, H. Kim, J. U. Lee, H. B. Lee, D. H. Choi, J. H. Lee, W. H. Lee, S. H. Jhang, B. H. Park, H. Cheong, S. W. Lee, H. J. Chung, *ACS Nano* **2015**, *9*, 6854.
[35] A. Eghbali, A. A. Vyshnevyy, A. V. Arsenin, V. S. Volkov, *Biosensors* **2022**, *12*, 582.
[36] C. Backes, K. R. Paton, D. Hanlon, S. Yuan, M. I. Katsnelson, J. Houston, R. J. Smith, D. McCloskey, J. F. Donegan, J. N. Coleman, *Nanoscale* **2016**, *8*, 4311.
[37] A. Griffin, A. Harvey, B. Cunningham, D. Scullion, T. Tian, C. J. Shih, M. Gruening, J. F. Donegan, E. J. G. Santos, C. Backes, J. N. Coleman, *Chem. Mater.* **2018**, *30*, 1998.
[38] T. P. Nguyen, W. Sohn, J. H. Oh, H. W. Jang, S. Y. Kim, *J. Phys. Chem. C* **2016**, *120*, 10078.
[39] S. M. Winata, V. Fauzia, in *Journal of Physics: Conf. Series*, Institute of Physics, Bristol **2022**.
[40] G. A. Ermolaev, Y. V. Stebunov, A. A. Vyshnevyy, D. E. Tatarkin, D. I. Yakubovsky, S. M. Novikov, D. G. Baranov, T. Shegai, A. Y. Nikitin, A. V. Arsenin, V. S. Volkov, *NPJ 2D Mater. Appl.* **2020**, *4*, 21.
[41] G. S. Bang, K. W. Nam, J. Y. Kim, J. Shin, J. W. Choi, S. Y. Choi, *ACS Appl. Mater. Interfaces* **2014**, *6*, 7084.
[42] T. Krasian, W. Punyodom, P. Worajittiphon, *Chem. Eng. J.* **2019**, *369*, 563.
[43] H. Li, Q. Zhang, C. C. R. Yap, B. K. Tay, T. H. T. Edwin, A. Olivier, D. Baillargeat, *Adv. Funct. Mater.* **2012**, *22*, 1385.
[44] B. Adilbekova, Y. Lin, E. Yengel, H. Faber, G. Harrison, Y. Firdaus, A. El-Labban, D. H. Anjum, V. Tung, T. D. Anthopoulos, *J. Mater. Chem* **2020**, *8*, 5259.
[45] B. Chakraborty, H. S. S. R. Matte, A. K. Sood, C. N. R. Rao, *J. Raman Spectrosc.* **2013**, *44*, 92.
[46] M. W. Iqbal, K. Shahzad, R. Akbar, G. Hussain, *Microelectron. Eng.* **2020**, *219*, 111152.
[47] Y. Zhao, Y. Sun, M. Bai, S. Xu, H. Wu, J. Han, H. Yin, C. Guo, Q. Chen, Y. Chai, Y. Guo, *J. Phys. Chem. C* **2020**, *124*, 11092.
[48] H. R. Gutiérrez, N. Perea-López, A. L. Elías, A. Berkdemir, B. Wang, R. Lv, F. López-Urías, V. H. Crespi, H. Terrones, M. Terrones, *Nano Lett.* **2013**, *13*, 3447.
[49] A. Berkdemir, H. R. Gutiérrez, A. R. Botello-Méndez, N. Perea-López, A. L. Elías, C. I. Chia, B. Wang, V. H. Crespi, F. López-Urías, J. C. Charlier, H. Terrones, M. Terrones, *Sci. Rep.* **2013**, *3*, 1755.
[50] M. Crisci, F. Boll, L. Merola, J. J. Pflug, Z. Liu, J. Gallego, F. Lamberti, T. Gatti, *Front. Chem.* **2022**, *10*, 1.
[51] A. M. Abdelkader, I. A. Kinloch, *ACS Sustainable Chem. Eng.* **2016**, *4*, 4465.
[52] J. Kim, S. Kwon, D. H. Cho, B. Kang, H. Kwon, Y. Kim, S. O. Park, G. Y. Jung, E. Shin, W. G. Kim, H. Lee, G. H. Ryu, M. Choi, T. H. Kim, J. Oh, S. Park, S. K. Kwak, S. W. Yoon, D. Byun, Z. Lee, C. Lee, *Nat. Commun.* **2015**, *6*, 8294.
[53] D. Sahoo, B. Kumar, J. Sinha, S. Ghosh, S. S. Roy, B. Kaviraj, *Sci. Rep.* **2020**, *10*, 10759.
[54] L. Ma, Z. Liu, Z. L. Cheng, *Ceram. Int.* **2020**, *46*, 3786.
[55] C. Verma, C. M. Hussain, M. A. Quraishi, A. Alfantazi, *Green Surfactants For Corrosion Control: Design, Performance and Applications*, Vol. *311*, Elsevier B.V., Amsterdam **2023**.

3.5.1. Supporting Information – Publication 3

WILEY-VCH

Supporting Information for:

Systematic investigation on the surfactant-assisted liquid phase exfoliation of MoS_2 and WS_2 in water for sustainable 2D material inks

Micaela Pozzati, Felix Boll, Matteo Crisci, Sara Domenici, Bernd Smarsly, Teresa Gatti and Mengjiao Wang**

Table S1. Parameters selected and varied during the LPE process for the two investigated TMDs.

TMD	Initial bulk concentration (mg/mL)	Surfactant	Surf. concentration (mM)	Exfoliation time
MoS_2, WS_2	10	SDS	8.2 4.1 2.0 1.0 0.5	3 h
MoS_2, WS_2	10	SDBS	8.2 4.1 2.0 1.0 0.5	3 h
MoS_2, WS_2	10	SHS	8.2 4.1 2.0 1.0 0.5	3 h

3.6. Publication 4

In a collaborative effort, similar to the previous publication of WS_2 and MoS_2 exfoliation, in this co-authorship I worked together with Matteo Crisci and Micaela Pozzati on the exfoliation of Bi_2S_3. 2D-Bi_2S_3 is potentially interesting for many applications like energy harvesting, for sensors, optoelectronics and in thermoelectricity. The low thermal conductivity, strong spin-orbit couple, high absorption coefficient and direct band structure in the bidimensional state are the most interesting properties related to this material.[231,234–240] We employed a similar exfoliation approach to our previous work with MoS_2 and WS_2, utilizing water-based methods and various surfactants to optimize the yield and quality of the exfoliated Bi_2S_3. Given Bi_2S_3's lamellar structure, characterized by covalent bonds in-plane and weaker Van-der-Waals interactions out-of-plane, it can be mechanically exfoliated much like other metal dichalcogenides.[12,14,32,33] Therefore, we treated the Bi_2S_3 in the same way as WS_2 and MoS_2 regarding surfactant choice and its concentrations. For experimental analysis we utilized TEM, SEM, Raman spectroscopy, UV-Vis absorption and DLS analysis for quantifying the concentration, band gap, average particle size and overall appearance of the suspended particles in the same manner as previous. In general, the highest yields of exfoliated product were obtained for 8.2 mM SHS surfactant independent from the TMDC. However, the maximum yield of Bi_2S3_3 of 1.4 % reaches almost half of the obtained yield for WS_2 as reported in **publication 3**. Further, the largest colloidal stability was achieved using SDBS as surfactant for produced suspensions. Using the suspensions, it was possible for Micaela Pozzati to show that a tuneable bandgap of the Bi_2S_3 thin films can be achieved by changing deposition parameters and film thickness.

colloids and interfaces

MDPI

Article

Water-Based Bi_2S_3 Nano-Inks Obtained with Surfactant-Assisted Liquid Phase Exfoliation and Their Direct Processing into Thin Films

Micaela Pozzati [1], Felix Boll [2], Matteo Crisci [2], Sara Domenici [1], Francesco Scotognella [1], Bernd Smarsly [2], Teresa Gatti [1,2,*] and Mengjiao Wang [1,*]

[1] Dipartimento Scienza Applicata e Tecnologia (DISAT), Politecnico di Torino, Corso Duca degli Abruzzi 24, 10129 Torino, Italy; micaela.pozzati@polito.it (M.P.); sara.domenici@polito.it (S.D.); francesco.scotognella@polito.it (F.S.)

[2] Center for Materials Research (LaMa), Justus Liebig University, Heinrich-Buff-Ring 17, 35392 Giessen, Germany; felix.boll@phys.chemie.uni-giessen.de (F.B.); matteo.crisci@phys.chemie.uni-giessen.de (M.C.); bernd.smarsly@phys.chemie.uni-giessen.de (B.S.)

* Correspondence: teresa.gatti@polito.it (T.G.); mengjiao.wang@polito.it (M.W.)

Abstract: Bi_2S_3 has gained considerable attention as a semiconductor for its versatile functional properties, finding application across various fields, and liquid phase exfoliation (LPE) serves as a straightforward method to produce it in nano-form. Till now, the commonly used solvent for LPE has been N-Methyl-2-pyrrolidone, which is expensive, toxic and has a high boiling point. These limitations drive the search for more sustainable alternatives, with water being a promising option. Nonetheless, surfactants are necessary for LPE in water due to the hydrophobic nature of Bi_2S_3, and organic molecules with amphoteric characteristics are identified as suitable surfactants. However, systematic studies on the use of ionic surfactants in the LPE of Bi_2S_3 have remained scarce until now. In this work, we used sodium dodecyl sulfate (SDS), sodium dodecylbenzene sulfonate (SDBS) and sodium hexadecyl sulfonate (SHS) as representative species and we present a comprehensive investigation into their effects on the LPE of Bi_2S_3. Through characterizations of the resulting products, we find that all surfactants effectively exfoliate Bi_2S_3 into few-layer species. Notably, SDBS demonstrates superior stabilization of the 2D layers compared to the other surfactants, while SHS becomes the most promising surfactant for obtaining products with high yield. Moreover, the resulting nano-inks are used for fabricating films using spray-coating, reaching a fine tuning of band gap by controlling the number of cycles, and paving the way for the utilization of 2D Bi_2S_3 in optoelectronic devices.

Keywords: Bi_2S_3; surfactant-assisted liquid phase exfoliation; nano-ink; spray-coating

Citation: Pozzati, M.; Boll, F.; Crisci, M.; Domenici, S.; Scotognella, F.; Smarsly, B.; Gatti, T.; Wang, M. Water-Based Bi_2S_3 Nano-Inks Obtained with Surfactant-Assisted Liquid Phase Exfoliation and Their Direct Processing into Thin Films. *Colloids Interfaces* **2024**, *8*, 28. https://doi.org/10.3390/colloids8030028

Received: 29 February 2024
Revised: 23 April 2024
Accepted: 24 April 2024
Published: 30 April 2024

1. Introduction

Metal chalcogenides cover a large family of 2D materials, which have gained recent attention due to their potential significance in many technological applications [1–6]. Among them, Bi_2S_3 emerges as a potential candidate in thermoelectric applications, energy harvesting, biomedicine, sensors and optoelectronics, due to its low thermal conductivity, strong spin-orbit coupling, direct band structure and high absorption coefficient [7–12]. As shown in Figure 1a, Bi_2S_3 possesses a lamellar structure in which the bismuth and sulfur atoms are bonded through strong covalent bonds inside the layer, and these layers are linked by van der Waals (vdW) forces to one another [13]. This unique layered structure allows the vdW interactions between layers in bulk Bi_2S_3 to be broken by mechanical force, thus producing 2D layered Bi_2S_3.

Colloids Interfaces **2024**, *8*, 28

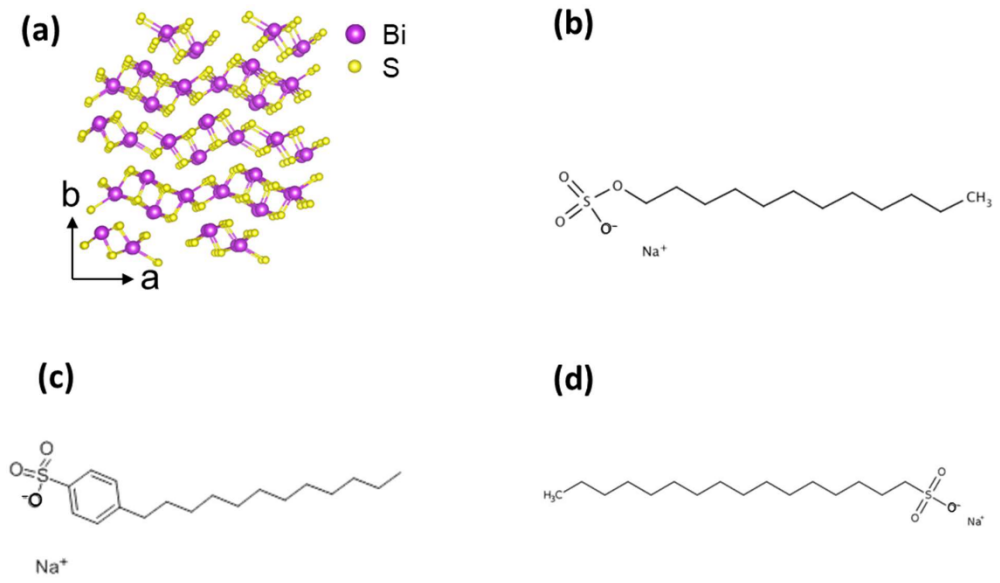

Figure 1. (**a**) Crystalline structure of Bi_2S_3 along the *c*-axis highlighting the vdW architecture and molecular structures of (**b**) SDS, (**c**) SDBS and (**d**) SHS.

Liquid phase exfoliation (LPE) is a simple and scalable technique used to produce 2D layered materials. This procedure consists of delaminating the layers of the material dispersed in a solvent by mechanical force. In sonication-assisted LPE, the sonication generates the growth and collapse of microbubbles in the solvents, thus resulting in shock waves. These waves can exert shear forces on bulk materials, disrupt the vdW interactions between the layers of the 2D structures and ultimately lead to the formation of layered materials [14–16]. The type of solvent plays an important role in the efficiency of the exfoliation, and the solvent typically used for exfoliating Bi_2S_3 is N-methyl-2-pyrrolidone (NMP) [17–20]. Considering the high cost, high boiling point and toxicity of NMP, replacing it with water has become a more eco-friendly and sustainable strategy.

Since Bi_2S_3 is hydrophobic, surfactants are needed to separate and stabilize the nanocrystals in H_2O. In LPE, the frequently used surfactants are anionic surfactants that can counteract vdW attraction between the material layers, inhibiting restacking by electrostatic force with each single layer [21,22]. One of the most employed surfactants for metal chalcogenides is the anionic surfactant sodium dodecyl sulfate (SDS), and its structure is shown in Figure 1b [23,24]. The molecule contains an anion with C_{12} alkyl chain and SO_4^- group on the terminal of the carbon chain. The carbon chains construct semi-micelles on the basal plane of metal chalcogenides to prevent the restacking of the exfoliated nanosheets, while the terminal SO_4^- group forms a H-bond with water and stabilizes the exfoliated layers [25]. Our previous work also proves the possibility of exfoliation of Bi_2S_3 with SDS [26]. Moreover, surfactants with a similar structure to SDS but different functional groups have been reported in LPE, such as sodium dodecylbenzene sulfonate (SDBS). It has been reported that the benzene ring in SDBS improves the colloidal stability of exfoliated MoS_2 [27]. Furthermore, it has been reported that by changing the alkyl chain length, the stability of the exfoliated suspension and optoelectronic property of the colloidal nanocrystals can be optimized as well [28]. However, a study regarding the influence of the carbon chain of the surfactant on the LPE process is still missing. In addition to the type of surfactant, the concentration of the surfactant significantly influences the quality and yield of exfoliated metal chalcogenides [21,29]. Therefore, surfactant concentration will be a crucial parameter in optimizing the harvesting of exfoliated Bi_2S_3 with good quality and high yield.

Based on the above background knowledge, in this work we systematically investigate how surfactant type and concentration impact the quality of exfoliated Bi_2S_3. Three different surfactants have been chosen, SDS, SDBS and sodium hexadecyl sulfate (SHS), to compare the influence of different functional groups and carbon chain lengths on the LPE of Bi_2S_3 (Figure 1). It has been reported that controlling the concentration of the surfactants less than their critical micelle concentration (CMC) can result in better-quality exfoliated samples, while other studies reached contradictory conclusions [30,31]. In our study, we set the concentrations from 8.2 mM to 0.5 mM for all the surfactants for better comparison, considering that the CMCs of SDS, SDBS and SHS are 8.2, 2.7 and 0.55 mM, respectively [32–35]. By assessing the band gap, stability and yield of the exfoliated Bi_2S_3, it is found that SHS results in the largest band gap and yield, while the colloidal suspension is more stable with SDBS. As to the influence of the concentration, a higher concentration of all the surfactants tends to form exfoliated samples with a higher band gap. Only SHS shows a correlation between the concentration and the sample yield, and the record yield of 1.4% is obtained with 8.2 mM SHS. Moreover, concentration does not influence the stability of the suspension. Eventually, we also show that the suspension can be made into Bi_2S_3 thin films with a tunable band gap through ultrasonic spray-coating, which is a promising perspective for the use of these nano-inks in the field of eco-friendly, solution-processed optoelectronics.

2. Materials and Methods

2.1. Materials and LPE Process

Fluorine-doped tin oxide (FTO) coated glass slides, Bi_2S_3 (99%), SDS and SDBS were purchased from Sigma Aldrich and used without further purification. SHS was purchased from TCI Chemicals and used without further purification. All the exfoliations were performed using a Baudelin Sonopuls tip sonicator and the samples were cooled to 0 °C with an ice bath during the process. The tip sonicator operated with 80% power using pulses of 1 s on/1 s off for 4 h.

In all the experiments, the suspension volume was 150 mL with a concentration of the bulk materials of 10 mg/mL. The concentrations of all the surfactants were adjusted to 8.2 mM, 4.1 mM, 2.0 mM, 1.0 mM and 0.5 mM, respectively. The suspensions obtained after the sonication were centrifuged firstly for 30 min at 1500 rpm to reserve the supernatant, then this supernatant was centrifuged for 30 min at a higher speed of 3000 rpm to obtain the final colloidal suspensions. A Universal 320 Hettich centrifuge was employed for the centrifuge treatment.

Thin Bi_2S_3 films were fabricated using the Nadetech Innovations Ultrasonic Lab Spray Coater on FTO glass substrates measuring 15 × 15 mm, and the suspensions from the previous steps were directly used as inks for the spray-coating. We used N_2 pressure with 0.10 bar to get a uniform spray. The speed of the nozzle was 400 mm/min, and the working flow of the suspension was 25 mL/h.

2.2. Characterizations

UV-visible (UV-vis) absorption spectra of the colloidal suspensions were captured using a Goebel Uvikon spectrometer, employing a quartz cuvette with an optical length of 1 cm. The spectra were recorded from 350 to 1000 nm with a scan interval of 0.25 nm. Raman spectra were acquired using a Bruker Senterra instrument equipped with a 532 nm laser excitation source at a power of 2 mW. Integration time was set to 6 s with 60 co-additions. Samples were prepared by drop-casting suspensions onto silicon slides for analysis. Dynamic Light Scattering (DLS) and Zeta potential (ZP) measurements were conducted on a Malvern Zetasizer Nano-ZS device, averaging results from three separate measurements for accuracy. Measurements were performed in Rotilabo precision glass cuvettes with a light path of 10 mm and a volume of 3.5 mL. High-Resolution Transmission Electron Microscopy (HRTEM) imaging was performed using a non-aberration-corrected Transmission Electron Microscope (TALOS F200X, Thermo Scientific, Eindhoven, The Netherlands) operating at

200 kV. Images were captured using a 16Mpxls CMOS camera with an exposure time of 1 s. The fast Fourier transform (FFT) pattern was converted with the Velox software (Thermo Scientific Velox Software, Thermo Fisher Scientific Inc., Waltham, MA, USA).

2.3. Calculation Methods of the Sample Concentration

UV-vis spectra were employed to calculate the final concentration of Bi_2S_3. A calibration line was obtained using a set of dilutions from a suspension with a known concentration, and this concentration of samples was obtained using filtration of the products. The slope of the calibration line corresponds to the extinction coefficient of the dispersed material. The final concentrations of Bi_2S_3 samples were obtained with the Lambert-Beer law (Equation (1)):

$$A = \varepsilon bc \quad (1)$$

where A represents the absorbance of the material, ε denotes the extinction coefficient of the dispersed nanosheets, and c signifies the concentration of the suspension. Specifically, we utilized the absorption value at 500 nm as A. The value of ε is derived from calibration lines established using several standard Bi_2S_3 suspensions with known concentrations. For Bi_2S_3, the calculated ε is determined to be 7.4 mg/mL·cm.

To compare with the concentration calculated from UV-vis spectra, freeze-drying was used to obtain the final concentration as well. Before freeze-drying, dialysis was performed using a cellulose dialysis bag (Carl Roth) 14 kDa, filling each bag with 20–25 mL of the desired suspension and closing both sides with a plastic pin once filled. The bag was then left in a suitable beaker with Milli-Q water for 3 days, changing the water 3 times per day. Freeze-drying was performed at −10 °C for 16 h and at a pressure of 1 mPa.

3. Results and Discussion

3.1. Characterizations of the Resulting Nanomaterials

3.1.1. TEM Analysis

The exfoliated Bi_2S_3 nano-inks were prepared using the surfactant-assisted LPE method outlined in Section 2.1 and a typical exfoliated Bi_2S_3 sample was used to characterize the morphology and crystal structure of the colloids. As depicted in Figure 2a–c, nanosheets of irregular shapes are observed, predominantly appearing as a few layers of around 10 nm of thickness rather than single layers. The size distribution of the exfoliated samples ranges from 50 to 350 nm, with the size of around 150–200 nm as the dominate value (Figure S1). Study of the selected area electron diffraction (SAED) illustrates that the crystalline nanosheets can be indexed to orthorhombic structured Bi_2S_3 (ICSD: 30775) (Figure 2d). Figure 2e,f depict the HRTEM image and its corresponding FFT pattern, revealing lattice planes within the nanosheets. These planes exhibit spacings of 0.79 nm and 0.36 nm, indicative of the 101 and 301 planes, respectively. This small nanosheet shows a [010] orientation, since it is possible to break the bulk Bi_2S_3 in the direction of [010] to obtain nanoribbons (Figure 1a) [31].

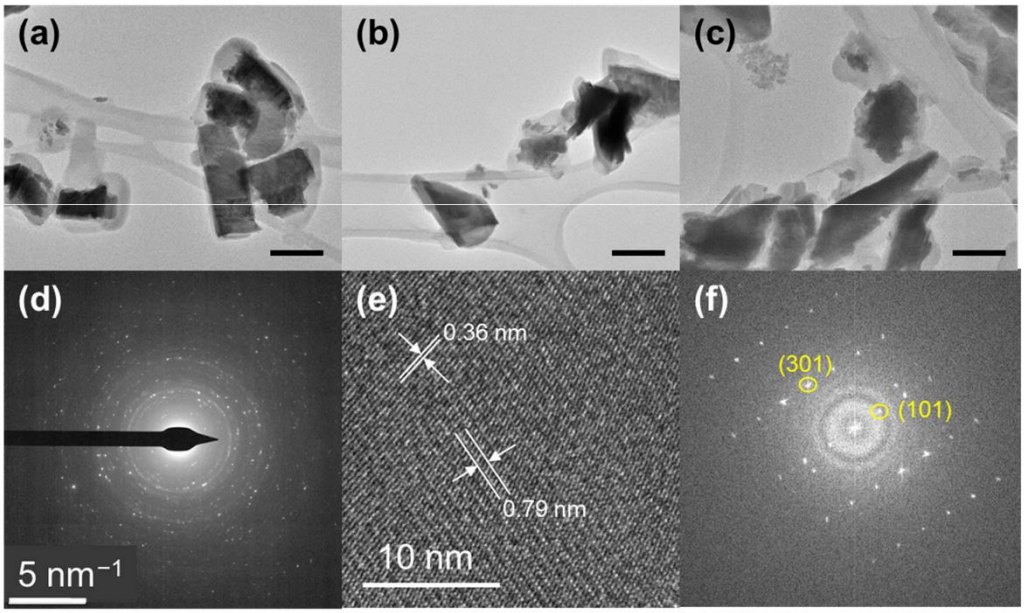

Figure 2. TEM image of exfoliated Bi_2S_3 with (**a**) SDS, (**b**) SDBS and (**c**) SHS. The scale bar in each panel is 200 nm. (**d**) SAED pattern and (**e**) HRTEM of typical Bi_2S_3 nanosheets. (**f**) is the FFT pattern of region (**e**).

3.1.2. UV-Vis Analysis

Figure 3a–c show the UV-vis absorption spectra of Bi_2S_3 samples exfoliated with different types and concentrations of surfactants. It can be observed that there is a growing absorption intensity when the wavelength decreases for all the samples [21,22]. In samples with the highest surfactant concentration, there is a notable rapid decline in absorption intensity beyond 550 nm. This phenomenon could likely be attributed to the strong influence exerted by the elevated concentration of surfactants (Figure S2). As a consequence, this high concentration of surfactant gives less scattering in the spectrum. The band gap of all the samples was calculated with the Tauc Plot equation (Equation (2)):

$$(\alpha h\upsilon)^{1/n} = A\,(h\upsilon - E_g) \quad (2)$$

where α is the absorption coefficient, h is the Plank constant, υ is the frequency, E_g is the band gap energy and n is 1/2 for Bi_2S_3 with a direct band gap [36]. The values are shown in Figure 3d–f and Table 1. In general, all the samples have a broader band gap ranging from 1.74 to 2.44 eV in comparison to the band gap of bulk Bi_2S_3 (1.3 eV) [37]. This is evidence that all the samples were exfoliated to nanoscale. Regarding the impact of surfactant type, SDS yielded nano-inks with a lower band gap ranging from 1.85 to 2.03 eV, whereas samples with SHS exhibited a higher band gap range of 2.08 to 2.3 eV. This indicates that samples derived from SHS possess a smaller size in terms of thickness or particle size. Concerning surfactant concentration, the overarching trend is that higher concentrations lead to broader band gaps. It is worth noting the detected non-linear change in band gap with surfactant concentration. This complexity arises from various factors influencing the band gap: not only is it connected to quantum confinement effects, but it is also significantly impacted by the atomistic arrangement on the nanosheet surface, which is dictated by the nature of the capping surfactant [28]. Though higher concentrations are not strictly related to higher band gap, all these concentrations still result in samples with a widened band gap, which is proof that all the concentrations can exfoliate bulk Bi_2S_3.

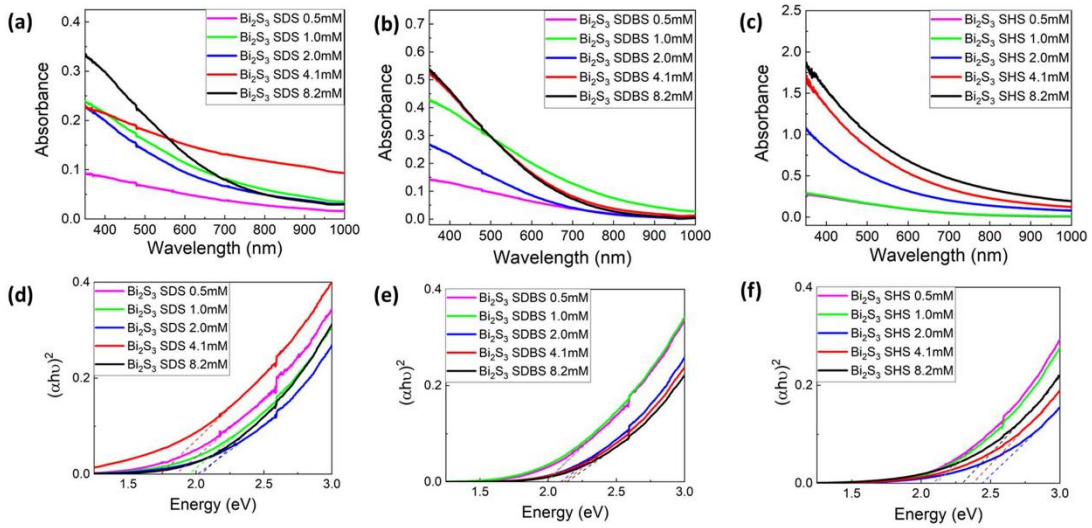

Figure 3. UV-vis absorption spectra and corresponding Tauc plots of exfoliated Bi_2S_3 nano-inks with (**a**,**d**) SDS, (**b**,**e**) SDBS and (**c**,**f**) SHS.

Table 1. Optical band gap values extrapolated from Tauc plots of all exfoliated Bi_2S_3 nano-inks.

Surfactant	Surf. Concentration (mM)	Band Gap (eV)
SDS	8.2	2.03
	4.1	1.74
	2.0	2.01
	1.0	1.95
	0.5	1.85
SDBS	8.2	2.13
	4.1	2.11
	2.0	2.10
	1.0	1.99
	0.5	1.97
SHS	8.2	2.30
	4.1	2.37
	2.0	2.44
	1.0	2.10
	0.5	2.08

3.1.3. Raman Analysis

Figure 4 displays the Raman spectra of Bi_2S_3 samples with all the surfactants. It is possible to identify two main active modes, namely the B_{1g} and A_g Raman modes, in all the samples. The peaks located at 188 cm^{-1} and 237 cm^{-1} belong to B_{1g} mode, which arises from longitudinal vibrations, while the A_g transversal modes are noticeable at 106 cm^{-1}, 170 cm^{-1} and 265 cm^{-1} [38] After the exfoliation of the material, the frequency of the longitudinal optical phonon is higher, so the ratio between the two modes decreases [39]. The two modes with the most identifiable peaks (B_{1g} mode at 237 cm^{-1} and A_g mode at 265 cm^{-1}) were chosen to characterize the surficial property of the exfoliated samples. Specifically, the intensity ratio of A_g mode and B_{1g} mode is calculated to determine whether the samples were exfoliated [19,40]. In bulk Bi_2S_3, the A_g/B_{1g} ratio is 1.68 [26], while for all the exfoliated Bi_2S_3, the A_g/B_{1g} ratio ranges from 1.02 to 1.32 (Table 2), which is clear evidence that all the samples were exfoliated, and the surficial molecular vibration modes are different from the bulk Bi_2S_3. When comparing band gap values with A_g/B_{1g} ratios

Colloids Interfaces **2024**, *8*, 28

in Raman spectra, a linear correlation is not emerging. Initially, a lower ratio of A_g/B_{1g} suggests a higher band gap, yet this association is due to the quantum confinement effect, which is related to layer count, nanosheet anisotropy and average size. In these experiments, the average size of the nanosheets is not controlled, thus it is difficult to build a linear relationship between the average number of layers and the band gap values. However, there is no report in the literature related to the values of A_g/B_{1g} ratio and its connection to any layer property of exfoliated Bi_2S_3, thus we do not obtain any further information from Raman spectra. Concerning the Raman mode shift in the samples, a distinct shift compared to bulk Bi_2S_3 was not observed, except for Bi_2S_3 SDBS 8.2 mM. This is likely due to the fact that the frequency of the Raman mode does not vary significantly whether Bi_2S_3 is in bulk form or exfoliated. Another prominent mode observed in the samples using SDBS appears at around 122 cm^{-1}. This mode corresponds to a Bi-O stretching characteristic of β-Bi_2O_3, which may be associated with a non-stable oxide phase likely induced by laser irradiation [41].

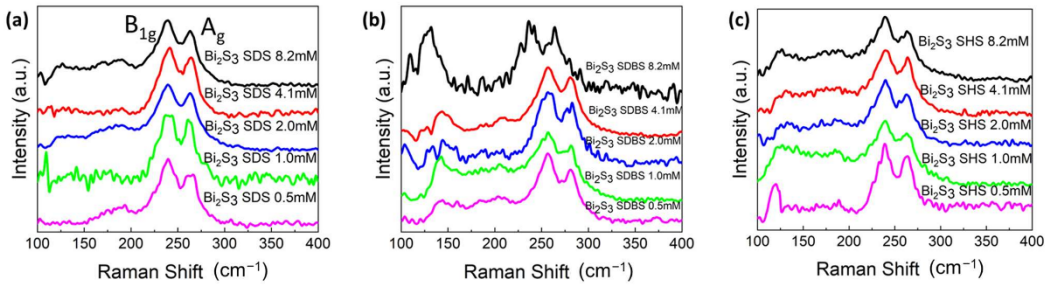

Figure 4. Raman spectra of Bi_2S_3 (**a**) SDS, (**b**) SDBS and (**c**) SHS.

Table 2. A_g/B_{1g} ratio of all Bi_2S_3 samples.

2D Material	Surfactant	Surf. Concentration (mM)	A_g/B_{1g} Ratio
Bi_2S_3	SDS	8.2	1.20
		4.1	1.18
		2.0	1.15
		1.0	1.07
		0.5	1.32
Bi_2S_3	SDBS	8.2	1.32
		4.1	1.25
		2.0	1.19
		1.0	1.17
		0.5	1.02
Bi_2S_3	SHS	8.2	1.30
		4.1	1.12
		2.0	1.30
		1.0	1.25
		0.5	1.25

3.1.4. Zeta Potenzial and DLS

ZP analysis was conducted to evaluate the stability of the Bi_2S_3 colloidal suspensions from the surfactant-assisted LPE method. Generally, when the ZP values are between −20 and −30 mV, the suspension shows a short-term stability, while samples with −30 mV ZP values show a long-term stability of up to several months [42]. Figure 5a illustrates that all Bi_2S_3 water-based inks exhibit a ZP value below −30 mV, indicating long-term colloidal stability of more than one month. Specifically, the ZP values of most Bi_2S_3 samples are in the range between −30 and −50 mV, and the surfactant concentration appears to

have minimal impact on them. An exceptional value of −80 mV is observed for the ink produced using 8.2 mM of SDBS, indicating that the colloidal suspension obtained under these experimental conditions exhibits outstanding stability.

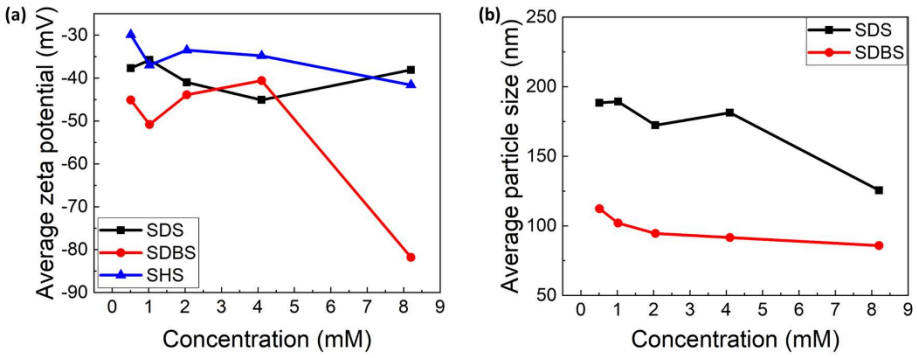

Figure 5. Zeta potential (**a**) and DLS (**b**) trends for the exfoliated Bi_2S_3 nano-inks.

The average particle size of each sample was estimated by DLS and the results are shown in Figure 5b. The average particle size of Bi_2S_3 remains approximately 100 nm for SDBS, and the particle size shows a slight decrease when the surfactant concentration increases. Upon comparing the concentration with the obtained band gap values, a positive correlation becomes evident. Higher band values correspond to increased surfactant concentration, resulting in a slight reduction in the average particle size. The sizes range from approximately 110 nm to 90 nm, spanning surfactant concentrations of 0.5 to 8.2 mM, respectively. With SDS, the average particle size of Bi_2S_3 ranges from around 200 nm to 125 nm from the lowest to highest surfactant concentration and it drops dramatically when increasing the concentration of SDS. It is apparent that some inconsistencies emerge in band gap values versus average particle size calculated from DLS. This discrepancy may arise from the fact that for 2D and 1D materials, DLS primarily estimates the lateral length of the nanosheet rather than the thickness [43]. Since both small thickness and small lateral length of the nanosheets correspond to higher band gap values, because of the quantum confinement, the influence of layer thickness is not considered in the values of DLS, thus causing the mismatch between band gap values and average particle size, as measured from DLS. Additionally, surface chemistry can influence band gap values as well, and this factor has not been well studied for exfoliated Bi_2S_3 with surfactants yet. Meanwhile, the trend in particle size using SHS shows a rough range mostly under 200 nm, but little correlation with the concentration of SHS and band gap values, as shown in Figure S3. This trend in particle size agrees with the result from the band gap calculation in Table 1, in which we expect samples with SDS to have roughly larger size than samples with SDBS.

3.2. Yield and Final Concentration of the Nanomaterials

The yield of the exfoliated material is another crucial metric used to evaluate the effects of the surfactants and the associated experimental variables. As described in Section 2.3, UV-vis spectra are employed to quantify the final concentration of the samples. All the results are listed in Table 3 and shown in Figure 6. Apparently, samples with SHS demonstrate superior values compared to those treated with the other two surfactants. Especially with surfactant concentrations higher than 2.0 mM, the concentration of SHS reaches more than 0.05 mg/mL and yields more than 0.5%, while all the samples obtained with SDS and SDBS have a concentration lower than this value. Moreover, higher SHS concentration can result in higher yield, and we are able to obtain the maximum sample concentration of 0.14 mg/mL and yield of 1.4% in this work with 8.2 mM of SHS.

Table 3. Product concentration and yield for LPE Bi_2S_3 calculated from Lambert-Beer law and from weighted freeze-dried samples.

Surfactant	Surfactant Concentration (mM)	Product Concentration with UV-Vis Absorption (mg/mL)	Product Concentration with Freeze-Drying (mg/mL)	Yield (%)
SDS	8.2	0.03		0.3
	4.1	0.02		0.2
	2.0	0.02		0.2
	1.0	0.02		0.2
	0.5	0.01		0.1
SDBS	8.2	0.04	0.04	0.4
	4.1	0.04		0.4
	2.0	0.02		0.2
	1.0	0.04		0.4
	0.5	0.01		0.1
SHS	8.2	0.14	0.08	1.4
	4.1	0.11	0.44	1.1
	2.0	0.07		0.7
	1.0	0.02		0.2
	0.5	0.02		0.2

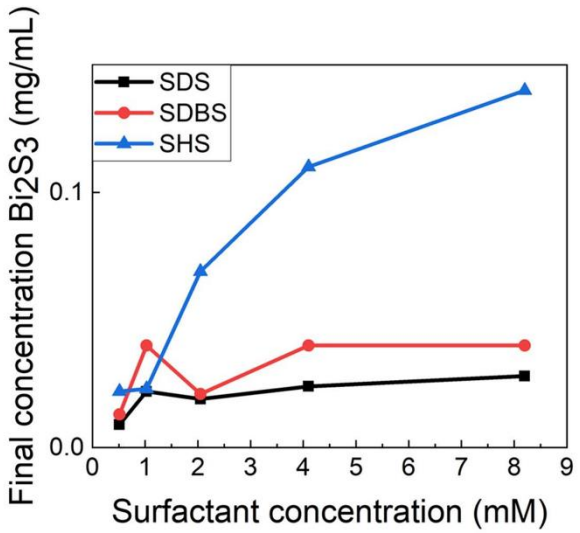

Figure 6. Final concentration exfoliated Bi_2S_3 nano-inks.

To validate this data, selected samples with higher concentrations were subjected to freeze-drying after removing the surfactant through dialysis, and different values compared to the calculated concentration from UV-vis spectra were obtained. This is probably due to the residual presence of surfactant in the dispersion or the loss of samples during the operation.

3.3. Production of Thin Films with Ultrasonic Spray-Coating

To test the potential for solution-processing of the prepared, water-based nano-inks, we produced thin films of Bi_2S_3 using the ultrasonic spray-coating method, which is very suitable for deposition of nanomaterial inks and might pave the way to potential applications of these colloids in the sustainable fabrication of optoelectronic devices. With the Bi_2S_3 nano-ink exfoliated with 2.0 mM of SDBS, we sprayed for multiple steps on

transparent substrates, to be able to detect the change in band gap as a function of the number of layers deposited. The colloidal ink was directly used without further dilution, since the concentration of the product was already very low (0.02 mg/mL). Figure 7 shows the UV-vis spectra of the thin films prepared from spraying exfoliated Bi_2S_3. From the corresponding Tauc plots, the band gap values of the Bi_2S_3 thin films are found to be 1.43 and 1.26 eV for 30 and 50 spray-steps, respectively (Figure 7b). The intense absorption is consistent with the remarkable extinction coefficient of Bi_2S_3 [44]. Furthermore, the absorption spectrum is clearly characterized by fringes. These fringes are evidently due to the FTO film between the glass substrate and Bi_2S_3 thin films. In fact, it is remarkable that, for the two different Bi_2S_3 thin films, the spectral position of the fringes is the same. It is evident that by adjusting the number of sprayed layers, the tuning of the band gap of the Bi_2S_3 film is possible. These values are smaller than the band gaps of the nanosheets in the suspension (Table 1), which is likely due to the nanosheets aggregation at the solid state, within the film. Figure 7c,d display the SEM images of the as-synthesized thin films. In Figure 7d, after 50 layers of spray coating, the sample shows a uniform Bi_2S_3 surface, while the sample with 30 layers is not fully covering the transparent conductive oxide substrate. The full-view images of Figure 7c,d are shown in Figure S4.

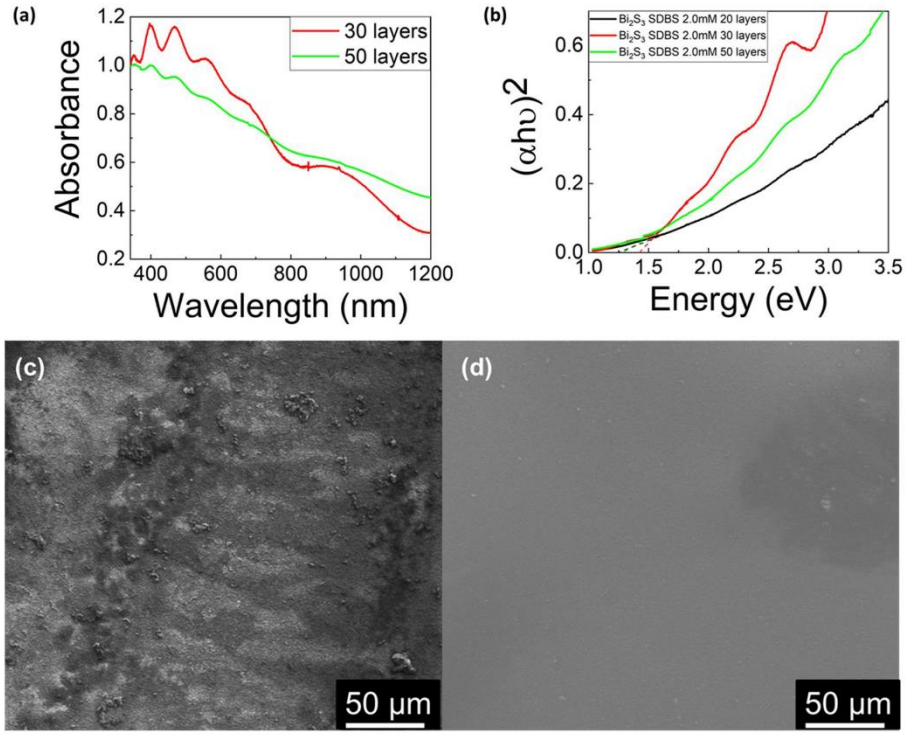

Figure 7. (**a**) UV-vis spectra and (**b**) Tauc Plot of Bi_2S_3 thin films produced from multiple ultrasonic spray-coating steps from the 2 mM SDBS nano-ink. Top-view SEM images of the Bi_2S_3 thin films with (**c**) 30 and (**d**) 50 sprayed layers.

4. Conclusions

In conclusion, we conducted a systematic investigation into the surfactant-assisted LPE of Bi_2S_3. Utilizing three distinct ionic surfactants (SDS, SDBS and SHS), we performed exfoliation processes in water to generate stable colloidal suspensions, through a green method that is a good alternative to the use of toxic organic solvents. Through comprehensive characterization employing various techniques, we compared the quality of the exfoliated 2D Bi_2S_3 nanosheets present in the inks in terms of layer size, colloidal stability

and product yield. It is found that with SHS, an exfoliated Bi_2S_3 with smaller particle size and higher yield can be obtained, but SDBS can lead to more stable colloidal suspensions compared to the other two surfactants investigated. Moreover, SHS with higher concentrations results in a higher yield in the exfoliated product, with the 8.2 mM concentration providing the optimal value of 1.4%. Considering that the CMC of SHS is only 0.55 mM, our results surprisingly indicate that the best concentration is high above the value of CMC. Moreover, we found that uniform Bi_2S_3 films with a tunable band gap can be obtained with ultrasonic spray-coating, while further optimization of the film fabrication process is needed to obtain films for practical applications in optoelectronic devices.

Supplementary Materials: The following supporting information can be downloaded at: https://www.mdpi.com/article/10.3390/colloids8030028/s1, Figure S1: Histogram of the distribution of particle size Bi_2S_3; Figure S2: UV-vis spectrum of SDS 8.2 mM; Figure S3: DLS Bi_2S_3 SHS; Figure S4: SEM images of the Bi_2S_3 thin films with (a) 30 (b) 50 layers. Table S1: Parameters of LPE process.

Author Contributions: Conceptualization, T.G. and M.W.; methodology, M.P., F.B., S.D. and M.C.; software, M.P.; validation, M.P. and M.W.; formal analysis, M.P., M.C., F.S. and F.B; investigation, M.W.; resources, B.S. and T.G.; data curation, M.P.; writing—original draft preparation, M.P.; writing—review and editing, M.W., T.G. and F.S.; supervision, M.W.; project administration, B.S. and T.G.; funding acquisition, T.G. and M.W. All authors have read and agreed to the published version of the manuscript.

Funding: This research was funded by the ERC StG project JANUS BI (grant agreement No. [101041229]) and by the Starting Grant ERC program of Compagnia di San Paolo.

Data Availability Statement: The data from this study are available upon request made to the corresponding author.

Acknowledgments: M.W. and T.G. thank Fondazione Compagnia di San Paolo for financial support through the "Bando TRAPEZIO—Paving the way to research excellence and talent attraction". M.C. and F.B. acknowledge the support of the European Commission through the H2020 FET-PROACTIVE-EIC-07-2020 project LIGHT-CAP (grant number 101017821).

Conflicts of Interest: The authors declare no conflicts of interest.

References

1. Shawky, A.; Alahmadi, N.; Mohamed, R.M.; Zaki, Z.I. Bi_2S_3-Sensitized TiO_2 Nanostructures Prepared by Solution Process for Highly Efficient Photoreduction of Hexavalent Chromium Ions in Water Under Visible Light. *Opt. Mater.* **2022**, *124*, 111964. [CrossRef]
2. Ott, S.; Wolff, N.; Rashvand, F.; Rao, V.J.; Zaumseil, J.; Backes, C. Impact of the MoS_2 Starting Material on the Dispersion Quality and Quantity after Liquid Phase Exfoliation. *Chem. Mater.* **2019**, *31*, 8424–8431. [CrossRef]
3. Han, M.; Jia, J. The Interlace of Bi_2S_3 Nanowires with TiO_2 Nanorods: An Effective Strategy for High Photoelectrochemical Performance. *J. Colloid Interface Sci.* **2016**, *481*, 91–99. [CrossRef] [PubMed]
4. Zhang, X.; Shi, Y.; Shi, Z.; Xia, H.; Ma, M.; Wang, Y.; Huang, K.; Wu, Y.; Gong, Y.; Fei, H.; et al. High-Pressure Synthesis of Single-Crystalline SnS Nanoribbons. *Nano Lett.* **2023**, *23*, 7449–7455. [CrossRef] [PubMed]
5. Barraza-Lopez, S.; Fregoso, B.M.; Villanova, J.W.; Parkin, S.S.P.; Chang, K. Colloquium: Physical Properties of Group-IV Monochalcogenide Monolayers. *Rev. Mod. Phys.* **2021**, *93*, 011001. [CrossRef]
6. Villanova, J.W.; Kumar, P.; Barraza-Lopez, S. Theory of Finite-Temperature Two-Dimensional Structural Transformations in Group-IV Monochalcogenide Monolayers. *Phys. Rev. B* **2020**, *101*, 184101. [CrossRef]
7. Xie, Y.; Zhou, Y.; Gao, C.; Liu, L.; Zhang, Y.; Chen, Y.; Shao, Y. Construction of AgBr/BiOBr S-Scheme Heterojunction Using Ion Exchange Strategy for High-Efficiency Reduction of CO_2 to CO under Visible Light. *Sep. Purif. Technol.* **2022**, *303*, 122288. [CrossRef]
8. Bai, Y.; Ouyang, T.; Li, X.; Yan, Y.; Kong, Z.; Ma, X.; Li, Z.; Li, Z.; Cai, X.; Cai, J.; et al. Boosting the Thermoelectric Performance of n-Type Bi_2S_3 by Compositing rGO. *J. Alloys Compd.* **2023**, *933*, 167814. [CrossRef]
9. Zhao, F.; Sheng, H.; Sun, Q.; Wang, J.; Liu, Q.; Hu, Z.; He, B.; Wang, Y.; Li, Z.; Liu, X. Harvesting the Infrared Part of Solar Light to Promote Charge Transfer in Bi_2S_3/WO_3 Photoanode for Enhanced Photoelectrochemical Water Splitting. *J. Colloid Interface Sci.* **2022**, *621*, 267–274. [CrossRef] [PubMed]
10. Xu, Y.; Chen, B.; Xu, L.; Zhang, G.; Cao, L.; Liu, N.; Wang, W.; Qian, H.; Shao, M. Urchin-like Fe_3O_4@Bi_2S_3 Nanospheres Enable the Destruction of Biofilm and Efficiently Antibacterial Activities. *ACS Appl. Mater. Interfaces* **2023**, *16*, 3215–3231. [CrossRef] [PubMed]

11. Zamani, M.; Jamali-Sheini, F.; Cheraghizade, M. Visible-Range and Self-Powered Bilayer p-Si/n-Bi_2S_3 Heterojunction Photodetector: The Effect of Au Buffer Layer on the Optoelectronics Performance. *J. Alloys Compd.* **2022**, *905*, 164119. [CrossRef]
12. Yang, Z.; Wang, Y.; Zhang, D.; Chen, C. A Sensitizing Photoelectrochemical Sensing Platform Strategy Based on Bio-Etching Preparation of Bi_2S_3/BiOCl p–n Heterojunction. *Talanta* **2018**, *190*, 357–362. [CrossRef] [PubMed]
13. Smith, R.J.; King, P.J.; Lotya, M.; Wirtz, C.; Khan, U.; De, S.; O'Neill, A.; Duesberg, G.S.; Grunlan, J.C.; Moriarty, G.; et al. Large-Scale Exfoliation of Inorganic Layered Compounds in Aqueous Surfactant Solutions. *Adv. Mater.* **2011**, *23*, 3944–3948. [CrossRef] [PubMed]
14. Li, Z.; Young, R.J.; Backes, C.; Zhao, W.; Zhang, X.; Zhukov, A.A.; Tillotson, E.; Conlan, A.P.; Ding, F.; Haigh, S.J.; et al. Mechanisms of Liquid-Phase Exfoliation for the Production of Graphene. *ACS Nano* **2020**, *14*, 10976–10985. [CrossRef] [PubMed]
15. Xu, Y.; Cao, H.; Xue, Y.; Li, B.; Cai, W. Liquid-Phase Exfoliation of Graphene: An Overview on Exfoliation Media, Techniques, and Challenges. *Nanomaterials* **2018**, *8*, 942. [CrossRef] [PubMed]
16. Sarkar, A.S.; Konidakis, I.; Gagaoudakis, E.; Maragkakis, G.M.; Psilodimitrakopoulos, S.; Katerinopoulou, D.; Sygellou, L.; Deligeorgis, G.; Binas, V.; Oikonomou, I.M.; et al. Liquid Phase Isolation of SnS Monolayers with Enhanced Optoelectronic Properties. *Adv. Sci.* **2023**, *10*, 2201842. [CrossRef] [PubMed]
17. Jawaid, A.; Nepal, D.; Park, K.; Jespersen, M.; Qualley, A.; Mirau, P.; Drummy, L.F.; Vaia, R.A. Mechanism for Liquid Phase Exfoliation of MoS_2. *Chem. Mater.* **2016**, *28*, 337–348. [CrossRef]
18. Hu, C.X.; Shin, Y.; Read, O.; Casiraghi, C. Dispersant-Assisted Liquid-Phase Exfoliation of 2D Materials beyond Graphene. *Nanoscale* **2021**, *13*, 460–484. [CrossRef] [PubMed]
19. Guo, Y.; Zhao, Q.; Yao, Z.; Si, K.; Zhou, Y.; Xu, X. Efficient Mixed-Solvent Exfoliation of Few-Quintuple Layer Bi_2S_3 and Its Photoelectric Response. *Nanotechnology* **2017**, *28*, 335602. [CrossRef] [PubMed]
20. Sarkar, A.S.; Stratakis, E. Dispersion Behaviour of Two Dimensional Monochalcogenides. *J. Colloid Interface Sci.* **2021**, *594*, 334–341. [CrossRef] [PubMed]
21. Griffin, A.; Nisi, K.; Pepper, J.; Harvey, A.; Szydłowska, B.M.; Coleman, J.N.; Backes, C. Effect of Surfactant Choice and Concentration on the Dimensions and Yield of Liquid-Phase-Exfoliated Nanosheets. *Chem. Mater.* **2020**, *32*, 2852–2862. [CrossRef]
22. Ying, G.G. Fate, Behavior and Effects of Surfactants and their Degradation Products in the Environment. *Environ. Int.* **2006**, *32*, 417–431. [CrossRef] [PubMed]
23. Gupta, A.; Arunachalam, V.; Vasudevan, S. Water Dispersible, Positively and Negatively Charged MoS_2 Nanosheets: Surface Chemistry and the Role of Surfactant Binding. *J. Phys. Chem. Lett.* **2015**, *6*, 739–744. [CrossRef] [PubMed]
24. Domínguez, H. Self-Aggregation of the SDS Surfactant at a Solid-Liquid Interface. *J. Phys. Chem. B* **2007**, *111*, 4054–4059. [CrossRef]
25. Yu, H.; Zhu, H.; Dargusch, M.; Huang, Y. A Reliable and Highly Efficient Exfoliation Method for Water-Dispersible MoS_2 Nanosheet. *J. Colloid Interface Sci.* **2018**, *514*, 642–647. [CrossRef] [PubMed]
26. Wang, M.; Crisci, M.; Pavan, M.; Liu, Z.; Gallego, J.; Gatti, T. New Insights into the Surfactant-Assisted Liquid-Phase Exfoliation of Bi_2S_3 for Electrocatalytic Applications. *Catalysts* **2023**, *13*, 551. [CrossRef]
27. Guan, Z.; Wang, C.; Li, W.; Luo, S.; Yao, Y.; Yu, S.; Sun, R.; Wong, C.P. A Facile and Clean Process for Exfoliating MoS_2 Nanosheets Assisted by a Surface Active Agent in Aqueous Solution. *Nanotechnology* **2018**, *29*, 425702. [CrossRef] [PubMed]
28. Zhang, B.; Wang, M.; Ghini, M.; Melcherts, A.E.M.; Zito, J.; Goldoni, L.; Infante, I.; Guizzardi, M.; Scotognella, F.; Kriegel, I.; et al. Colloidal Bi-Doped $Cs_2Ag_{1-x}Na_xInCl_6$ Nanocrystals: Undercoordinated Surface Cl Ions Limit Their Light Emission Efficiency. *ACS Mater. Lett.* **2020**, *2*, 1442–1449. [CrossRef]
29. Lotya, M.; King, P.J.; Khan, U.; De, S.; Coleman, J.N. High-Concentration, Surfactant-Stabilized Graphene Dispersions. *ACS Nano* **2010**, *4*, 3155–3162. [CrossRef]
30. Abreu, B.; Almeida, B.; Ferreira, P.; Fernandes, R.M.F.; Fernandes, D.M.; Marques, E.F. A Critical Assessment of the Role of Ionic Surfactants in the Exfoliation and Stabilization of 2D Nanosheets: The Case of the Transition Metal Dichalcogenides MoS_2, WS_2 and $MoSe_2$. *J. Colloid Interface Sci.* **2022**, *626*, 167–177. [CrossRef] [PubMed]
31. Wang, S.; Yi, M.; Shen, Z. The Effect of Surfactants and Their Concentration on the Liquid Exfoliation of Graphene. *RSC Adv.* **2016**, *6*, 56705–56710. [CrossRef]
32. Markarian, S.A.; Harutyunyan, L.R.; Harutyunyan, R.S. The Properties of Mixtures of Sodium Dodecylsulfate and Diethylsulfoxide in Water. *J. Solution Chem.* **2005**, *34*, 361–368. [CrossRef]
33. Yang, K.; Zhu, L.; Xing, B. Enhanced Soil Washing of Phenanthrene by Mixed Solutions of TX100 and SDBS. *Environ. Sci. Technol.* **2006**, *40*, 4274–4280. [CrossRef] [PubMed]
34. Muzzalupo, R.; Gente, G.; La Mesa, C.; Caponetti, E.; Chillura-Martino, D.; Pedone, L.; Saladino, M.L. Micelles in Mixtures of Sodium Dodecyl Sulfate and a Bolaform Surfactant. *Langmuir* **2006**, *22*, 6001–6009. [CrossRef]
35. Antonioli Júnior, R.; Poloni, J.d.F.; Pinto, É.S.M.; Dorn, M. Interdisciplinary Overview of Lipopeptide and Protein-Containing Biosurfactants. *Genes* **2023**, *14*, 76. [CrossRef] [PubMed]
36. Messalea, K.A.; Zavabeti, A.; Mohiuddin, M.; Syed, N.; Jannat, A.; Atkin, P.; Ahmed, T.; Walia, S.; McConville, C.F.; Kalantar-Zadeh, K.; et al. Two-Step Synthesis of Large-Area 2D Bi_2S_3 Nanosheets Featuring High In-Plane Anisotropy. *Adv. Mater. Interfaces* **2020**, *7*, 2001131. [CrossRef]

37. Dhar, N.; Syed, N.; Mohiuddin, M.; Jannat, A.; Zavabeti, A.; Zhang, B.Y.; Datta, R.S.; Atkin, P.; Mahmood, N.; Esrafilzadeh, D.; et al. Exfoliation Behavior of van Der Waals Strings: Case Study of Bi_2S_3. *ACS Appl. Mater. Interfaces* **2018**, *10*, 42603–42611. [CrossRef] [PubMed]
38. Yang, D.; Lu, C.; Ma, J.; Luo, M.; Zhao, Q.; Jin, Y.; Xu, X. Enhanced Nonlinear Saturable Absorption from Type III van Der Waals Heterostructure Bi_2S_3/MoS_2 by Interlayer Electron Transition. *Appl. Surf. Sci.* **2021**, *538*, 147989. [CrossRef]
39. Zumeta-Dubé, I.; Ortiz-Quiñonez, J.L.; Díaz, D.; Trallero-Giner, C.; Ruiz-Ruiz, V.F. First Order Raman Scattering in Bulk Bi_2S_3 and Quantum Dots: Reconsidering Controversial Interpretations. *J. Phys. Chem. C* **2014**, *118*, 30244–30252. [CrossRef]
40. Clark, R.M.; Kotsakidis, J.C.; Weber, B.; Berean, K.J.; Carey, B.J.; Field, M.R.; Khan, H.; Ou, J.Z.; Ahmed, T.; Harrison, C.J.; et al. Exfoliation of Quasi-Stratified Bi_2S_3 Crystals into Micron-Scale Ultrathin Corrugated Nanosheets. *Chem. Mater.* **2016**, *28*, 8942–8950. [CrossRef]
41. Ni, J.; Bi, X.; Jiang, Y.; Li, L.; Lu, J. Bismuth Chalcogenide Compounds $Bi_{2\times3}$ (X=O, S, Se): Applications in Electrochemical Energy Storage. *Nano Energy* **2017**, *34*, 356–366. [CrossRef]
42. Kim, J.; Kwon, S.; Cho, D.H.; Kang, B.; Kwon, H.; Kim, Y.; Park, S.O.; Jung, G.Y.; Shin, E.; Kim, W.G.; et al. Direct Exfoliation and Dispersion of Two-Dimensional Materials in Pure Water via Temperature Control. *Nat. Commun.* **2015**, *6*, 8294. [CrossRef] [PubMed]
43. Ni, P.; Dieng, M.; Vanel, J.C.; Florea, I.; Bouanis, F.Z.; Yassar, A. Liquid Shear Exfoliation of MoS_2: Preparation, Characterization, and NO_2-Sensing Properties. *Nanomaterials* **2023**, *13*, 2502. [CrossRef] [PubMed]
44. Medles, M.; Benramdane, N.; Bouzidi, A.; Nakrela, A.; Tabet-Derraz, H.; Kebbab, Z.; Mathieu, C.; Khelifa, B.; Desfeux, R. Optical and Electrical Properties of Bi_2S_3 Films Deposited by Spray Pyrolysis. *Thin Solid Film.* **2006**, *497*, 58–64. [CrossRef]

3.6.1. Supporting Information – Publication 4

colloids and interfaces

MDPI

Supporting information

Water-Based Bi2S3 Nano-Inks Obtained with Surfactant-Assisted Liquid Phase Exfoliation and Their Direct Processing into Thin Films

Micaela Pozzati [1], Felix Boll [2], Matteo Crisci [2], Sara Domenici[1], Francesco, Scotognella,[1] Bernd Smarsly[2], Teresa Gatti [1,2]* and Mengjiao Wang [1]*

1 Dipartimento Scienza Applicata e Tecnologia (DISAT), Politecnico di Torino, Corso Duca degli Abruzzi 24, 10129 Torino, Italy; micaela.pozzati@polito.it (M.P.)
2 Center for Materials Research (LaMa), Justus Liebig University, Heinrich-Buff-Ring 17, 35392 Giessen, Germany
*Correspondence: teresa.gatti@polito.it (T.G.); mengjiao.wang@polito.it (M.W.)

Table S1: Parameters of LPE process

MC	Initial bulk concentration (mg/mL)	Surfactant	Surf. concentration (mM)	Exfoliation time
Bi_2S_3	10	SDS	8.2	3 h
			4.1	
			2.0	
			1.0	
			0.5	
Bi_2S_3	10	SDBS	8.2	3 h
			4.1	
			2.0	
			1.0	
			0.5	
Bi_2S_3	10	SHS	8.2	3 h
			4.1	
			2.0	
			1.0	
			0.5	

Figure S1: Histogram of the distribution of particle size Bi_2S_3

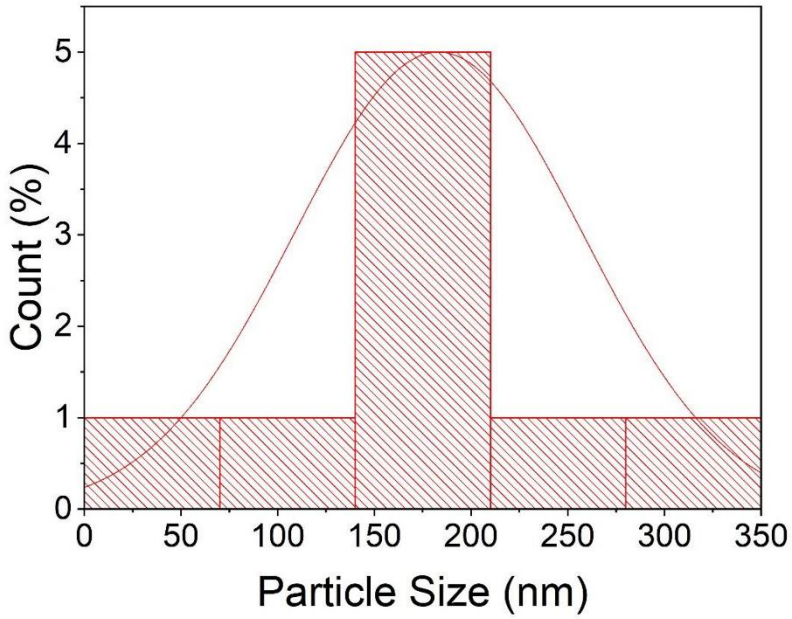

47

Figure S2: U-Vis spectrum of SDS 8.2mM.

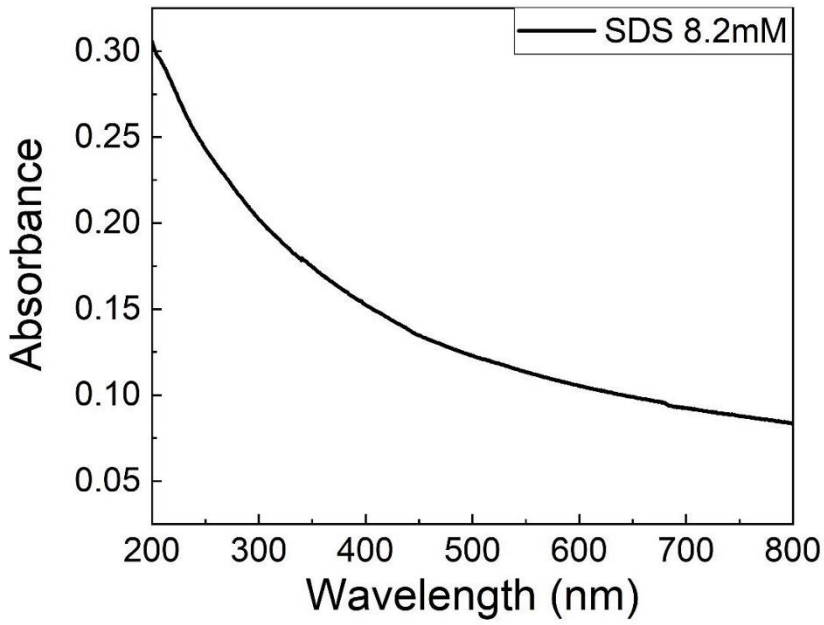

Figure S3: DLS of Bi_2S_3 SHS

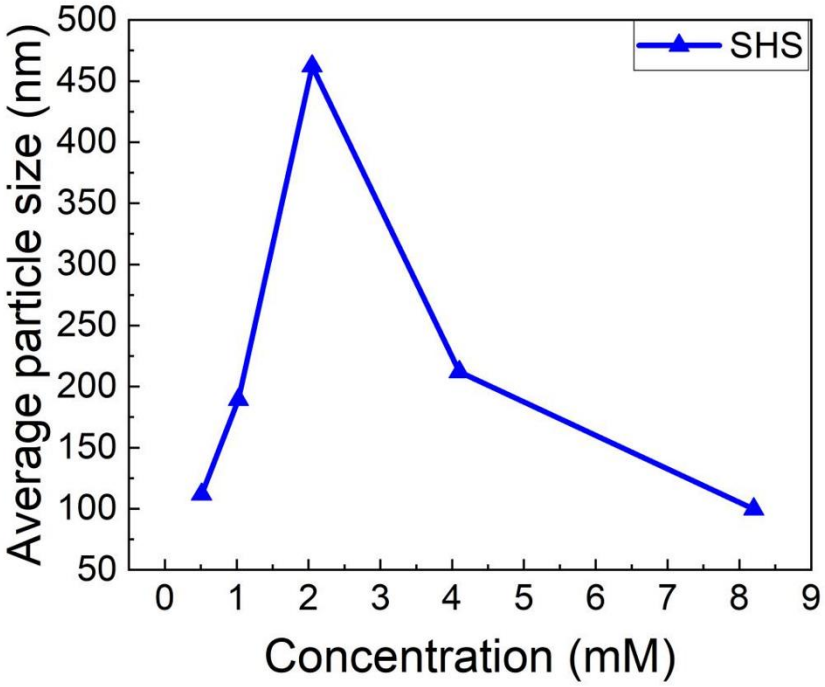

Figure S4: SEM images of the Bi_2S_3 thin films with (a) 30 (b) 50 layers.

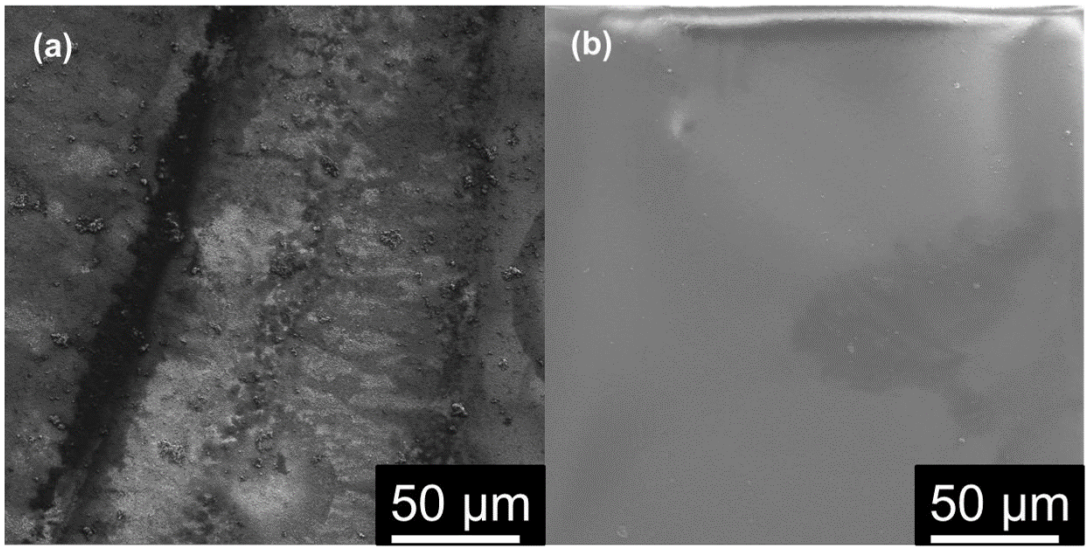

3.7. Publication 5

Matteo Crisi produced different hydrogels from WS_2 and PANI hybrids for electrochemical applications as supercapacitors. By using a cost-effective and straightforward templating approach with NaCl, he was able to tune the morphological characteristics and performance of these materials as energy storage devices. The observed capacitive behaviour was linked to structural changes induced by varying the ratio of active materials and NaCl loadings. It is desirable to integrate these hybrid materials into wearable and flexible electronics, utilizing gel or fiber-type scaffolds in future projects. To produce these hybrid materials, I contributed by exfoliating WS_2 in a sustainable approach using IPA and H_2O as solvents in a 7:3 v/v ratio.[14,223] As proof of exfoliation I also performed Raman spectroscopy measurements and UV-Vis spectroscopy measurements as well as analysed the excitons and vibration modes to show the shift and intensity changes of the wavenumber correlated to the degree of exfoliation.[12,58,87,241] By implementing conductive agents like PANI into hybrid materials the low conductivity of exfoliated WS_2 can be surmounted and combined properties are obtained as well as it was done with WS_2-carbon hybrids in **publication 5**.[9,168,169,242]

frontiers | Frontiers in Chemistry

TYPE Original Research
PUBLISHED 08 September 2022
DOI 10.3389/fchem.2022.1000910

OPEN ACCESS

EDITED BY
Hai-Chao Chen,
Qingdao University, China

REVIEWED BY
Pingping Yu,
Jiangnan University, China
Mao-Cheng Liu Liu,
Lanzhou University of Technology, China

*CORRESPONDENCE
Teresa Gatti,
teresa.gatti@phys.chemie.uni-giessen.de

SPECIALTY SECTION
This article was submitted to Electrochemistry, a section of the journal Frontiers in Chemistry

RECEIVED 22 July 2022
ACCEPTED 23 August 2022
PUBLISHED 08 September 2022

CITATION
Crisci M, Boll F, Merola L, Pflug JJ, Liu Z, Gallego J, Lamberti F and Gatti T (2022), Nanostructured 2D WS_2@PANI nanohybrids for electrochemical energy storage.
Front. Chem. 10:1000910.
doi: 10.3389/fchem.2022.1000910

Nanostructured 2D WS_2@PANI nanohybrids for electrochemical energy storage

Matteo Crisci[1,2], Felix Boll[1,2], Leonardo Merola[1,3], Jonas Johannes Pflug[1], Zheming Liu[3], Jaime Gallego[1,2], Francesco Lamberti[4] and Teresa Gatti[1,2]*

[1]Institute of Physical Chemistry, Justus Liebig University, Giessen, Germany, [2]Center for Materials Research, Justus Liebig University, Giessen, Germany, [3]Nanochemistry Department, Istituto Italiano di Tecnologia, Genova, Italy, [4]Department of Chemical Sciences, University of Padova, Padova, Italy

2D materials are interesting flat nanoplatforms for the implementation of different electrochemical processes, due to the high surface area and tunable electronic properties. 2D transition metal dichalcogenides (TMDs) can be produced through convenient top-down liquid-phase exfoliation (LPE) methods and present capacitive behaviour that can be exploited for energy storage applications. However, in their thermodynamically stable 2H crystalline phase, they present poor electrical conductivity, being this phase a purely semiconducting one. Combination with conducting polymers like polyaniline (PANI), into nanohybrids, can provide better properties for the scope. In this work, we report on the preparation of 2D WS_2@PANI hybrid materials in which we exploit the LPE TMD nanoflakes as scaffolds, onto which induce the *in-situ* aniline polymerization and thus achieve porous architectures, with the help of surfactants and sodium chloride acting as templating agents. We characterize these species for their capacitive behaviour in neutral pH, achieving maximum specific capacitance of 160 F/g at a current density of 1 A/g, demonstrating the attractiveness of similar nanohybrids for future use in low-cost, easy-to-make supercapacitor devices.

KEYWORDS

2D material, transition metal dichacogenide, nanohybrid, nanostructuring, energy storage

Introduction

Electrochemical energy storage is a central topic in current technology-oriented research (Zhang, 2013; Dutta et al., 2022) and the need to develop devices for different type of applications, ranging from automotive (Xu et al., 2020; Rajagopal et al., 2022) up to wearable electronics (Sumboja et al., 2018) and health monitoring platforms (Chen et al., 2020), triggers the continuous search for novel active materials that can satisfy these variable price and performance/durability demands. In this context, two-dimensional (2D) materials are attracting considerable attention, due to their high surface area and highly tunable electronic and electrochemical properties (Cui et al., 2020), as well as

convenient methods for their large scale production. In particular, the top-down liquid-phase exfoliation (LPE) of bulk layered crystals (Hernandez et al., 2008; Nicolosi et al., 2013; Paton et al., 2014) is a very promising production method, allowing to obtain 2D nanosheets in colloidal form, i.e., as functional inks (Hu et al., 2018; Tian, 2021; Pinilla et al., 2022), suitable for the subsequent processing of solid-state architectures.

Among the many different 2D materials that have been produced and studied in the last decade, 2D transition metal dichalcogenides (TMDs) display interesting electronic and mechanical properties for use in energy storage systems (Cherusseri et al., 2019): in fact, the combination of large surface area and variable oxidation states opens up the possibility to store charges through both the electrical double layer and the pseudocapacitive mechanisms. Unfortunately, the most thermodynamically stable crystalline phase of TMDs, i.e., the 2H phase, is semiconducting, strongly limiting the charge/discharge potential achievable from these nanomaterials. The metastable metallic 1T phase can be alternatively produced through LPE by pre-treating the bulk crystalline material with organolithium compounds (Qian et al., 2020), but concerns about stability under prolonged operation in devices are still an open issue (Tang and Jiang, 2015; Jenjeti et al., 2021). An alternative to the use of bare 2D TMDs comes from the combination of these last ones with other (electro)active functional materials, into composite or nanohybrid (Osella et al., 2021; Versaci et al., 2022) structures. Since many years, conducting polymers represent a valuable option for this type of functional hybridization approach: they are low-cost and light-weight materials, they can be pre-synthesized or directly polymerized *in-situ* and they feature a wide range of convenient electronic properties, which can be exploited for energy conversion and storage applications (Sajedi-Moghaddam et al., 2017). Polyaniline (PANI) in particular, represents a sort of benchmark material for the construction of easy-to-make electrochemical energy storage platforms, due to its excellent environmental and thermal stability, coupled to the high electrical conductivity, typical of the emeraldine salt form, obtained when polymerization is carried out in acidic conditions (Beygisangchin et al., 2021).

In this work, we study nanohybrids of 2D WS_2, prepared from LPE of bulk WS_2 powder in environmentally friendly water/isopropanol mixtures (LPE WS_2), and *in situ* polymerized PANI (defined from now on 2D WS_2@PANI), for electrochemical energy storage. Similar composite materials have been studied by Jelinek and co-workers in a recent contribution, targeting the formation of microporous frameworks, in which efficient ion diffusion takes place, and revealing interesting performance in a symmetric supercapacitor architecture (De Adhikari et al., 2021). In order to obtain well-integrated and porous nanoarchitectures, we here adopt a templating strategy that makes use of two different ionic surfactants, namely sodium dodecyl sulphate (SDS) and sodium cholate (NaCh), to promote the effective mixing of the 2D nanosheets and the conducting polymer and of sodium chloride, to tune the morphology and nanostructure of the hybrids, following an example already reported for pure PANI electrodes by Anbalagan and Sawant (2016). The choice of these two specific surfactants is based on their well-known and largely studied ability to efficiently disperse in water-based environments many low-dimensional materials and, in particular, TMDs, as thoroughly discussed in a recent, very comprehensive review on the topic (Hu et al., 2021). The thus obtained different hybrid species are characterized for their structural and electrochemical performance, revealing important structure-to-property-to-function relationships which can be exploited to identify the most promising combinations for use in supercapacitor-like devices.

Experimental section

Materials and methods

All chemicals and solvents were purchased from Sigma-Aldrich and used without any further purification. Raman spectra were recorded on a Bruker Senterra instrument using a 514 nm laser excitation source, a ×50 magnification lens, 2 mW laser power, a 5 s integration time and 20 co-additions. The samples were analysed in solution (LPE WS_2 and LPE WS_2 re-dispersed) or prepared by disposing powders over a silicon slide (Bulk WS_2 and filtered LPE WS_2) and then analysed. Powder X-ray diffraction (P-XRD) measurements were performed on PANanalytical B.V. Empyrean in the 5–75° range using a measurement step of 0.013° and hold time of 75 s. Transmission electron microscopy (TEM) was carried out on a JEOL-1100 transmission electron microscope with an acceleration voltage of 100 kV. The sample was prepared by dropping dilute suspensions of LPE WS_2 onto carbon film-coated 200 mesh copper grids. Scanning electron microscopy (SEM) was performed on a Zeiss Merlin instrument at a working potential of 4 kV. Energy-dispersive x-ray analysis (EDX) was performed on the same instrument at a working potential of 8 kV, an electron beam current of 8 nA and a X-Max 50 Silicon Drift Detector with 50 mm^2 active area and polymer window was used. Nitrogen physisorption experiments were performed at 77 K with an automated gas adsorption station Quadrasorb EVO by Quantachrome Instruments. Prior to the measurements, the samples were degassed in vacuum for 12 h at 50°C. The surface area was determined using the BET method, and the pore size distributions were calculated *via* the nonlocal density functional theory (NLDFT) approach, using the adsorption branch of the isotherm. X-ray photoelectron spectroscopy (XPS) measurements were conducted with a PHI 5000 VersaProbe II Scanning ESCA Microprobe (Physical Electronics) with monochromatized Al Kα X-ray source in

high power mode (beam size 1,300 µm × 100 µm, X-ray power: 100 W). Time steps of 50 ms, a step size of 0.2 eV and an analyzer pass energy of 46.95 eV were used for measuring the detail spectra. The sample surface was charge neutralized with slow electrons and argon ions, and the pressure was in the range from 10^{-7} to 10^{-6} Pa during the measurement. Data analysis was performed using the CasaXPS software.

Liquid-phase exfoliation of WS_2

For LPE, WS_2 powder with a particle size of 2 µm and a purity of 99% and sodium cholate hydrate (NaCh, from bovine and/or ovine bile) with a purity of 99% were employed. Up to a volume of 500 ml, LPE was carried out in a mixture of isopropanol and demineralized water at a ratio of 7:3 v/v. First, 1 mg/ml of NaCh was added to the solvent mixture and stirred until a clear solution was obtained. Afterwards, 10 mg/ml of the bulk WS_2 powder was added to the solution under continuous stirring for 10 min. The suspension was then further homogenized for 30 min in an ultrasonic bath. The LPE was carried out employing an IKA T25 digital Ultra-Turrax shear mixer at 8,000 RPM for 4 h, while the suspension was covered and cooled in an ice bath to avoid solvent evaporation. The final mixture was allowed to undergo gravitational sedimentation for 4 days, after which the colour changed from black to a yellow-brown nuance in the supernatant, which was thus separated from the precipitate (pellet). This final LPE WS_2 ink was filtered on an Omnipore-Teflon-Membrane (0.2 µm, from Merck Millipore), washed thoroughly on the filter with water to remove any NaCh residue and dried in vacuum, to determine the yield in 2D WS_2 (~2%). The LPE WS_2 was then recovered from the filter by re-dispersing it in isopropanol with the help of the ultrasonic bath and isolated as a powder after isopropanol evaporation under reduced pressure.

Synthesis of 2D WS_2@PANI hybrids

Pure PANI was synthesized through oxidative polymerization by first preparing a 0.1 M solution of aniline in 1 M HCl saturated with NaCl (brine). In another container, a 1.15 M solution of $K_2S_2O_8$ was prepared in 1 M HCl (also saturated with NaCl). Both solutions were then combined together and cooled to 0°C using an ice bath. After stirring for 30 min, the suspension was filtrated under vacuum and washed with 200 ml of 1 M HCl and twice with 25 ml of acetone. The formed product was dried at 40°C in a vacuum oven overnight. 0.4893 g of a dark green, almost black solid was obtained, which corresponds to a yield of 98%. For synthesis of the 2D WS_2@PANI hybrids, a slightly modified procedure was used: first the surfactant (1.25 mg/ml for SDS, 1.5 mg/ml for NaCh) was dissolved in 1 M HCl saturated with brine. Afterwards the respective amount of the LPE WS_2 powder (0.01, 0.02 and 0.05 equivalents compared to the used aniline) was added and dispersed by sonicating in an ultrasound bath at 37 Hz, 60% power for 15 min. Then, 0.245 ml of aniline were added to still form a 0.1 M solution. Afterwards, the mixture was combined with the same oxidant solution, as previously described, and the protocol continued as above. Since different WS_2/PANI molar ratio were prepared, Table 1 summarizes the relative quantities for each involved chemical and the quantity of product obtained.

Electrochemical testing

The electrochemical performance of the 2D WS_2@PANI hybrids was characterized by galvanostatic charge-discharge (GCD) and electrochemical impedance spectroscopy (EIS) using a three-electrode set up based on a glassy carbon electrode (GC) as working electrode (WE), a platinum wire as counter electrode (CE) and an Ag/AgCl reference electrode (RE). The data have been then translated against the reversible hydrogen electrode (RHE), for the sake of clarity. The tests were performed on an Autolab PGSTAT302 equipped with the Nova (2.1.1.) software. The WE was prepared as follows: an ink of 5 mg/ml of active material was produced by weighting the desired hybrid and dispersing it in 2 ml of H_2O/EtOH (1:1 v/v). Afterwards 60 µl of Nafion (30 µl/ml of ink) were added to the suspension and the final ink was sonicated in ultrasonic bath (40% power, room temperature, 37 kHz frequency) for 1 h. Afterwards, 5 µl of the resulting ink were drop casted on top of the GC WE and dried in oven at 100°C for 1 h before use. The measurements were performed in 0.5 M Na_2SO_4 electrolyte. GCD measurements were performed in the voltage range 0–0.8 V at the different current densities of 0.2, 0.5, 1, 2, 5, 10 A/g. Based on the GCD curve, specific capacitance (C_S) for the single electrode material was calculated using the equation:

$$C_s = \frac{I*\Delta t}{m*\Delta V} \quad (1)$$

where I is the discharge current applied, Δt is the discharge time of the curve, m is the mass of active material on the electrode and ΔV is the potential window. EIS measurements were carried out on a BioLogic SP 200 potentiostat at a constant potential mode of 0 V. Frequency range was varied between 200 kHz and 10 Hz at an amplitude of 5 mV.

Results and discussion

For the production of LPE WS_2, we have optimized a protocol that resorts to the use of shear mixing in green isopropanol/water solvent mixtures (Crisci et al., 2022) in the presence of NaCh as surfactant, to assist the mechanical

10.3389/fchem.2022.1000910

TABLE 1 Relative quantities (mg, mmol) for each involved reagent in the preparation of 2D WS_2@PANI nanohybrids and the quantity of product obtained.

WS_2/PANI molar ratio	$K_2S_2O_8$ (mg, mmol)	Surfactant (mg, mmol)	LPE WS_2 (mg, mmol)	Product (mg)
1:20 (+SDS)	919, 9.9	66, 0.2	35, 0.14	281
1:20 (+NaCh)	919, 9.9	77, 0.18	35, 0.14	370
1:50 (+SDS)	919, 9.9	66, 0.2	14, 0.06	331
1:50 (+NaCh)	919, 9.9	77, 0.18	14, 0.06	165
1:100 (+SDS)	919, 9.9	66, 0.2	7, 0.03	284
1:100 (+NaCh)	919, 9.9	77, 0.18	7, 0.03	345

exfoliation by properly adjusting the liquid medium surface tension. Optimization has mostly been addressed at reducing as much as possible the amount of surfactant, while still obtaining a good yield in exfoliated 2D material ink, as well as to be able to scale-up the production up to 500 ml per batch. Remarkably, this process is providing yields that are similar to those obtained by resorting to more classical LPE in high boiling solvents like N-methylpyrrolidone (NMP), while being undoubtedly more suitable from an environmental perspective for the future industrialization of similar inks (Hu et al., 2021). We have then proceeded through a filtration, accompanied by thorough washings, to remove all the surfactant and obtain a powder of the LPE WS_2, directly usable for the preparation of the 2D WS_2@PANI nanohybrids. Although NaCh is also employed within this last process, we had the need to remove the native one, being interested also in testing another surfactant, namely SDS, to compare the effect of the two different molecular structures on the quality of the 2D WS_2@PANI species.

In order to rule out the extensive re-aggregation of the individual few-layers WS_2 nanosheets during filtration and to demonstrate the reversibility of such aggregation following a simple re-dispersion step in ultrasonic bath, we have carried out a thorough Raman analysis, following the detailed description reported in the work of Terrones and coworkers (Berkdemir et al., 2013). The results of this analysis are displayed in Supplementary Figure S1 of the Supplementary Material (SM). By examining the position and relative intensity of the 2LA + E^12g peak in the range 350–375 cm^{-1} and of the A_{1g} peak in the range 410–430 cm^{-1}, it is possible to estimate the average number of layers present in a given WS_2 sample. In Supplementary Figure S1, we show the spectra of the starting bulk WS_2 in powder compared to that of the LPE WS_2 ink in liquid, of the filtered LPE WS_2 ink (as powder) and of the re-dispersed nanomaterial in 1 M HCl in brine in the presence of freshly added surfactant (as a suspension). In these spectra, the two Raman modes under investigation change significantly in position when going from the bulk to the LPE material (the 2LA + E^12g mode shifts from 348 to 364 cm^{-1} and the A_{1g} mode from 413 to 433 cm^{-1}). Also in the filtered material, they never return to the original bulk position, although a slight shift to lower wavenumbers is detectable after filtration. The average number of layers in the nanosheets can be quantified by considering the ratio between the intensities of the 2LA + E^12g mode and the A_{1g} mode. This ratio is lower than 1 (0.95) in bulk WS_2 and increases to a value higher than 2 (2.08) in the LPE WS_2, indicating the production of nanosheets with an average number of layers between 1 and 3, thus a highly exfoliated nanomaterial. TEM images of this material (Supplementary Figure S2) demonstrate their few-layers nature (possibly some mono, bi and tri-layer species are distinguishable), although strong aggregation at the solid-state (i.e., in this case on the TEM grid) takes place, making difficult to distinguish individual flakes. In the filtered species, we observe a decrease of the ratio to values similar to the bulk (0.95), which anyway reconverts to 1.6 in the re-dispersed powder, typical of 2–5 layers nanosheets (Berkdemir et al., 2013), thus again mostly 2D layered species.

The procedure adopted to prepare nanostructured 2D WS_2@PANI hybrids is depicted in Figure 1A, in which the effective mixing between the nanosheets and aniline is ensured by the presence of one of the two investigated surfactants (SDS or NaCh) and the formation of porous architectures is templated by the concomitant action of NaCl crystals (Anbalagan and Sawant, 2016) during the *in situ* oxidative polymerization, triggered by potassium persulfate used as the oxidant. The trapped NaCl crystals are then removed after thorough washings of the filtered composite materials, leaving behind the target 2D WS_2@PANI hybrids. Other than varying the surfactant, we have also tuned the relative molar ratio between LPE WS_2 and aniline, to produce hybrids with different stoichiometries, ranging from 1:20 to 1:50 and up to 1:100.

All the samples have been investigated through Raman and P-XRD analysis, of which prototypical spectra and diffractograms are reported in Figures 1B,C, respectively. The results are compared with the Raman spectra and P-XRD patterns of the two individual components, namely LPE WS_2 and pure PANI, also prepared with the NaCl templating method. From Raman, we can distinguish in the nanohybrid the presence of the two previously discussed 2LA + E^12g and A^{1g} modes of layered WS_2, with positions unvaried with respect to LPE WS_2

10.3389/fchem.2022.1000910

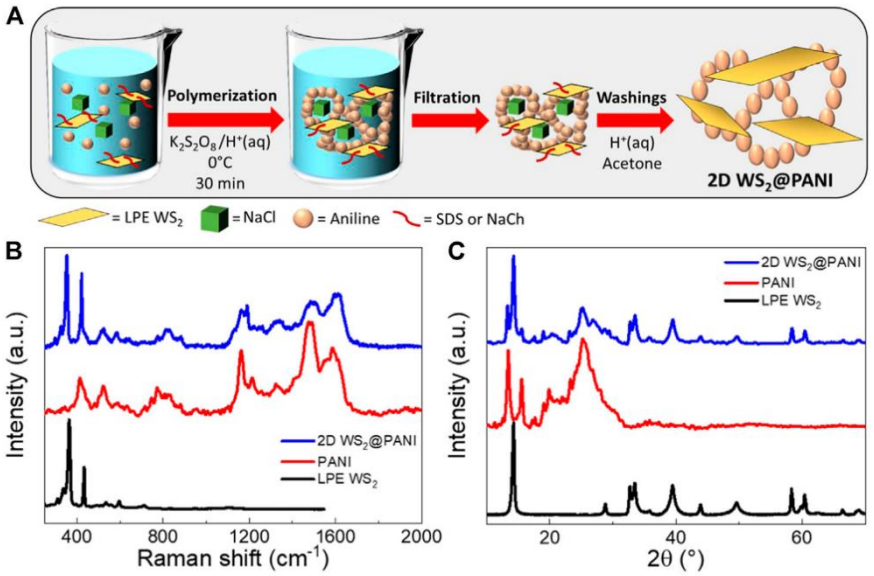

FIGURE 1
(A) Schematic representation of the template-assisted synthesis of nanostructured 2D WS_2@PANI nanohybrids. **(B)** Raman spectra and **(C)** P-XRD diffractograms of the nanostructured 2D WS_2@PANI nanohybrids, of template-assisted synthesized pure PANI and of LPE WS_2 (the P-XRD pattern of this last one has been obtained from the filtered powder).

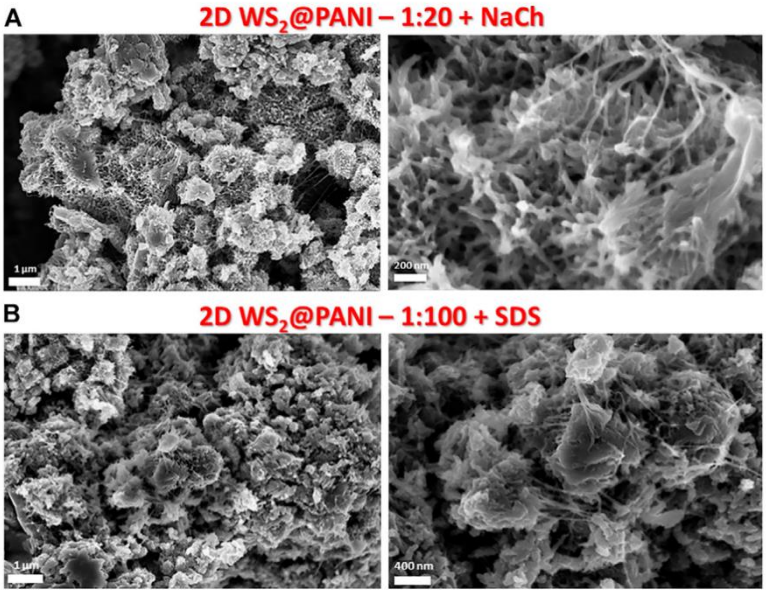

FIGURE 2
SEM images at different magnifications of prototypical nanostructured 2D WS_2@PANI nanohybrids obtained with different LPE WS_2/PANI molar ratios and with different surfactants favouring the proper mixing of the two individual components in the composite. **(A)** 2D WS_2@PANI with 1:20 molar ratio prepared in the presence of NaCh as surfactant. **(B)** 2D WS_2@PANI with 1:100 molar ratio prepared in the presence of SDS as surfactant.

and intensity ratio typical of highly exfoliated material, although not precisely determinable due to overlapping of the A_{1g} mode with a vibration of PANI (out of plane deformation of the ring structure). Concerning the PANI component in the hybrids, we can observe a change in the relative intensities of the two signals at around 1,600 cm^{-1} (stretching of the conjugated C-C bonds in the quinoid form) and at around 1,480 cm^{-1} (stretching of the C=N bond) with respect to pure PANI, likely indicating a change in the supramolecular structure of the polymeric/oligomeric chains, although extremely complex to exactly determine (Trchová et al., 2014; Stejskal et al., 2017). P-XRD also confirms the presence of the two crystalline components in the hybrids, although no particular additional information can be inferred, if not that residual NaCl is not present in the sample at detectable levels (the typical intense reflex of this last one at $2\theta = 31.7^{\circ}$ is absent in the diffractograms).

The templating and nano-structuring effect of the particular synthetic method here employed is strongly recognizable from the SEM characterization of the resulting nanohybrid materials. First of all, it should be pointed out that the mixing effect of the surfactant is essential to not achieve phase separation during the *in situ* aniline polymerization in the presence of the LPE WS_2 flakes, as it is testified by the SEM image reported in Supplementary Figure S3 (right) of the SM. This was recorded on a 1:20 2D WS_2@PANI sample, for which individual and aggregated 2D material flakes emerge within a background of the sole polymer scaffold (a SEM detail of the nanomorphology of pure PANI is also provided in the same figure, left, for the sake of comparison). The tendency to self-aggregate is indeed typical of the LPE WS_2 material when casted from the liquid phase onto substrates, as it can be seen from the SEM image also reported in Supplementary Figure S3 (bottom image).

Then, what clearly emerges from SEM images reported in Figure 2 and in Supplementary Figures S4, S5, is a certain difference in the nanomorphology of the different hybrids, obtained in the presence of either NaCh or SDS as the compatibilizer. In particular, for the NaCh-based 2D WS_2@PANI hybrids we can distinguish already at the lowest 2D WS_2/PANI ratio (1:20, Figure 2A) the formation of fractal-like nanostructures, most likely due to the NaCl-templated growth of PANI on the surface of the 2D WS_2 nanosheets, coupled to filaments of the same polymer connecting different areas. These peculiar morphological characteristics are further maintained in the samples with higher 2D material/polymer ratios (Supplementary Figure S4). On the contrary, in the hybrids synthesized in the presence of SDS, the formation of similar complex nano-architectures is only detectable within the 1:100 2D WS_2@PANI sample (Figure 2B), while at the higher TMD contents, the presence of aggregated TMD flakes separated from PANI aggregates is distinguishable. These data might indicate a different ability of the two surfactants to act as proper compatibilizers between the two materials in the composites. In particular, the more extended molecular structure of NaCh,

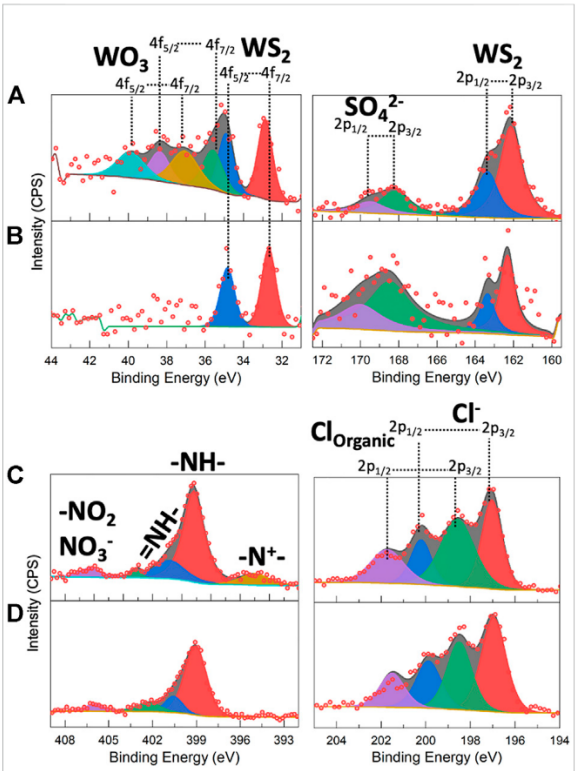

FIGURE 3
XPS spectra of **(A,C)** 2D WS_2@PANI with 1:20 molar ratio prepared in the presence of SDS and **(B,D)** 2D WS_2@PANI with 1:20 molar ratio prepared in the presence of NaCh in the W 4f, S 2p (top panels) and N 1s and Cl 2p (bottom panels) regions.

compared to the mostly linear one of SDS, seems to better provide efficient intermixing between the 2D WS_2 nanosheets and the conjugated polymer. Further studies are anyway necessary to better understand this behaviour. In addition, it is worthy to specify that the formation of the peculiar filament-like nanostructures in these composites is most likely attributed to the use of the saturated brine solution during the synthesis. During this process, NaCl crystallizes from the saturated solution and then re-dissolves during the washings, allowing the formation of short chains and filaments of PANI between the different polymeric domains.

Although the degree of nano-structuring in the synthesized hybrids seems to point out at different overall surface areas for the various type of samples, physisorption data were not varying significantly across both the NaCh- and SDS-based series. Type III N_2 physisorption isotherms were found for all the investigated species (a prototypical one is reported in Supplementary Figure S6), indicating the presence of mostly macropores and surface areas from Brunauer–Emmett–Teller (BET) analysis all in the range 23–27 m^2/g, thus considerably lower than what found for similar species recently (up 70 m^2/g in the work of De Adhikari

10.3389/fchem.2022.1000910

TABLE 2 Comparison between atomic % of different elements in 2D WS2@PANI nanohybrids as obtained from XPS and EDX analysis.

At. %	C	N	O	Cl	W	S	S/W ratio	Cl/N ratio
2D-WS2@PANI 1:20 + SDS								
XPS	76.4	11.3	6.1	4.1	0.15	2.05	13.6	0.4
EDX	82.5	10.5	1.1	3.5	0.3	0.4	1.33	0.33
2D-WS2@PANI 1:20 + NaCh								
XPS	74.7	7.8	7.5	4	0.1	0.8	12	0.5
EDX	85.2	10.7	0.8	1.3	0.8	1.2	1.5	0.12

et al. (2021). We completed the compositional analysis of the 2D WS_2@PANI hybrids by comparing XPS and SEM-EDX data for the 1:20 samples prepared in the presence of both SDS and NaCh as compatibilizers. XPS spectra of the tungsten, sulphur, nitrogen and chlorine regions of these species are reported in Figure 3, while the entire spectra are displayed in Supplementary Figure S6, for the sake of completeness. From the W 4f region of the SDS-based hybrid, it is clearly distinguishable the presence of tungsten oxide species together with the native sulphide (Figure 3A). As the oxide is not detectable from P-XRD, it must be related to the sole surface, coming from the there-happening partial oxidation of WS_2. These oxidized species are not detected in the XPS spectrum of the NaCh-based hybrid (Figure 3B), in which only the signals of WS_2 are present: we can therefore argue that the PANI nanostructures seen in the SEM images of the latter and not in those of the former (at least not in the 1:20 sample), act as an effective protecting layer against the surface oxidation of the TMD nanosheets. The S 2p region shows in both samples the presence of WS_2 and of sulfate species, which are most likely related to residues of the oxidant used for PANI polymerization. From N 1s region, it is detected the PANI component in the hybrids, characterized by mostly -NH- and = NH- groups along the chains coming from the aromatic and quinoid polymer forms, but also from small cationic and oxidized nitrogen species, particularly in the SDS-based sample. The level of PANI p-doping can be inferred by analysing the Cl 2p region, where both chloride ions and organic chloride (i.e., chloride directly bonded to carbon atoms) can be distinguished (still, uncertainty would remain on whether some of the chloride signals are not originating from not perfectly washed away NaCl used during the synthesis, although no sodium signal is seen in the XPS spectra, Supplementary Figure S7, indicating the lack of this element on the surface). Qualitatively, the spectra of the two species are not differing significantly, but it is possible to quantify the atomic percentage of the various elements and calculate from that the Cl/N ratio, which is directly related to the extent of doping, since chlorides act as counter-ions for the doped form of the polymer.

In Table 2, we show this quantitative data for the 1:20 SDS- and NaCh-based 2D WS_2@PANI hybrids, calculated from both XPS and SEM-EDX analysis, with the former providing information on the surface composition while the latter of the bulk. As it can be inferred from this numbers, the Cl/N ratio is slightly higher in the NaCh-based sample, although here no clear signal of $-N^+-$ species (that are counterions of Cl^- in the p-doped PANI) are present in the N 1s region (Figure 3C).

The S/W ratio could provide some information on the stoichiometry of the WS2 component, although this number is strongly influenced by the presence of the oxidant residues (SO_4^{2-}) and of the sulphate polar head in SDS molecules. Indeed, this ratio is considerably high on the surface, where mot likely these sulphur-containing species are prevalently located, while in the bulk it is closed to the expected value (2), with a slight under-stoichiometric tendency that might be related to sulphur-vacancies present on the 2D WS2 nanosheets (most likely on the edges). Supplementary Figure S8 reports the SEM-EDX maps of the different analysed elements in the 1:20 2D WS2@PANI hybrids prepared in the presence of SDS and NaCh. Here, we can notice the inhomogeneous nature of the former composite, characterized by areas in which WS2 seems confined (W and S signals distribution), while the PANI component is present everywhere (N, C and Cl signals). These data further reinforce the previous speculation made from simple observation of the SEM micrographs, i.e., the low extent of intimate mixing between the two materials in the SDS-containing 1:20 2D WS2@PANI hybrid. On the other hand, for the NaCh-containing hybrid, we can further confirm from Supplementary Figure S7 the highly homogenous nature, with the W and S signals extending over a large part of the mapped area as are those of N and C.

The series of synthesized 2D WS2@PANI hybrids has been characterized for its electrochemical performance in light of the charge storage capability at neutral pH (Figure 4), by investigating them through GCD. The materials have been displaced in the form of powder samples on a GC electrode with the help of Nafion as binder to ensure their safe and stable attachment. The choice of operating at neutral pH is specific for the perspective of employing them in wearable electronics, although it is well known that PANI-based species demonstrate higher capacitances in strongly acidic media (Li et al., 2009).

Figures 4A,B display the calculated CS from GCD curves (Supplementary Figure S9, Figures 4C,D) as a function of the current density for the composites prepared in the presence of, respectively, NaCh and SDS at the different 2D WS2/PANI ratios.

The performance of the two NaCh-containing samples featuring the lowest amount of PANI (1:20 and 1:50) is rather similar and always surpassing that of pure PANI up to high current densities. Remarkably, the CS value at 1 A/g of the 1:20 sample is 160 F/g, thus almost doubling that of pure PANI. In addition, this value is also slightly higher than the CS value at such current density reported by De Adhikari et al. (2021) from similar hybrid materials (140 F/@ 1 A/g) featuring even higher surface areas,

10.3389/fchem.2022.1000910

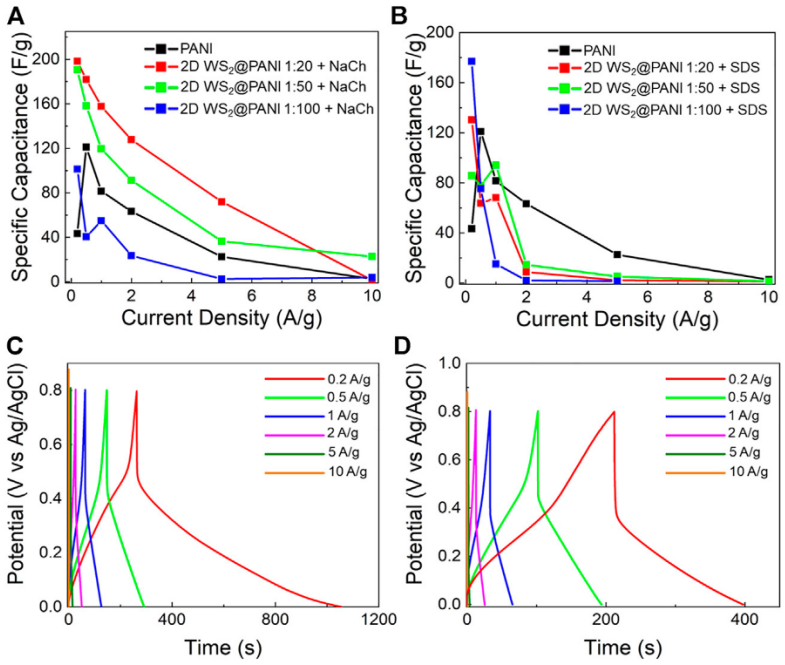

FIGURE 4
Electrochemical performance of 2D WS2@PANI nanohybrids at neutral pH (in 0.5 M Na2SO4 electrolyte). Specific capacitance as a function of current density for 2D WS2@PANI nanohybrids at different molar ratios prepared in the presence of **(A)** NaCh and **(B)** SDS. The data for pure PANI are also provided for the sake of comparison. GCD curves at increasing current densities for **(C)** the 1:20 2D WS2@PANI nanohybrid prepared in the presence of NaCh and **(D)** for pure PANI.

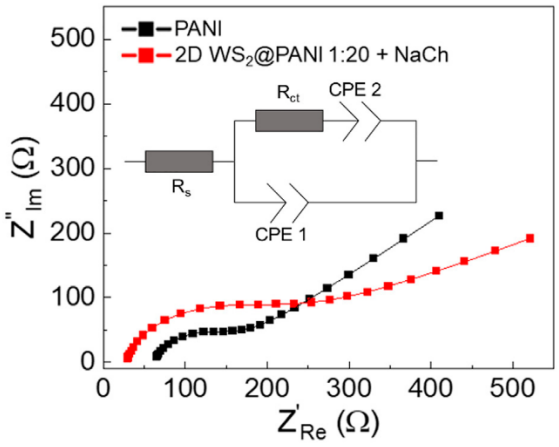

FIGURE 5
EIS analysis-derived Nyquist plots with relative equivalent circuit for the NaCh-based 1:20 2D WS2@PANI nanohybrid and for pure PANI as measured after GCD analysis.

pointing out at the existence of other effects governing the capacitive behaviour in these systems. However, the same cannot be observed for the SDS-based samples, which overall have worst performances than the pristine PANI reference, with the exception of the extremely low current densities regime. The present data seem to confirm the generally lower quality of the constituent materials mutual mixing and nano/microstructure in the SDS-based composites in comparison with the NaCh-based ones, which translates in a poorer electrochemical charge storage ability. The WS2 surface oxidation detected by XPS in these systems, might also be a partial cause of their poor performance, as generally the oxide is less conductive than the sulphide (Liu et al., 2015). Since the capacitive behaviour of pure 2D WS2 is almost negligible (and for this reason not shown here), the results obtained for the 1:20 2D WS2@PANI hybrid prepared in presence of NaCh point out at a notable cooperative effect between the TMD nanosheets and the conducting polymer, which allows to overperform both the individual species involved. This is even more evident when considering that by increasing the conducting polymer content, and thus going more in the

10.3389/fchem.2022.1000910

TABLE 3 Fitted values from the EIS characterization of the NaCh-based 1:20 2D WS_2@PANI nanohybrid and for pure PANI after GCD analysis.

Sample	Rs (Ω)	Rct (Ω)	CPE1 (S)	N1	Cdl (uF)	CPE2 (S)	N2
PANI	63	89	1.49e-6	0.87	0.39	0.00051	0.45
2D WS2@ PANI	29	113	7.79e-7	0.89	0.24	0.00076	0.29

direction of a mostly polymer-based active material, the energy storage capability worsens progressively and becomes even lower than that of pure PANI (in the 1:100 sample).

To better characterize the electrochemical behaviour of the champion composite (i.e., the 1:20 2D WS2@PANI + NaCh), we examined more in detail the GCD curves of this material at increasing current densities (Figure 4C). The GCD curves allow to appreciate the longer discharge time typical of the hybrid in comparison to the pure PANI reference (Figure 4D), which contribute to the higher CS measured for the former. In addition, their asymmetric shape is a sign of the pseudocapacitive behaviour of these materials over the range of current densities examined (Chen et al., 2013).

Stability is a key issue when dealing with modified electrodes: delamination of the coating may occur during measurements and EIS is a really sensitive tool for this scope (Jorcin et al., 2006). To further try to understand the long-term energy storage properties of the NaCh-based 1:20 2D WS2@PANI nanohybrid (the best performing sample) in comparison with the reference PANI sample, EIS analysis was carried out on the electrode after GCD characterization, working in the same electrolyte medium, with the relative Nyquist plots reported in Figure 5. Cyclability of the electrodes was indeed an unsuccessful method to understand durability, since it was visually clear that the active materials were progressively detaching from GC during scans. The results of EIS thus provide information about the electrode-electrolyte interface, i.e., the kinetics of the charge transfer mechanisms happening between WS2 and PANI, as well as about the electrode surface area. The experimental data are fitted using a Randles modified cell (Nguyen and Breitkopf, 2018), choosing a constant phase element (CPE) for modeling the double layer capacitance and the Warburg element (Lamberti et al., 2013): in this way the non-ideality of the whole system can be modeled emphasizing the role of each constituent in the composite electrode. In particular, Rs refers to the saturated resistance, Rct is the charge transfer resistance associated to the sodium cations discharge in the underlying GC electrode, the CPE1 is the associated double layer capacitance and CPE2 represents the Warburg element related to the semi-infinite linear diffusion of the ions from the electrolyte towards the electrode. Fitted values are reported in Table 3. The associated Cdl values from the CPE1 values are calculated using the equations reported in reference (Bard and Faulkner, 2000).

The Rct for pure PANI is slightly smaller than the one of the 2D WS_2@PANI best sample (113 vs. 89 Ω), reflecting a reduced conductivity for the TMD-modified PANI electrode: this result suggests a slower charge discharge at the modified electrode after prolonged GCD characterization. This result is also justified by the steeper slope of the Nyqvist plot (i.e., smaller Warburg impedance) for the pristine PANI sample: the diffusion of ions towards the working electrode is therefore strongly limited by the presence of WS_2. Furthermore, the presence of a depressed semicircle in both samples (and therefore the use of a CPE instead of an ideal C) accounts for the inhomogeneity of the surface as supported by SEM analysis (Figure 2): more specifically, one expects to find a quasi-tridimensional surface (Mulder et al., 1990). This is the case of the hybrid sample at least, where a fractal morphology is found. However, the N1 fitted value for the two samples (0.87 for PANI sample and 0.89 for the 2D WS_2@PANI sample) is almost the same thus corroborating the idea that the surface roughness for the two samples is comparable (as also suggested by BET analysis). The delimitation occurred after intense electrochemical characterization accounts for the decrease of about 40% of the value of the Cdl for the composite electrode (0.39 uF for pristine PANI and 0.24 uF for 2D WS_2@PANI sample) that reflects a smaller surface area for this sample.

The EIS results as a whole suggest that capacitive measurements are not conservative for the electrodes as they have been here characterized (i.e., by relatively simple deposition on a GC) and in order to obtain durable devices, it will be necessary to develop an optimized process for their preparation. We further proof this issue by carrying out multiple cycles of charge/discharge on two prototypical composites (the 1:20 2D WS_2@PANI hybrids prepared with both NaCh and SDS) at 1 A/g current density. The results, reported in Supplementary Figure S10 over 100 cycles, show how an almost immediate drop in C_S of almost 30% takes place after only 10 cycles, likely due to progressive detachment of the active material from the GC electrode during cycling. In general, anyway, we can observe a slightly higher stability of the NaCh-based composite, confirming the better agglomeration between the components in this active material. The incorporation within a gel matrix of the 2D WS_2@PANI hybrid material is indeed the next step that we are currently exploring in order to produce stable supercapacitors retaining the capacitive properties found in the current study.

Conclusion

In this work, we report on a series of electro-active composite materials between LPE WS_2 nanoflakes and *in-situ* polymerized

PANI with large interest for application into the next-generation of low-cost, light-weight energy storage devices. We show how the use of different compatibilizers can strongly influence the level of mixing between the two components and consequently the surface properties, with strong implications into charge accumulation mechanisms. In addition, the concomitant effect of using a simple, inexpensive and easy-to-remove templating agent like NaCl during the synthetic process, allows to tune the nano-structuring of the resulting species, with peculiar morphological features emerging in combination with the compatibilizer, which have likely a large influence on the observed capacitive behaviour.

The combined physico-chemical and electrochemical characterization of these species provides significant hints on the structure-property-function relationships, which will serve for the design of even more active nano-structured energy storage materials. Our future plans include their integration into flexible supercapacitor architectures by previous incorporation into hydrogel scaffolds, targeting the field of wearable technologies, which will likely cover a large portion of the market for electronic products in the up-coming decades.

Data availability statement

The raw data supporting the conclusion of this article will be made available by the authors, without undue reservation.

Author contributions

MC, FB, JP, and LM prepared the materials and studied their properties. JG carried out XPS analysis. ZL performed TEM characterization. TG supervised the work and wrote the manuscript. All authors have revised the final manuscript.

Funding

This work was supported by the European Commission through the H2020 FET-PROACTIVE-EIC-07-2020 project LIGHT-CAP (project number 101017821).

Conflict of interest

The authors declare that the research was conducted in the absence of any commercial or financial relationships that could be construed as a potential conflict of interest.

Publisher's note

All claims expressed in this article are solely those of the authors and do not necessarily represent those of their affiliated organizations, or those of the publisher, the editors and the reviewers. Any product that may be evaluated in this article, or claim that may be made by its manufacturer, is not guaranteed or endorsed by the publisher.

Supplementary material

The Supplementary Material for this article can be found online at: https://www.frontiersin.org/articles/10.3389/fchem.2022.1000910/full#supplementary-material

References

Anbalagan, A. C., and Sawant, S. N. (2016). Brine solution-driven synthesis of porous polyaniline for supercapacitor electrode application. *Polymer* 87, 129–137. doi:10.1016/j.polymer.2016.01.049

Bard, A. J., and Faulkner, L. R. (2000). *Electrochemical methods: Fundamentals and applications*. 2nd Edition. New York: John Wiley & Sons.

Berkdemir, A., Gutiérrez, H. R., Botello-Méndez, A. R., Perea-López, N., Elías, A. L., Chia, C.-I., et al. (2013). Identification of individual and few layers of WS2 using Raman Spectroscopy. *Sci. Rep.* 3, 1755. doi:10.1038/srep01755

Beygisangchin, M., Abdul Rashid, S., Shafie, S., Sadrolhosseini, A. R., and Lim, H. N. (2021). Preparations, properties, and applications of polyaniline and polyaniline thin films a review. *Polym. (Basel).* 13, 2003. doi:10.3390/polym13122003

Chen, W., Rakhi, R. B., and Alshareef, H. N. (2013). Facile synthesis of polyaniline nanotubes using reactive oxide templates for high energy density pseudocapacitors. *J. Mat. Chem. A* 1, 3315–3324. doi:10.1039/C3TA00499F

Chen, X., Villa, N. S., Zhuang, Y., Chen, L., Wang, T., Li, Z., et al. (2020). Stretchable supercapacitors as emergent energy storage units for health monitoring bioelectronics. *Adv. Energy Mat.* 10, 1902769. doi:10.1002/aenm.201902769

Cherusseri, J., Choudhary, N., Sambath Kumar, K., Jung, Y., and Thomas, J. (2019). Recent trends in transition metal dichalcogenide based supercapacitor electrodes. *Nanoscale Horiz.* 4, 840–858. doi:10.1039/C9NH00152B

Crisci, M., Dolcet, P., Yang, J., Salerno, M., Bélteky, P., Kukovecz, Á., et al. (2022). Design principles and insights into the liquid-phase exfoliation of alpha-MoO3 for the production of colloidal 2D nano-inks in green solvents. *J. Phys. Chem. C* 126, 404–415. doi:10.1021/acs.jpcc.1c09221

Cui, H., Guo, Y., Ma, W., and Zhou, Z. (2020). 2 D materials for electrochemical energy storage: Design, preparation, and application. *ChemSusChem* 13, 1155–1171. doi:10.1002/cssc.201903095

De Adhikari, A., Shauloff, N., Turkulets, Y., Shalish, I., and Jelinek, R. (2021). Tungsten-Disulfide/polyaniline high frequency supercapacitors. *Adv. Electron. Mat.* 7, 2100025. doi:10.1002/aelm.202100025

Dutta, A., Mitra, S., Basak, M., and Banerjee, T. (2022). A comprehensive review on batteries and supercapacitors: Development and challenges since their inception. *Energy Storage*, e339. doi:10.1002/est2.339

Hernandez, Y., Nicolosi, V., Lotya, M., Blighe, F. M., Sun, Z., De, S., et al. (2008). High-yield production of graphene by liquid-phase exfoliation of graphite. *Nat. Nanotechnol.* 39 (3), 563–568. doi:10.1038/nnano.2008.215

Hu, C.-X., Shin, Y., Read, O., and Casiraghi, C. (2021). Dispersant-assisted liquid-phase exfoliation of 2D materials beyond graphene. *Nanoscale* 13, 460–484. doi:10.1039/D0NR05514J

Hu, G., Kang, J., Ng, L. W. T., Zhu, X.i, Howe, R. C. T., Jones, C. G., et al. (2018). Functional inks and printing of two-dimensional materials. *Chem. Soc. Rev.* 47, 3265–3300. doi:10.1039/C8CS00084K

Jenjeti, R. N., Kumar, R., Sellam, A., and Sampath, S. (2021). High stability of 1T-phase $MoS_{2x}Se_{2(1-x)}$ monolayers under ambient conditions. *J. Phys. Chem. C* 125, 8407–8417. doi:10.1021/acs.jpcc.1c00212

Jorcin, J.-B., Aragon, E., Merlatti, C., and Pébère, N. (2006). Delaminated areas beneath organic coating: A local electrochemical impedance approach. *Corros. Sci.* 48, 1779–1790. doi:10.1016/j.corsci.2005.05.031

Lamberti, F., Ferraro, D., Giomo, M., and Elvassore, N. (2013). Enhancement of heterogeneous electron transfer dynamics tuning single-walled carbon nanotube forest height and density. *Electrochim. Acta* 97, 304–312. doi:10.1016/j.electacta.2013.02.119

Li, H., Wang, J., Chu, Q., Wang, Z., Zhang, F., and Wang, S. (2009). Theoretical and experimental specific capacitance of polyaniline in sulfuric acid. *J. Power Sources* 190, 578–586. doi:10.1016/j.jpowsour.2009.01.052

Liu, H., Han, N., and Zhao, J. (2015). Atomistic insight into the oxidation of monolayer transition metal dichalcogenides: From structures to electronic properties. *RSC Adv.* 5, 17572–17581. doi:10.1039/C4RA17320A

Mulder, W. H., Sluyters, J. H., Pajkossy, T., and Nyikos, L. (1990). Tafel current at fractal electrodes: Connection with admittance spectra. *J. Electroanal. Chem. Interfacial Electrochem.* 285, 103–115. doi:10.1016/0022-0728(90)87113-X

Nguyen, T. Q., and Breitkopf, C. (2018). Determination of diffusion coefficients using impedance spectroscopy data. *J. Electrochem. Soc.* 165, E826–E831. doi:10.1149/2.1151814jes

Nicolosi, V., Chhowalla, M., Kanatzidis, M., Strano, M., and Coleman, J. (2013). Liquid exfoliation of layered materials. *Science* 340, 1226419. doi:10.1126/science.1226419

Osella, S., Wang, M., Menna, E., and Gatti, T. (2021). (INVITED) Lighting-up nanocarbons through hybridization: Optoelectronic properties and perspectives. *Opt. Mater. X* 12, 100100. doi:10.1016/j.omx.2021.100100

Paton, K. R., Varrla, E., Backes, C., Smith, R. J., Khan, U., O'Neill, A., et al. (2014). Scalable production of large quantities of defect-free few-layer graphene by shear exfoliation in liquids. *Nat. Mat.* 13, 624–630. doi:10.1038/nmat3944

Pinilla, S., Coelho, J., Li, K., Liu, J., and Nicolosi, V. (2022). Two-dimensional material inks. *Nat. Rev. Mat.*. doi:10.1038/s41578-022-00448-7

Qian, Z., Jiao, L., and Xie, L. (2020). Phase engineering of two-dimensional transition metal dichalcogenides. *Chin. J. Chem.* 38, 753–760. doi:10.1002/cjoc.202000064

Rajagopal, S., Pulapparambil Vallikkattil, R., Mohamed Ibrahim, M., and Velev, D. G. (2022). Electrode materials for supercapacitors in hybrid electric vehicles: Challenges and current progress. *Condens. Matter* 7, 6. doi:10.3390/condmat7010006

Sajedi-Moghaddam, A., Saievar-Iranizad, E., and Pumera, M. (2017). Two-dimensional transition metal dichalcogenide/conducting polymer composites: Synthesis and applications. *Nanoscale* 9, 8052–8065. doi:10.1039/C7NR02022H

Stejskal, J., Mrlík, M., Plachý, T., Trchová, M., Kovářová, J., and Li, Y. (2017). Molybdenum and tungsten disulfides surface-modified with a conducting polymer, polyaniline, for application in electrorheology. *React. Funct. Polym.* 120, 30–37. doi:10.1016/j.reactfunctpolym.2017.09.004

Sumboja, A., Liu, J., Zheng, W. G., Zong, Y., Zhang, H., and Liu, Z. (2018). Electrochemical energy storage devices for wearable technology: A rationale for materials selection and cell design. *Chem. Soc. Rev.* 47, 5919–5945. doi:10.1039/C8CS00237A

Tang, Q., and Jiang, D. (2015). Stabilization and band-gap tuning of the 1T-MoS2 monolayer by covalent functionalization. *Chem. Mat.* 27, 3743–3748. doi:10.1021/acs.chemmater.5b00986

Tian, X. (2021). Direct ink writing of 2D material-based supercapacitors. *2D Mat.* 9, 012001. doi:10.1088/2053-1583/ac3f43

Trchová, M., Morávková, Z., Bláha, M., and Stejskal, J. (2014). Raman spectroscopy of polyaniline and oligoaniline thin films. *Electrochim. Acta* 122, 28–38. doi:10.1016/j.electacta.2013.10.133

Versaci, D., Canale, I., Goswami, S., Amici, J., Francia, C., Fortunato, E., et al. (2022). Molybdenum disulfide/polyaniline interlayer for lithium polysulphide trapping in lithium-sulphur batteries. *J. Power Sources* 521, 230945. doi:10.1016/j.jpowsour.2021.230945

Xu, C., Dai, Q., Gaines, L., Hu, M., Tukker, A., and Steubing, B. (2020). Future material demand for automotive lithium-based batteries. *Commun. Mat.* 1, 99. doi:10.1038/s43246-020-00095-x

Zhang, S. (2013). Status, opportunities, and challenges of electrochemical energy storage. *Front. Energy Res.* 1, 8. doi:10.3389/fenrg.2013.00008

3.7.1. Supporting Information – Publication 5

Supplementary Material for:

Nanostructured 2D WS_2@PANI nanohybrids for electrochemical energy storage

Matteo Crisci,[1,2] Felix Boll,[1,2] Jonas Johannes Pflug,[1] Leonardo Merola,[1,3] Zheming Liu,[4] Jaime Gallego,[1,2] Francesco Lamberti,[3] Teresa Gatti[1,2*]

[1] Institute of Physical Chemistry, Justus Liebig University, Heinrich-Buff-Ring 17, 35392 Giessen, Germany

[2] Center for Materials Research, Justus Liebig University, Heinrich-Buff-Ring 17, 35392 Giessen, Germany

[3] Department of Chemical Sciences, University of Padova, via Marzolo 1, 35131 Padova, Italy

[4] Nanochemistry Department, Istituto Italiano di Tecnologia, via Morego 30, 16163 Genova, Italy

Table of Contents

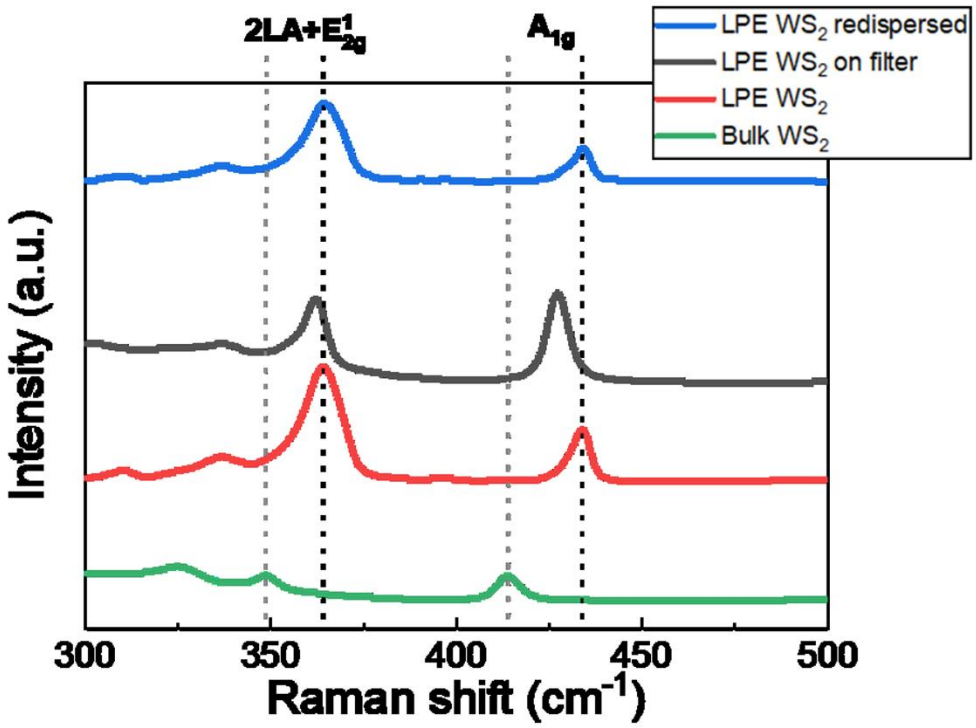

Figure S1. Raman spectra LPE WS_2 pre- and post-filtration and after redispersion of the filtrated material in 1 HCL in brine in the presence of a freshly added surfactant. The spectrum of bulk WS_2 powder is also shown for the sake of comparison.

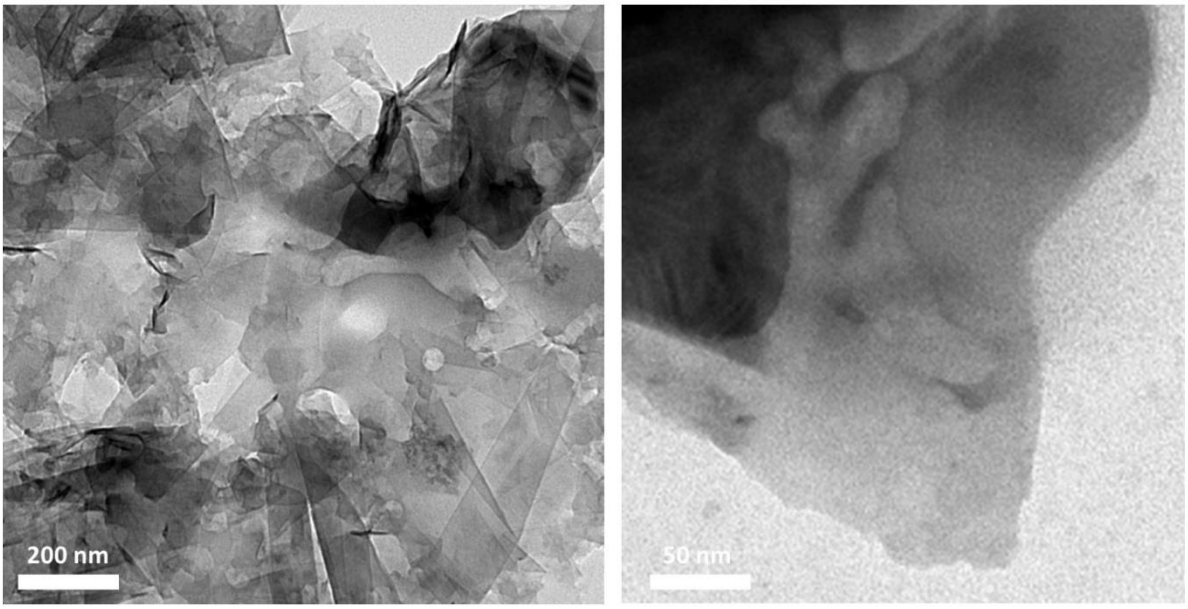

Figure S2. TEM images of LPE WS_2.

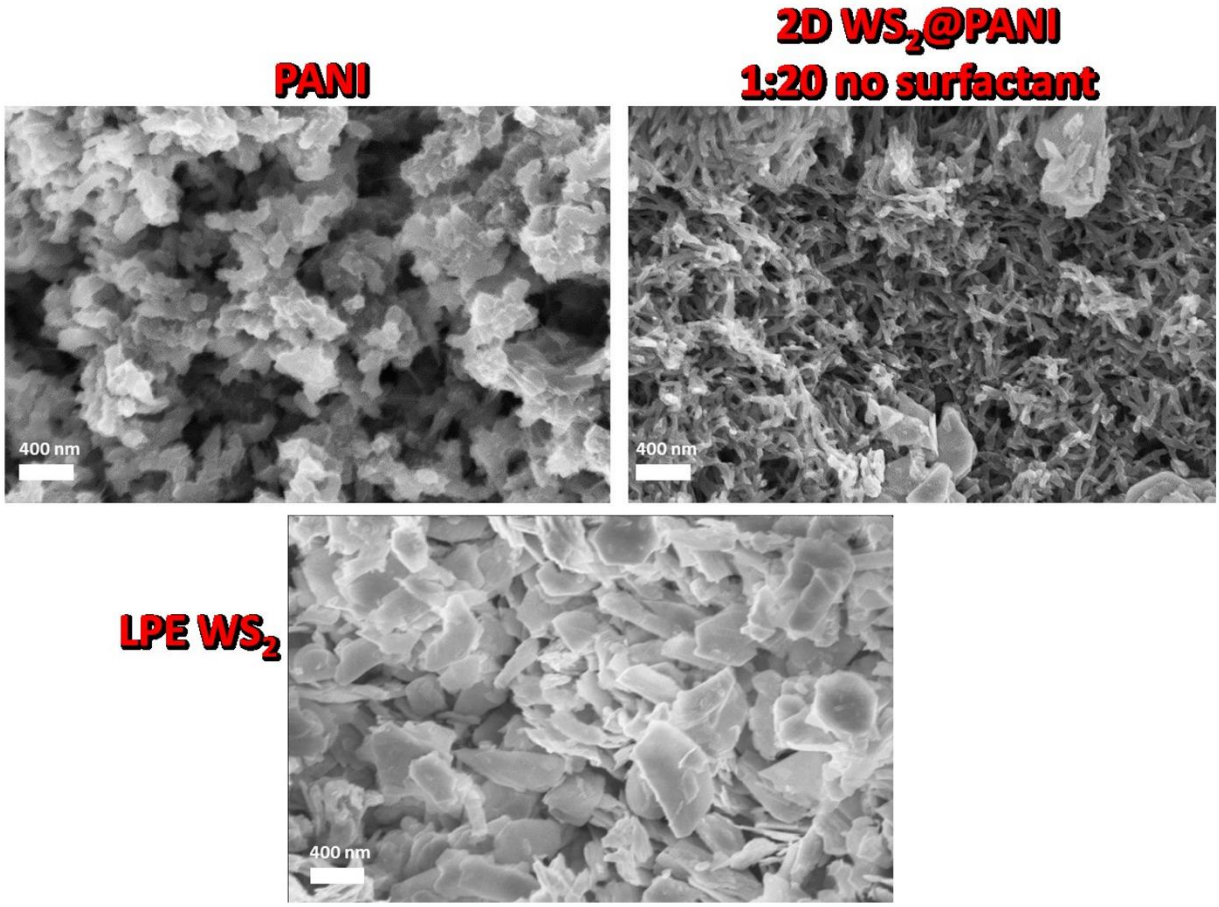

Figure S3. SEM images of template-assisted oxidatively polymerized pure PANI, of a 2D WS2@PANI nanohybrid prepared without the addition of any surfactant and of LPE WS_2 casted from the colloidal phase onto a substrate.

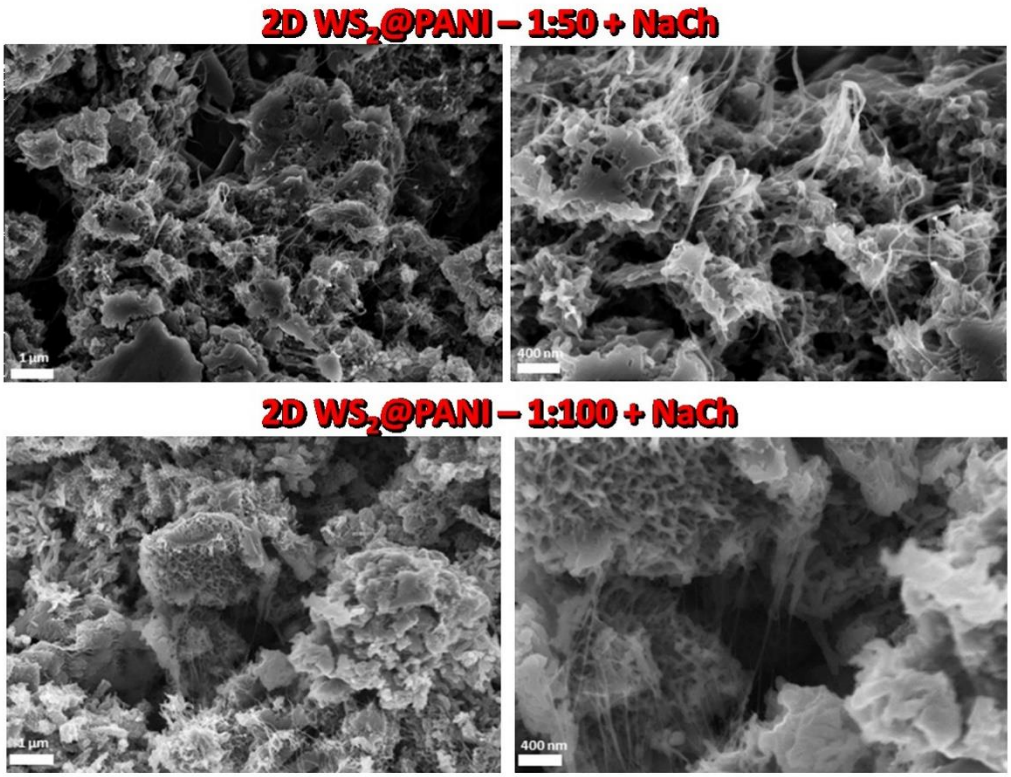

Figure S4. SEM images of 2D WS2@PANI nanohybrids obtained with different LPE WS_2/PANI molar ratios in the presence of NaCh.

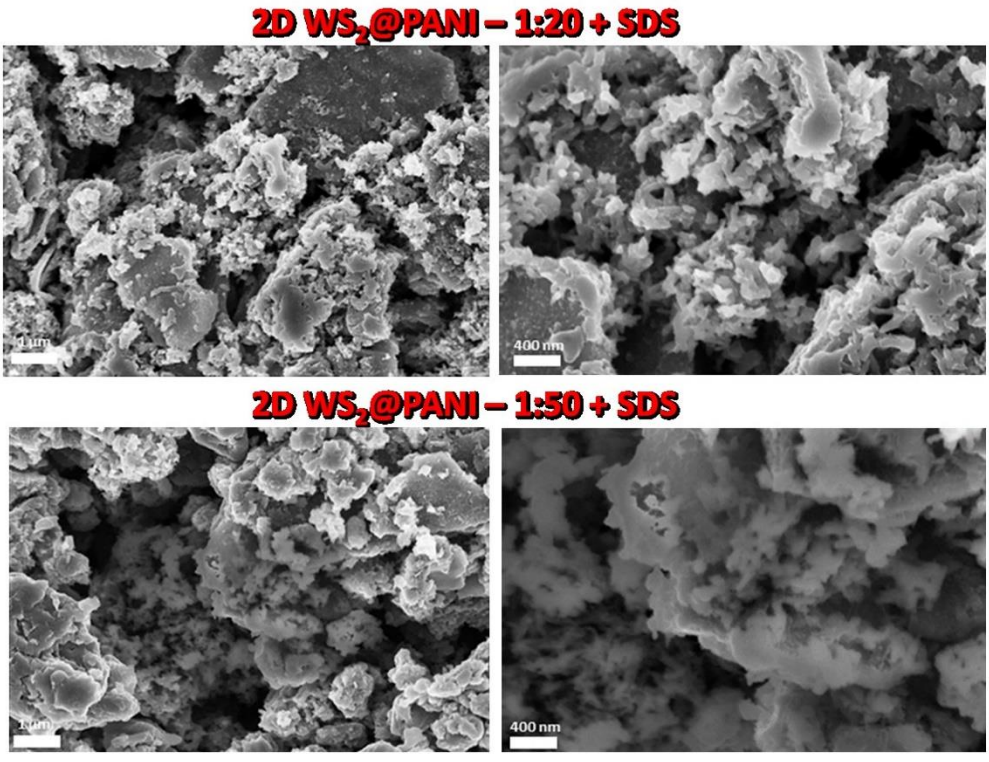

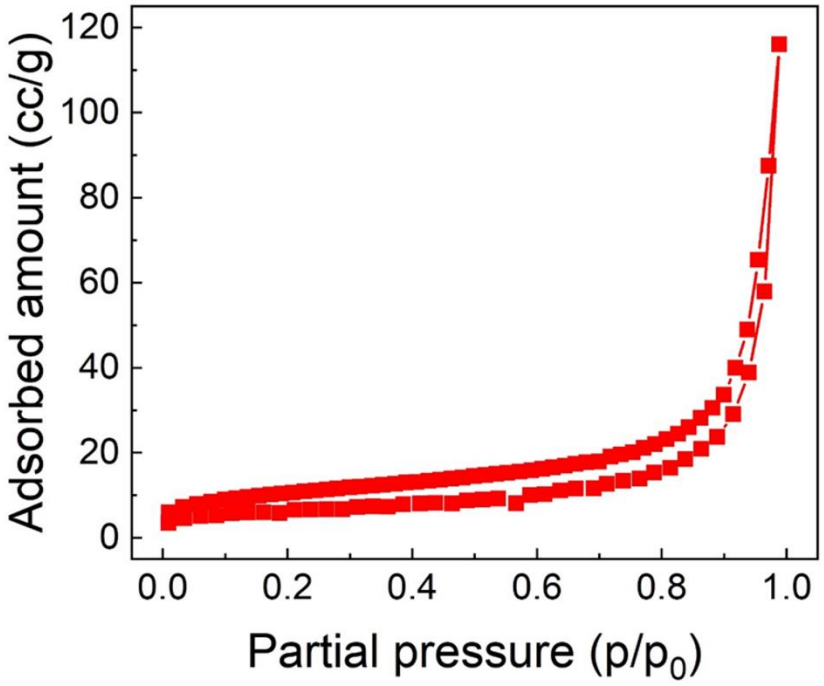

Figure S6. a) N_2 (77 K) physisorption isotherm of a prototypical 2D WS2@PANI nanohybrid. The total surface area is calculated from the adsorption and desorption branches using the NLDFT method.

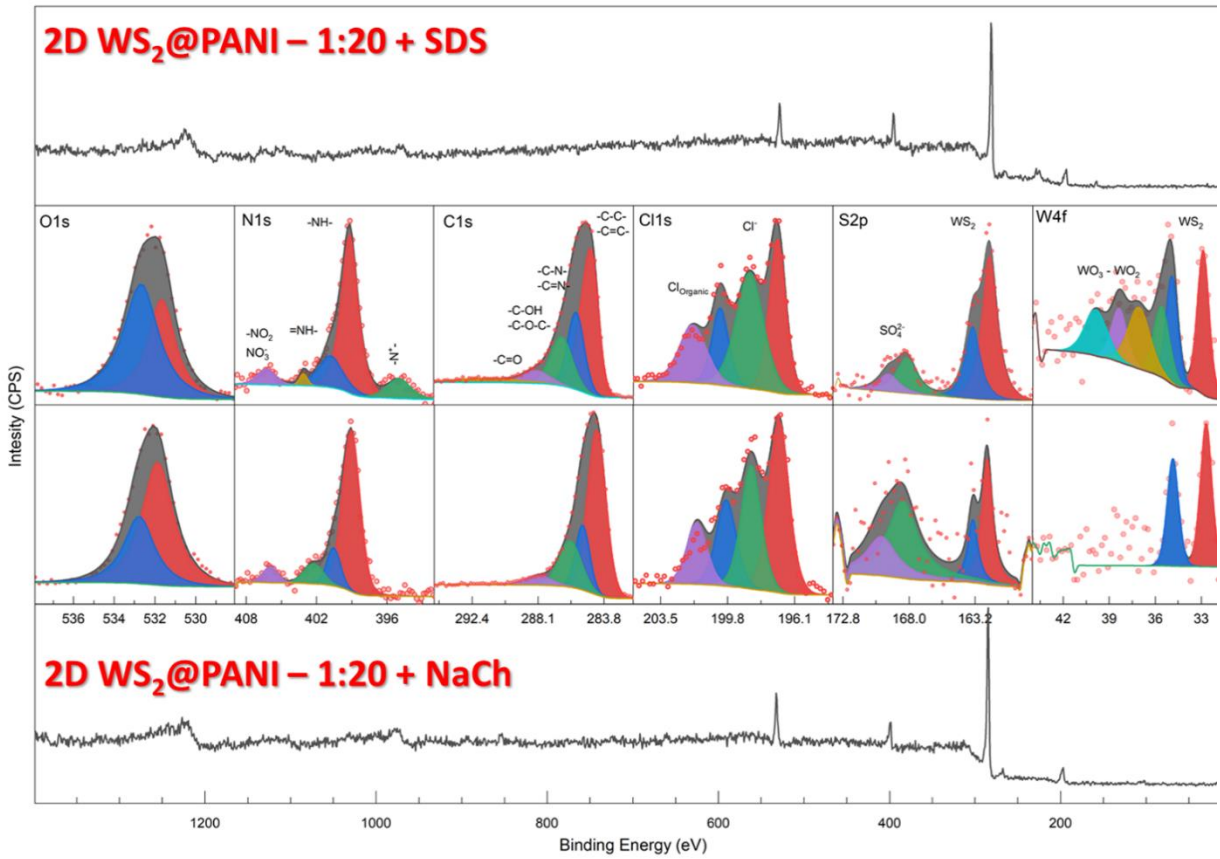

Figure S7. Full XPS spectra of 1:20 2D WS2@PANI nanohybrids prepared in the presence of SDS and NaCh.

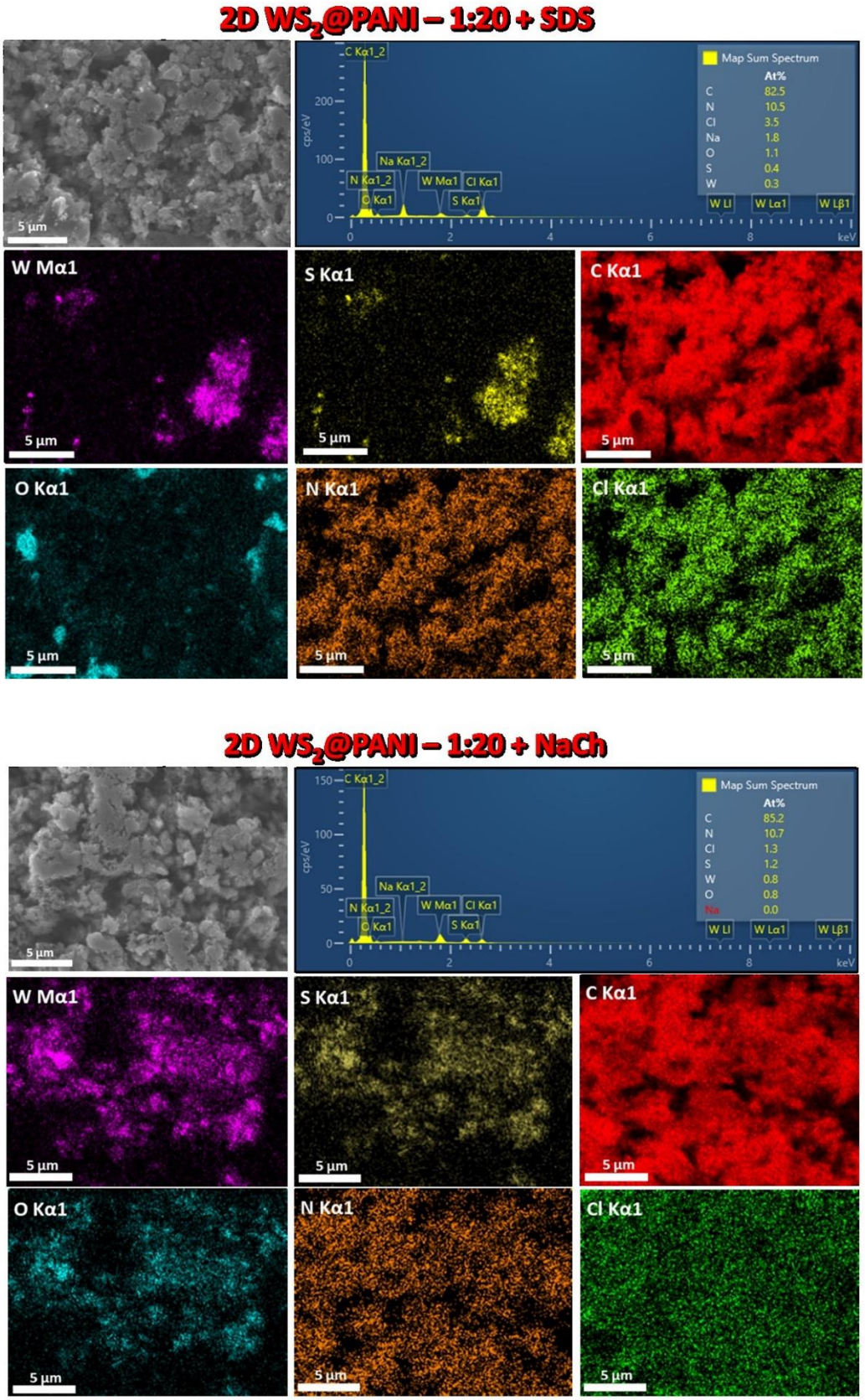

Figure S8. EDX maps of different elements in 1:20 2D WS_2@PANI nanohybrids prepared in

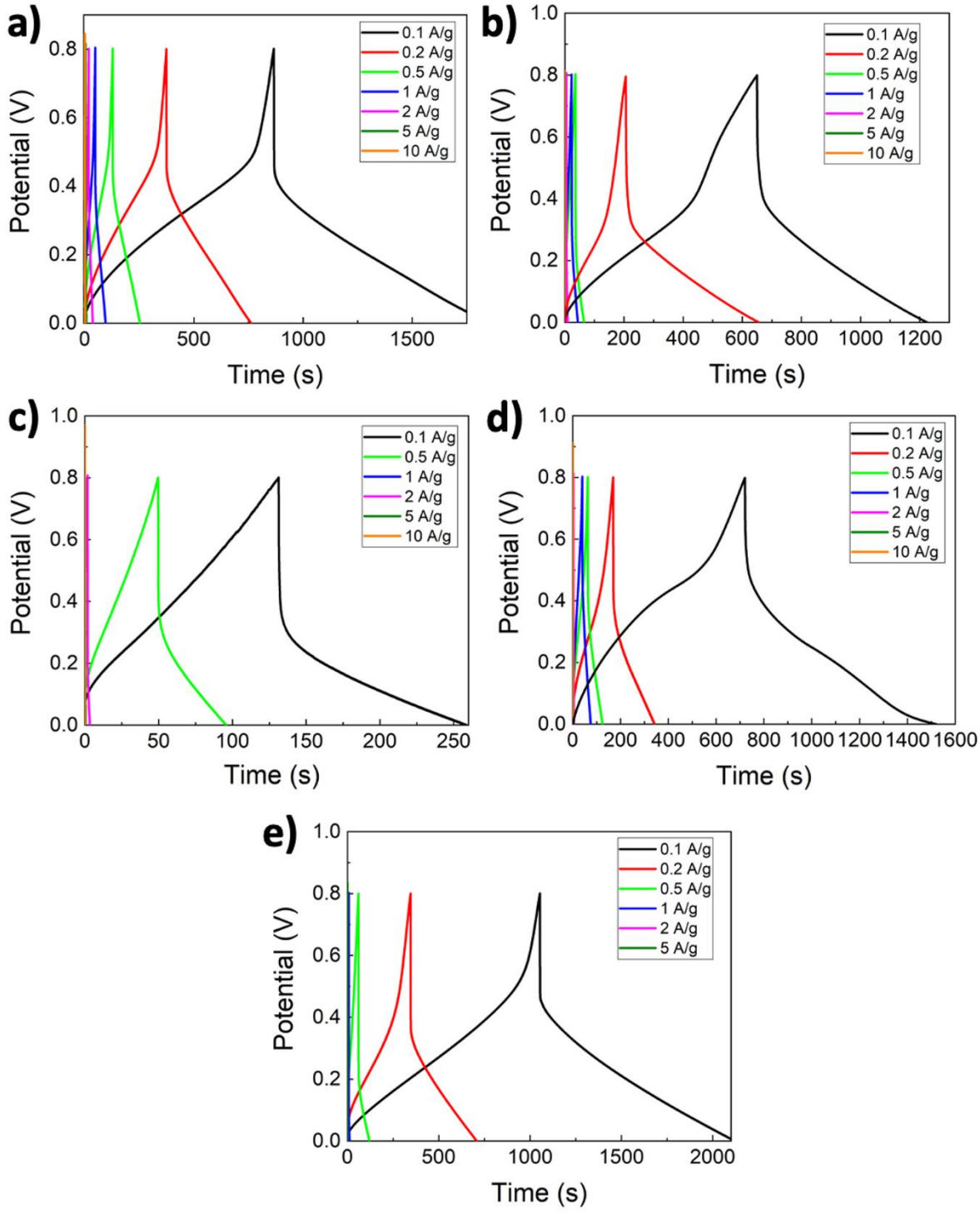

Figure S9. GCD curves at increasing current densities for different 2D WS2@PANI nanohybrids: a) 1:50 + NaCh, b) 1:100 + NaCh, c) 1:20 + SDS, d) 1:50 + SDS, e) 1:100 + SDS.

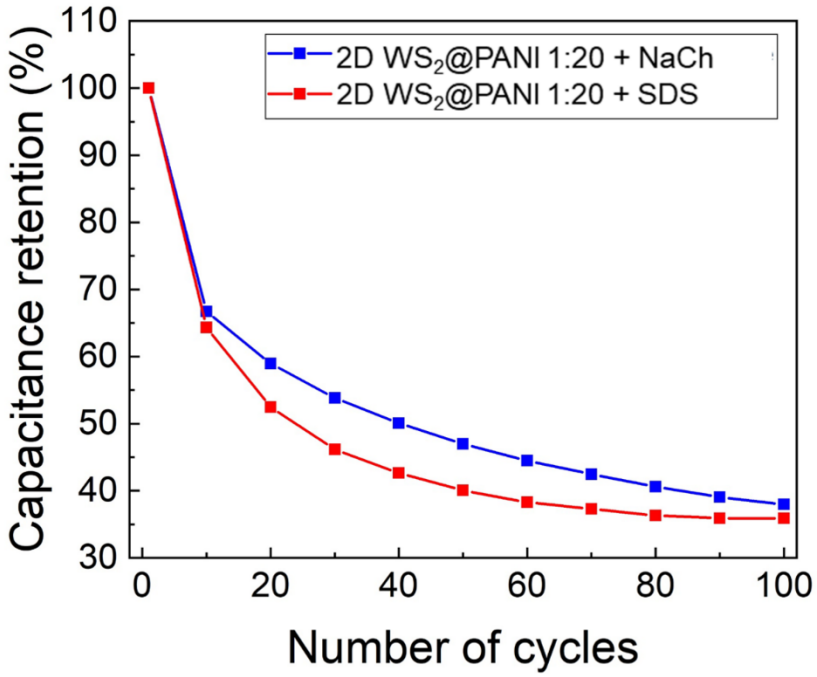

Figure S10. Cyclability of the 1:20 2D WS_2@PANI nanohybrids prepared in the presence of SDS and NaCh measured at a current density of 1 A/g over 100 cycles in a three electrode system (with the active materials deposited on the GC electrode).

4. Conclusion & Outlook

This dissertation contributes to three key areas: electrospinning, exfoliation and flexible energy storage. The process of electrospinning has shown to be a versatile technique, both for producing flexible backbone materials as well as the preparation and improvement of carbon materials using polymer solutions as precursors. Throughout the research, I gained significant expertise in the method, particularly in electrospinning PAN fibers (**publication 1**) and PEO fibers (**publication 2**), as well as exploring other materials. Produced fibers were specifically tailored for applications in flexible energy storage devices, widely known in literature, like carbon-based fibers, polymer fibers using conductive polymers like PEDOT:PSS and other composites as well as core-shell structures.[48,215,243–246] During the optimization, a study was conducted to examine the effects of heat treatment on electrospun CNFs by varying T_s and T_c. After electrospinning, the conversion of PAN fibers to CNFs is attained by these two heat treatment steps. The specific surface area, the nitrogen ratio and bonding types turned out to be strongly dependent on the specific temperatures chosen with optimum C_s achieved at T= 325 °C and T_c= 800 °C of about 49 F g^{-1} at 0.5 A g^{-1}.

Using this combination of heat treatment, the degree of graphitization in combination with the largest accessible surface area leads to the highest C_s. However, at carbonization temperatures above 800 °C, C_s decreased due to a nitrogen loss, which reduced the pseudocapacitive contributions from pyridinic and pyrrolic species in the carbon lattice. This highlights the importance of carefully optimizing the thermal treatment process for energy storage devices and the many steps in a process that need to be addressed for the optimization of a product or device. Moreover, in terms of recyclability, optimizing simple materials is crucial, as complex composites and doped systems are much harder to recycle in line with circular economy principles. Thus, refining processes at each stage cannot only improve properties like C_s in this particular case but also contribute to more sustainable energy storage solutions acknowledging the bigger picture.[247]

However, due to the limited flexibility of CNFs, other approaches were followed involving material mixtures and compositions of carbon-based materials. Here, TMDCs were selected as active species having versatile properties ranging from their large surface area, electronic properties, adjustable bandgap and their possible phase transitions from the semiconducting towards the metallic phase.[18,29,248] In supercapacitor applications these materials are ideal candidates in combination with conductive carbon species, as previously reported in the literature.[9]

To fully utilize the wide range of TMDC properties, exfoliation throughout top-down approaches is necessary. Choosing the top-down methods comes with several benefits regarding yield, costs and sustainability. Using water or alcohol as solvents instead of NMP as the most efficient solvent for most exfoliation processes, the toxicity and costs are reduced drastically.[32] The usage of water typically results in lower yields, which can be faced by employing surfactants as suspension-stabilizing agents for the exfoliation process. This combination helps to maximize the efficiency of TMDC exfoliation while maintaining environmental and economic viability.

Working on the exfoliation process of TMDCs, two studies were published (**publications 3** & **4**) that explored the impact of various surfactants and concentrations on the exfoliation efficiency of MoS_2, WS_2 and Bi_2S_3. It was revealed that MoS_2 aqueous solutions with concentrations of 8.2 mM SHS lead to highly stable suspensions while 1.0 mM SDBS suspensions remain less stable but produce the highest yield. For WS_2 the highest yield was obtained using 8.2 mM SHS aqueous solutions as exfoliation medium. However, exfoliation efficiency is low since it lacks in the degree of exfoliation. Here, 4.2 mM SHS was considered to be the best choice in terms of stability and monolayer production of the inks. For Bi_2S_3 the aqueous solution containing 8.2 mM SDBS provided the most stable suspensions but the yield of SHS at 8.2 mM suspensions was higher compared to SDBS.

Overall, SHS at high concentrations proved to be the most efficient surfactant across various TMDCs. Notably the best-performing surfactant concentrations have been far above the CMC of SHS which is 0.55 mM. The results suggest that depending on the application, the preparation of stable suspensions of TMDCs should be varied in terms of concentration and surfactant to obtain either high concentrations, a higher degree of exfoliation or more stable suspensions. Depending on the application as a high-energy material or for electronics, changing the exfoliation medium can be a wise choice for optimizing processes.

The combination of TMDCs with carbon-based materials was utilized afterwards to produce flexible energy storage devices based on PEO fibers in **publication 2**. In addition to electrochemical characterization and capacitance retention, the flexibility and mechanical resilience of the devices were studied. The bending of the pristine cell led to a strong increase of C_s rising from 7.77 F g^{-1} to 14.35 F g^{-1} due to pressurization. After three bending cycles, a plateau around 5.70 F g^{-1} was reached in the flattened cell. The addition of MWCNTs as nanofillers improved the fiber stability and further increased C_s. Although the Young's Modulus of the PEO fibers decreased with the inclusion of WS_2, MWCNTs enhanced the tensile stiffness, raising it from 42.99 ± 11.92 MPa to 96.47 ± 31.90 MPa. Most importantly, the preparation of the composites exposed a synergistic effect of the exfoliated WS_2, MWCNTs and CB leading to higher C_s which does not derive from the simple sum of all components. The attractive interaction between the materials was also seen in TEM images, where WS_2 particles are surrounded by carbon material and vice versa highlighting the strong material synergy.[62,249]

Further research should focus on identifying the exact mechanism behind the observed synergy between carbon materials and TMDCs, which has also been reported in the literature for MoS_2-carbon composites in intercalation processes.[19] To further explore this, the same types of flexible energy storage devices should be produced using MoS_2 instead of WS_2, allowing for performance comparisons and a deeper understanding of this synergy.

This interaction might stem from phase transitions of TMDCs near the carbon surface, possibly involving the more conductive metallic 1T-phase. Here, other approaches using the 1T-phase can be followed as well since its electrical conductivity is superior to the 2H phase. The optimized CNFs from **publication 1** could be a considerable backbone material for the deposition of TMDCs on the surface using hydrothermal reactions using bottom-up approaches.

Additionally, since nitrogen is used in CNF production, preventing the oxidation of TMDCs, TMDCs could be directly integrated into the spinning suspensions to create TMDC-CNF composites. Here, the synergy effects between TMDCs and carbon could play a major role as well for the performance as an energy storage device. The combination of TMDCs and CNFs could further benefit from past optimizations in both material systems. By embedding TMDCs into CNFs during the electrospinning process, the resulting composite could leverage the conductive and surface properties of both materials taking advantage of the expected synergy.

The synergy effect between TMDCs and carbon is not the only noteworthy aspect of these studies. Changes in C_s were obtained from the pressurized cells in **publication 2**. This opens up the possibility of using flexible, symmetric capacitor devices in pressure sensor applications. Such devices could be implemented to detect high-pressure areas on non-flat surfaces to identify weaknesses or abrasion regions. Additionally, they could be used as inserts in shoes to map the load distribution on the sole for medical and ergonomic applications. This highlights the multifunctional approaches and possible potential of the flexible composites and the individual materials beyond energy storage, broadening the scope and giving space for creativity regarding their application.[249]

5. References

(1) Statista 2024. Oil production worldwide from 1998 to 2023 https://www.statista.com/statistics/265203/global-oil-production-in-barrels-per-day/.

(2) Birol, F. *The Future of Petrochemicals*; 2024. https://doi.org/10.1787/9789264307414-en.

(3) Official website of the Council of the EU and the European Council https://www.consilium.europa.eu/en/infographics/how-is-eu-electricity-produced-and-sold/#:~:text=How does the EU produce,and nuclear electricity over 20%25.

(4) Dunn, B.; Kamath, H.; Tarascon, J. M. Electrical Energy Storage for the Grid: A Battery of Choices. *Science (80-.).* **2011**, *334* (6058), 928–935. https://doi.org/10.1126/science.1212741.

(5) Mohl, M.; Rautio, A. R.; Asres, G. A.; Wasala, M.; Patil, P. D.; Talapatra, S.; Kordas, K. 2D Tungsten Chalcogenides: Synthesis, Properties and Applications. *Adv. Mater. Interfaces* **2020**, *7* (13). https://doi.org/10.1002/admi.202000002.

(6) Lee, Y. Y.; Park, G. O.; Choi, Y. S.; Shon, J. K.; Yoon, J.; Kim, K. H.; Yoon, W. S.; Kim, H.; Kim, J. M. Mesoporous Transition Metal Dichalcogenide ME2 (M = Mo, W; E = S, Se) with 2-D Layered Crystallinity as Anode Materials for Lithium Ion Batteries. *RSC Adv.* **2016**, *6* (17), 14253–14260. https://doi.org/10.1039/c5ra19799f.

(7) Kumar, P.; Abuhimd, H.; Wahyudi, W.; Li, M.; Ming, J.; Li, L.-J. Review—Two-Dimensional Layered Materials for Energy Storage Applications. *ECS J. Solid State Sci. Technol.* **2016**, *5* (11), Q3021–Q3025. https://doi.org/10.1149/2.0051611jss.

(8) David, L.; Bhandavat, R.; Singh, G. MoS2/Graphene Composite Paper for Sodium-Ion Battery Electrodes. *ACS Nano* **2014**, *8* (2), 1759–1770. https://doi.org/10.1021/nn406156b.

(9) Li, X.; Zhang, J.; Liu, Z.; Fu, C.; Niu, C. WS2 Nanoflowers on Carbon Nanotube Vines with Enhanced Electrochemical Performances for Lithium and Sodium-Ion Batteries. *J. Alloys Compd.* **2018**, *766*, 656–662. https://doi.org/10.1016/j.jallcom.2018.07.008.

(10) Hu, G.; Kang, J.; Ng, L. W. T.; Zhu, X.; Howe, R. C. T.; Jones, C. G.; Hersam, M. C.; Hasan, T. Functional Inks and Printing of Two-Dimensional Materials. *Chem. Soc. Rev.* **2018**, *47* (9), 3265–3300. https://doi.org/10.1039/c8cs00084k.

(11) Mendoza-Sánchez, B.; Gogotsi, Y. Synthesis of Two-Dimensional Materials for Capacitive Energy Storage. *Adv. Mater.* **2016**, *28* (29), 6104–6135. https://doi.org/10.1002/adma.201506133.

(12) Berkdemir, A.; Gutiérrez, H. R.; Botello-Méndez, A. R.; Perea-López, N.; Elías, A. L.; Chia, C. I.; Wang, B.; Crespi, V. H.; López-Urías, F.; Charlier, J. C.; Terrones, H.; Terrones, M. Identification of Individual and Few Layers of WS2 Using Raman Spectroscopy. *Sci. Rep.* **2013**, *3*, 1–8. https://doi.org/10.1038/srep01755.

(13) Novoselov, K. S.; Geim, A. K.; Morozov, S. V.; Jiang, D.; Zhang, Y.; S.V, D.; Grigorieva, S. V.; Firsov, A. A. Novoselov 2004. **2004**, *306* (October), 666–669. https://doi.org/10.1126/science.1102896.

(14) Coleman, J. N.; Lotya, M.; O'Neill, A.; Bergin, S. D.; King, P. J.; Khan, U.; Young, K.; Gaucher, A.; De, S.; Smith, R. J.; Shvets, I. V.; Arora, S. K.; Stanton, G.; Kim, H. Y.; Lee, K.; Kim, G. T.; Duesberg, G. S.; Hallam, T.; Boland, J. J.; Wang, J. J.; Donegan, J. F.; Grunlan, J. C.; Moriarty, G.; Shmeliov, A.; Nicholls, R. J.; Perkins, J. M.; Grieveson, E. M.; Theuwissen, K.; McComb, D. W.; Nellist, P. D.; Nicolosi, V. Two-Dimensional Nanosheets Produced by Liquid Exfoliation of Layered Materials. *Science (80-.).* **2011**, *331* (6017), 568–571. https://doi.org/10.1126/science.1194975.

(15) Tian, X.; Li, X.; Yang, T.; Wang, K.; Wang, H.; Song, Y.; Liu, Z.; Guo, Q.; Chen, C. Flexible Carbon Nanofiber Mats with Improved Graphitic Structure as Scaffolds for Efficient All-Solid-State Supercapacitor. *Electrochim. Acta* **2017**, *247*, 1060–1071. https://doi.org/10.1016/j.electacta.2017.07.103.

(16) Ghorai, A.; Midya, A.; Ray, S. K. Superior Charge Storage Performance of WS2 Quantum Dots in a Flexible Solid State Supercapacitor. *New J. Chem.* **2018**, *42* (5), 3609–3613. https://doi.org/10.1039/c7nj03869k.

(17) Shiva, K.; Ramakrishna Matte, H. S. S.; Rajendra, H. B.; Bhattacharyya, A. J.; Rao, C. N. R. Employing Synergistic Interactions between Few-Layer WS2 and Reduced Graphene Oxide to Improve Lithium Storage, Cyclability and Rate Capability of Li-Ion Batteries. *Nano Energy* **2013**, *2* (5), 787–793. https://doi.org/10.1016/j.nanoen.2013.02.001.

(18) Lin, T. W.; Sadhasivam, T.; Wang, A. Y.; Chen, T. Y.; Lin, J. Y.; Shao, L. D. Ternary Composite Nanosheets with MoS2/WS2/Graphene Heterostructures as High-Performance Cathode Materials for Supercapacitors. *ChemElectroChem* **2018**, *5* (7), 1024–1031. https://doi.org/10.1002/celc.201800043.

(19) Mahmood, Q.; Park, S. K.; Kwon, K. D.; Chang, S. J.; Hong, J. Y.; Shen, G.; Jung, Y. M.; Park, T. J.; Khang, S. W.; Kim, W. S.; Kong, J.; Park, H. S. Transition from Diffusion-Controlled Intercalation into Extrinsically Pseudocapacitive Charge Storage of MoS2 by Nanoscale Heterostructuring. *Adv. Energy Mater.* **2016**, *6* (1), 1–10. https://doi.org/10.1002/aenm.201501115.

(20) Cárdenas-Martínez, J.; España-Sánchez, B. L.; Esparza, R.; Ávila-Niño, J. A. Flexibleand Transparent Supercapacitors Using Electrospun PEDOT:PSS Electrodes. *Synth. Met.* **2020**, *267* (March), 116436. https://doi.org/10.1016/j.synthmet.2020.116436.

(21) Liang, A.; Li, D.; Zhou, W.; Wu, Y.; Ye, G.; Wu, J.; Chang, Y.; Wang, R.; Xu, J.; Nie, G.; Hou, J.; Du, Y. Robust Flexible WS2/PEDOT:PSS Film for Use in High-Performance Miniature Supercapacitors. *J. Electroanal. Chem.* **2018**, *824*, 136–146. https://doi.org/10.1016/j.jelechem.2018.07.040.

(22) Novoselov, K. S.; Jiang, D.; Schedin, F.; Booth, T. J.; Khotkevich, V. V.; Morozov, S. V.; Geim, A. K. Two-Dimensional Atomic Crystals. *Proc. Natl. Acad. Sci. U. S. A.* **2005**, *102* (30), 10451–10453. https://doi.org/10.1073/pnas.0502848102.

(23) Geim, A. K.; Novoselov, K. S. The Rise of Graphene PROGRESS. *Nat. Mater.* **2007**, *6* (3), 183–191.

(24) Papageorgiou, D. G.; Kinloch, I. A.; Young, R. J. Mechanical Properties of Graphene and Graphene-Based Nanocomposites. *Prog. Mater. Sci.* **2017**, *90*, 75–127. https://doi.org/10.1016/j.pmatsci.2017.07.004.

(25) Min, K.; Aluru, N. R. Mechanical Properties of Graphene under Shear Deformation. *Appl. Phys. Lett.* **2011**, *98* (1), 1–4. https://doi.org/10.1063/1.3534787.

(26) Yu, M. F.; Lourie, O.; Dyer, M. J.; Moloni, K.; Kelly, T. F.; Ruoff, R. S. Strength and Breaking Mechanism of Multiwalled Carbon Nanotubes under Tensile Load. *Science (80-.).* **2000**, *287* (5453), 637–640. https://doi.org/10.1126/science.287.5453.637.

(27) Liu, L.; Zhang, J.; Zhao, J.; Liu, F. Mechanical Properties of Graphene Oxides. *Nanoscale* **2012**, *4* (19), 5910–5916. https://doi.org/10.1039/c2nr31164j.

(28) Faccio, R.; Denis, P. A.; Pardo, H.; Goyenola, C.; Mombrú, Á. W. Mechanical Properties of Graphene Nanoribbons. *J. Phys. Condens. Matter* **2009**, *21* (28). https://doi.org/10.1088/0953-8984/21/28/285304.

(29) Iqbal, M. W.; Shahzad, K.; Akbar, R.; Hussain, G. A Review on Raman Finger Prints of Doping and Strain Effect in TMDCs. *Microelectron. Eng.* **2020**, *219* (September 2019). https://doi.org/10.1016/j.mee.2019.111152.

(30) Gutiérrez, H. R.; Perea-López, N.; Elías, A. L.; Berkdemir, A.; Wang, B.; Lv, R.; López-Urías, F.; Crespi, V. H.; Terrones, H.; Terrones, M. Extraordinary Room-Temperature Photoluminescence in Triangular WS 2 Monolayers. *Nano Lett.* **2013**, *13* (8), 3447–3454. https://doi.org/10.1021/nl3026357.

(31) Kuc, A.; Zibouche, N.; Heine, T. Influence of Quantum Confinement on the Electronic Structure of the Transition Metal Sulfide TS2. *Phys. Rev. B - Condens. Matter Mater. Phys.* **2011**, *83* (24), 1–4. https://doi.org/10.1103/PhysRevB.83.245213.

(32) Smith, R. J.; King, P. J.; Lotya, M.; Wirtz, C.; Khan, U.; De, S.; O'Neill, A.; Duesberg, G. S.; Grunlan, J. C.; Moriarty, G.; Chen, J.; Wang, J.; Minett, A. I.; Nicolosi, V.; Coleman, J. N. Large-Scale Exfoliation of Inorganic Layered Compounds in Aqueous Surfactant Solutions. *Adv. Mater.* **2011**, *23* (34), 3944–3948. https://doi.org/10.1002/adma.201102584.

(33) Splendiani, A.; Sun, L.; Zhang, Y.; Li, T.; Kim, J.; Chim, C. Y.; Galli, G.; Wang, F. Emerging Photoluminescence in Monolayer MoS2. *Nano Lett.* **2010**, *10* (4), 1271–1275. https://doi.org/10.1021/nl903868w.

(34) Kumar, A.; Ahluwalia, P. K. Tunable Dielectric Response of Transition Metals Dichalcogenides MX 2 (M=Mo, W; X=S, Se, Te): Effect of Quantum Confinement. *Phys. B Condens. Matter* **2012**, *407* (24), 4627–4634. https://doi.org/10.1016/j.physb.2012.08.034.

(35) Radisavljevic, B.; Radenovic, A.; Brivio, J.; Giacometti, V.; Kis, A. Single-Layer MoS2 Transistors. *Nat. Nanotechnol.* **2011**, *6* (3), 147–150. https://doi.org/10.1038/nnano.2010.279.

(36) Wang, M.; Langer, M.; Altieri, R.; Crisci, M.; Osella, S.; Gatti, T. Two-Dimensional Layered Heterojunctions for Photoelectrocatalysis. *ACS Nano* **2024**, *18* (13), 9245–9284. https://doi.org/10.1021/acsnano.3c12274.

(37) Abid, N.; Khan, A. M.; Shujait, S.; Chaudhary, K.; Ikram, M.; Imran, M.; Haider, J.; Khan, M.; Khan, Q.; Maqbool, M. Synthesis of Nanomaterials Using Various Top-down and Bottom-up Approaches, Influencing Factors, Advantages, and Disadvantages: A Review. *Adv. Colloid Interface Sci.* **2022**, *300* (December 2021), 102597. https://doi.org/10.1016/j.cis.2021.102597.

(38) Samadi, M.; Sarikhani, N.; Zirak, M.; Zhang, H.; Zhang, H. L.; Moshfegh, A. Z. Group 6 Transition Metal Dichalcogenide Nanomaterials: Synthesis, Applications and Future Perspectives. *Nanoscale Horizons* **2018**, *3* (2), 90–204. https://doi.org/10.1039/c7nh00137a.

(39) Yin, H.; Zhang, X.; Lu, J.; Geng, X.; Wan, Y.; Wu, M.; Yang, P. Substrate Effects on the CVD Growth of MoS2 and WS2. *J. Mater. Sci.* **2020**, *55* (3), 990–996. https://doi.org/10.1007/s10853-019-03993-9.

(40) Yang, W.; Shang, J.; Wang, J.; Shen, X.; Cao, B.; Peimyoo, N.; Zou, C.; Chen, Y.; Wang, Y.; Cong, C.; Huang, W.; Yu, T. Electrically Tunable Valley-Light Emitting Diode (VLED) Based on CVD-Grown Monolayer WS2. *Nano Lett.* **2016**, *16* (3), 1560–1567. https://doi.org/10.1021/acs.nanolett.5b04066.

(41) Cong, C.; Shang, J.; Wu, X.; Cao, B.; Peimyoo, N.; Qiu, C.; Sun, L.; Yu, T. Synthesis and Optical Properties of Large-Area Single-Crystalline 2D Semiconductor WS2 Monolayer from Chemical Vapor Deposition. *Adv. Opt. Mater.* **2014**, *2* (2), 131–136. https://doi.org/10.1002/adom.201300428.

(42) Nandi, D. K.; Sen, U. K.; Dhara, A.; Mitra, S.; Sarkar, S. K. Intercalation Based Tungsten Disulfide (WS2) Li-Ion Battery Anode Grown by Atomic Layer Deposition. *RSC Adv.* **2016**, *6* (44), 38024–38032. https://doi.org/10.1039/c6ra00468g.

(43) Balasubramanyam, S.; Merkx, M. J. M.; Verheijen, M. A.; Kessels, W. M. M.; Mackus, A. J. M.; Bol, A. A. Area-Selective Atomic Layer Deposition of Two-Dimensional WS2 Nanolayers. *ACS Mater. Lett.* **2020**, *2* (5), 511–518. https://doi.org/10.1021/acsmaterialslett.0c00093.

(44) Tang, G.; Tang, H.; Li, C.; Li, W.; Ji, X. Surfactant-Assisted Hydrothermal Synthesis and Characterization of WS 2 Nanorods. *Mater. Lett.* **2011**, *65* (23–24), 3457–3460. https://doi.org/10.1016/j.matlet.2011.07.033.

(45) Nagaraju, C.; Gopi, C. V. V. M.; Ahn, J. W.; Kim, H. J. Hydrothermal Synthesis of MoS2 and WS2 Nanoparticles for High-Performance Supercapacitor Applications. *New J. Chem.* **2018**, *42* (15), 12357–12360. https://doi.org/10.1039/c8nj02822b.

(46) Therese, H. A.; Li, J.; Kolb, U.; Tremel, W. Facile Large Scale Synthesis of WS 2 Nanotubes from WO 3 Nanorods Prepared by a Hydrothermal Route. *Solid State Sci.* **2005**, *7* (1), 67–72. https://doi.org/10.1016/j.solidstatesciences.2004.10.006.

(47) Cao, S.; Liu, T.; Hussain, S.; Zeng, W.; Peng, X.; Pan, F. Hydrothermal Synthesis of Variety Low Dimensional WS2 Nanostructures. *Mater. Lett.* **2014**, *129*, 205–208. https://doi.org/10.1016/j.matlet.2014.05.013.

(48) Wu, C.; Zeng, X.; He, P.; Chen, L.; Wei, W. Flexible WS2@CNFs Membrane Electrode with Outstanding Lithium Storage Performance Derived from Capacitive Behavior. *Adv. Mater. Interfaces* **2018**, *5* (3), 1–8. https://doi.org/10.1002/admi.201701080.

(49) Manzeli, S.; Ovchinnikov, D.; Pasquier, D.; Yazyev, O. V.; Kis, A. 2D Transition Metal Dichalcogenides. *Nat. Rev. Mater.* **2017**, *2*. https://doi.org/10.1038/natrevmats.2017.33.

(50) Zhang, P.; Wang, F.; Yu, M.; Zhuang, X.; Feng, X. Two-Dimensional Materials for Miniaturized Energy Storage Devices: From Individual Devices to Smart Integrated Systems. *Chem. Soc. Rev.* **2018**, *47* (19), 7426–7451. https://doi.org/10.1039/c8cs00561c.

(51) Alfihed, S.; Hossain, M.; Alharbi, A.; Alyamani, A.; Alharbi, F. H. PLD Grown Polycrystalline Tungsten Disulphide (WS 2) Films . *J. Mater.* **2013**, *2013*, 1–5. https://doi.org/10.1155/2013/603648.

(52) Tian, K.; Baskaran, K.; Tiwari, A. Growth of Two-Dimensional WS2 Thin Films by Pulsed Laser Deposition Technique. *Thin Solid Films* **2018**, *668* (October), 69–73. https://doi.org/10.1016/j.tsf.2018.10.015.

(53) Yao, J. D.; Zheng, Z. Q.; Shao, J. M.; Yang, G. W. Stable, Highly-Responsive and Broadband Photodetection Based on Large-Area Multilayered WS2 Films Grown by Pulsed-Laser Deposition. *Nanoscale* **2015**, *7* (36), 14974–14981. https://doi.org/10.1039/c5nr03361f.

(54) Yi, M.; Shen, Z. A Review on Mechanical Exfoliation for the Scalable Production of Graphene. *J. Mater. Chem. A* **2015**, *3* (22), 11700–11715. https://doi.org/10.1039/c5ta00252d.

(55) Backes, C.; Campi, D.; Szydlowska, B. M.; Synnatschke, K.; Ojala, E.; Rashvand, F.; Harvey, A.; Griffin, A.; Sofer, Z.; Marzari, N.; Coleman, J. N.; O'Regan, D. D. Equipartition of Energy Defines the Size-Thickness Relationship in Liquid-Exfoliated Nanosheets. *ACS Nano* **2019**. https://doi.org/10.1021/acsnano.9b02234.

(56) Tao, H.; Zhang, Y.; Gao, Y.; Sun, Z.; Yan, C.; Texter, J. Scalable Exfoliation and Dispersion of Two-Dimensional Materials-an Update. *Phys. Chem. Chem. Phys.* **2017**, *19* (2), 921–960. https://doi.org/10.1039/c6cp06813h.

(57) Xu, Y.; Cao, H.; Xue, Y.; Li, B.; Cai, W. Liquid-Phase Exfoliation of Graphene: An Overview on Exfoliation Media, Techniques, and Challenges. *Nanomaterials* **2018**, *8* (11). https://doi.org/10.3390/nano8110942.

(58) Abdelkader, A. M.; Kinloch, I. A. Mechanochemical Exfoliation of 2D Crystals in Deep Eutectic Solvents. *ACS Sustain. Chem. Eng.* **2016**, *4* (8), 4465–4472. https://doi.org/10.1021/acssuschemeng.6b01195.

(59) Dresselhaus, M. S.; Dresselhaus, G. Intercalation Compounds of Graphite. *Adv. Phys.* **1981**, *30* (2), 139–326. https://doi.org/10.1080/00018738100101367.

(60) Backes, C.; Higgins, T. M.; Kelly, A.; Boland, C.; Harvey, A.; Hanlon, D.; Coleman, J. N. Guidelines for Exfoliation, Characterization and Processing of Layered Materials Produced by Liquid Exfoliation. *Chemistry of Materials*. American Chemical Society 2017, pp 243–255. https://doi.org/10.1021/acs.chemmater.6b03335.

(61) Casiraghi, C.; Pisana, S.; Novoselov, K. S.; Geim, A. K.; Ferrari, A. C. Raman Fingerprint of Charged Impurities in Graphene. *Appl. Phys. Lett.* **2007**, *91* (23), 1–4. https://doi.org/10.1063/1.2818692.

(62) Boll, F.; Fadda, M.; Happel, M.; Crisci, M.; Athanassiou, A.; Smarsly, B.; Bella, F.; Lamberti, F.; Perotto, G.; Gatti, T. Multicomponent Synergistic Contribution in Nanoengineered Nanofibers for Flexible Energy Storage. **2024**. https://doi.org/10.1021/acsaem.4c00417.

(63) Pozzati, M.; Boll, F.; Crisci, M.; Domenici, S.; Smarsly, B.; Gatti, T.; Wang, M. Systematic Investigation on the Surfactant-Assisted Liquid-Phase Exfoliation of MoS 2 and WS 2 in Water for Sustainable 2D Material Inks. **2024**, *2400039*, 1–9. https://doi.org/10.1002/pssr.202400039.

(64) Crisci, M.; Boll, F.; Merola, L.; Pflug, J. J.; Liu, Z.; Gallego, J.; Lamberti, F.; Gatti, T. Nanostructured 2D-WS2@PANI Nanohybrids for Electrochemical Energy Storage. *Front. Chem.* **2022**, *10* (September), 1–11. https://doi.org/10.3389/fchem.2022.1000910.

(65) Karbstein, H.; Schubert, H. Developments in the Continuous Mechanical Production of Oil-in-Water Macro-Emulsions. *Chem. Eng. Process. Process Intensif.* **1995**, *34* (3), 205–211. https://doi.org/10.1016/0255-2701(94)04005-2.

(66) Utomo, A. T.; Baker, M.; Pacek, A. W. Flow Pattern, Periodicity and Energy Dissipation in a Batch Rotor-Stator Mixer. *Chem. Eng. Res. Des.* **2008**, *86* (12), 1397–1409. https://doi.org/10.1016/j.cherd.2008.07.012.

(67) Biccai, S.; Barwich, S.; Boland, D.; Harvey, A.; Hanlon, D.; McEvoy, N.; Coleman, J. N. Exfoliation of 2D Materials by High Shear Mixing. *2D Mater.* **2019**, *6* (1). https://doi.org/10.1088/2053-1583/aae7e3.

(68) Liu, L.; Shen, Z.; Yi, M.; Zhang, X.; Ma, S. A Green, Rapid and Size-Controlled Production of High-Quality Graphene Sheets by Hydrodynamic Forces. *RSC Adv.* **2014**, *4* (69), 36464–36470. https://doi.org/10.1039/c4ra05635c.

(69) Pilli, S.; Bhunia, P.; Yan, S.; LeBlanc, R. J.; Tyagi, R. D.; Surampalli, R. Y. Ultrasonic Pretreatment of Sludge: A Review. *Ultrason. Sonochem.* **2011**, *18* (1), 1–18. https://doi.org/10.1016/j.ultsonch.2010.02.014.

(70) Flint, E. B.; Suslick, K. S. The Temperature of Cavitation. *Science (80-.).* **1991**, *253* (5026), 1397–1399. https://doi.org/10.1126/science.253.5026.1397.

(71) Hai, X.; Chang, K.; Pang, H.; Li, M.; Li, P.; Liu, H.; Shi, L.; Ye, J. Engineering the Edges of MoS2 (WS2) Crystals for Direct Exfoliation into Monolayers in Polar Micromolecular Solvents. *J. Am. Chem. Soc.* **2016**, *138* (45), 14962–14969. https://doi.org/10.1021/jacs.6b08096.

(72) Sutkar, V. S.; Gogate, P. R. Design Aspects of Sonochemical Reactors: Techniques for Understanding Cavitational Activity Distribution and Effect of Operating Parameters. *Chem. Eng. J.* **2009**, *155* (1–2), 26–36. https://doi.org/10.1016/j.cej.2009.07.021.

(73) Yi, M.; Shen, Z.; Zhang, X.; Ma, S. Vessel Diameter and Liquid Height Dependent Sonication-Assisted Production of Few-Layer Graphene. *J. Mater. Sci.* **2012**, *47* (23), 8234–8244. https://doi.org/10.1007/s10853-012-6720-8.

(74) Asakura, Y.; Nishida, T.; Matsuoka, T.; Koda, S. Effects of Ultrasonic Frequency and Liquid Height on Sonochemical Efficiency of Large-Scale Sonochemical Reactors. *Ultrason. Sonochem.* **2008**, *15* (3), 244–250. https://doi.org/10.1016/j.ultsonch.2007.03.012.

(75) Kojima, Y.; Koda, S.; Nomura, H. Effects of Sample Volume and Frequency on Ultrasonic Power in Solutions on Sonication. *Japanese J. Appl. Physics, Part 1 Regul. Pap. Short Notes Rev. Pap.* **1998**, *37* (5 SUPPL. B), 2992–2995. https://doi.org/10.1143/jjap.37.2992.

(76) Nanzai, B.; Okitsu, K.; Takenaka, N.; Bandow, H.; Tajima, N.; Maeda, Y. Effect of Reaction Vessel Diameter on Sonochemical Efficiency and Cavitation Dynamics. *Ultrason. Sonochem.* **2009**, *16* (1), 163–168. https://doi.org/10.1016/j.ultsonch.2008.05.016.

(77) Long, H.; Tao, L.; Tang, C. Y.; Zhou, B.; Zhao, Y.; Zeng, L.; Yu, S. F.; Lau, S. P.; Chai, Y.; Tsang, Y. H. Tuning Nonlinear Optical Absorption Properties of WS2 Nanosheets. *Nanoscale* **2015**, *7* (42), 17771–17777. https://doi.org/10.1039/c5nr04389a.

(78) Nakamoto, K. *Infrared and Raman Spectra of Inorganic and Coordination Compounds*; Wiley-VCH Verlag, 1986. https://doi.org/10.1366/0003702981943761.

(79) Elstner, M. *Physikalische Chemie II: Quantenmechanik Und Spektroskopie*; 2021. https://doi.org/10.1007/978-3-662-61462-4.

(80) Morse, P. M. Phys. Rev. *Phys. Rev.* **1929**, *34* (1927), 57–64.

(81) Toh, R. J.; Sofer, Z.; Luxa, J.; Sedmidubský, D.; Pumera, M. 3R Phase of MoS2 and WS2 Outperforms the Corresponding 2H Phase for Hydrogen Evolution. *Chem. Commun.* **2017**, *53* (21), 3054–3057. https://doi.org/10.1039/c6cc09952a.

(82) Kolobov, A. V.; Tominaga, J. *Tow-Dimensional Transition-Metal Dichalcogenides*; 2016; Vol. 11. https://doi.org/10.1039/9781782620112-00001.

(83) Lu, N.; Zhang, C.; Lee, C. H.; Oviedo, J. P.; Nguyen, M. A. T.; Peng, X.; Wallace, R. M.; Mallouk, T. E.; Robinson, J. A.; Wang, J.; Cho, K.; Kim, M. J. Atomic and Electronic Structures of WTe2 Probed by High Resolution Electron Microscopy and Ab Initio Calculations. *J. Phys. Chem. C* **2016**, *120* (15), 8364–8369. https://doi.org/10.1021/acs.jpcc.6b01044.

(84) Acerce, M.; Voiry, D.; Chhowalla, M. Metallic 1T Phase MoS2 Nanosheets as Supercapacitor Electrode Materials. *Nat. Nanotechnol.* **2015**, *10* (4), 313–318. https://doi.org/10.1038/nnano.2015.40.

(85) Gong, C.; Zhang, H.; Wang, W.; Colombo, L.; Wallace, R. M.; Cho, K. Band Alignment of Two-Dimensional Transition Metal Dichalcogenides: Application in Tunnel Field Effect Transistors. *Appl. Phys. Lett.* **2013**, *103* (5). https://doi.org/10.1063/1.4817409.

(86) Zhang, X.; Qiao, X. F.; Shi, W.; Wu, J. Bin; Jiang, D. S.; Tan, P. H. Phonon and Raman Scattering of Two-Dimensional Transition Metal Dichalcogenides from Monolayer, Multilayer to Bulk Material. *Chem. Soc. Rev.* **2015**, *44* (9), 2757–2785. https://doi.org/10.1039/c4cs00282b.

(87) Griffin, A.; Nisi, K.; Pepper, J.; Harvey, A.; Szydłowska, B. M.; Coleman, J. N.; Backes, C. Effect of Surfactant Choice and Concentration on the Dimensions and Yield of Liquid-Phase-Exfoliated Nanosheets. *Chem. Mater.* **2020**, *32* (7), 2852–2862. https://doi.org/10.1021/acs.chemmater.9b04684.

(88) Choi, S.; Lee, H.; Ghaffari, R.; Hyeon, T.; Kim, D. H. Recent Advances in Flexible and Stretchable Bio-Electronic Devices Integrated with Nanomaterials. *Adv. Mater.* **2016**, *28* (22), 4203–4218. https://doi.org/10.1002/adma.201504150.

(89) Mathis, T. S.; Kurra, N.; Wang, X.; Pinto, D.; Simon, P.; Gogotsi, Y. Energy Storage Data Reporting in Perspective—Guidelines for Interpreting the Performance of Electrochemical Energy Storage Systems. *Adv. Energy Mater.* **2019**, *9* (39), 1–13. https://doi.org/10.1002/aenm.201902007.

(90) Rayleigh, Lord. XX. On the Equilibrium of Liquid Conducting Masses Charged with Electricity . *London, Edinburgh, Dublin Philos. Mag. J. Sci.* **1882**, *14* (87), 184–186. https://doi.org/10.1080/14786448208628425.

(91) Morton, W. J. Method of Dispersing Fluids. *US Pat. 705, 691* **1902**, *28* (2), 131–134.

(92) A., F. Process and Apparatus For Preparing Artificial Threads. *US Pat.* **1934**, *53*, 1–3. https://doi.org/10.1016/0042-6822(72)90565-x.

(93) Teo, W. E.; Ramakrishna, S. A Review on Electrospinning Design and Nanofibre Assemblies. *Nanotechnology* **2006**, *17* (14). https://doi.org/10.1088/0957-4484/17/14/R01.

(94) Li, Y.; Zhu, J.; Cheng, H.; Li, G.; Cho, H.; Jiang, M.; Gao, Q.; Zhang, X. Developments of Advanced Electrospinning Techniques: A Critical Review. *Adv. Mater. Technol.* **2021**, *6* (11), 1–29. https://doi.org/10.1002/admt.202100410.

(95) Geoffrey, T. Disintegration of Water Drops in an Electric Field. *R. Soc. Stable* **1964**, *280*, 383–397.

(96) Taylor, G.; A, P. R. S. L. Electrically Driven Jets. *Proc. R. Soc. London. A. Math. Phys. Sci.* **1969**, *313* (1515), 453–475. https://doi.org/10.1098/rspa.1969.0205.

(97) Jaeger, R.; Bergshoeft, M. M.; Martin, C.; Vancso, S. G. J. Electrospinning of Ultra-Thin Polymer Fibers. *Macromol. Symp.* **1998**, 141–150.

(98) Kishan, A. P.; Cosgriff-Hernandez, E. M. Recent Advancements in Electrospinning Design for Tissue Engineering Applications: A Review. *J. Biomed. Mater. Res. - Part A* **2017**, *105* (10), 2892–2905. https://doi.org/10.1002/jbm.a.36124.

(99) Doshi, J.; Reneker, D. H. Electrospinning Process and Applications of Electrospun Fibers. *Conf. Rec. - IAS Annu. Meet. (IEEE Ind. Appl. Soc.* **1995**, *3*, 151–160. https://doi.org/10.1109/ias.1993.299067.

(100) Cui, L.; Song, Y.; Wang, F.; Sheng, Y.; Zou, H. Electrospinning Synthesis of SiO2-TiO2 Hybrid Nanofibers with Large Surface Area and Excellent Photocatalytic Activity. *Appl. Surf. Sci.* **2019**, *488* (January), 284–292. https://doi.org/10.1016/j.apsusc.2019.05.151.

(101) Eichhorn, S. J.; Sampson, W. W. Relationships between Specific Surface Area and Pore Size in Electrospun Polymer Fibre Networks. *J. R. Soc. Interface* **2010**, *7* (45), 641–649. https://doi.org/10.1098/rsif.2009.0374.

(102) Park, Y. S.; Kim, J.; Oh, J. M.; Park, S.; Cho, S.; Ko, H.; Cho, Y. K. Near-Field Electrospinning for Three-Dimensional Stacked Nanoarchitectures with High Aspect Ratios. *Nano Lett.* **2020**, *20* (1), 441–448. https://doi.org/10.1021/acs.nanolett.9b04162.

(103) Zheng, G.; Jiang, J.; Wang, X.; Li, W.; Yu, Z.; Lin, L. High-Aspect-Ratio Three-Dimensional Electrospinning via a Tip Guiding Electrode. *Mater. Des.* **2021**, *198*, 109304. https://doi.org/10.1016/j.matdes.2020.109304.

(104) Tang, X.; Yu, Y. Electrospinning Preparation and Characterization of Alumina Nanofibers with High Aspect Ratio. *Ceram. Int.* **2015**, *41* (8), 9232–9238. https://doi.org/10.1016/j.ceramint.2015.04.157.

(105) Ramos, A.; Cameán, I.; García, A. B. Graphitization Thermal Treatment of Carbon Nanofibers. *Carbon N. Y.* **2013**, *59* (March), 2–32. https://doi.org/10.1016/j.carbon.2013.03.031.

(106) Rashid, T. U.; Gorga, R. E.; Krause, W. E. Mechanical Properties of Electrospun Fibers—A Critical Review. *Adv. Eng. Mater.* **2021**, *23* (9), 1–26. https://doi.org/10.1002/adem.202100153.

(107) Ahmed, F. E.; Lalia, B. S.; Hashaikeh, R. A Review on Electrospinning for Membrane Fabrication: Challenges and Applications. *Desalination* **2015**, *356*, 15–30. https://doi.org/10.1016/j.desal.2014.09.033.

(108) Yarin, A. L.; Koombhongse, S.; Reneker, D. H. Bending Instability in Electrospinning of Nanofibers. *J. Appl. Phys.* **2001**, *89* (5), 3018–3026. https://doi.org/10.1063/1.1333035.

(109) Dror, Y.; Salalha, W.; Khalfin, R. L.; Cohen, Y.; Yarin, A. L.; Zussman, E. Carbon Nanotubes Embedded in Oriented Polymer Nanofibers by Electrospinning. *Langmuir* **2003**, *19* (17), 7012–7020. https://doi.org/10.1021/la034234i.

(110) Reneker, D. H.; Yarin, A. L.; Fong, H.; Koombhongse, S. Bending Instability of Electrically Charged Liquid Jets of Polymer Solutions in Electrospinning. *J. Appl. Phys.* **2000**, *87* (9 I), 4531–4547. https://doi.org/10.1063/1.373532.

(111) Li, D.; Xia, Y. Electrospinning of Nanofibers: Reinventing the Wheel? *Adv. Mater.* **2004**, *16* (14), 1151–1170. https://doi.org/10.1002/adma.200400719.

(112) Rutledge, G. C.; Fridrikh, S. V. Formation of Fibers by Electrospinning. *Adv. Drug Deliv. Rev.* **2007**, *59* (14), 1384–1391. https://doi.org/10.1016/j.addr.2007.04.020.

(113) Katti, D. S.; Robinson, K. W.; Ko, F. K.; Laurencin, C. T. Bioresorbable Nanofiber-Based Systems for Wound Healing and Drug Delivery: Optimization of Fabrication Parameters. *J. Biomed. Mater. Res. - Part B Appl. Biomater.* **2004**, *70* (2), 286–296. https://doi.org/10.1002/jbm.b.30041.

(114) Deitzel, J. M.; Kleinmeyer, J.; Harris, D.; Beck Tan, N. C. The Effect of Processing Variables on the Morphology of Electrospun. *Polymer (Guildf).* **2001**, *42*, 261–272.

(115) Chowdhury, M.; Stylios, G. Process Optimization and Alignment of PVA/FeCl3 Nano Composite Fibres by Electrospinning. *J. Mater. Sci.* **2011**, *46* (10), 3378–3386. https://doi.org/10.1007/s10853-010-5226-5.

(116) Lee, K. H.; Kim, H. Y.; La, Y. M.; Lee, D. R.; Sung, N. H. Influence of a Mixing Solvent with Tetrahydrofuran and N,N-Dimethylformamide on Electrospun Poly(Vinyl Chloride) Nonwoven Mats. *J. Polym. Sci. Part B Polym. Phys.* **2002**, *40* (19), 2259–2268. https://doi.org/10.1002/polb.10293.

(117) Haider, A.; Haider, S.; Kang, I. K. A Comprehensive Review Summarizing the Effect of Electrospinning Parameters and Potential Applications of Nanofibers in Biomedical and Biotechnology. *Arab. J. Chem.* **2018**, *11* (8), 1165–1188. https://doi.org/10.1016/j.arabjc.2015.11.015.

(118) Jarusuwannapoom, T.; Hongrojjanawiwat, W.; Jitjaicham, S.; Wannatong, L.; Nithitanakul, M.; Pattamaprom, C.; Koombhongse, P.; Rangkupan, R.; Supaphol, P. Effect of Solvents on Electro-Spinnability of Polystyrene Solutions and Morphological Appearance of Resulting Electrospun Polystyrene Fibers. *Eur. Polym. J.* **2005**, *41* (3), 409–421. https://doi.org/10.1016/j.eurpolymj.2004.10.010.

(119) Greiner, A.; Wendorff, J. H. Electrospinning: A Fascinating Method for the Preparation of Ultrathin Fibers. *Angew. Chemie - Int. Ed.* **2007**, *46* (30), 5670–5703. https://doi.org/10.1002/anie.200604646.

(120) Bagchi, S.; Brar, R.; Singh, B.; Ghanshyam, C. Instability Controlled Synthesis of Tin Oxide Nanofibers and Their Gas Sensing Properties. *J. Electrostat.* **2015**, *78*, 68–78. https://doi.org/10.1016/j.elstat.2015.11.001.

(121) Xia, Y.; Yang, P.; Sun, Y.; Wu, Y.; Mayers, B.; Gates, B.; Yin, Y.; Kim, F.; Yan, H. One-Dimensional Nanostructures of Silicon: Synthesis, Characterization and Applications. *Adv. Mater.* **2003**, No. 5, 353–389.

(122) Barannyk, L. L.; Papageorgiou, D. T.; Petropoulos, P. G. Suppression of Rayleigh-Taylor Instability Using Electric Fields. *Math. Comput. Simul.* **2012**, *82* (6), 1008–1016. https://doi.org/10.1016/j.matcom.2010.11.015.

(123) Hohman, M. M.; Shin, M.; Rutledge, G.; Brenner, M. P. Electrospinning and Electrically Forced Jets. I. Stability Theory. *Phys. Fluids* **2001**, *13* (8), 2201–2220. https://doi.org/10.1063/1.1383791.

(124) Shin, Y. M.; Hohman, M. M.; Brenner, M. P.; Rutledge, G. C. Experimental Characterization of Electrospinning: The Electrically Forced Jet and Instabilities. *Polymer (Guildf).* **2001**, *42* (25), 09955–09967. https://doi.org/10.1016/s0032-3861(01)00540-7.

(125) Azad, A. M. Fabrication of Transparent Alumina (Al2O3) Nanofibers by Electrospinning. *Mater. Sci. Eng. A* **2006**, *435–436*, 468–473. https://doi.org/10.1016/j.msea.2006.07.075.

(126) Zhang, Y.; Shi, R.; Yang, P.; Song, X.; Zhu, Y.; Ma, Q. Fabrication of Electronspun Porous CeO2 Nanofibers with Large Surface Area for Pollutants Removal. *Ceram. Int.* **2016**, *42* (12), 14028–14035. https://doi.org/10.1016/j.ceramint.2016.06.009.

(127) Werner, S.; Seitz, C.; Beck, G.; Hennemann, J.; Smarsly, B. M. Porous SiO2Nanofibers Loaded with CuO Nanoparticles for the Dosimetric Detection of H2S. *ACS Appl. Nano Mater.* **2021**, *4* (5), 5004–5013. https://doi.org/10.1021/acsanm.1c00518.

(128) Ding, Y.; Wang, Y.; Su, L.; Bellagamba, M.; Zhang, H.; Lei, Y. Electrospun Co3O4 Nanofibers for Sensitive and Selective Glucose Detection. *Biosens. Bioelectron.* **2010**, *26* (2), 542–548. https://doi.org/10.1016/j.bios.2010.07.050.

(129) Einert, M.; Ostermann, R.; Weller, T.; Zellmer, S.; Garnweitner, G.; Smarsly, B. M.; Marschall, R. Hollow α-Fe2O3 Nanofibres for Solar Water Oxidation: Improving the Photoelectrochemical Performance by Formation of α-Fe2O3/ITO-Composite Photoanodes. *J. Mater. Chem. A* **2016**, *4* (47), 18444–18456. https://doi.org/10.1039/c6ta06979g.

(130) Wang, Z. M.; Liu, P.; Cao, Y. P.; Ye, F.; Xu, C.; Du, X. Z. Characterization and Electrocatalytic Properties of Electrospun Pt-IrO2 Nanofiber Catalysts for Oxygen Evolution Reaction. *Int. J. Energy Res.* **2021**, *45* (4), 5841–5851. https://doi.org/10.1002/er.6204.

(131) Mizuno, Y.; Hosono, E.; Saito, T.; Okubo, M.; Nishio-Hamane, D.; Oh-Ishi, K.; Kudo, T.; Zhou, H. Electrospinning Synthesis of Wire-Structured LiCoO 2 for Electrode Materials of High-Power Li-Ion Batteries. *J. Phys. Chem. C* **2012**, *116* (19), 10774–10780. https://doi.org/10.1021/jp2123482.

(132) Liu, S.; Zhang, X.; Shao, H.; Xu, J.; Chen, F.; Feng, Y. Preparation of MoS 2 Nanofibers by Electrospinning. *Mater. Lett.* **2012**, *73*, 223–225. https://doi.org/10.1016/j.matlet.2012.01.024.

(133) Aravindan, V.; Suresh Kumar, P.; Sundaramurthy, J.; Ling, W. C.; Ramakrishna, S.; Madhavi, S. Electrospun NiO Nanofibers as High Performance Anode Material for Li-Ion Batteries. *J. Power Sources* **2013**, *227*, 284–290. https://doi.org/10.1016/j.jpowsour.2012.11.050.

(134) Wen, S.; Liu, L.; Zhang, L.; Chen, Q.; Zhang, L.; Fong, H. Hierarchical Electrospun SiO2 Nanofibers Containing SiO2 Nanoparticles with Controllable Surface-Roughness and/or Porosity. *Mater. Lett.* **2010**, *64* (13), 1517–1520. https://doi.org/10.1016/j.matlet.2010.04.008.

(135) Zhang, Y.; He, X.; Li, J.; Miao, Z.; Huang, F. Fabrication and Ethanol-Sensing Properties of Micro Gas Sensor Based on Electrospun SnO2 Nanofibers. *Sensors Actuators, B Chem.* **2008**, *132* (1), 67–73. https://doi.org/10.1016/j.snb.2008.01.006.

(136) Park, J. A.; Moon, J.; Lee, S. J.; Lim, S. C.; Zyung, T. Fabrication and Characterization of ZnO Nanofibers by Electrospinning. *Curr. Appl. Phys.* **2009**, *9* (3 SUPPL.), S210–S212. https://doi.org/10.1016/j.cap.2009.01.044.

(137) Leng, J. yan; Xu, X. juan; Lv, N.; Fan, H. tao; Zhang, T. Synthesis and Gas-Sensing Characteristics of WO3 Nanofibers via Electrospinning. *J. Colloid Interface Sci.* **2011**, *356* (1), 54–57. https://doi.org/10.1016/j.jcis.2010.11.079.

(138) Song, M. Y.; Kim, D. K.; Ihn, K. J.; Jo, S. M.; Kim, D. Y. Electrospun TiO2 Electrodes for Dye-Sensitized Solar Cells. *Nanotechnology* **2004**, *15* (12), 1861–1865. https://doi.org/10.1088/0957-4484/15/12/030.

(139) Ferrone, E.; Araneo, R.; Notargiacomo, A.; Pea, M.; Rinaldi, A. ZnO Nanostructures and Electrospun ZnO–Polymeric Hybrid Nanomaterials in Biomedical, Health, and Sustainability Applications. *Nanomaterials* **2019**, *9* (10), 1–33. https://doi.org/10.3390/nano9101449.

(140) Yu, S.; Jung, J. W.; Kim, I. D. Single Layers of WS2 Nanoplates Embedded in Nitrogen-Doped Carbon Nanofibers as Anode Materials for Lithium-Ion Batteries. *Nanoscale* **2015**, *7* (28), 11945–11950. https://doi.org/10.1039/c5nr02425k.

(141) Brettmann, B. K.; Tsang, S.; Forward, K. M.; Rutledge, G. C.; Myerson, A. S.; Trout, B. L. Free Surface Electrospinning of Fibers Containing Microparticles. *Langmuir* **2012**, *28* (25), 9714–9721. https://doi.org/10.1021/la301422x.

(142) Helmholtz, H. Der Phpsik Und Chemie. *Ann. der Phys. und Chemie* **1879**, *7*, 22.

(143) Baumgärtel, H. *Electrochemistry*; DE GRUYTER, 2019.

(144) Lechner, D. M. *Einführung in Die Elektrochemie*; Springer: Berlin, 2023. https://doi.org/10.1007/978-3-663-07703-9_20.

(145) Stern, O. Zur Theorie Der Elektrolytischen Doppelschicht. *Zeitschrift für Elektrochemie und Angew. Phys. Chemie* **1924**, *30* (21–22), 508–516. https://doi.org/10.1002/bbpc.192400182.

(146) Winter, M.; Brodd, R. J. What Are Batteries, Fuel Cells, and Supercapacitors? *Chem. Rev.* **2004**, *104* (10), 4245–4270. https://doi.org/10.1021/cr020730k.

(147) BOCKRIS, J. O.; DEVANATHAN, M. A. V.; MÜLLER, K. *On the Structure of Charged Interfaces*; Pergamon Press Ltd, 1965; Vol. 541. https://doi.org/10.1016/b978-1-4831-9831-6.50068-0.

(148) Beyers, I.; Bensmann, A.; Hanke-Rauschenbach, R. Ragone Plots Revised: A Review of Methodology and Application across Energy Storage Technologies. *J. Energy Storage* **2023**. https://doi.org/https://doi.org/10.1016/j.est.2023.109097.

(149) Christen, T.; Carlen, M. W. Theory of Ragone Plots. *J. Power Sources* **2000**, *91* (2), 210–216. https://doi.org/10.1016/S0378-7753(00)00474-2.

(150) Pell, W. G.; Conway, B. E. Quantitative Modeling of Factors Determining Ragone Plots for Batteries and Electrochemical Capacitors. *J. Power Sources* **1996**, *63* (2), 255–266. https://doi.org/10.1016/S0378-7753(96)02525-6.

(151) Rountree, K. J.; Mccarthy, B. D.; Rountree, E. S.; Eisenhart, T. T.; Dempsey, J. L. A Practical Beginner ' s Guide to Cyclic Voltammetry. *J. Chem. Educ.* **2017**. https://doi.org/10.1021/acs.jchemed.7b00361.

(152) Stephenson, T.; Li, Z.; Olsen, B.; Mitlin, D. Lithium Ion Battery Applications of Molybdenum Disulfide (MoS2) Nanocomposites. *Energy Environ. Sci.* **2014**, *7* (1), 209–231. https://doi.org/10.1039/c3ee42591f.

(153) Liu, J.; Xue, Y.; Zhang, M.; Dai, L. Graphene-Based Materials for Energy Applications. *MRS Bull.* **2012**, *37* (12), 1265–1272. https://doi.org/10.1557/mrs.2012.179.

(154) Kang, J.; Sangwan, V. K.; Wood, J. D.; Hersam, M. C. Solution-Based Processing of Monodisperse Two-Dimensional Nanomaterials. *Acc. Chem. Res.* **2017**, *50* (4), 943–951. https://doi.org/10.1021/acs.accounts.6b00643.

(155) Sambath Kumar, K.; Choudhary, N.; Pandey, D.; Ding, Y.; Hurtado, L.; Chung, H. S.; Tetard, L.; Jung, Y.; Thomas, J. Investigating 2D-WS2supercapacitor Electrode Performance by Kelvin Probe Force Microscopy. *J. Mater. Chem. A* **2020**, *8* (25), 12699–12704. https://doi.org/10.1039/d0ta03383a.

(156) Wang, Y. X.; Seng, K. H.; Chou, S. L.; Wang, J. Z.; Guo, Z.; Wexler, D.; Liu, H. K.; Dou, S. X. Reversible Sodium Storage via Conversion Reaction of a MoS2–C Composite. *Chem. Commun.* **2014**, *50* (73), 10730–10733. https://doi.org/10.1039/c4cc00294f.

(157) Dupont, M. F.; Donne, S. W. Charge Storage Mechanisms in Electrochemical Capacitors: Effects of Electrode Properties on Performance. *J. Power Sources* **2016**, *326*, 613–623. https://doi.org/10.1016/j.jpowsour.2016.03.073.

(158) Zhai, Y.; Dou, Y.; Zhao, D.; Fulvio, P. F.; Mayes, R. T.; Dai, S. Carbon Materials for Chemical Capacitive Energy Storage. *Adv. Mater.* **2011**, *23* (42), 4828–4850. https://doi.org/10.1002/adma.201100984.

(159) Grahame, D. C. The Thermodynamic Theory of Electrocapillarity The Kinetic Theory of the Diffuse Double Layer The Theory of the Compact Double Layer ..... Potential Differenc. *Philos. Mag. Ser. 6* **1947**, 441–501.

(160) Jung, D.; Kim, D.; Yang, W. J.; Cho, E. S.; Kwon, S. J.; Han, J.-H. Surface Functionalization of Liquid-Phase Exfoliated, Two-Dimensional MoS 2 and WS 2 Nanosheets with 2-Mercaptoethanol . *J. Nanosci. Nanotechnol.* **2018**, *18* (9), 6265–6269. https://doi.org/10.1166/jnn.2018.15652.

(161) Yu, X.; Pei, C.; Chen, W.; Feng, L. 2 Dimensional WS2 Tailored Nitrogen-Doped Carbon Nanofiber as a Highly Pseudocapacitive Anode Material for Lithium-Ion Battery. *Electrochim. Acta* **2018**, *272*, 119–126. https://doi.org/10.1016/j.electacta.2018.03.201.

(162) Mahmood, Q.; Kim, M. G.; Yun, S.; Bak, S. M.; Yang, X. Q.; Shin, H. S.; Kim, W. S.; Braun, P. V.; Park, H. S. Unveiling Surface Redox Charge Storage of Interacting Two-Dimensional Heteronanosheets in Hierarchical Architectures. *Nano Lett.* **2015**, *15* (4), 2269–2277. https://doi.org/10.1021/nl504200y.

(163) Chen, W.; Yu, X.; Zhao, Z.; Ji, S.; Feng, L. Hierarchical Architecture of Coupling Graphene and 2D-WS 2 for High-Performance Supercapacitor. *Electrochim. Acta* **2019**, *298*, 313–320. https://doi.org/10.1016/j.electacta.2018.12.096.

(164) Da Silveira Firmiano, E. G.; Rabelo, A. C.; Dalmaschio, C. J.; Pinheiro, A. N.; Pereira, E. C.; Schreiner, W. H.; Leite, E. R. Supercapacitor Electrodes Obtained by Directly Bonding 2D MoS2 on Reduced Graphene Oxide. *Adv. Energy Mater.* **2014**, *4* (6), 1–8. https://doi.org/10.1002/aenm.201301380.

(165) Pumera, M.; Sofer, Z.; Ambrosi, A. Layered Transition Metal Dichalcogenides for Electrochemical Energy Generation and Storage. *J. Mater. Chem. A* **2014**, *2* (24), 8981–8987. https://doi.org/10.1039/c4ta00652f.

(166) Chu, C. Y.; Tsai, J. T.; Sun, C. L. Synthesis of PEDOT-Modified Graphene Composite Materials as Flexible Electrodes for Energy Storage and Conversion Applications. *Int. J. Hydrogen Energy* **2012**, *37* (18), 13880–13886. https://doi.org/10.1016/j.ijhydene.2012.05.017.

(167) Liu, X.; Zhang, S.; Yu, M.; Zhao, X.; Jia, Y.; Huang, Y.; Zong, M. WS2 Nanosheets Anchored on N-Doped Carbon Fibers for Superior Electromagnetic Wave Absorption. *Chem. Eng. J.* **2023**, *465* (November 2022), 142932. https://doi.org/10.1016/j.cej.2023.142932.

(168) Zhao, Z.; Wang, F.; Yuan, H.; Yang, Z.; Qin, Y.; Zheng, X.; Yang, Y. N-Doped Carbon-WS2Nanosheet Composites for Lithium-Ion Storage. *ACS Appl. Nano Mater.* **2021**, *4* (8), 7781–7787. https://doi.org/10.1021/acsanm.1c01069.

(169) Luhrs, C. C.; Moberg, M.; Maxson, A.; Brewer, L.; Menon, S. IF-WS2/Nanostructured Carbon Hybrids Generation and Their Characterization. *Inorganics* **2014**, *2* (2), 211–232. https://doi.org/10.3390/inorganics2020211.

(170) Sun, C. Bin; Zhong, Y. W.; Fu, W. J.; Zhao, Z. Q.; Liu, J.; Ding, J.; Han, X. P.; Deng, Y. Da; Hu, W. Bin; Zhong, C. Tungsten Disulfide-Based Nanomaterials for Energy Conversion and Storage. *Tungsten* **2020**, *2* (2), 109–133. https://doi.org/10.1007/s42864-020-00038-6.

(171) Piao, M.; Li, C.; Joo, M. K.; Chu, J.; Wang, X.; Chi, Y.; Zhang, H.; Shi, H. Hydrothermal Synthesis of Stable 1T-WS2 and Single-Walled Carbon Nanotube Hybrid Flexible Thin Films with Enhanced Thermoelectric Performance. *Energy Technol.* **2018**, *6* (10), 1921–1928. https://doi.org/10.1002/ente.201800025.

(172) Sun, G.; Zhang, X.; Lin, R.; Yang, J.; Zhang, H.; Chen, P. Hybrid Fibers Made of Molybdenum Disulfide, Reduced Graphene Oxide, and Multi-Walled Carbon Nanotubes for Solid-State, Flexible, Asymmetric Supercapacitors. *Angew. Chemie - Int. Ed.* **2015**, *54* (15), 4651–4656. https://doi.org/10.1002/anie.201411533.

(173) Huang, Y.; Liang, J.; Chen, Y. An Overview of the Applications of Graphene-Based Materials in Supercapacitors. *Small* **2012**, *8* (12), 1805–1834. https://doi.org/10.1002/smll.201102635.

(174) Ratha, S.; Rout, C. S. Supercapacitor Electrodes Based on Layered Tungsten Disulfide-Reduced Graphene Oxide Hybrids Synthesized by a Facile Hydrothermal Method. *ACS Appl. Mater. Interfaces* **2013**, *5* (21), 11427–11433. https://doi.org/10.1021/am403663f.

(175) Kulkarni, B.; Alsaiari, M.; M S, J.; J, K.; Jalalah, M.; Harraz, F. A.; Balakrishna, R. G. Performance of Functionalized 1T-MoS2 as Composite Counter Electrode Material for QDSSCs and Its Analogy with 2H-MoS2. *Mater. Res. Bull.* **2021**, *134* (October 2020), 111096. https://doi.org/10.1016/j.materresbull.2020.111096.

(176) Piao, M.; Chu, J.; Wang, X.; Chi, Y.; Zhang, H.; Li, C.; Shi, H.; Joo, M. K. Hydrothermal Synthesis of Stable Metallic 1T Phase WS2 Nanosheets for Thermoelectric Application. *Nanotechnology* **2018**, *29* (2). https://doi.org/10.1088/1361-6528/aa9bfe.

(177) Zhang, D.; Wang, H.; Cheng, J.; Han, C.; Yang, X.; Xu, J.; Shan, G.; Zheng, G.; Cao, M. Conductive WS2-NS/CNTs Hybrids Based 3D Ultra-Thin Mesh Electromagnetic Wave Absorbers with Excellent Absorption Performance. *Appl. Surf. Sci.* **2020**, 147052. https://doi.org/10.1016/j.apsusc.2020.147052.

(178) Solomon, G.; Mazzaro, R.; Morandi, V.; Concina, I.; Vomiero, A. Microwave-Assisted vs. Conventional Hydrothermal Synthesis of Mos2 Nanosheets: Application towards Hydrogen Evolution Reaction. *Crystals* **2020**, *10* (11), 1–12. https://doi.org/10.3390/cryst10111040.

(179) Beidaghi, M.; Gogotsi, Y. Capacitive Energy Storage in Micro-Scale Devices: Recent Advances in Design and Fabrication of Micro-Supercapacitors. *Energy Environ. Sci.* **2014**, *7* (3), 867–884. https://doi.org/10.1039/c3ee43526a.

(180) Chen, W.; Xie, X.; Zong, J.; Chen, T.; Lin, D.; Yu, F.; Jin, S.; Zhou, L.; Zou, J.; Sun, J.; Xi, X.; Zhang, Y. Growth and Thermo-Driven Crystalline Phase Transition of Metastable Monolayer 1T'-WSe 2 Thin Film. *Sci. Rep.* **2019**, *9* (1), 1–6. https://doi.org/10.1038/s41598-019-39238-7.

(181) Nie, G.; Zhao, X.; Luan, Y.; Jiang, J.; Kou, Z.; Wang, J. Key Issues Facing Electrospun Carbon Nanofibers in Energy Applications: On-Going Approaches and Challenges. *Nanoscale* **2020**, *12* (25), 13225–13248. https://doi.org/10.1039/d0nr03425h.

(182) Nataraj, S. K.; Yang, K. S.; Aminabhavi, T. M. Polyacrylonitrile-Based Nanofibers - A State-of-the-Art Review. *Prog. Polym. Sci.* **2012**, *37* (3), 487–513. https://doi.org/10.1016/j.progpolymsci.2011.07.001.

(183) Habazaki, H.; Kiriu, M.; Hayashi, M.; Konno, H. Structure of the Carbon Nanofilaments Formed by Liquid Phase Carbonization in Porous Anodic Alumina Template. *Mater. Chem. Phys.* **2007**, *105* (2–3), 367–372. https://doi.org/10.1016/j.matchemphys.2007.04.074.

(184) Wang, M.; Huang, Z. H.; Wang, L.; Wang, M. X.; Kang, F.; Hou, H. Electrospun Ultrafine Carbon Fiber Webs for Electrochemical Capacitive Desalination. *New J. Chem.* **2010**, *34* (9), 1843–1845. https://doi.org/10.1039/c0nj00407c.

(185) Kim, C.; Yang, K. S. Electrochemical Properties of Carbon Nanofiber Web as an Electrode for Supercapacitor Prepared by Electrospinning. *Appl. Phys. Lett.* **2003**, *83* (6), 1216–1218. https://doi.org/10.1063/1.1599963.

(186) Lafdi, K.; Fox, W.; Matzek, M.; Yildiz, E. Effect of Carbon Nanofiber Heat Treatment on Physical Properties of Polymeric Nanocomposites - Part I. *J. Nanomater.* **2007**, *2007*. https://doi.org/10.1155/2007/52729.

(187) Ponomarev, I. I.; Zhigalina, O. M.; Skupov, K. M.; Modestov, A. D.; Basu, V. G.; Sufiyanova, A. E.; Ponomarev, I. I.; Razorenov, D. Y. Preparation and Thermal Treatment Influence on Pt-Decorated Electrospun Carbon Nanofiber Electrocatalysts. *RSC Adv.* **2019**, *9* (47), 27406–27418. https://doi.org/10.1039/c9ra05910e.

(188) Zhang, C.; Liang, Y.; Yao, L.; Qiu, Y. Effect of Thermal Treatment on the Properties of Electrospun LiFePO4-Carbon Nanofiber Composite Cathode Materials for Lithium-Ion Batteries. *J. Alloys Compd.* **2015**, *627*, 91–100. https://doi.org/10.1016/j.jallcom.2014.12.067.

(189) Kim, C. H.; Kim, B. H. Effects of Thermal Treatment on the Structural and Capacitive Properties of Polyphenylsilane-Derived Porous Carbon Nanofibers. *Electrochim. Acta* **2014**, *117*, 26–33. https://doi.org/10.1016/j.electacta.2013.11.082.

(190) Lee, S.; Da, S. Y.; Ogale, A. A.; Kim, M. S. Effect of Heat Treatment of Carbon Nanofibers on Polypropylene Nanocomposites. *J. Phys. Chem. Solids* **2008**, *69* (5–6), 1407–1410. https://doi.org/10.1016/j.jpcs.2007.10.030.

(191) Choi, J.; Kim, S. S.; Chung, Y. S.; Lee, S. Evolution of Structural Inhomogeneity in Polyacrylonitrile Fibers by Oxidative Stabilization. *Carbon N. Y.* **2020**, *165*, 225–237. https://doi.org/10.1016/j.carbon.2020.04.027.

(192) Mie-Jie, Y.; Cheng-Guo, W.; Bai, Y.-J.; Yong, X.; Bo, Z. Effect of Oxygen Uptake and Aromatization on the Skin–Core Morphology During the Oxidative Stabilizationof Polyacrylonitrile Fibers. *J. Appl. Polym. Sci.* **2007**, *107* (5), 1939–1945. https://doi.org/10.1002/app.

(193) Liu, X.; Zhu, C.; Guo, J.; Liu, Q.; Dong, H.; Gu, Y.; Liu, R.; Zhao, N.; Zhang, Z.; Xu, J. Nanoscale Dynamic Mechanical Imaging of the Skin-Core Difference: From PAN Precursors to Carbon Fibers. *Mater. Lett.* **2014**, *128*, 417–420. https://doi.org/10.1016/j.matlet.2014.04.176.

(194) Wang, J.; Hu, L.; Yang, C.; Zhao, W.; Lu, Y. Effects of Oxygen Content in the Atmosphere on Thermal Oxidative Stabilization of Polyacrylonitrile Fibers. *RSC Adv.* **2016**, *6* (77), 73404–73411. https://doi.org/10.1039/c6ra15308a.

(195) Lv, M. Y.; Ge, H. Y.; Chen, J. Study on the Chemical Structure and Skin-Core Structure of Polyacrylonitrile-Based Fibers during Stabilization. *J. Polym. Res.* **2009**, *16* (5), 513–517. https://doi.org/10.1007/s10965-008-9254-7.

(196) Einert, M.; Wessel, C.; Badaczewski, F.; Leichtweiß, T.; Eufinger, C.; Janek, J.; Yuan, J.; Antonietti, M.; Smarsly, B. M. Nitrogen-Doped Carbon Electrodes: Influence of Microstructure and Nitrogen Configuration on the Electrical Conductivity of Carbonized Polyacrylonitrile and Poly(Ionic Liquid) Blends. *Macromol. Chem. Phys.* **2015**, *216* (19), 1930–1944. https://doi.org/10.1002/macp.201500169.

(197) Peng, Z.; Lin, J.; Ye, R.; Samuel, E. L. G.; Tour, J. M. Flexible and Stackable Laser-Induced Graphene Supercapacitors. *ACS Appl. Mater. Interfaces* **2015**, *7* (5), 3414–3419. https://doi.org/10.1021/am509065d.

(198) Minus, M. L.; Kumar, S. The Processing, Properties, and Structure of Carbon Fibers. *Jom* **2005**, *57* (2), 52–58. https://doi.org/10.1007/s11837-005-0217-8.

(199) Frank, E.; Hermanutz, F.; Buchmeiser, M. R. Carbon Fibers: Precursors, Manufacturing, and Properties. *Macromol. Mater. Eng.* **2012**, *297* (6), 493–501. https://doi.org/10.1002/mame.201100406.

(200) Electrodes, N. Flexible Supercapacitors Based on Graphene / Boron Nitride Nanosheets Electrodes and PVA / PEI Gel Electrolytes. **2021**.

(201) Lu, C.; Chen, X. All-Temperature Flexible Supercapacitors Enabled by Antifreezing and Thermally Stable Hydrogel Electrolyte. *Nano Lett.* **2020**, *20* (3), 1907–1914. https://doi.org/10.1021/acs.nanolett.9b05148.

(202) Zhang, L.; Fan, W.; Liu, T. Flexible Hierarchical Membranes of WS2 Nanosheets Grown on Graphene-Wrapped Electrospun Carbon Nanofibers as Advanced Anodes for Highly Reversible Lithium Storage. *Nanoscale* **2016**, *8* (36), 16387–16394. https://doi.org/10.1039/c6nr04241d.

(203) Deitzel, J. M.; Kleinmeyer, J. D.; Hirvonen, J. K.; Beck Tan, N. C. Controlled Deposition of Electrospun Poly(Ethylene Oxide) Fibers. *Polymer (Guildf).* **2001**, *42* (19), 8163–8170. https://doi.org/10.1016/S0032-3861(01)00336-6.

(204) Wang, J.; Li, X.; Zi, Y.; Wang, S.; Li, Z.; Zheng, L.; Yi, F.; Li, S.; Wang, Z. L. A Flexible Fiber-Based Supercapacitor-Triboelectric-Nanogenerator Power System for Wearable Electronics. *Adv. Mater.* **2015**, *27* (33), 4830–4836. https://doi.org/10.1002/adma.201501934.

(205) Ding, Y.; Xu, W.; Wang, W.; Fong, H.; Zhu, Z. Scalable and Facile Preparation of Highly Stretchable Electrospun PEDOT:PSS@PU Fibrous Nonwovens toward Wearable Conductive Textile Applications. *ACS Appl. Mater. Interfaces* **2017**, *9* (35), 30014–30023. https://doi.org/10.1021/acsami.7b06726.

(206) Na, W.; Jun, J.; Park, J. W.; Lee, G.; Jang, J. Highly Porous Carbon Nanofibers Co-Doped with Fluorine and Nitrogen for Outstanding Supercapacitor Performance. *J. Mater. Chem. A* **2017**, *5* (33), 17379–17387. https://doi.org/10.1039/c7ta04406b.

(207) Yang, X.; Li, J.; Hou, C.; Zhang, Q.; Li, Y.; Wang, H. Skeleton-Structure WS2@CNT Thin-Film Hybrid Electrodes for High-Performance Quasi-Solid-State Flexible Supercapacitors. *Front. Chem.* **2020**, *8* (June), 1–10. https://doi.org/10.3389/fchem.2020.00442.

(208) European Parliament. EU Legislation in Progress - Critical Raw Materials Act. **2023**, No. September, 12.

(209) Kassim, S. M. The Importance of Recycling in Solid Waste Management. *Macromol. Symp.* **2012**, *320* (1), 43–50. https://doi.org/10.1002/masy.201251005.

(210) Natarajan, S.; Divya, M. L.; Aravindan, V. Should We Recycle the Graphite from Spent Lithium-Ion Batteries? The Untold Story of Graphite with the Importance of Recycling. *J. Energy Chem.* **2022**, *71*, 351–369. https://doi.org/10.1016/j.jechem.2022.04.012.

(211) Lv, W.; Wang, Z.; Cao, H.; Sun, Y.; Zhang, Y.; Sun, Z. A Critical Review and Analysis on the Recycling of Spent Lithium-Ion Batteries. *ACS Sustain. Chem. Eng.* **2018**, *6* (2), 1504–1521. https://doi.org/10.1021/acssuschemeng.7b03811.

(212) Li, L.; Zhang, X.; Li, M.; Chen, R.; Wu, F.; Amine, K.; Lu, J. The Recycling of Spent Lithium-Ion Batteries: A Review of Current Processes and Technologies. *Electrochem. Energy Rev.* **2018**, *1* (4), 461–482. https://doi.org/10.1007/s41918-018-0012-1.

(213) Blengini, G. A. *Assessment of the Methodology for Establishing the EU List of Critical Raw Materials*; 2017. https://doi.org/10.2760/73303.

(214) Tomala, J.; Urbaniec, M. Towards Sustainable Development in the European Union: A Critical Raw Materials Perspective. *Econ. Environ.* **2024**, *88* (1), 1–14. https://doi.org/10.34659/eis.2024.88.1.654.

(215) Jin, L.; Wang, T.; Feng, Z. Q.; Leach, M. K.; Wu, J.; Mo, S.; Jiang, Q. A Facile Approach for the Fabrication of Core-Shell PEDOT Nanofiber Mats with Superior Mechanical Properties and Biocompatibility. *J. Mater. Chem. B* **2013**, *1* (13), 1818–1825. https://doi.org/10.1039/c3tb00448a.

(216) Liu, S.; Zeng, Y.; Zhang, M.; Xie, S.; Tong, Y.; Cheng, F.; Lu, X. Binder-Free WS2 Nanosheets with Enhanced Crystallinity as a Stable Negative Electrode for Flexible Asymmetric Supercapacitors. *J. Mater. Chem. A* **2017**, *5* (40), 21460–21466. https://doi.org/10.1039/c7ta07009h.

(217) Lyu, L.; Hooch Antink, W.; Kim, Y. S.; Kim, C. W.; Hyeon, T.; Piao, Y. Recent Development of Flexible and Stretchable Supercapacitors Using Transition Metal Compounds as Electrode Materials. *Small* **2021**, *17* (36), 1–41. https://doi.org/10.1002/smll.202101974.

(218) Yun, Q.; Lu, Q.; Zhang, X.; Tan, C.; Zhang, H. Three-Dimensional Architectures Constructed from Transition-Metal Dichalcogenide Nanomaterials for Electrochemical Energy Storage and Conversion. *Angew. Chemie - Int. Ed.* **2018**, *57* (3), 626–646. https://doi.org/10.1002/anie.201706426.

(219) Zhang, X.; Zhang, Q.; Sun, Y.; Zhang, P.; Gao, X.; Zhang, W.; Guo, J. MoS2-Graphene Hybrid Nanosheets Constructed 3D Architectures with Improved Electrochemical Performance for Lithium-Ion Batteries and Hydrogen Evolution. *Electrochim. Acta* **2016**, *189*, 224–230. https://doi.org/10.1016/j.electacta.2015.12.082.

(220) Zeng, H.; Liu, G. Bin; Dai, J.; Yan, Y.; Zhu, B.; He, R.; Xie, L.; Xu, S.; Chen, X.; Yao, W.; Cui, X. Optical Signature of Symmetry Variations and Spin-Valley Coupling in Atomically Thin Tungsten Dichalcogenides. *Sci. Rep.* **2013**, *3*, 2–6. https://doi.org/10.1038/srep01608.

(221) Stacy, A. M.; Hodul, D. T. Raman Spectra of IVB and VIB Transition Metal Disulfides Using Laser Energies near the Absorption Edges. *J. Phys. Chem. Solids* **1985**, *46* (4), 405–409. https://doi.org/10.1016/0022-3697(85)90103-9.

(222) Wells, R. A.; Zhang, M.; Chen, T. H.; Boureau, V.; Caretti, M.; Liu, Y.; Yum, J. H.; Johnson, H.; Kinge, S.; Radenovic, A.; Sivula, K. High Performance Semiconducting Nanosheets via a Scalable Powder-Based Electrochemical Exfoliation Technique. *ACS Nano* **2022**, *16* (4), 5719–5730. https://doi.org/10.1021/acsnano.1c10739.

(223) Luo, S.; Dong, S.; Lu, C.; Yu, C.; Ou, Y.; Luo, L.; Sun, J.; Sun, J. Rational and Green Synthesis of Novel Two-Dimensional WS2/MoS2 Heterojunction via Direct Exfoliation in Ethanol-Water Targeting Advanced Visible-Light-Responsive Photocatalytic Performance. *J. Colloid Interface Sci.* **2018**, *513*, 389–399. https://doi.org/10.1016/j.jcis.2017.11.044.

(224) Adilbekova, B.; Lin, Y.; Yengel, E.; Faber, H.; Harrison, G.; Firdaus, Y.; El-Labban, A.; Anjum, D. H.; Tung, V.; Anthopoulos, T. D. Liquid Phase Exfoliation of MoS2 and WS2 in Aqueous Ammonia and Their Application in Highly Efficient Organic Solar Cells. *J. Mater. Chem. C* **2020**, *8* (15), 5259–5264. https://doi.org/10.1039/d0tc00659a.

(225) Zhao, W.; Yalcin, B.; Cakmak, M. Dynamic Assembly of Electrically Conductive PEDOT:PSS Nanofibers in Electrospinning Process Studied by High Speed Video. *Synth. Met.* **2015**, *203*, 107–116. https://doi.org/10.1016/j.synthmet.2015.02.018.

(226) Latonen, R. M.; Cabrera, J. A. W.; Lund, S.; Kosourov, S.; Vajravel, S.; Boeva, Z.; Wang, X.; Xu, C.; Allahverdiyeva, Y. Electrospinning of Electroconductive Water-Resistant Nanofibers of PEDOT-PSS, Cellulose Nanofibrils and PEO: Fabrication, Characterization, and Cytocompatibility. *ACS Appl. Bio Mater.* **2021**, *4* (1), 483–493. https://doi.org/10.1021/acsabm.0c00989.

(227) Mir, S. M.; Jafari, S. H.; Khonakdar, H. A.; Krause, B.; Pötschke, P.; Taheri Qazvini, N. A Promising Approach to Low Electrical Percolation Threshold in PMMA Nanocomposites by Using MWCNT-PEO Predispersions. *Mater. Des.* **2016**, *111*, 253–262. https://doi.org/10.1016/j.matdes.2016.08.073.

(228) Cai, Z.; Liu, B.; Zou, X.; Cheng, H. M. Chemical Vapor Deposition Growth and Applications of Two-Dimensional Materials and Their Heterostructures. *Chem. Rev.* **2018**, *118* (13), 6091–6133. https://doi.org/10.1021/acs.chemrev.7b00536.

(229) Delabie, A.; Caymax, M.; Groven, B.; Heyne, M.; Haesevoets, K.; Meersschaut, J.; Nuytten, T.; Bender, H.; Conard, T.; Verdonck, P.; Van Elshocht, S.; De Gendt, S.; Heyns, M.; Barla, K.; Radu, I.; Thean, A. Low Temperature Deposition of 2D-WS2 Layers from WF6 and H2S Precursors: Impact of Reducing Agents. *Chem. Commun.* **2015**, *51* (86), 15692–15695. https://doi.org/10.1039/c5cc05272f.

(230) Hernandez, Y.; Nicolosi, V.; Lotya, M.; Blighe, F. M.; Sun, Z.; De, S.; McGovern, I. T.; Holland, B.; Byrne, M.; Gun'ko, Y. K.; Boland, J. J.; Niraj, P.; Duesberg, G.; Krishnamurthy, S.; Goodhue, R.; Hutchison, J.; Scardaci, V.; Ferrari, A. C.; Coleman, J. N. High-Yield Production of Graphene by Liquid-Phase Exfoliation of Graphite. *Nat. Nanotechnol.* **2008**, *3* (9), 563–568. https://doi.org/10.1038/nnano.2008.215.

(231) Ott, S.; Wolff, N.; Rashvand, F.; Rao, V. J.; Zaumseil, J.; Backes, C. Impact of the Mos2 Starting Material on the Dispersion Quality and Quantity after Liquid Phase Exfoliation. *Chem. Mater.* **2019**, *31* (20), 8424–8431. https://doi.org/10.1021/acs.chemmater.9b02336.

(232) Abreu, B.; Almeida, B.; Ferreira, P.; M. F. Fernandes, R.; Fernandes, D. M.; Marques, E. F. A Critical Assessment of the Role of Ionic Surfactants in the Exfoliation and Stabilization of 2D Nanosheets: The Case of the Transition Metal Dichalcogenides MoS2, WS2 and MoSe2. *J. Colloid Interface Sci.* **2022**, *626*, 167–177. https://doi.org/10.1016/j.jcis.2022.06.097.

(233) Gupta, A.; Arunachalam, V.; Vasudevan, S. Water Dispersible, Positively and Negatively Charged MoS2 Nanosheets: Surface Chemistry and the Role of Surfactant Binding. *J. Phys. Chem. Lett.* **2015**, *6* (4), 739–744. https://doi.org/10.1021/acs.jpclett.5b00158.

(234) Zamani, M.; Jamali-Sheini, F.; Cheraghizade, M. Visible-Range and Self-Powered Bilayer p-Si/n-Bi2S3 Heterojunction Photodetector: The Effect of Au Buffer Layer on the Optoelectronics Performance. *J. Alloys Compd.* **2022**, *905*, 164119. https://doi.org/10.1016/j.jallcom.2022.164119.

(235) Xie, Y.; Zhou, Y.; Gao, C.; Liu, L.; Zhang, Y.; Chen, Y.; Shao, Y. Construction of AgBr/BiOBr S-Scheme Heterojunction Using Ion Exchange Strategy for High-Efficiency Reduction of CO2 to CO under Visible Light. *Sep. Purif. Technol.* **2022**, *303* (October), 122288. https://doi.org/10.1016/j.seppur.2022.122288.

(236) Bai, Y.; Ouyang, T.; Li, X.; Yan, Y.; Kong, Z.; Ma, X.; Li, Z.; Li, Z.; Cai, X.; Cai, J.; Tan, H. Boosting the Thermoelectric Performance of N-Type Bi2S3 by Compositing RGO. *J. Alloys Compd.* **2023**, *933*, 167814. https://doi.org/10.1016/j.jallcom.2022.167814.

(237) Zhao, F.; Sheng, H.; Sun, Q.; Wang, J.; Liu, Q.; Hu, Z.; He, B.; Wang, Y.; Li, Z.; Liu, X. Harvesting the Infrared Part of Solar Light to Promote Charge Transfer in Bi2S3/WO3 Photoanode for Enhanced Photoelectrochemical Water Splitting. *J. Colloid Interface Sci.* **2022**, *621*, 267–274. https://doi.org/10.1016/j.jcis.2022.04.052.

(238) Xu, Y.; Chen, B.; Xu, L.; Zhang, G.; Cao, L.; Liu, N.; Wang, W.; Qian, H.; Shao, M. Urchin-like Fe3O4@Bi2S3 Nanospheres Enable the Destruction of Biofilm and Efficiently Antibacterial Activities. *ACS Appl. Mater. Interfaces* **2024**, *16* (3), 3215–3231. https://doi.org/10.1021/acsami.3c17888.

(239) Yang, Z.; Wang, Y.; Zhang, D.; Chen, C. A Sensitizing Photoelectrochemical Sensing Platform Strategy Based on Bio-Etching Preparation of Bi2S3/BiOCl p–n Heterojunction. *Talanta* **2018**, *190* (April), 357–362. https://doi.org/10.1016/j.talanta.2018.08.004.

(240) Chitara, B.; Kolli, B. S. C.; Yan, F. Near-Infrared Photodetectors Based on 2D Bi2S3. *Chem. Phys. Lett.* **2022**, *804* (July), 139876. https://doi.org/10.1016/j.cplett.2022.139876.

(241) Wu, H.; Chen, X.; Qian, C.; Yan, H.; Yan, C.; Xu, N.; Piao, Y.; Diao, G.; Chen, M. Confinement Growth of Layered WS2 in Hollow Beaded Carbon Nanofibers with Synergistic Anchoring Effect to Reinforce Li+/Na+ Storage Performance. *Small* **2020**, *16* (26), 1–10. https://doi.org/10.1002/smll.202000695.

(242) Zhou, H.; Liu, Y.; Ren, M.; Zhai, H. J. Mechanically Exfoliated Graphite Paper with Layered Microstructures for Enhancing Flexible Electrochemical Energy Storage. *Inorg. Chem. Front.* **2022**, *9* (9), 1920–1930. https://doi.org/10.1039/d1qi01601f.

(243) McDonough, J. R.; Choi, J. W.; Yang, Y.; La Mantia, F.; Zhang, Y.; Cui, Y. Carbon Nanofiber Supercapacitors with Large Areal Capacitances. *Appl. Phys. Lett.* **2009**, *95* (24). https://doi.org/10.1063/1.3273864.

(244) Liu, Y.; Zhou, J.; Chen, L.; Zhang, P.; Fu, W.; Zhao, H.; Ma, Y.; Pan, X.; Zhang, Z.; Han, W.; Xie, E. Highly Flexible Freestanding Porous Carbon Nanofibers for Electrodes Materials of High-Performance All-Carbon Supercapacitors. *ACS Appl. Mater. Interfaces* **2015**, *7* (42), 23515–23520. https://doi.org/10.1021/acsami.5b06107.

(245) Zhang, Q.; Wang, X.; Fu, J.; Liu, R.; He, H.; Ma, J.; Yu, M.; Ramakrishna, S.; Long, Y. Electrospinning of Ultrafine Conducting Polymer Composite Nanofibers with Diameter Less than 70 Nm as High Sensitive Gas Sensor. *Materials (Basel).* **2018**, *11* (9). https://doi.org/10.3390/ma11091744.

(246) Liu, N.; Fang, G.; Wan, J.; Zhou, H.; Long, H.; Zhao, X. Electrospun PEDOT:PSS-PVA Nanofiber Based Ultrahigh-Strain Sensors with Controllable Electrical Conductivity. *J. Mater. Chem.* **2011**, *21* (47), 18962–18966. https://doi.org/10.1039/c1jm14491j.

(247) Boll, F.; Crisci, M.; Merola, L.; Lamberti, F.; Smarsly, B.; Gatti, T. Assessing the Effect of Stabilization and Carbonization Temperatures on Electrochemical Performance of Electrospun Carbon Nanofibers from Polyacrylonitrile. *Adv. Energy Sustain. Res.* **2023**, *4* (11). https://doi.org/10.1002/aesr.202300121.

(248) Raja, A.; Chaves, A.; Yu, J.; Arefe, G.; Hill, H. M.; Rigosi, A. F.; Berkelbach, T. C.; Nagler, P.; Schüller, C.; Korn, T.; Nuckolls, C.; Hone, J.; Brus, L. E.; Heinz, T. F.; Reichman, D. R.; Chernikov, A. Coulomb Engineering of the Bandgap and Excitons in Two-Dimensional Materials. *Nat. Commun.* **2017**, *8* (May), 1–7. https://doi.org/10.1038/ncomms15251.

(249) Zhou, L.; Xing, L.; Zheng, Y.; Lai, X.; Su, J.; Deng, C.; Sun, T. A Study of External Surface Pressure Effects on the Properties for Lithium-Ion Pouch Cells. *Int. J. Energy Res.* **2020**, *44* (8), 6778–6791. https://doi.org/10.1002/er.5415.